Galaxy Evolution at High Redshift Exploiting Large Galaxy Surveys

by

Pierandrea Guarnieri

This thesis is submitted in partial fulfilment of
the requirements for the award of the degree of
Doctor of Philosophy of the University of Portsmouth.

March 29, 2019

Abstract

In this thesis I summarise the work done along with my supervisors and collaborators during my Doctor of Philosophy degree at the Institute of Cosmology and Gravitation, University of Portsmouth.

We performed multiple studies to further investigate galaxy formation and evolution with a special focus on the high-redshift universe. We made use of some of the most advanced galaxy surveys accessible to my supervisors, namely the Dark Energy Survey and the Spitzer Extra-galactic Volume Representative Survey.

Data from the former survey was utilised for the first time to probe the existence and properties of the most massive galaxies right after their formation at primordial times ($\gtrsim 10^{11}$ $M_{\odot}$, $z \sim 4$). My work exploited the theoretical predictions made by my supervisors and their previous collaborators, and I was the first one testing those predictions with the real Dark Energy Survey data. Starting from $\sim$ 5 million sources we first performed extensive data cleaning and analysis, such as removing stars and artefacts as well as prioritising the most promising initial candidates using colour-colour selection maps. We then used a photometric redshift code and stellar population models to fit the observed data and calculate the photometric redshift and physical properties of each candidate. We further developed a series of selection cuts, including goodness of fit and probability distribution functions, to finally narrow down our final selection of best candidates to 233 individual massive, high-z galaxies. This is the largest sample of massive, high-z candidate galaxies published so far. I led the refereed publication which describes

all the work. Our work provides the general community with a precious sample to be followed-up with current and future telescopes to acquire spectra and confirm their cosmic distances. We started this process with a Gemini Telescope proposal aimed at observing three of these sources. We have been granted time and the data obtained is currently under processing.

My other main research project utilised - again for the first time - a 13-band photometry catalogue of $\sim 750,000$ galaxies from ~ 5 sq. deg. of the Spitzer Extra-galactic Volume Representative Survey to investigate the mass assembly of massive galaxies across cosmic time. For this research I have calculated the galaxy stellar mass function up to $z \sim 4.5$. I have first fitted stellar population models to all the galaxy data in order to calculate their photometric redshifts, ages and stellar masses. The uniqueness of this survey is its unparalleled combination of width and depth as well as the sampling of rest-frame near-IR bands. These features make this survey especially important to investigate the massive ($\sim 10^{12.5}$ $M_{\odot}$) end of the galaxy stellar mass function at high redshift. Our results will compose the most ambitious measurements performed in this context. Within this project, we present detailed analysis of our photometric redshift validation procedure, by investigating any specific population of outliers (based on their stellar mass, age and more) and by utilising a set of spectroscopic data for $\sim 40,000$ galaxies. We also explore their consequences in the galaxy stellar mass function context. This extensive material will be published by my collaborators, including myself in the future.

Further contributions of mine to other scientific publications are presented at the end.

Table of Contents

List of Tables

List of Figures

Declaration

Whilst registered as a candidate for the above degree, I have not been registered for any other research award. The results and conclusions embodied in this thesis are the work of the named candidate and have not been submitted for any other academic award.

Word count: 35,429 words.

Acknowledgements

Firstly, I would like to thank my supervisors Claudia Maraston, Daniel Thomas, and Violeta Gonzalez-Perez for all their support and guidance throughout my time at the ICG. They were always there to help and encourage me.

Many thanks also to all the collaborators I have interacted with, and especially to Janine Pforr, Mark Lacy, Kristina Nyland, and Christopher Conselice for their help, and Micol Bolzonella for providing the HyperZ code. Thanks to Gary Burton and Jascha Schewtschenko, for any Sciama-related support I needed, and to all the rest of the ICG administration staff and members.

Many thanks to the University of Portsmouth for having funded my research, and to the Dark Energy Survey[1] and the Spitzer Extra-Galactic Representative Volume Survey collaborations.

[1]Funding for the DES Projects has been provided by the U.S. Department of Energy, the U.S. National Science Foundation, the Ministry of Science and Education of Spain, the Science and Technology Facilities Council of the United Kingdom, the Higher Education Funding Council for England, the National Center for Supercomputing Applications at the University of Illinois at Urbana-Champaign, the Kavli Institute of Cosmological Physics at the University of Chicago, the Center for Cosmology and Astro-Particle Physics at the Ohio State University, the Mitchell Institute for Fundamental Physics and Astronomy at Texas A&M University, Financiadora de Estudos e Projetos, Fundação Carlos Chagas Filho de Amparo à Pesquisa do Estado do Rio de Janeiro, Conselho Nacional de Desenvolvimento Científico e Tecnológico and the Ministério da Ciência, Tecnologia e Inovação, the Deutsche Forschungsgemeinschaft and the Collaborating Institutions in the Dark Energy Survey.

I would like to thank my parents and Alessandro as well as my grandparents and Walter for being the most supportive family I could have hoped for.

A special thank you to Sunita Ghalley, for all her love and for always being there for me. A big thank you also to her family, for always making me feel at home.

Lastly, I want to thank all my fellow PhD students and friends for making the office a welcoming and stimulating place. I will always remember with joy all our discussions and time spent together.

Dissemination

First-author Papers

- P. Guarnieri et al., *Candidate massive galaxies at $z \sim 4$ in the Dark Energy Survey.* MNRAS, 483:3060-3081, Mar 2019. doi: 10.1093/mnras/sty3305

- P. Guarnieri et al., *The Galaxy Stellar Mass Function with the Spitzer Extra-Galactic Representative Volume Survey. in prep.*

Co-author Papers

- Dark Energy Survey Collaboration, *The Dark Energy Survey: more than dark energy - an overview*, MNRAS, Aug 2016. doi: 10.1093/mnras/stw641

- M. Lacy et al., *A Subarcsecond Near-infrared View of Massive Galaxies at $z \sim 1$ with Gemini Multi-conjugate Adaptive Optics*, ApJ, Sep 2018. doi: 10.3847/1538-4357/aad27d

- I. Lonoce et al., *Stellar population properties of individual massive early-type galaxies at $1.4 < z < 2$, sub.*

Talks

- The Dark Energy Collaboration Meeting, Topic: *Candidate massive galaxies at $z \sim 4$ in the Dark Energy Survey*, SLAC, Stanford University, Menlo Park, USA, May 2016

- Annual Research and Innovation Conference, Topic: *Candidate massive galaxies at $z \sim 4$ in the Dark Energy Survey*, University of Portsmouth, Portsmouth, UK, June 2016

- The Spitzer Extra-galactic Volume Representative Survey Collaboration Meeting, Topic: *The Galaxy Stellar Mass Function with the Spitzer Extra-Galactic Representative Volume Survey*, Laboratoire d'Astrophysique de Marseille, Marseille, France, June 2016

- The Dark Energy Collaboration Meeting, Topic: *Candidate massive galaxies at $z \sim 4$ in the Dark Energy Survey*, The University of Cambridge, Cambridge, UK, December 2016

- The Spitzer Extra-galactic Volume Representative Survey Collaboration Meeting, Topic: *The Galaxy Stellar Mass Function with the Spitzer Extra-Galactic Representative Volume Survey*, Tufts University, Boston, USA, June 2017

- Wetton Workshop, Topic: *Candidate massive galaxies at $z \sim 4$ in the Dark Energy Survey*, The University of Oxford, Oxford, UK, May 2016

Notation

BOSS - Baryonic Oscillation Spectroscopic Survey
BPZ - Bayesian Photometric Redshift
CDM - Cold Dark Matter
CMB - Cosmic Microwave Background
D13 - Davies et al. (2013)
DES - Dark Energy Survey
DM - Dark Matter
GSMF - Galaxy Stellar Mass Function
HFF - Hubble Frontier Fields
M05 - Maraston (2005)
PDF - Probability Distribution Function
SDSS-III - Sloan Digital Sky Survey Data Release 3
SED - Spectral Energy Distribution
SERVS - Spitzer Extra-Galactic Volume Representative Survey
SFH - Star Formation History
SFR - Star Formation Rate
SV - Science Verification
VHS - Vista Hemisphere Survey
Y3 - Year 3

Chapter 1

Introduction

Since 1929 and Hubble's discovery of galaxies as the building blocks of our universe, extra-galactic astrophysics has quickly become one of the most intensive areas of research. Despite major steps forward over the last few decades, we are still at the beginning of our path to understanding the fundamental processes that govern galaxy formation and evolution, both internally and in a cosmological context. We are now in the privileged position to give our small contribution to the knowledge of the laws that control our universe, as other astronomers and curious gazers have done for thousands of years.

1.1 A Historical Review

All major civilisations always showed an interest in astronomy. From ancient Egypt to Babylonian ruins, we find numerous documents showing early studies of the cosmos.

However, the ancient Greek Pythagoras was the first scholar to have developed a complete, although basic, cosmological model. This placed the Sun, the Earth, the Moon, and all known planets (Mercury to Jupiter) in concentric spheres filled of air rotating around an unknown 'Central Fire'. The stars would instead collectively populate the outermost sphere.

Interestingly, Pythagoras did not place the Earth at the centre of the universe, but it was Ptolemy to first do so in the second century A.D. His model described the Earth at the centre of a circular orbit inhabited by the Sun. All other planets would then orbit around the Sun in circular orbits themselves. This extra complexity was necessary to try and explain the observed irregularities of the motion of planets with respect to the stars. With the Roman Empire crumbling and the Church pushing for a literal interpretation of the Bible, geocentric theories remained unchallenged until the end of the Middle Ages.

During the Renaissance, it was thanks to the work of Copernicus, among others, to better describe the observed trajectories of celestial bodies, and Galileo's studies of Venus's phases and Jupiter's moons that the world started accepting heliocentric cosmological models.

Herschel's work on what he defined as 'nebulae' in the early 19th century as well as, one hundred years later, Hubble's efforts to understand the place of these 'nebulae' in the universe gave birth to the modern age of cosmology. The 'nebulae' were really what today we know to be galaxies and, crucially for the scope of this thesis, this was the start of galactic and extra-galactic astrophysics.

1.2 The Structure of the Universe

As astronomers discovered that the universe far exceeded the size of the Milky Way, they realised that parallax-like effects were not enough to determine the distance of some celestial objects, such as galaxies. Hubble used Cepheids, a type of variable pulsating stars, from other galaxies to determine their distance from us, exploring the real size of the universe for the first time. Hubble also discovered that the farther away galaxies are, the faster they recede away from us. They effectively discovered the expansion of the universe by looking at the spectral features of other galaxies and noticing that it underwent a Doppler-like effect, or 'redshifting'. The redshift then became the standard

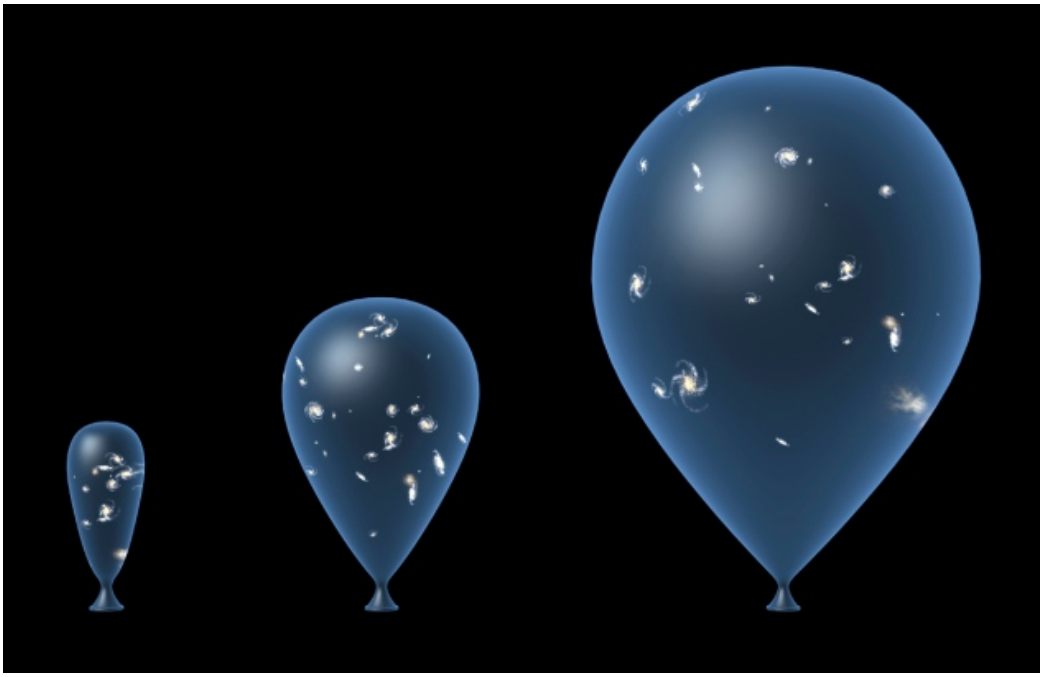

Figure 1.1: The universe can be visualised as an inflatable balloon where each galaxy is represented by a dot on it. As the universe expands, all galaxies recede from one another and they do so faster as the farther they are from each other. Credits: Nature, https://www.nature.com/news/cosmologist-claims-universe-may-not-be-expanding-1.13379

way of quantifying the distance of a source from us. On large scales galaxies all recede from us because the universe is expanding everywhere. This does not mean that we are at the centre of it, as many old scholars assumed, but rather that the universe behaves like an inflatable balloon and each galaxy is a point on it. Figure 1.1 visualises this concept. It is important to note that on smaller scales the gravitational pull can still be strong enough to counteract this effect. This is why some nearby galaxies like Andromeda are actually moving towards us.

Still in the first half of the 20th century, Einstein had contemplated a homogeneous and isotropic universe. This means that over large scales the universe is the same and it looks the same when seen in all directions from a

given point. This cosmological principle, along with the observational effects studied by Hubble, allowed Lemaitre and Friedmann to finally kill any steady-state universe conjectures, which were popular at the time, and to formulate the 'Big Bang' theory. In fact, it seems natural nowadays to think that if the universe is currently expanding then as we go through cosmic time backwards we must get to an arbitrary point in time (around 14 billion years ago) when matter and the universe itself were created. This first moment would be the Big Bang.

The evolution of the universe since the Big Bang until modern times can be visualised in Figure 1.2. This diagram shows the most important milestones of the universe as far as extra-galactic studies are concerned. We first see the original density fluctuations that we today observe in the form of the Cosmic Microwave Background (CMB), then the first stars are born around 400 million years after the Big Bang, and finally galaxies as large collections of stars are formed. The initial inhomogeneities were crucial to kickstart structure formation as we see it today. These were just the first steps that allowed gravity to do its course and slowly assemble increasingly larger mass, from stars to galaxies and even large scale structures (filaments of galaxies and clusters of galaxies that permeate the universe). This type of structure does not violate the Cosmological Principle as this structure is significant only on smaller scales, compared to the size of the universe. We know today that the visible (baryonic) mass we observe could not be enough to drive so quickly the formation of structure as we detect it. Fundamental to this outcome is Dark Matter (DM), an exotic type of matter that we cannot observe directly but we can detect through its gravitational influence. In the 1930s Zwicky was among the first to postulate the existence of DM while studying the behaviour of galaxies around the Coma Cluster. It was later understood that DM is necessary to also explain the rotation curve of galaxies in the outer regions (Rubin et al., 1985). DM is now known to constitute around 26% of the universe, while baryonic matter accounts only for $\sim 5\%$ (the rest is made of Dark Energy, the driving force behind the accelerating

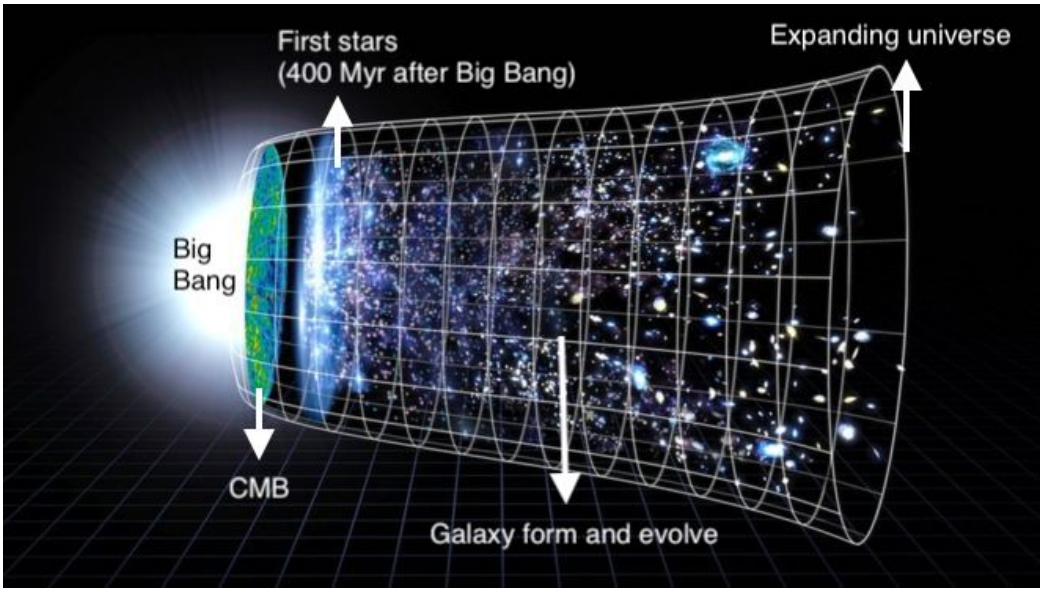

Figure 1.2: The most important milestones of the universe as far as extra-galactic studies are concerned are shown. We first see the original density fluctuations that we today observe in the form of the Cosmic Microwave Background (CMB), then the first stars are born around 400 million years after the Big Bang, and finally galaxies as large collections of stars are formed. Credits: NASA

expansion of the universe; Planck Collaboration et al., 2018; Riess et al., 1998; Perlmutter et al., 1999). The theory of the Big Bang, baryonic matter, Dark Matter, and Dark Energy constitute the fundamental elements of the widely accepted modern cosmological model, ΛCDM (Λ refers to an option for Dark Energy, while CDM stands for Cold, as weakly-interacting, Dark Matter).

In this type of universe as described just above, it is clear that galaxies are the fundamental blocks of the structure we observe, and therefore their formation and evolution are central to the understanding the cosmos as a whole.

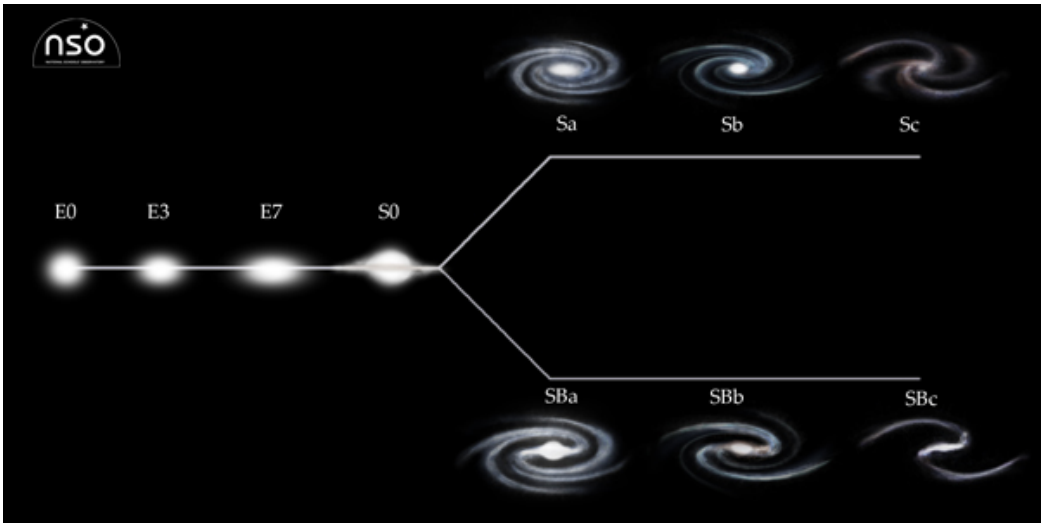

Figure 1.3: The Hubble sequence, or 'Tuning Fork'. This type of classification separate elliptical, or early-type, galaxies (left-hand side) from spirals, or late-type, galaxies (right-hand side). Moreover, spirals can be split between barred and un-barred. Bars are over-densities of stars in the central regions of some spirals and are thought to be due to dynamical processes that change and form these structures during time. Credits: NSO, Liverpool John Moores University, https://www.schoolsobservatory.org/learn/astro/gals/class

1.3 Galaxies

Hubble's work included classifying galaxies according to their morphology through the famous Hubble sequence, or 'Tuning Fork'. An example diagram of this is shown in Figure 1.3. This type of classification separate elliptical, or early-type, galaxies (left-hand side) from spirals, or late-type, galaxies (right-hand side). Moreover, spirals can be split between barred and un-barred. Bars are over-densities of stars in the central regions of some spirals and are thought to be due to dynamical processes that change and form these structures during time. While Hubble's classification implied ellipticals being progenitors of spiral galaxies, it is now accepted that the 'Tuning Fork' is not an evolutionary sequence and, as described later, more complex processes are at play.

As telescopes improved, astronomers could observe fainter galaxies and realised that dwarf galaxies are actually the most common type across the universe. These are similar to ellipticals, but much smaller and therefore were largely unnoticed by Hubble. Furthermore, galaxies with an unclear shape are also classified today as 'irregulars'. This happens relatively often due to merging processes or tidal stripping due to the gravitational pull of nearby galaxies.

Other than shape, ellipticals and spirals differ in several other ways. Firstly, ellipticals are generally the largest types of galaxies and because of this, despite spirals being more abundant, they account for most of the baryonic mass in the local universe (Bell et al., 2003). In terms of colour, ellipticals are much redder (at least in the local universe), while spirals are bluer. As we will describe in Section 1.4, this means that elliptical galaxies host older stellar populations and contain higher fraction of heavy elements (high metallicity). On the other hand, late-type galaxies have more gas content and are dominated by young, bright stars. Ellipticals are also generally found in clusters, while spirals are more common in the field (Dressler, 1980).

This bimodality results in two mostly distinct populations of galaxies. By plotting colour against the mass (or luminosity) of a galaxy it was possible to identify two separate regions of the parameter space: the 'red sequence', inhabited by early-type galaxies, and the 'blue cloud', populated by spirals (Faber et al., 2007). In the middle, the so-called 'green valley' is occupied by only a relatively small number of galaxies. This picture is exemplified by the diagram shown in Figure 1.4, which is an adapted version of the plots shown in Faber et al. (2007). The arrows show the assumed evolutionary steps in the merging model (see next section). At a fundamental level, the aim of studies of galaxy formation and evolution is to understand what internal or external processes govern the position of a given galaxy in this type of diagram.

These studies also aim to verify whether what we observe in the local universe is valid across cosmic time. We can reconstruct the history of the universe by looking increasingly farther away, which thanks to the finite speed

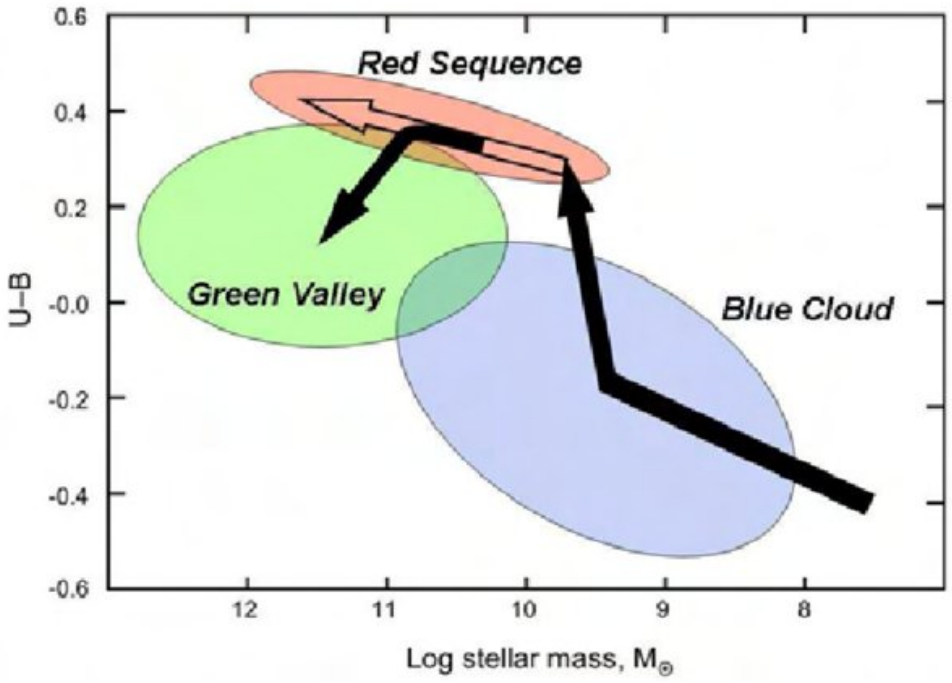

Figure 1.4: Galaxies are plotted with their colour as a function of their mass (or luminosity). On this diagram ellipticals and spirals inhabit different parts of the parameter space. The former are found in the red sequence, and the latter constitute the blue cloud. The transitioning area in between has few observed galaxies and is the so-called green valley. This is a diagram adapted from one of the figures of Faber et al. (2007) and the arrows correspond to the merging model. Credits: Research Gate

of light also means back in time.

Only in recent years the latest telescopes in combination with modern data reduction techniques allowed astronomers to investigate the high-redshift universe up to galaxy formation times. The limits have been pushed in particular by programmes like the Hubble Frontier Fields (HFF). This project used gravitational lensing to detect galaxies, and potentially proto-galaxies, up to $z \sim 11$ hidden behind galaxy clusters. This type of work clearly could not systematically analyse galaxies at such high redshifts, but paved the way for what will be possible to observe directly with future telescopes, such as the James Webb Space Telescope, currently planned for 2021.

At the same time, other surveys like the ones used for this work, i.e. the Dark Energy Survey and the Spitzer Extragalactic Representative Volume Survey, allowed researchers to investigate the older universe with increasingly better statistics. As it will be described in chapters 2 and 3, these two surveys combined enough width and depth to improve our understanding of what types of galaxies inhabit the universe at redshifts close to $z \sim 5$.

We are still in the early days before being able to fully investigate the morphology of these high-redshift galaxies through full-fledged spectroscopic observation programmes (see Section 1.5), but photometric work can already estimate their basic properties. These include the photometric redshift, the stellar mass, the age, the star formation history, and the metallicity and they can be calculated by comparing the galaxy photometric data to stellar populations models (see Chapter 2 and 3).

If we are to investigate the galaxy evolution and formation processes at increasingly higher redshifts, it is first important to identify the most promising theoretical models describing these phenomena.

1.3.1 Models of Galaxy Formation and Evolution

Today's generally accepted cosmological model is the so-called ΛCDM model. This predicts structure to form hierarchically during the lifetime of the universe. In particularly, this model assumes that baryonic matter largely traces

DM and the largest galaxies are formed through merging of smaller ones.

Computational simulation can easily reconstruct DM behaviour across cosmic time, as it is solely dependent on gravitational effects. This means that we can effectively recover the 'dark universe' based on current theory. On the other hand, the baryonic universe (i.e. stars, galaxies, gas, and dust) not only is under the influence of gravity, but more complex processes also need to be considered to replicate what we observe. These physical phenomena include star formation, supernova and AGN feedback, and heating and cooling processes. These are implemented in modern simulations by utilising semi-analytical models.

The theory of hierarchical galaxy formation dates back to studies like Press and Schechter (1974). As explained earlier, the basic assumption is that galaxy form as relatively small-mass disc galaxies and slowly merge to form larger-mass ellipticals. However, originally the predominant galaxy evolution framework was though to be monolithic collapse (Eggen et al., 1962). This formalism, also called 'downsizing' (Cowie et al., 1996), is in contradiction with the canonical ΛCDM model as it predicts the largest early-type galaxies to have formed directly via the simple gravitational collapse of gas. These two models of galaxy formation and evolution are exemplified in Figure 1.5 on the left-hand and right-hand panels, respectively.

Discerning which of the two models apply to our universe is a matter of active research. While hierarchical galaxy formation matches ΛCDM predictions, there seems to be increasingly higher evidence of downsizing. For instance, Cimatti et al. (2006) showed that massive ($\log(M/M_{\odot})> 11$) elliptical galaxies are in place since $z \sim 0.8$, and the downsizing behaviour covers both the star formation and the mass assembly. Thomas et al. (2005) and Thomas et al. (2010) also concluded on downsizing by determining the formation epochs and star formation duration as a function of mass using chemical evolution arguments. Moreover, these studies, along with Cimatti et al. (2004), found that massive galaxies quickly formed first at high redshifts, while smaller-mass systems display on-going star formation for longer

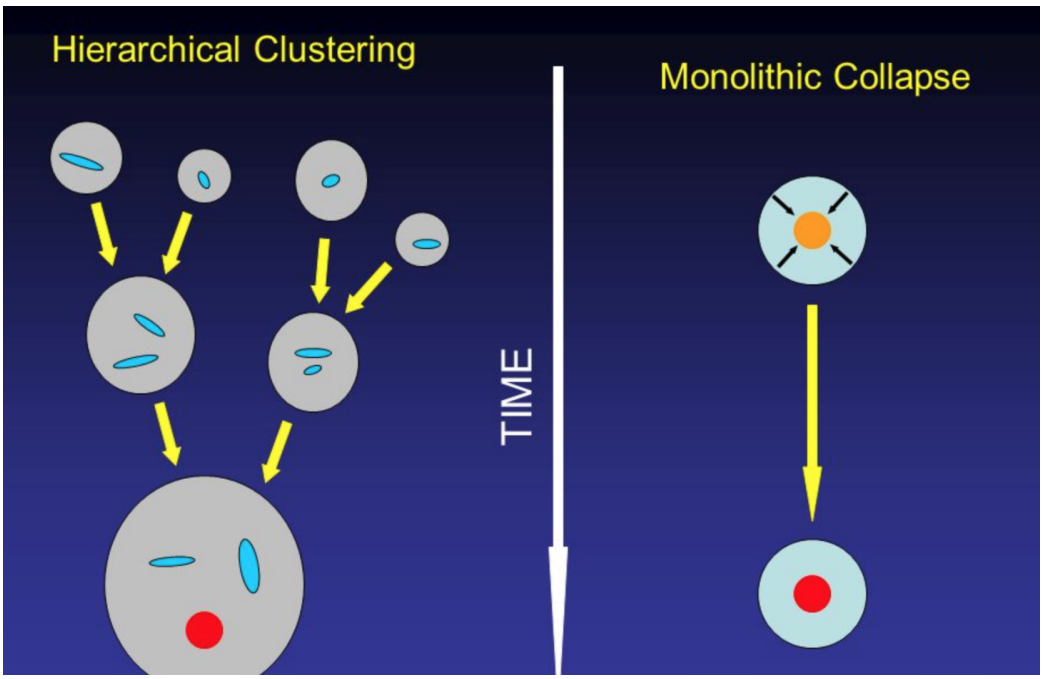

Figure 1.5: The two major models of galaxy formation and evolution are shown. On the left-hand side, hierarchical clustering shows smaller-mass spirals merge across cosmic time to create the most massive ellipticals. On the other hand, under monolithic collapse, or downsizing, (right-hand side) large gas clouds are expected to directly form the massive ellipticals seen in the local universe. Credits: Ricardo Schiavon, University of Virginia, https://slideplayer.com/slide/8963517/

times.

In order to further probe galaxy formation and evolution, it is not only important to analyse the models described above that operate at scales comparable to the size and lifetime of the universe, but also to better comprehend the fundamental parts that compose galaxies themselves. These are the stars and more information on these is found in the following section.

1.4 Stars

As gas clouds collapse on themselves due to the pull of gravity, they slowly split in smaller clumps that eventually give birth to stars. The gravitational collapse leads to an increase of inward pressure until temperatures at the centre of the clump are high enough to ignite the fusion of hydrogen. From this follows the emission of outward radiation, and once this balances the inward collapse it can be said that the star has formed. This position of balance is the so-called hydrostatic equilibrium.

By looking at the relationship between star luminosity and temperature (see Figure 1.6) it is possible to infer the star's evolutional phase. This type of diagram is called the Hertzsprung-Russell (or H-R) diagram, from the names of its creators. When a star is formed it sits on the Main Sequence, where it spends the most of its lifetime. The more massive a star is the hotter, and thus bluer, it tends to be. Massive, blue stars tend to have relatively short life-spans, while redder stars have longer and more complex lives.

When stars with masses smaller than 8 solar masses approach the end of their hydrogen resources at their core, the outer hydrogen shells start burning initiating their transition to giant stars. The helium core also starts burning, the stars have fully become red giants. When the core has turned into carbon and oxygen, only the outer shells continue to burn until the envelope gets expelled. This process leaves behind a white dwarf (bottom-left of the diagram) for stars with a mass less than 8 solar masses. For stars with higher masses, their final stages involve violent explosions called

Supernovae. These happen after their cores have formed heavier elements up to iron, the chemical limit at which fusion can produce energy. At this stage, the cores collapse until the stars explode as Supernovae. If the initial star mass undergoing this process is between 8 and 40 solar masses, Supernovae leave behind neutron stars, while for higher masses black holes are created.

1.5 Spectroscopy and Photometry For Galaxy Data

In order to learn more about a given observed star it would be ideal to observe its spectrum. This is a complete measurement of its flux for a predetermined wavelength range, depending on the telescope instrument specifications. From these types of observations it is possible to identify absorption or emission lines that allow astronomers to know which elements make up the observed star.

Spectroscopic techniques are also useful to study the content of galaxies to further understand how the stellar content affects galaxy evolution. As galaxies comprise multiple stars, spectroscopic observation of galaxies result in spectra that are different from those of single stars. The resulting spectra are summations of the spectra on the stars contained in a given galaxy. Galaxy spectra therefore tend to have wider absorption and emission lines (due to the inherent movement of internal stars) and stellar population models are used to infer the physical properties of galaxies (including star formation history and age). Moreover, the intensity of specific emission or absorption lines allow astronomers to infer the precise fractions of elements that belong to a galaxy.

It is important to note, however, that spectroscopic observations are very expensive and require a considerable amount of time. From this follows that large surveys can rarely spectroscopically observe large quantities of galaxies, especially farther than the local universe. The most ambitious spectroscopic survey so far is the SDSS-III/BOSS survey (Dawson et al., 2013), which

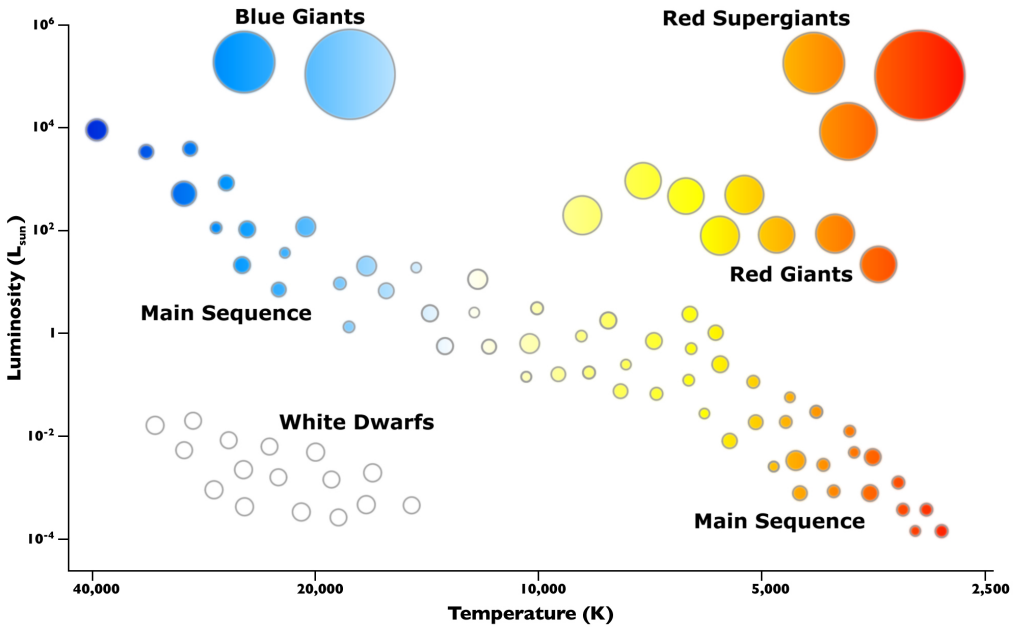

Figure 1.6: Diagram of luminosity vs. temperature of stars. This picture helps classify stars efficiently and from their position on the parameter space it is possible to infer the evolutional phase of a given star. Stars spend most of their lives in the Main Sequence, where blue stars tend to die quickly, while red stars have longer lifetimes. While blue giants are generally simply very massive blue stars, red giants and supergiants are mid-temperature to colder stars that started burning heavier elements as they approached the end of their lives. The least massive of these end up expelling their outer layers leaving behind white dwarves (bottom-left area of the diagram), while the more massive ones can end up forming neutron stars or even black holes. Credits: Stefan V., https://socratic.org/questions/what-is-the-hertzsprung-russell-diagram-and-why-is-it-so-important-to-astronomy-

observed $\sim$ 1.3 million spectra. Its efficiency still cannot compete with other photometric surveys like the Dark Energy Survey that in a similar amount of time has observed almost 400 million galaxies. Moreover, MaNGA is another type of spectroscopic survey that has the additional benefit of providing IFU spectroscopic data, meaning that each pixel contains a full independent spectrum and so we can study how the spectrum of the galaxy varies as a function of the radius. However, even this ambitious project will 'only' have observed up to $\sim$ 10000 nearby galaxies at completion.

Photometric data is effectively spectroscopic data with much lower resolution. While spectroscopy manages to almost measure the spectra continuously over a wavelength range, photometry measures the flux for just a few effective wavelength values. The difference between the two methods can be visualised in Figure 1.7. This data comes from an arbitrary example galaxy whose spectrum is shown as a black solid line and whose photometry is indicated by the red dots. It can be understood that the photometric points shown here correspond to what the spectrograph would observe, were its resolution considerably lower.

It is also important to note that the photometry is measured by the telescope using filters that have a pre-determined sensitivity to different wavelengths. This means that the photometric measurement is not always exactly at the same flux level as the spectrum because it is influenced by neighbouring flux readings. As an example, we can look at the fifth photometric point from the left (at wavelength $\sim 4800\mathring{A}$) of Figure 1.7. This datapoint is found to be higher than the value of the observed spectrum at the same wavelength. This is because the photometric reading has likely been affected by the nearby bright emission line. From this we can infer also that because of the lower resolution of photometric observations, these are much less likely to directly detect emission or absorption lines and therefore have clear limitations compared to spectroscopy.

On the other hand, as described earlier, photometric studies are crucial to investigate an amount of galaxies orders of magnitudes higher than it

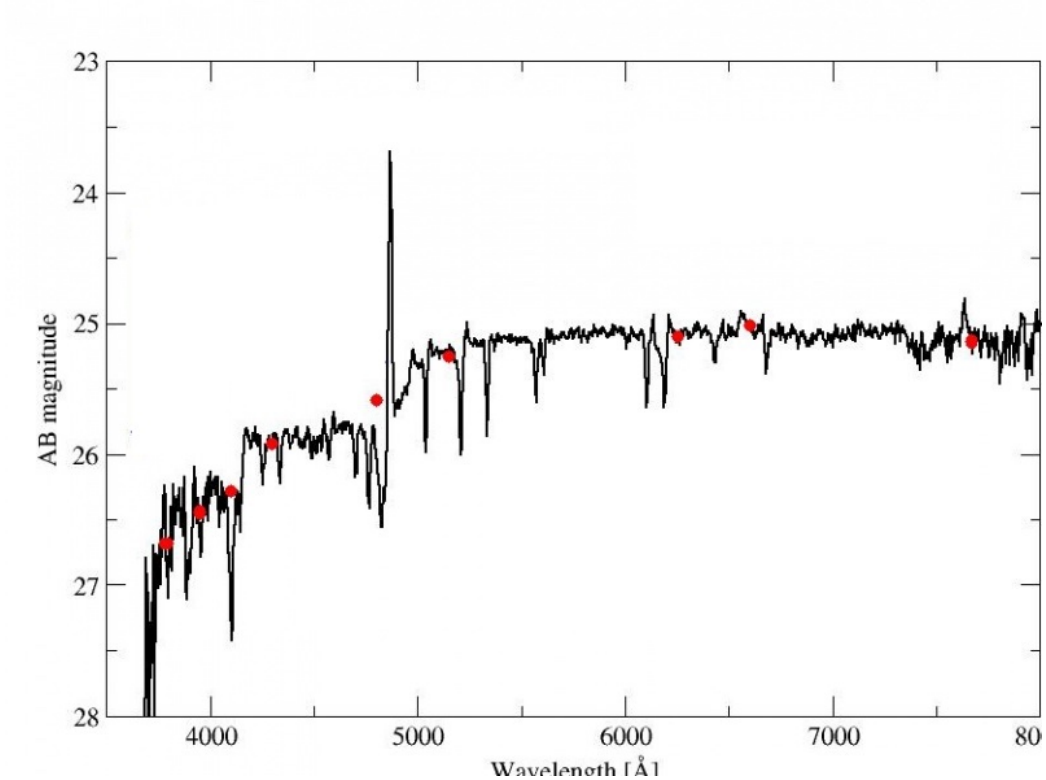

Figure 1.7: For an example galaxy, its spectrum is shown as a black line and corresponds to what would be observed with a spectrograph. The red points show what would instead be observed as part of a photometric programme. This is in essence a very low resolution spectroscopic observation. Because of this, photometric observations may miss important emission or absorption lines and therefore have limitations compared to spectroscopic ones, although the latter are order of magnitudes more expensive in terms of observation time. Credits: J-PLUS, http://www.j-plus.es/survey/high-redshift_galaxies

would be possible with spectroscopy alone. Crucial to the work presented in this manuscript, photometry allowed us to probe galaxies at very high redshifts (up to $z \sim 4.5$) which would not have been possible with any other spectroscopic dataset. While high-redshift morphological studies will require better instruments in the future, fitting photometric data to stellar populations models is already allowing us to push the boundaries of observational astrophysics.

1.5.1 Galaxy Physical Properties from Stellar Population Models

The best way to calculate the physical properties of galaxies from their photometry is to use the spectra energy distribution (SED) fitting procedure. This methodology fits the photometric data of a given galaxy to a chosen set of stellar population models, or templates. The properties of the galaxy are therefore calculated to be those associated with the best-fit model. These include ages, dust content, metallicity, and star formation history.

Results are, however, not always easy to interpret as it is possible that wildly different models have a similar spectrum. For example, an old, dust-free galaxy may look very similar to a young and dusty one.

It can be visualised how the spectrum of a galaxy changes at different stages of its life. In Figure 1.8, the spectrum for a simple stellar population model with solar metallicity is plotted at different ages, from 1 Myr (top curve) to 10 Gyr (bottom curve). It can be noticed that the younger a galaxy is, the brighter it appears at shorter wavelengths. This suggests that the range of the photometric data available can play a crucial role in distinguishing between galaxies with very different ages (or other parameters). For example, if we only had bands covering the near-infrared part of the spectrum it would be difficult to fully discern the age of this galaxy.

It follows that in most cases further considerations and detailed analysis are required in order to reliably pin down the nature of observed galaxies and from these draw conclusions on galaxy evolution and formation.

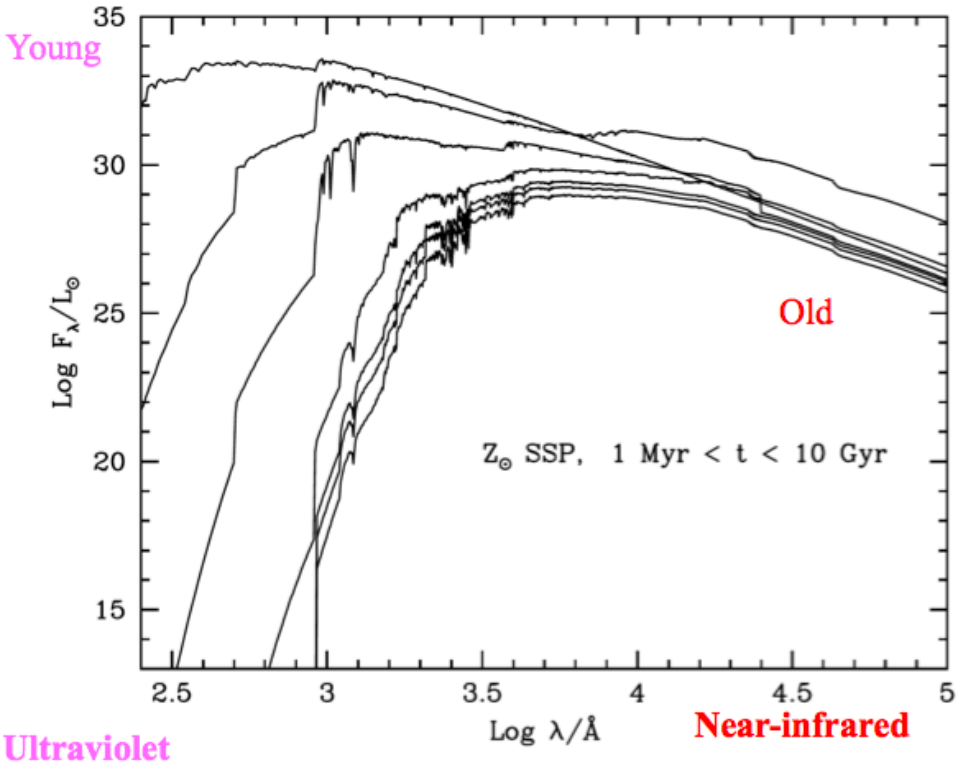

Figure 1.8: The spectrum for an arbitrary simple stellar population model with solar metallicity is shown for different ages, from 1 Myr to 10 Gyr. It can be appreciated that the younger a galaxy is, the brighter it is at shorter wavelengths. Moreover, it can be seen that the wavelengths range observed can play an important role in order to differentiate between models with different ages, and different models altogether. Credits: Cimatti, courtesy of Maraston

1.6 Thesis Motivation and Structure

In this work, we aimed to make use of some of the latest state-of-the-art datasets available at the University of Portsmouth to push our understanding of galaxies evolution with a focus on high redshifts.

In Chapter 2, we present our work using the Dark Energy Survey data to search for massive galaxies at $z \sim 4$ in order to try and build up evidence in favour or against downsizing.

In Chapter 3, we instead study the galaxy stellar mass function up to $z \sim 4.5$ to gain more insights on galaxy evolution across cosmic time.

In Chapter 4, we validate our photometric results from Chapter 3 and we investigate the limitations of photometry within the galaxy stellar mass function context.

After these three main chapters, Chapter 5 describes extra work that has been done along with other collaborators and some yet incomplete spectroscopic observations related to our work on the Dark Energy Survey. Lastly, Chapter 6 summarises the main points of the thesis and draws the most important conclusions.

Preambles summarising the chapters or specific literature reviews to each branch of work are found at the beginning of each chapter whenever relevant.

Chapter 2

Candidate Massive Galaxies at $z \sim 4$ in the Dark Energy Survey

2.1 Preamble

Using stellar population models, we predicted that the Dark Energy Survey (DES) - due to its special combination of area (5000 deg.sq.) and depth ($i = 24.3$) - would be in the position to detect massive ($\gtrsim 10^{11}$ $M_{\odot}$) galaxies at $z \sim 4$. We confront those theoretical calculations with the first ~ 150 deg. sq. of DES data reaching nominal depth. From a catalogue containing $\sim$ 5 million sources, $\sim$ 26000 were found to have observed-frame $g - r$ vs $r - i$ colours within the locus predicted for $z \sim 4$ massive galaxies. We further removed contamination by stars and artefacts, obtaining 606 galaxies lining up by the model selection box. We obtained their photometric redshifts and physical properties by fitting model templates spanning a wide range of star formation histories, reddening and redshift. Key to constrain the models is the addition, to the optical DES bands g, r, i, z, and Y, of near-IR J, H, K_s data from the Vista Hemisphere Survey. We further applied several quality cuts to the fitting results, including goodness of fit

and a unimodal redshift probability distribution. We finally select 233 candidates whose photometric redshift probability distribution function peaks around $z \sim 4$, have high stellar masses ($\log(M^*/M_\odot) \sim 11.7$ for a Salpeter IMF) and ages around 0.1 Gyr, i.e. formation redshift around 5. These properties match those of the progenitors of the most massive galaxies in the local universe. This is an ideal sample for spectroscopic follow-up to select the fraction of galaxies which is truly at high redshift. These initial results and those at the survey completion, which we shall push to higher redshifts, will set unprecedented constraints on galaxy formation, evolution, and the re-ionisation epoch.

2.2 Introduction and Motivation

The formation and evolution of the most massive galaxies in the universe remains an open problem in cosmology and astrophysics.

The fossil stellar population in the local universe shows that the most massive galaxies host the oldest stellar populations and that they should have formed around $z \sim 5$ (Cowie, Songaila, and Barger, 1999; Thomas et al., 2005, 2010; Cowie and Barger, 2008). Radial gradients in stellar populations which are flat in age and element abundance ratios (Mehlert et al., 2003; Pipino et al., 2007; Goddard et al., 2017; Sánchez et al., 2012) suggest that the early formation is a global property of the galaxy rather than of just its inner core.

Within the hierarchical galaxy formation paradigm (White and Rees, 1978), the most massive objects assemble last, at relatively low redshift ($z \sim 0.5$) even if their building blocks may contain ancient stellar populations that later merge (De Lucia et al., 2006; Ricciardelli and Franceschini, 2010). This model implies a scarcity of massive galaxies at high redshift and their gradual build-up towards our epoch (Gonzalez-Perez et al., 2009). Hence, one key approach for constraining galaxy formation on a cosmological scale is to search for the progenitors of the most massive galaxies at an

increasingly larger look-back time.

Massive galaxies are indeed being found spectroscopically at increasingly higher redshifts, in the range $z \sim 1.5 - 3.0$ (Lonoce et al., 2015; Yan et al., 2004; Onodera et al., 2012; Cimatti et al., 2004; Kriek et al., 2016; Straatman et al., 2014; Conselice et al., 2007; Whitaker et al., 2013) and even $z \sim 3 - 4$ (Mancini et al., 2009; Santini et al., 2009; Caputi et al., 2012, 2015b; Guo, 2013; Ilbert et al., 2013b; Muzzin et al., 2013b; Stefanon et al., 2013; Marsan et al., 2017). At such high redshifts, usually the word 'massive' refers to stellar masses up to $\sim \ 10^{11} \ M_{\odot}$. The highest value reported so far is a $1.7 \times 10^{11} \ M_{\odot}$ galaxy at a spectroscopic redshift of 3.717 (Glazebrook et al., 2017). The detection of such an impressively massive galaxy at such a high redshift is a challenge to galaxy formation models. We shall return to these works in relation to our project.

In order to bridge the fossil record with the formation event and trace galaxy evolution over cosmic time, many works have attacked the problem in a statistical sense, by probing number density evolution as a function of galaxy mass. Studies of the galaxy mass function over the past decade reached the uniform conclusion that the abundance of the most massive galaxies ($M/M_{\odot} > 10^{11.5}$) hardly evolves since $z \sim 1$ (Cimatti, Daddi, and Renzini, 2006; Wake et al., 2006; Pozzetti et al., 2010b; Marchesini et al., 2010; Muzzin et al., 2013b; Gonzalez-Perez et al., 2009; Mortlock et al., 2015). One caveat to these studies has been that the observational database was drawn from small area, deep surveys, which carry the problem of cosmic variance. This is particularly severe at the highest mass where the galaxy mass function is steep and errors on photometric data are large. However, this has been recently solved by using the cosmological SDSS-III/BOSS survey (10,000 deg. sq.). This survey has allowed the calculation of the galaxy mass function around $M^* \sim 10^{12} \ M_{\odot}$ with unprecedented statistics (Maraston et al., 2013) thanks to the large area and the target selection centred on massive galaxies. The conclusion of this work is that the abundance of the most massive galaxies is constant in the redshift range 0.4-0.6, and larger

than what is predicted by galaxy formation models. Bundy et al. (2017) using deeper photometry from the so-called Stripe82 region reached the same conclusion and showed that it is robust against the way stellar masses are calculated. Furthermore, Etherington et al. (2017), using data from the Dark Energy Survey (DES) survey (see below), showed that the evolution of the high-mass end of the galaxy mass function does not seem to depend on the environment. Thomas et al. (2010) reached the same conclusion performing a different analysis, namely using the chemical information in the fossil stellar population properties of the most massive galaxies. They showed that ages, metallicities and chemical abundance ratios of the most massive galaxies do not depend on the environment, leading to the inference that their formation and evolution are mainly driven by internal processes, reinforcing downsizing as the evolution paradigm for these galaxies (Peng et al. 2010).

As just mentioned, probing the massive end of the galaxy population requires a wide survey area. The Dark Energy Survey (DES) is a galaxy survey aimed at probing cosmic acceleration. The survey is collecting galaxy photometric data in the southern sky at magnitude depths of ∼25.5, 25.0, 24.4, 23.9 and 22.0 in the g, r, i, z and Y bands respectively, for a very large portion of sky (5000 deg. sq.) (Rossetto et al., 2011; The Dark Energy Survey Collaboration, 2005). At completion ($\sim$ 2019), DES will have observed on the order of 300 million galaxies.

Davies et al. (2013) (hereafter D13) forecasted that - by virtue of its suitable combination of area and depth - DES is currently the best survey to detect the rare, massive ($\sim 10^{12} M_{\odot}$) galaxies at high redshift ($z \gtrsim 4$), should these exist (see Figure 2 in D13). D13 used stellar population models spanning a wide range of properties (e.g. age, metallicity, star formation history, stellar mass and dust reddening) to model galaxies as a function of DES magnitude, colours and redshift, identifying colour-colour selection maps for redshifts $z \sim 4, 5$, and 6 (see Figures 7,8,9 in D13).

The scope of the present paper is to apply the D13 theoretical selection maps to a sample of real DES data for the first time, specifically the latest

available set of Year 3 (Y3) data, in order to find candidate massive high-z galaxies. The data we use consist of observations completed on a limited sky region (~ 150 sq. deg.) probed since the Science Verification (SV) programme (thus at the DES nominal depth) in order to test the observational process and general workflow.

We first proceed by plotting the new DES data on the D13 colour-colour plots, and then calculate the photometric redshifts and physical properties of those sources falling into the predicted boxes for $z \sim 4$ galaxies, after carefully removing artefacts of various kinds. We focus on $z \sim 4$, rather than on $z \sim 5$ or $z \sim 6$, as if these rare massive galaxies exist they are more likely to be observed at lower redshifts. We need to maximise our chances given the smaller area covered by the SV footprint compared to the one that will be available at DES completion.

Calculations of template-based photometric redshift are the common procedure at high redshift, but we shall also discuss the effect of using alternative redshifts from the DES neural network pipeline Sánchez et al. (2014). Instrumental to the robustness of our fitting is the availability of near-IR bands from the Vista Hemisphere Survey (VHS) McMahon (2012); Banerji et al. (2015a), which could extend the baseline photometry to a total of 8 filters. It is interesting to test whether the final results are consistent with the D13 predictions, which were based on the sole g, r, i, z, Y DES magnitudes.

We then analyse in detail the fitting results for all candidates and conservatively retain only those obeying several quality criteria, including a unimodal probability distribution function in redshift, a good χ^2_r and other model parameters.

At the end of the procedure we select 233 individual galaxies, of which some are selected with both reddening options. We find 109 using the SMC reddening law and 203 using the Calzetti law. For these, we examine their properties (including mass, age, SFR, SFH) and draw initial conclusions on galaxy evolution, using also galaxy formation simulations as a comparison.

The chapter is structured as follows. Section 2.3 describes our method

to find high-z candidates, which includes an initial colour selection (Section 2.3.2) and photometric template fittings to calculate photometric redshifts and physical properties (Section 2.3.3). In Section 2.4 we describe in detail our best candidate selection, including their physical properties. In the same section we detail further tests we completed to check the reliability of our sample. In Section 2.5 we perform a comparison with the literature. Lastly, in Section 2.7 we summarise our work and discuss our key findings as well as their relevance for future work and in the context of current research.

2.3 Method

2.3.1 Overview

Our aim is to identify the most likely high redshift ($z \sim 4$) massive galaxy candidates within a dataset of $\sim$ 4.9 million objects. Starting from the simulations performed by D13 we proceed using real DES data in this context for the first time. In this work we focused on the $z \sim 4$ case in order to maximise the chance to find objects in the small area covered by the SV data.[1] The process we followed in order to identify the best candidates is comprised of different steps. We summarise them here and discuss each of them in separate sections below.

At first all Y3 data were placed on the D13 colour-colour plots (Figure 2.1, top left-hand panel). Then, the catalogue was scanned to remove sources that could potentially be stars and/or those affected by the largest errors. The sources passing these two criteria (non-stars and small errors) are plotted in Figure 2.1, top right-hand panel. From this point, we focus on the objects lying within the D13 selection box for massive, $z \sim 4$ galaxies (solid black line in Figure 2.1). These candidates were further pruned of those potentially

[1] An initial look at the $z \sim 5$ and 6 selection maps (from D13) did not result in any high-z candidates, but this does not exclude the possibility that they exist and it may be due simply to the fact that the SV data cover only $\sim$ 150 deg. sq. We shall pursue the higher redshift bins when we look at the entire database.

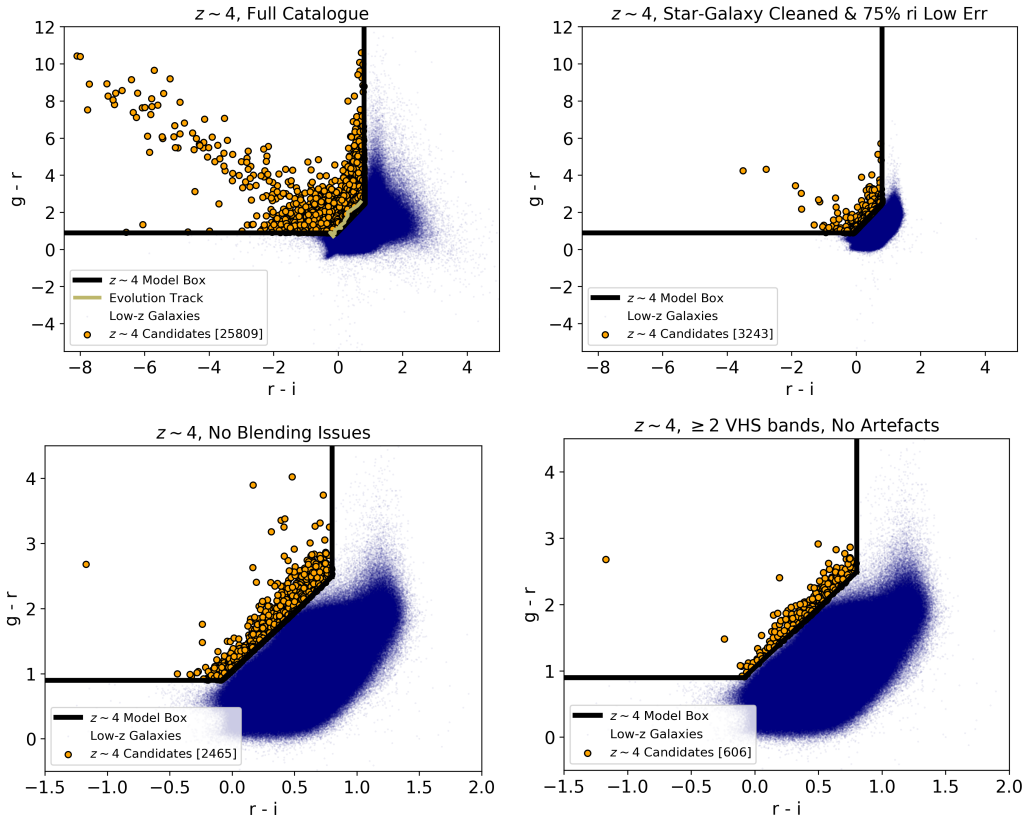

Figure 2.1: Colour-colour selection maps for selecting massive $z \sim 4$ candidates using DES photometry, as from D13. Black solid lines define the predicted selection boxes for $z \sim 4$ (red g-r, blue r-i relative to the black line), with the khaki line in the top left panel showing the redshift evolution track for a model galaxy as illustration. Orange dots correspond to sources identified as high-z candidate galaxies lying in the model selection area. Objects that fall outside the selection area are plotted as a density map in blue (darker is denser). The top-left panel shows the full Commodore-selected Y3 catalogue without any cut applied. The top-right panel shows the map after the cuts for star-galaxy separation and against large errors in r and i. The bottom-left panel shows the final selection map after removal of objects potentially affected by blending and the bottom-right one contains only those sources with at least 2 VHS bands and no visual artefacts near the galaxies in the image cutouts. We use MAG_DETMODEL AB photometry.

affected by blending (using the DES pipeline flags). The result of this further selection is shown in Figure 2.1, lower left-hand panel. Last, VHS archive data were matched to the selected sources in order to extend their DES photometry with J, H, and K_s bands. Some sources lacked one or more VHS bands and, as explained later, this has been taken into account when estimating the reliability of our fits. The matching was done automatically by inserting the RA and Dec coordinates of each DES object in the VHS data access pages[2] to find the closest VHS source. The maximum matching radius was kept to the web utility default value of 5 arcsec. However, we have visually checked every single image for each source to confirm that the DES and VHS photometry was matched correctly.

Those sources passing the condition of having data in at least two VHS bands populate the selection box in the lower right-hand panel of Figure 2.1. For these we calculated the photometric redshift and stellar population properties using a template fitting procedure. Photometric redshifts and their probability distribution functions were compared to those calculated by the DES pipeline working groups (more details in Section 2.3.2.1).

Lastly, a full-fledged analysis of the results for each candidate was performed in order to identify only those that are convincing $z \sim 4$ galaxies.

2.3.2 Initial Selection

2.3.2.1 DES Data Catalogue & Colour Selection Cuts

We used photometric data in the g, r, i, z, and Y bands from the DES Y3 Gold 2.0 release, which contains the latest, highest quality photometry for DES. Among the magnitude options, we use MAG_DETMODEL photometry (in the AB system), as it refers to the same physical aperture hence it is optimal for template fitting. As described in Melchior et al. (2015), magnitudes are measured by SExtractor in each filter using a model fit to the surface brightness of the source in each image. The detection image for each

[2]http://horus.roe.ac.uk/vsa/index.html

object was created by the DES pipeline by linearly combining the r, i, and z images Abbott et al. (2018).

From the Y3 catalogue we wanted to choose those objects that had been observed since the SV stage, meaning that their photometry matches the full nominal depth of the survey. In order to select them, we used the *COMMODORE* catalogue (for details see Etherington et al., 2017, and Capozzi et al., *sub.*) which refers to the SV data and provides, among other entries[3] the sky position (RA and Dec), the neural network redshift and a flag for performing star-galaxy separation.

The crossmatch between Y3 and the COMMODORE SV data resulted in $\sim$ 4.9 million sources. The rest of the sources in Y3 (the vast majority, amounting to the impressive figure of 394 million objects) will need further observations for reaching the same depth levels.

First, we considered the star-galaxy separation parameter included in the catalogue and validated by the *COMMODORE* team (and detailed in Kim et al., 2015). This method uses a supervised machine learning technique to provide the probability of a given source of being either a galaxy or a star. Note that this procedure may lead to the exclusion of compact galaxies, and many high-z massive galaxies are compact Straatman et al. (2014), but it makes it much more likely that we avoid star or pure AGN contamination (this last point is discussed in more detail in Section 2.4.1.1). Quantitatively, we kept those sources with $\geq 99.977\%$ probability of being a galaxy[4]. This first cleaning left us 73% of the original sample (i.e. $\sim$ 3.7 million sources). We further performed a cut in photometric errors. We examined the error distributions in r and i separately and we conservatively decided to remove the tail of largest errors (i.e. $r_{err} < 0.060$ mag and $i_{err} < 0.063$ mag), which

[3] The COMMODORE catalogue also contains the DES SV photometry (which was not used for this work as the Y3 one is of higher quality) and galaxy physical properties obtained with the same models and procedure as here, but using the neural network redshift as fixed redshift for the given source.

[4]For DES users: the entry we used is called TPZ_{SG_CLASS} and we excluded sources with TPZ_{SG_CLASS} ¿ 0.00023

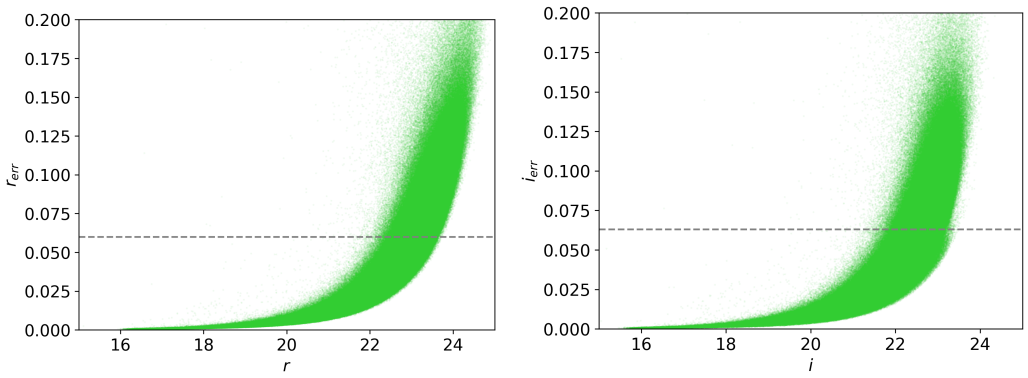

Figure 2.2: Error against magnitude for r and i bands. The horizontal lines mark the error cuts we applied (i.e. $r_{err} < 0.060$ and $i_{err} < 0.063$). These identify the effective magnitude limits of our analysis as ~ 23.7 and ~ 23.5 for the r and i bands, respectively.

means removing $\sim 25\%$ of objects in each band. These cuts effectively identify the magnitude limits of our work in the r and i bands, which are ~ 23.7 and ~ 23.5, respectively. This can be appreciated by looking at Figure 2.2, where we plot error against magnitude for the r and i bands (left-hand and right-hand panel, respectively) of our full catalogue after star-galaxy separation. The horizontal lines indicate our error cuts.

We then matched objects satisfying the error cuts in both bands. Note that we considered these bands as they were the ones used for the theoretical colour selection, see Section 2.3.2.2. We left the g band free of constraints as it is the drop-out band at high redshifts (see Figure 2.7 and visit this link[5] for several examples).

After the star-galaxy separation and the lowest error cut, we were left with ~ 2.7 million candidate galaxies. Furthermore, we removed all galaxies whose photometry was marked by the DES pipeline as being potentially affected by blending. Lastly, we extended the photometric baseline of the DES data with near-IR VHS data, and we decided to consider only those sources for which we could add at least two additional photometric data to

[5]Un-hidden hyperlink: `http://icg.port.ac.uk/~guarniep/`

the DES data (see Section 2.3.2.3 for more details).

It should be noted that the Y3 Gold 2.0 catalogue also contains a photometric redshift estimate for each source as calculated by the DES pipeline. This redshift is calculated using the so-called Bayesian Photometric Redshift (BPZ) code Hoyle et al. (2017). The prior used in BPZ strongly disfavours high-z solutions for bright galaxies. This does not mean, however, that higher redshift objects do not exist and this is exactly what we aimed to find out. Later in the chapter we shall also perform a comparison of the physical properties we would have obtained for galaxies had we used the z_{BPZ}.

2.3.2.2 Theoretical Colour - Colour Selection Maps

As recalled in the Introduction, D13 investigated colour combinations of DES bands for stellar population models Maraston (2005); Maraston et al. (2006) with various parameters such as age, star formation history, dust, and stellar mass, as placed at various redshifts, in order to select those corresponding to the mass-redshift combinations of interest (from here on these models will often be referred to as the M05 models). The resulting selection boxes display regions within the colour-colour diagrams where high-z objects should be found.

Hence, our first step was to plot the DES galaxy candidates on the D13 $g-r$ vs $r-i$ plots in order to single out those entering the $z \gtrsim 4$ box. Note that by using this mapping first it is possible to substantially reduce the number of candidates for fitting, which is helpful because running a template fitting code for photometric redshift and physical properties for millions of sources is very time consuming. Even more importantly, using such a colour selection box is crucial to maximise the likelihood of the candidates to truly be at high redshift.

The colour-colour $g-r$ vs $r-i$ diagram using Y3 photometry for the sources in the *COMMODORE* catalogue is shown in the top-left panel of Figure 2.1, where the selection box for $z \sim 4$ objects is highlighted with a black solid line. In the same panel, the khaki line depicts the redshift evolu-

tion track for a model galaxy as taken from D13. The vast majority of the sources are consistent with being low-redshift objects (plotted as small, blue points; the darker, the denser). The high-z candidates falling in the selection area are plotted in orange. They total 25809 sources (top-left panel). After application of the cuts described in Section 2.3.2.1 - namely star-galaxy separation and removal of sources with highest error in bands r and i (for a total of 25% in each of the two bands) - we are left with 3243 objects as potential high-z candidates (top-right panel). We then removed candidates with blending issues, which left us with 2465 galaxies (bottom-left panel). Further visual inspection of the cutout images allowed us to remove any source that showed artefact traits, such as satellite trails and black-out areas, near the selected source. This does not mean that their photometry is necessarily compromised (as these were not flagged by the pipeline), but we decided to exclude them as we could not verify their photometric quality. This is done along with further considerations on the number of near-IR bands we could match to our galaxies, as described in the next section.

2.3.2.3 Extending the Photometry to the Near-IR

As is well known, the accuracy of spectro-photometric model fitting depends on the number of available data points and especially on the baseline in wavelength they cover (e.g. Pforr et al., 2012, 2013; Banerji et al., 2008, 2015a). In order to strengthen the reliability of our photometric fitting procedure, as mentioned in the previous sections, we looked for additional bands for the sources within the colour-colour map. We were able to cross-match the DES optical data with the VHS survey McMahon (2012), thereby extending our photometric catalogue to the near-infrared bands J, H, and K_s[6]. We used the *Petrosian magnitudes* from the VHS Data Release 5, which rely on the

[6]The VHS photometry, in the Vega magnitude system, was converted to the AB system to match the DES one according to the following relations: $J_{AB} = J_{Vega} + 0.916$, $H_{AB} = H_{Vega} + 1.366$, and $K_{sAB} = K_{sVega} + 1.827$. Source: http://casu.ast.cam.ac.uk/surveys-projects/vista/technical/filter-set

Petrosian radii of galaxies to determine the photometric aperture. This allows to recover the flux also for extended sources, making them ideal to work in combination with the DES DET_MODEL magnitudes discussed earlier. We do not expect the atmospheric seeing to have an effect on our template fitting results since we use extended magnitude types (DES DET_MODEL and VHS *Petrosian*; Cross et al., 2012) and the median seeing among the eight DES+VHS bands was shown to be similar Banerji et al. (2015a). Additionally, the point spread function (PSF) full width at half maximum (FWHM) of the DES and VHS camera and telescope configurations are 0.49 arcsec[7] and 0.51 arcsec[8], respectively. Therefore we consider DES and VHS photometry to be compatible without further manipulation.

We noted that the majority of DES sources does not have all three VHS bands available. There could be several reasons for this. First of all, VHS has not imaged in the H band all regions overlapping with DES Reed et al. (2017). Additionally, VHS is shallower than DES and the optimal depth depends on the nature of the candidates. For example, young star forming objects could be faint in the rest-frame optical (sampled by the VHS at high-z) simply because they are dominated by massive hot stars.

In order to retain only those candidates for which the model fitting would be better constrained (see Section 2.3.3.2), we decided to focus on objects having observation in at least 2 VHS bands, which means to fit a minimum of 7 photometric bands.

This further selection criterium, along with the removal of artefacts as described in the previous section, led us to identify 606 galaxies (bottom-right panel of Figure 2.1). These correspond to $\sim 0.01\%$ of the whole 5-million sources DES catalogue. Template fittings and analysis have been performed on these 606 objects only, as described in the next section.

[7]https://www.noao.edu/meetings/decam/media/DECam_Technical_specifications.pdf

[8]https://www.eso.org/sci/facilities/paranal/telescopes/vista.html

2.3.3 Determining Redshift and Physical Properties

2.3.3.1 Template Fitting Procedure

In order to confirm candidate $z \sim 4$ massive galaxies, the redshift and physical properties of the sources selected up to this stage were calculated. This was done using the photometric redshift code HyperZ (Bolzonella et al., 2000) combined with ancillary scripts for the calculation of the stellar mass, as in our previous works (Daddi et al., 2005; Maraston et al., 2006). HyperZ compares model spectral energy distributions of stellar populations (which are referred to as templates) to observed photometric data, and selects the best models using a χ^2 minimisation method. HyperZ outputs the photometric redshift, the best-fitting template, and a reduced χ^2 value (χ^2_r) for the best-fitting template, calculated as $\chi^2/(N-1)$, where N is the number of filters.

Additionally, a series of input parameters can be modified in order to more finely control the way HyperZ operates. These are: age limits, magnitude limits, redshift range and binning, reddening law, and template setup. We discuss them later. For a full description of HyperZ see Appendix A.

We have explored different combinations for fitting and model setup, which we now describe. We should say in advance that the final results are robust against these parameter variations.

Each galaxy spectral energy distribution model (the template) is calculated assuming a star formation history (SFH, detailing the mode of star formation, e.g. single burst, exponentially-declining star formation, etc.), an age (t parameter, which runs from the start of star formation at $t = 0$ through the galaxy evolution, at logarithmic time steps from 1 Myr to the age of the Universe at the given redshift and assumed cosmology), a chemical composition, and a reddening by dust. Each model is redshifted at various values of redshift and a χ^2 is calculated for each redshifted model.

The redshift range we explored here varied from 0 to 6 in steps of 0.05, consistently for each fitting run. A variegated selection of 32 sets of model

spectral energy distributions based on the Maraston (2005) evolutionary population synthesis models (M05) was used at each run, spanning a wide variety of star formation histories (SFHs; as in Maraston et al., 2006). These include single-bursts simple stellar populations, τ (exponentially declining), truncated (constant until an instantaneous decline to zero, to simulate rapid quenching), and constant SFHs, each of them calculated for a grid of 221 ages and four metallicities ranging between 1/5 to twice solar. All the runs were repeated for two reddening laws: the so-called 'SMC' law (Prevot et al., 1984; Bouchet et al., 1985) and the well-known 'Calzetti' law (Calzetti et al., 2000). For each the extinction parameter A_V was allowed to vary between 0 and 3, in steps of 0.5. These two reddening laws were selected because they are maximally different among the options offered by HyperZ and they are appropriate for different classes of high-z galaxies. Maraston et al. (2006), by exploring all options in HyperZ, concluded that these two are those identifying the best fits in most cases of $z \sim 2$ galaxies, and that while Calzetti's law is calibrated with starbursts, the SMC seems to be more appropriate for passive galaxies (as also concluded by Kriek and Conroy, 2013). We assumed a Salpeter (1955) IMF for all model options. Furthermore, we used an age cut to retain only solutions older than 0.1 Gyr, which is commonly used in order to avoid age-dust degeneracy pushing the fits towards low ages; we have tested that our results, as far our best candidates are concerned, do not depend on this choice (see Section 2.4.4.4). Lastly, we ran the code with loose absolute magnitude limits (i.e. between -12 and -30) for all sources as we found that thanks to using at least 7 photometric bands (DES + VHS) we would instead obtain stable results and also avoid the risk of over-fitting.

Relevant to this work, we have expanded the public version of HyperZ by adding the calculation of the redshift probability distribution function (PDF; see also Pforr et al., 2018). HyperZ provides the probabilities associated with the χ^2 of all the fitted models. We calculate the PDF for the photometric redshift by summing up all the probabilities for each redshift step (0 to 6, in this case) and then normalising by the number of models (32). The sum of the

discrete probabilities of each model over the redshift range equals to one. As we use the same redshift bin (0.05) throughout the explored redshift range (0 to 6) for all fitting runs and the model templates contain the same number of ages (221) we should be minimising the risk of artificially favouring particular solutions. [9] The photometric redshift PDF is critical in order to distinguish high-probability high-redshift from lower-redshift distributions. We shall use PDFs, among other indicators, in order to determine the robustness of our final candidates.

2.3.3.2 Visualisation and Analysis of the Results

For each candidate, we then analysed simultaneously both the best-fit result (the photometric data along with the best-fitting model) as well as the photometric redshift PDF. Examples are shown in the top two panels of Figure 2.3.

In the model fitting plot (left-hand side) the photometric data (red) are matched to the template fluxes (blue), corresponding to the best fitted model (solid black line) when adjusted for the response function of the telescope camera in each band. The physical parameters of the best fitting model, the age (in Gyr), the stellar mass (in $M_{\odot}$) and the χ^2_r are labelled. Axis labels include observed and emitted wavelengths.

The probability distribution of photometric redshifts is shown in the upper right-hand panel (in red for the curve relative to the fit in the top-left panel), where a vertical line is drawn at the value corresponding to the best-fitting model.

In some cases, the most probable solution (i.e. the peak of the curve) may not correspond to the redshift of the best fitted model. This happens when several less probable solutions (model fits with worse χ^2_r) have similar redshift value and therefore sum up to show a higher peak in the PDF plots. It can happen that the less likely, but numerous solutions sum up such as

[9] We note, however, that as galaxy colours may vary non-linearly, the colour-space may not be evenly sampled in spite of an homogeneous age sampling in all templates.

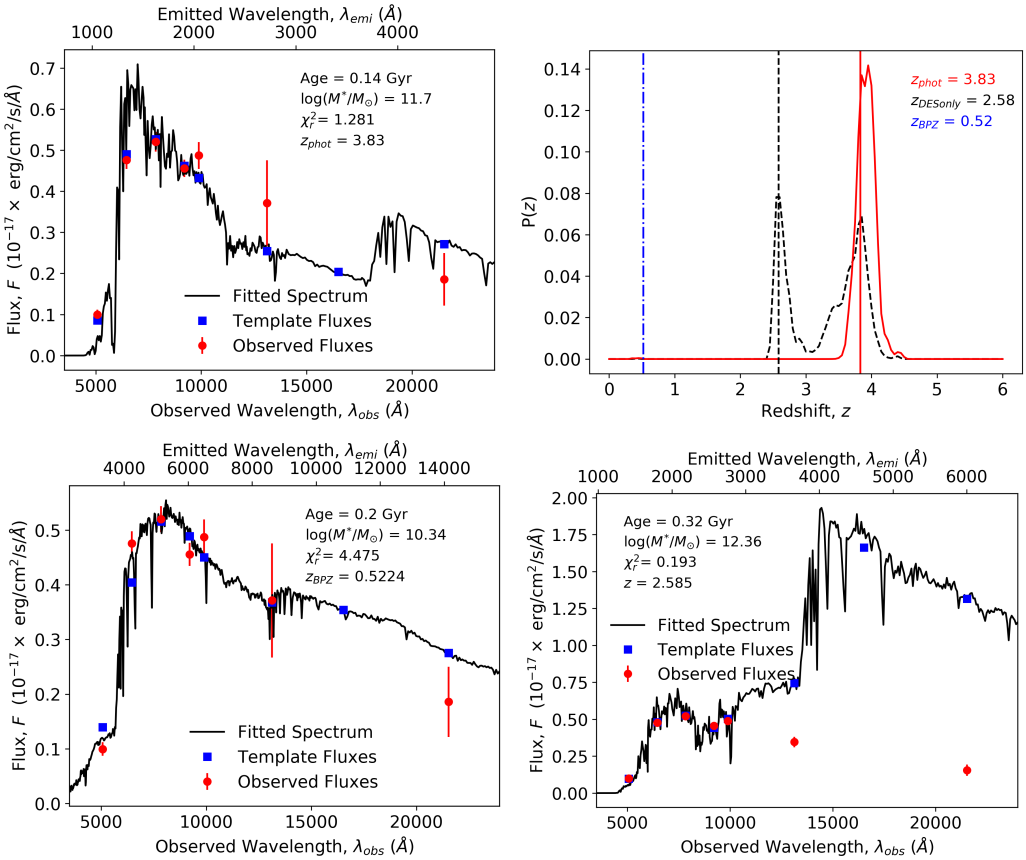

Figure 2.3: This is a figure spanning multiple pages. The full caption is found at the end of the figure.

to create another maximum which competes with the one of the best-fitted solution. As it will be described later, we only accept as massive high-z galaxies those for which the best fitted model's redshift matches the most probable solution (i.e. peak of the curve).

Additionally, we also indicate the value of the z_{BPZ} as calculated by the DES pipeline (dotted-dashed vertical blue line). It is important to stress again that the DES z_{BPZ} was trained with sources up to $z \sim 1.3$ therefore this procedure could not produce any solution at higher redshift.

For each candidate, we further tested the effect of assuming the DES BPZ redshift as its true redshift, and explored the resulting quality of fit

Figure 2.3: A comprehensive display of template fitting results (for object with ID 494790027 as an example). **Top-left:** Template fitting showing the best fitting model spectrum (solid black line) with overlaid data (red circles) with error bars, and the template fluxes (blue squares) to which the data have been fit. The derived properties age (Gyr) and stellar mass (in log and solar units) are labelled, along with the reduced χ^2 and redshift of the best fitting model. **Top-right:** The PDF of the template-fitting redshift is shown as a solid red line (the best result is marked by a vertical line), the same for the case of only using DES bands for the fitting is shown in dashed black, and the DES BPZ value in dotted-dashed blue. **Bottom-left:** Template fitting having fixed the redshift to the value of z fixed according to the DES BPZ. This results in a considerably worse fit than when the redshift is allowed to vary (top-left), suggesting that the most likely solution is the high-redshift one. **Bottom-right:** Fitting as in top-left, but only for the DES bands while the VHS bands are plotted for reference; the redshift result confirms a high redshift (i.e. 3.28 instead of 3.80), but it can be seen that, since the overlaid VHS band fluxes are far from the model template fluxes, the result does not represent the correct template.

and the derived physical parameters. To this aim we run a different version of HyperZ (named HyperZ-spec), which fixes the redshift to a known value, and repeated the fitting runs keeping the stellar population model setup as before. The result for the same high-z candidate can be seen in Figure 2.3 (bottom-left). In this case we must compare absolute and not reduced χ^2 values as the χ^2_r figures are calculated in the same way in both codes (as $\chi^2/(N-1)$), but in HyperZ-spec the redshift is fixed.

We find that the absolute χ^2 of the fit at the fixed DES BPZ redshift is considerably larger than the one obtained leaving the redshift free (26.850 vs 7.686). The $\Delta\chi^2$ in this example ($\sim$ 19) implies that the low-redshift solution is inconsistent with the best-fit high-redshift solution at the $> 2\sigma$ confidence level. The best fit corresponding to the DES BPZ redshift is also visually less convincing. The physical properties (lower mass and older age) are consistent with a low-redshift solution.

Lastly, we tested the effect of fitting only DES data vs fitting DES+VHS data. An example is shown in Figure 2.3 (bottom-right). The fit obtained without VHS bands (hence with the 5 DES bands only) is different in terms of physical parameters (compared to the top-left panel fit, in which VHS bands were fit as well) and the very low χ^2_r value (0.045) indicates that DES-only fits are prone to over-fitting due to the low number of bands. When the same galaxy is fitted with the additional VHS bands (top-left panel) we verify, as we saw earlier, that the 'only-DES' fitting did not correspond to the real solution, showing the importance of extending the photometric data to, in this case, the near-IR (see Section 2.4.3 for a quantitative evaluation on the effects of using the VHS bands in model fitting). The PDF of this type of fit is plotted in black on the top-right panel plot.

In Figure 2.4, as an illustration, we show the effect of the assumed reddening prescription on the fitting results. For this specific galaxy, the fit performed with the SMC-law releases a slightly lower redshift and χ^2_r value, along with minor changes in terms of mass and age, compared to the results obtained using the Calzetti-law. A similar trend is seen in the correspondent

PDFs. The PDFs referred to the fits with only DES bands are somewhat broader, but still peak at high redshift.

2.4 Results

Starting from $\sim$ 5 million sources, the exclusion of stars, blended sources, galaxies with uncertain data (large errors) and objects lacking VHS photometry was followed by a filtering with the theoretical colour-colour selection maps and a final visual inspection, which left us with 606 candidate massive high-z galaxies. These candidates were submitted to stellar population model fitting.

Since we focus on the high-redshift population in this work, we proceed with a series of selection cuts (described in the next section) in order to identify the best high-z, massive galaxy candidates. In future studies, we shall explore the wider zoology of all sources falling into the selection box.

2.4.1 Selection of the Best Candidates

From now on, we consider the results from HyperZ runs for all 606 sources as obtained with the two reddening laws mentioned earlier. This results in two fitting results for each object. We then proceed to select the most secure sub-sample of galaxies at $z \geq 3$. To this aim, we performed three additional cuts, namely: i) we excluded those galaxies with unphysical stellar mass ($\log_{10}(M^*/M_\odot) > 12.5$); ii) we excluded objects whose fits have $\chi^2_r > 3$ (this value was chosen considering the number of fitted bands and values typical of high-z galaxies, e.g. Maraston et al., 2006); iii) we excluded objects for which the probability of a $z \geq 3$ solution is less than 95% (corresponding to a 2σ confidence level), determined by looking at the PDFs of each object.

The number of individual galaxies passing all selection cuts is 233. With respect to the adopted reddening, 109 fitting results pass our selection criteria when using the SMC law and 203 with the Calzetti law case. This means that some galaxies satisfy the selection criteria for both reddening laws and

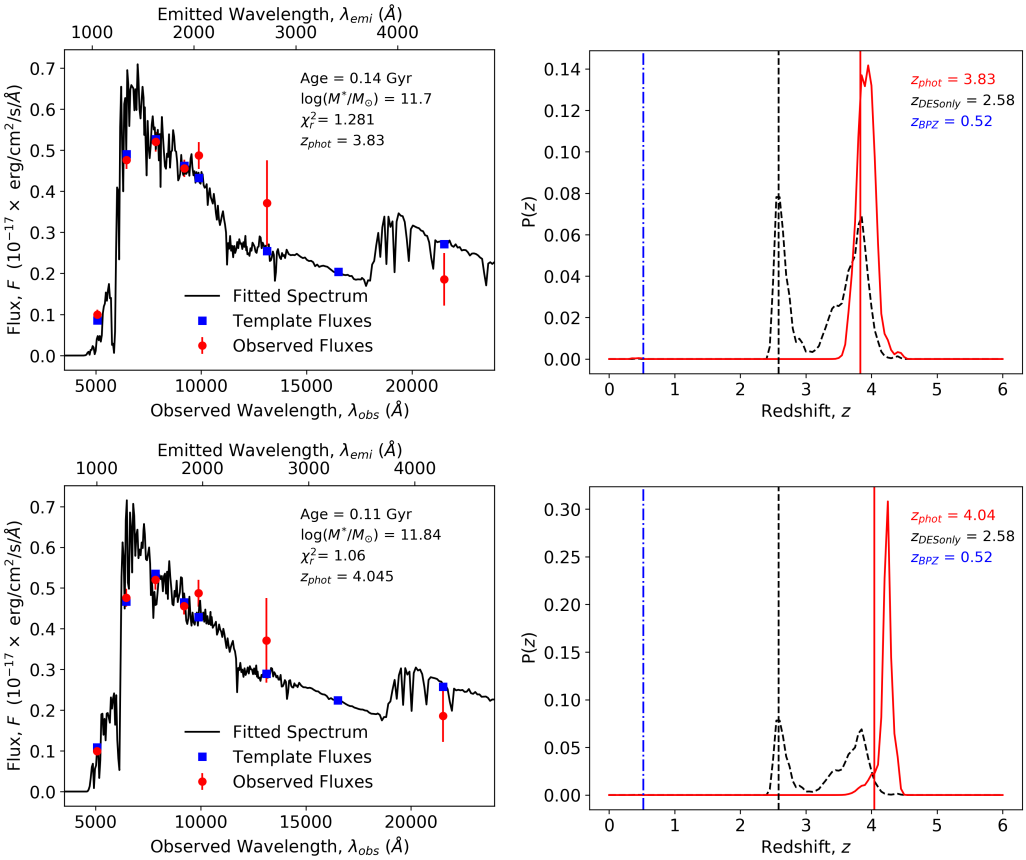

Figure 2.4: Legend as Figure 2.3. Fittings and PDFs for a high-z candidate for the various reddening laws (one in each row respectively), from top to bottom: SMC law, and Calzetti law. Compared to the SMC result for this object, the solution obtained with the Calzetti law has got a negligibly higher redshift and lower χ^2_r, and displays minor changes in mass and age. ID of object shown here: 494790027.

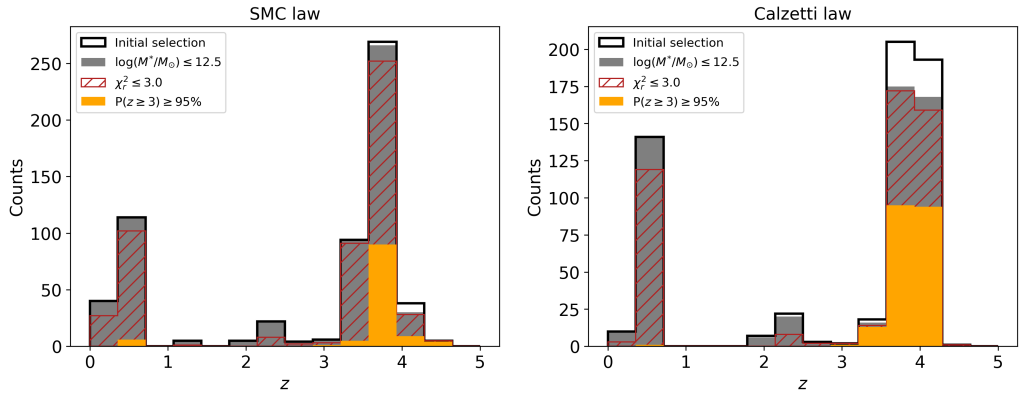

Figure 2.5: Redshift distribution for the 606 galaxies as found in the selection box of Figure 2.1 (bottom-right panel). The different cuts, applied in series, shown on the histograms illustrate our selection procedure, namely: all fitted galaxies (solid black line); those with a physical mass (filled grey bars); those fitted with a $\chi^2_r \leq 3.0$ (hatched red); those passing our photometric redshift PDF criteria (orange bars). The two panels display the cases of SMC law on the left and Calzetti law on the right.

therefore have been selected twice. The sample of 233 galaxies constitutes our *best candidate* pool. Their fitting properties are given in full in Appendix B.1.

The redshift distribution before and after all the cuts described above is shown in Figure 2.5 (here we also show template-fitting photometric redshift results for galaxies at $z < 3$) for the SMC-type of runs and the Calzetti-type in the left-hand and right-hand panels, respectively. The 606 sources from the $z \sim 4$ selection box of Figure 2.1 (bottom-right panel) are shown by the solid black line; the objects with $\log_{10}(M^*/M_\odot) > 12.5$ are identified by a grey shaded area; the red hatching indicates galaxies with $\chi^2_r > 3$; the shaded orange area finally highlights the sources with high-z probability of at least 95% (note again that the best redshift solution may not correspond to the most probable one). The cuts are applied in series, as shown.

If we consider an average mass value of $\sim 10^{11.7}\ M_\odot$, the expected counts according to De Lucia et al. (2006) galaxy formation models, as plotted in Figure 1 of D13, are ~ 1000 at completion of DES. For our case (~ 2.7 million

sources, when including star-galaxy separation and error cuts, instead of the expected value of 300 million upon completion, i.e. 1%) this would mean ~ 10 objects. We find 233 candidates, a value which lies an order of magnitude above the prediction of those models. Before drawing conclusions, however, we intend to spectroscopically confirm our best candidates.

We should also stress again that we have been very conservative for this initial work. For example, galaxies with non-detections in VHS bands could still be high-z objects perhaps dominated by very young stars and faint in rest-frame optical, and objects with potential blending issues are not necessarily low-redshift interlopers. It will be the subject of future work to study the excluded objects.

2.4.1.1 On AGN contamination

A further source of uncertainty is the random presence of AGNs in the best candidates, whose effect could be to make some magnitudes brighter thereby possibly affecting the derived stellar mass. On the other hand, the AGN can be obscured and buried in the centre of the galaxy host which would not affect our template-fitting results. High-z galaxies dominated by AGNs are expected to look like point-like sources (even though not all point-like sources are expected to host an AGN and not all galaxies hosting an AGN would have their flux dominated by it). A way to quantify the point-likeness of a source is to compare the magnitudes of the object over an extended aperture with its PSF magnitude, as for a pure AGN these two quantities are the same. For all our best candidates we have evaluated a parameter, dubbed σ_{AGN}, which is meant to quantify this magnitude difference and is defined as:

$$\sigma_{AGN} = |\frac{i - i_{PSF}}{\sqrt{i_{err}^2 + i_{PSFerr}^2}}|, \tag{2.1}$$

where i and i_{PSF} are an object extended and PSF i-band magnitudes, respectively, and err are their respective errors.

Figure 2.6 show the results, by plotting the magnitude difference to the PSF vs the PSF magnitude, with each object being coloured according to

the σ_{AGN} parameter, a 0 value of which means a complete point-like case. We also plot as blue crosses three, randomly selected objects from the COMMODORE catalogue with $\sim$ 100% probability of being stars. They do lie precisely at the PSF zero-level (dashed line), as expected.

We see that our candidates span a range in 'extension', but several lie on the point-source line although they have been classified as galaxies rather than stars by the DES pipeline. This may imply that they lie at very high redshift or that they host an AGN or a combination of both. As using this information in any quantitative way would be completely arbitrary, we just provide the σ_{AGN} values in the data tables along with all other template-fitting results (Appendix B.1), but we do not include it in our selection process.

2.4.2 Properties of the Best Candidates

The fitting results for the best candidates are given in Tables B.1 and B.2 for the two reddening laws, respectively. The results include, along with the photometric redshift, mass, and age, the star formation history (SFH) and its corresponding metallicity, Z/H ($Z_{\odot}$), of the best-fit template, and the absolute magnitude in the i band as calculated by HyperZ. All the outlined results are obtained using the photometry, with relevant errors, reported in Table B.3.

Figure 2.7 shows all relevant plots for one candidate as an example. The same plots for the other candidates can be downloaded at this link.

First we show image cutouts in the various photometric bands available, with a green circle indicating the galaxy position. Notice how, as expected, the galaxy is barely visible in the bluest band (g band), which is the drop-out band at these redshifts. We also point out when bands are not available. The panels below the tiles display: the spectrophotometric model fitting (upper-left), the redshift PDFs (upper-right), the spectrophotometric model fitting obtained when the redshift is fixed to the z_{BPZ} value (bottom-left), and when only the DES bands are used (bottom-right).

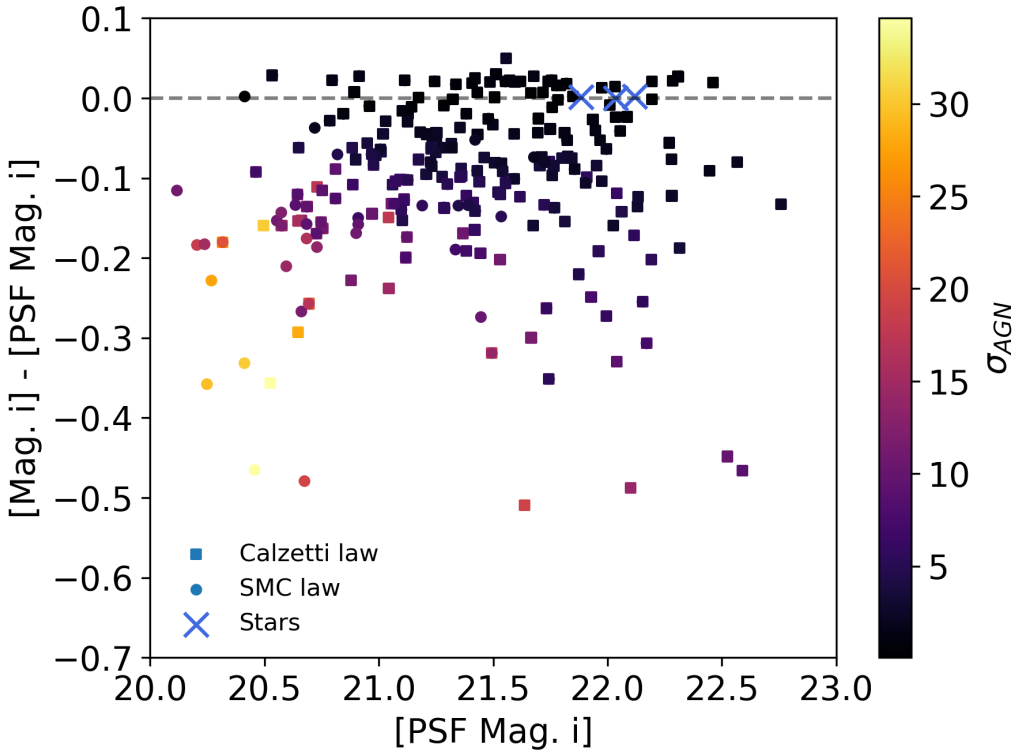

Figure 2.6: Difference between measured magnitude (MAG_DETMODEL) and PSF magnitude in the i band for the best candidates (distinguishing between those found with the SMC or the Calzetti law) plotted against the PSF i magnitude. Symbols are coloured by their σ_{AGN} values (see text). The further away a galaxy is from the zero-level (dashed line), the brighter it is compared to the PSF magnitude, suggesting that it is resolved and less likely to be an AGN. Three stars are also plotted as blue crosses and they lie on the zero-level line, as expected for clear point sources.

ID: 494790027

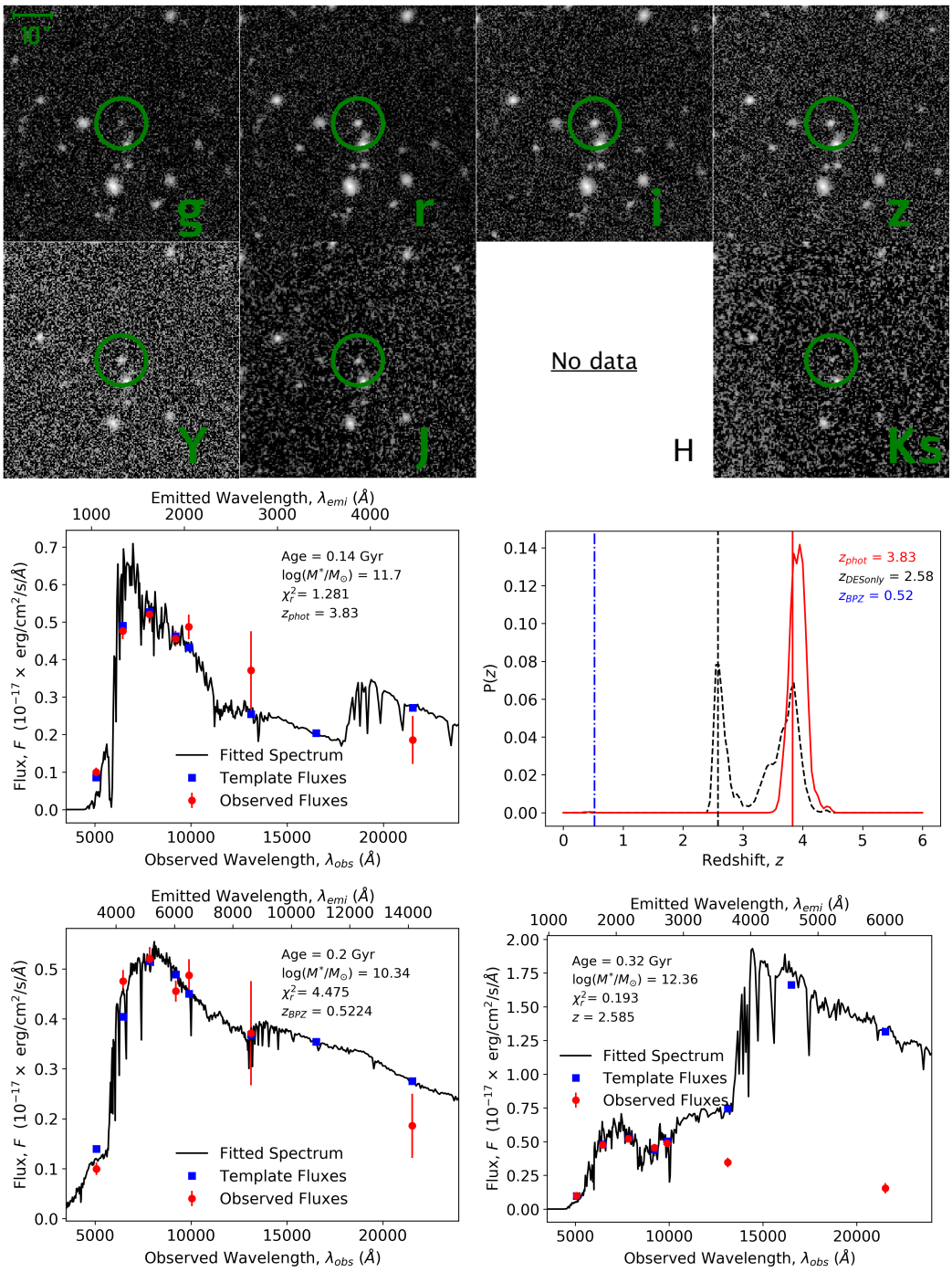

Figure 2.7: This is a figure spanning multiple pages. The full caption is found at the end of the figure.

Figure 2.7: The observation images for all available bands (DES and VHS), the best fit, the PDF, the fit with fixed redshift according to z_{BPZ}, and the fit only using DES bands for one of our best candidates. For the galaxy images the green circles indicate the sky position of the galaxy; if the circle is red it means that the photometry is not available for that given filter. If VHS observations are not available, for one or more filters, the image is replaced by text saying so. For the plots below the images (bottom four panels) the legend is the same as in Figure 2.3. The rest of the best candidate plots and images can be found following this link.

In the spectrophotometric model fitting plots (similar to what was shown before in Figure 2.3), the black line shows the best-fitting model spectrum, the blue squares the fluxes of that model in the DES and VHS filters and the red points the observed data in the same filters. Some key parameters of the model[10] are printed on the plot, the age (in Gyr) and the stellar mass (in $\log M_{\odot}$), along with the χ^2_r.

The upper right plot shows the photometric redshift PDF using all available bands (red), DES only bands (black), and the best redshift from the DES pipeline run of BPZ (blue). Not surprisingly, the DES BPZ redshift favours lower solutions, typically around 0.3. In order to probe the type of fitting we would obtain had we assumed the low-z solution as the correct one, we use the DES BPZ value as the true redshift and run HyperZ-spec, keeping all other parameters identical.

The result for this type of run is shown, for instance, in the bottom-left panel of Figure 2.7 (and at this URL for other objects). As expected due to the small redshift, the model fitting results in a lower mass galaxy ($\log M \sim 10.3\ M_{\odot}$), though with a similar age, and generally a worse fit. The bottom-right panel instead shows the fit for the case when only DES bands have been used to run HyperZ. We can see that the fit remains good, but as a very small portion of the spectrum is fitted (corresponding to the

[10]The other model parameters are given in Table B.1

rest-frame UV at these redshift) the physical solution differs from the one obtained when fitting all available bands. Interestingly, the photometric redshift remains high (although not as much), which reinforces the use of DES-only bands in D13 as a discriminator of high-z, massive galaxies. This can be appreciated by looking at Figure 2.8. Here, all best candidate galaxies' three types of redshifts ($z_{DES+VHS}$, $z_{DESonly}$, and z_{BPZ}) are shown as red, black, and blue histograms, respectively. In Section 2.4.3 we shall discuss in more detail how the addition of VHS data to the DES data affects our fitting results.

We summarise the properties of our best candidate galaxies in Figure 2.9, in comparison with the initial sample of 606 galaxies (among these here we only show galaxies at $z \geq 3$). The solid orange bars show the distribution of stellar masses, ages, and the goodness of these fits (i.e. χ^2_r), for the best candidates. Objects from 606 at $z > 3.0$ are distributed according to the solid black line, with those having physical mass $\log_{10}(M^*/M_\odot \leq 12.5)$ shown by the filled grey bars. The cut in $\chi^2_r \leq 3.0$ is highlighted by hatched red bars. Furthermore, the PDF cut (probability of at least 95% of being at $z \geq 3$) shrinks the distribution in what is shown with the filled orange bars which match also correspond to the best candidates. The final histograms show that the many quality cuts we apply do not distort the initial distribution of galaxies. More quantitatively, performing a K-S test, we find that we cannot reject the null hypothesis that the distributions are the same with p-values, on average for the two reddening options, of 0.27, 0.29, and 0.24, respectively for mass, age, and χ^2_r. Even the objects with poorer fits trace similar galaxy physical properties. All the cuts are applied in series, one after the other.

Our best candidate galaxies have large stellar masses $10^{11.5} \leq M/M_\odot \leq 10^{12.5}$, ages ~ 0.1 Gyr, have been forming stars following a rapid mode generally consistent with an exponentially-declining mode with short e-folding time, $\tau = 0.1 - 0.3$ Gyr, or a truncated model with similarly short timescales. Metallicity is generally high ($Z > \mathrm{Z}_\odot$). Our derived ages tend to cluster around the lower age limit set in HyperZ (0.1 Gyr). This is to be expected

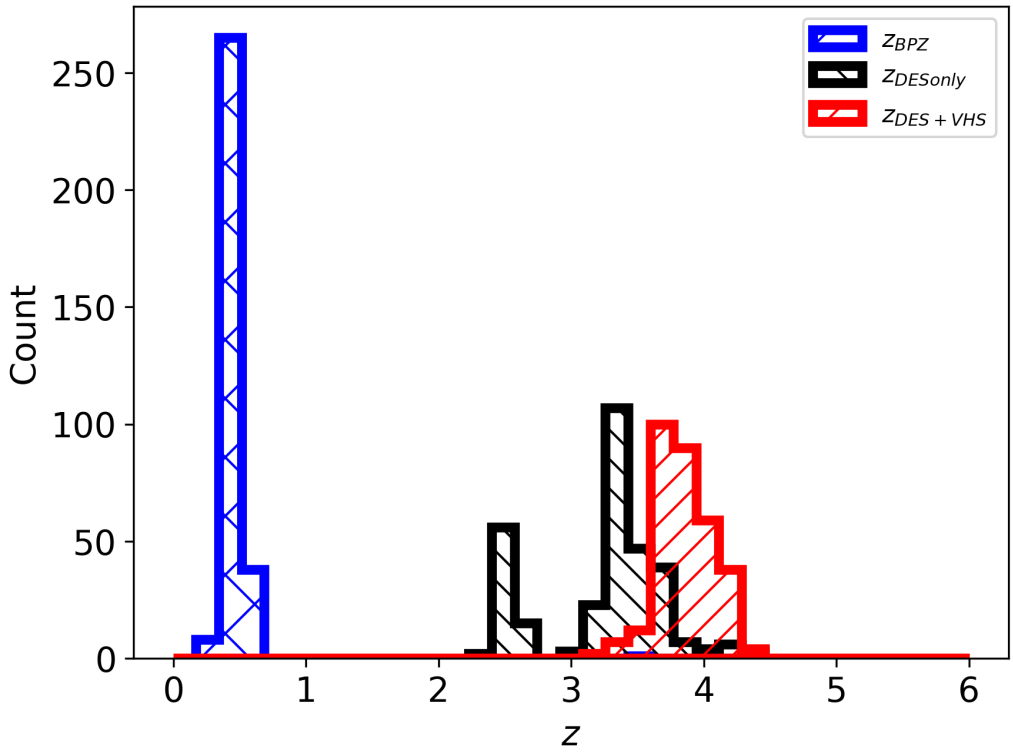

Figure 2.8: The distributions of $z_{DES+VHS}$, $z_{DESonly}$, and z_{BPZ} for the best candidate galaxies are plotted as red, black, and blue histograms, respectively. It can be seen that even when using only DES bands to fit these galaxies, the results still tend to be at high-z and relatively close to the $z_{DES+VHS}$ ones; on the other hand, as explained earlier, z_{BPZ} values stay below $z = 1$.

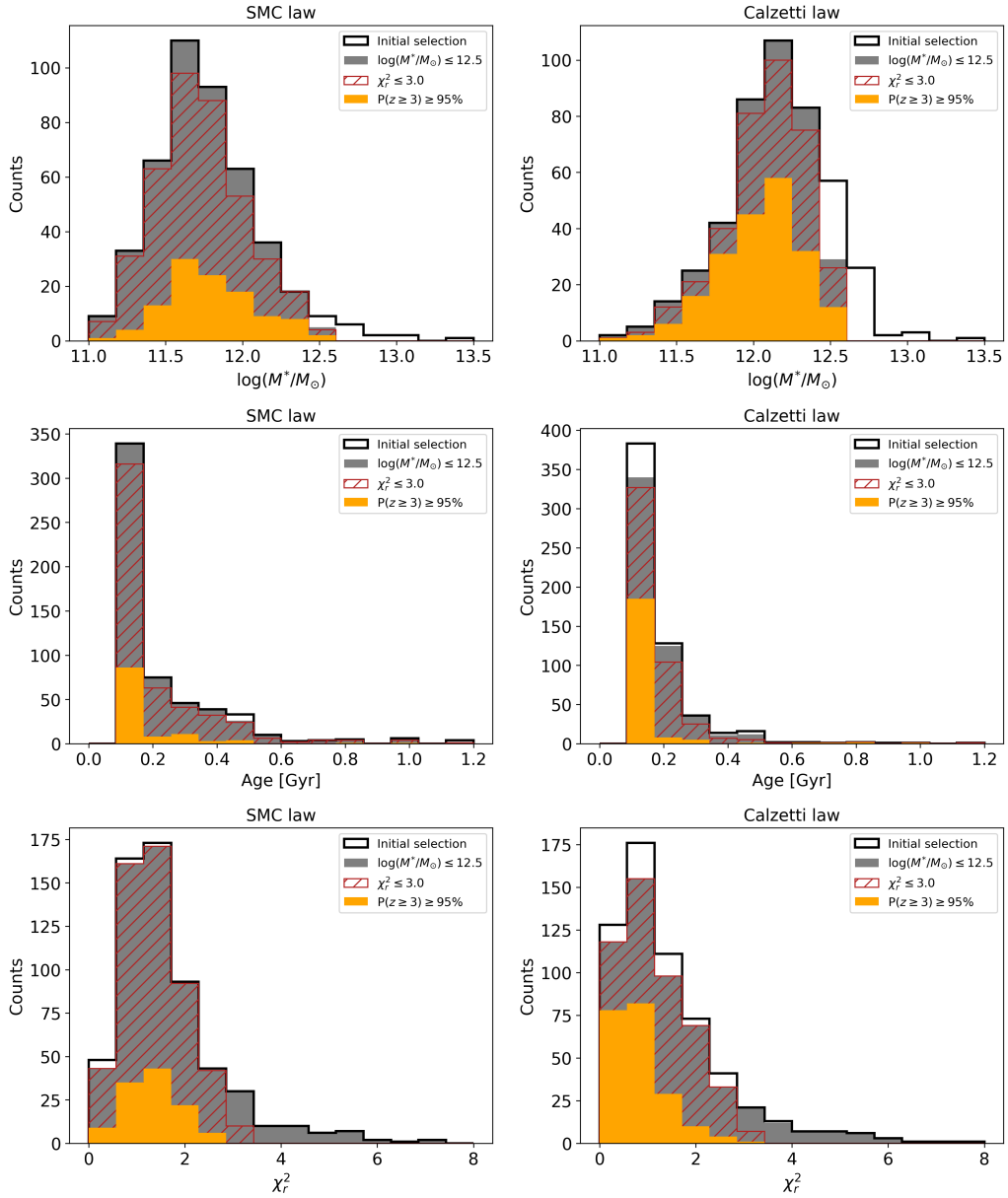

Figure 2.9: M^*, age, and χ^2_r for the $z > 3$ candidates within the sample of 606 sources from the colour selection box. Legend as in Figure 2.5 (except for redshift cut (i.e. $z \geq 3$) applied to the initial selection). This is shown for all two reddening options (SMC law and Calzetti law) in the first and second columns, respectively.

as - in χ^2 minimisation fitting of stellar populations containing young components - the best-fitting model tend to be associated to the youngest possible age, especially when only UV/optical bands are fitted. When this happens, as the energy emission of young stellar populations is order of magnitudes higher than that of older populations, the youngest models will dominate the fit, an effect that is known as 'over-shining' (Maraston et al. 2010). Hence, if we allow the fitting procedure to use any value of age, rather than an age estimate for the whole galaxy, we tend to obtain the age of the last generation of stars, which may contribute very little by mass. This over-shining effect may hamper us to recover realistic galaxy stellar population properties, in particular making stellar mass estimates unreliable. In order to circumvent this problem, it is common to adopt a lower age limit in the fitting procedure (e.g. Daddi et al. 2005), which is usually set to an age (0.1 Gyr) when the most massive stars are already dead (for passive models). It is not guaranteed that such a limit ensures fully realistic ages for all galaxies, which may still be biased low. If this is the case, our stellar mass estimates will be lower limits of the true stellar mass.

In Section 2.4.4.4 we shall assess the effect of this assumption on the two main properties we are interested in, namely the photometric redshift and the stellar mass.

Results are summarised in Table B.1 and B.2. The results of the model fitting are also consistent with the simulations of D13 and with being a younger version of the stellar populations inhabiting the most massive galaxies in the local universe (Thomas et al., 2010).

Looking in more detail at the redshift and physical properties of the best candidates we can see that, compared to the assumption of an SMC law, the use of the Calzetti law often pushes redshifts and masses to higher values. All this information is summarised in Figure 2.10, where we show fractional distributions for each reddening law (hatched dark red for SMC law and deep pink solid line for Calzetti law) in terms of redshift, mass, and age, respectively.

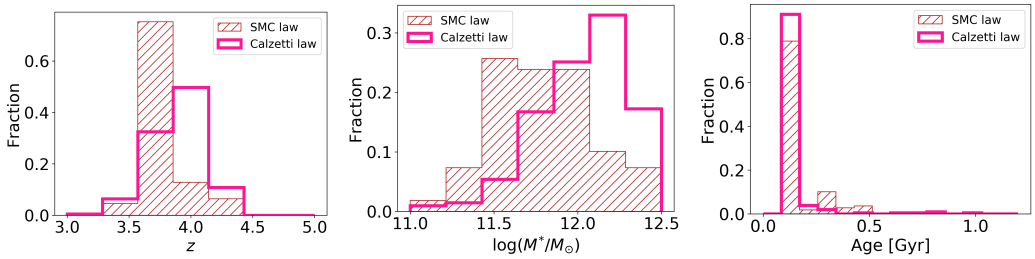

Figure 2.10: Distributions of (from left to right) photometric redshift, stellar mass, and age in terms of fraction for the best candidates found with the two different reddening laws: SMC law (hatched dark red bars) and Calzetti law (solid deep pink line).

The SFHs of these candidates also allow us to create a visual representation of the mass assembly and SFR of such galaxies. These are shown for two different types of SFH in Figure 2.11, which represent the vast majority of the best candidates. They are: $t_{trunc} = t$ and $e^{-t/\tau}$ (red and blue, respectively), plotted in the left panel for the mass assembly and in the right one for the SFR. These rapid timescales point to formation redshifts close to $z \sim 5$, which is in agreement with what is deduced from the fossil record of local high stellar mass galaxies (we shall return to this point in the discussion). Note that even if these SFRs appear extreme, values of tens of thousands of solar masses per year have already been recorded in the literature (e.g. Rowan-Robinson et al., 2016). The results from both reddening options are plotted together.

Let us conclude with a comment on the population model effect. Here we assume Maraston's models, while results in the literature are usually based on Bruzual & Charlot (BC) models. As is well known, ages derived with Maraston models for high-z galaxies are smaller than those based on BC models, which results in smaller stellar masses M^* by e.g. ~ 0.2 dex (depending on the fitted ages). This is due to the different prescriptions for the thermally pulsing asymptotic giant branch (TP-AGB) and to the different onset age for the RGB assumed in the underlying stellar tracks (see

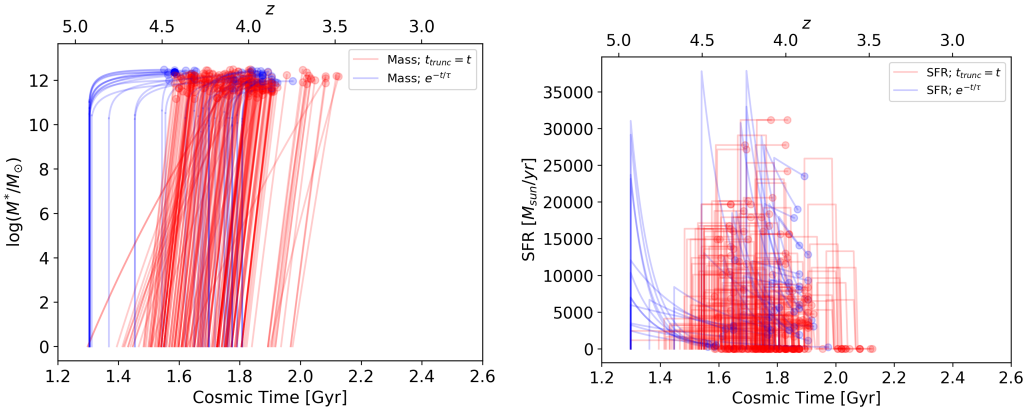

Figure 2.11: Galaxy mass assembly derived for the best candidate galaxies. Typical SFHs as $t_{trunc} = t$ and $e^{-t/\tau}$ are plotted in red and blue respectively for the mass assembly (left panel) and for the SFR (right panel). A few candidates with SFHs different from those two laws have not been plotted. Candidates from all two reddening options have been plotted together.

Maraston et al., 2006). Hence, our estimates of age and M^* lie likely on the lower side than what we would obtain had we used BC-type models.

In Section 2.5 we shall discuss the results we obtain when we re-fit some of the galaxies recently reported in the literature, including the Glazebrook et al. (2017) object, with Maraston models and our fitting procedure.

2.4.3 The Effects of Fitting DES-only vs. DES+VHS Bands

Given our database and modelling, we are in the best position of quantitatively assessing the effect of using only DES bands and DES+VHS bands on the results of template fitting. Figure 2.12 summarises the results. Here we plot photometric redshifts (left-hand panel) and stellar masses (right-hand panel) for all 606 sources as determined via template fittings using only DES bands (y-axis) or DES+VHS bands (x-axis). The best candidates are highlighted in dark red and deep pink, also distinguishing those obtained when assuming SMC (circles) or Calzetti (squares) reddening types, respectively.

The fitting performed with DES bands gives photometric redshifts that are always larger than 2 and very high, possibly unphysical stellar masses ($\log_{10}(M^*/M_\odot) > 12.5$), for $\sim 60\%$ of the galaxies. The inclusion of VHS bands in the fitting pushes the photometric redshift down to values below 2 for 25% of the sample (150 galaxies, independently of the reddening law) and their stellar masses also become lower. More generally, the addition of VHS bands results in a healthier distribution of stellar masses overall ($9 < \log_{10}(M^*/M_\odot) < 12.5$), with only $\sim 2\%$ of objects having $\log_{10}(M^*/M_\odot) > 12.5$. This confirms the notion that by fitting a wider wavelength range in the data we recover the physical properties of galaxies (as shown, for example, by Pforr et al., 2012, 2013).

More importantly for the present work, we find that the subsample of galaxies (~ 233) defining our best candidate sample remain at high redshift and with a large stellar mass independently of whether we fit only DES bands or DES+VHS bands. This confirms that our selection cut based on DES-only bands (as in Davies et al., 2013) plus the additional criteria put forward in this work (goodness of fits, unimodal PDF of redshift and the addition of VHS bands) are effective at selecting a robust sample of very massive, high-redshift galaxies. The combination of DES and VHS allows us to obtain more robust galaxy properties and to limit the number of low-z contaminants.

2.4.4 Caveats and Reliability Tests

In this section we test the reliability of our method and results. In 2.4.4.1 we quantify the number of low-z contaminants we found after performing spectral fitting and in 2.4.4.2 we comment on the number of sources expected to scatter in and out of the colour map selection box because of photometric errors. In the remaining subsections we test the effect of various parameters on photometric fitting results.

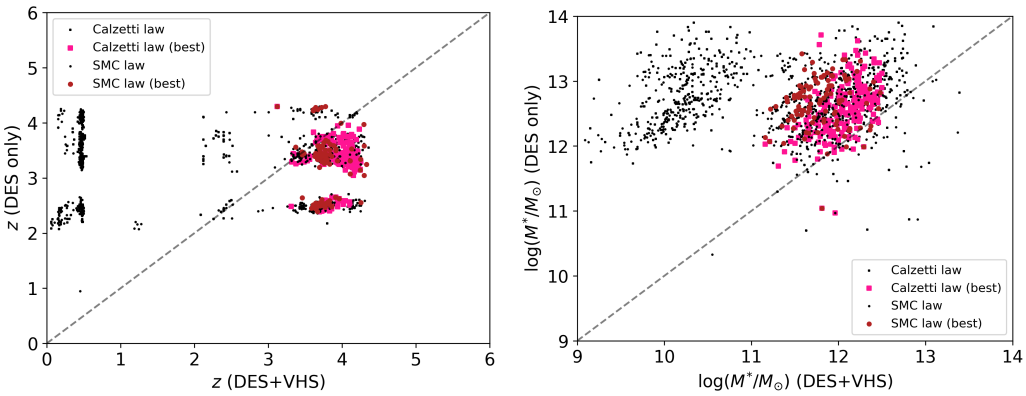

Figure 2.12: Comparison of the results for photometric redshift (left panel) and stellar mass (right panel) of the 606 template-fitted galaxies depending on the use of DES+VHS photometry versus the DES only data option. This is shown for both the SMC law (circles) and the Calzetti law (squares). The best candidates are highlighted in dark red and deep pink for the two reddening types, respectively, with the other sources being plotted in black. It can be appreciated that near-IR data is essential to successfully recover the true photometric redshift and mass of lower-redshift galaxies.

2.4.4.1 Contamination in the Selection Box

Colour selection based on models is a commonly adopted method to prioritise the galaxies one would like to obtain before performing the (time consuming) model fitting (e.g. Daddi et al. 2005). A certain level of contaminants of various kind is expected due to various types of objects having similar colours.

D13 quantify and discuss the types of expected contaminants using DES galaxy simulations as well as real objects, and find that contamination in the $z \sim 4$ box is mostly due to intermediate-redshift galaxies (of similar colour because of their Balmer/4000$\mathring{A}$ break) and quasars (D13, Figure 7). Using both DES galaxy simulations as well as real data from the MUltiwavelength Survey by Yale-Chile (MUSYC; Gawiser et al. 2006), D13 find (their Figure 11) that the $z < 2.5$ contamination in the $z \sim 4$ selection box should be 38% (consistent with the previous study by Douglas et al., 2009). Here we have the possibility of checking the D13 prediction with the real DES data after model fitting is performed. After fitting the 606 sources selected in the box, we find 34% and 32% lower-redshift galaxies for the SMC-type and Calzetti-type runs, respectively. These figures are in excellent agreement with the D13 estimates.

In conclusion, it seems unlikely that undetected lower redshift contaminants pass through the further best candidate selection cuts (in particular the redshift PDF and χ^2_r cuts), while the PSF cut should prune most pure quasars (see Figure 2.6).

2.4.4.2 Number of Sources Scattered Into the Selection Box

Photometric errors may affect the position of galaxies on our colour selection plot (specifically of the ~ 2.7 million sources without large errors and stellar contamination, see top-right panel of Figure 2.1). If we perturb the position (i.e. the colors) of the 3243 sources found within the $z \sim 4$ selection box according to their photometric errors in the g, r, and i bands and assuming a normal distribution, we find that $\sim 29\%$ of these sources scatter outside the box.

We can conclude therefore that of the 606 galaxies from the selection box, around 176 (or around 68 of the 233 best candidates) could have gone unselected purely because of their random error, while the rest sits well inside the box within their error. On the other hand, it is also possible that galaxies that would be truly outside the selection box have scattered inside, which is non-trivial to model because of the non-gaussianity of the distribution. Overall, however, we stress that the colour selection served purely as a way to prioritise the galaxies to fit using stellar population models. It would be unlikely that all fitted photometric bands for the 606 sources would be affected by their errors in such a way to spuriously produce high-z massive galaxy candidates in such numbers (i.e. 233 candidates out of 606 fitted galaxies in total). Future simulation work could investigate these uncertainties quantitatively.

2.4.4.3 Detections vs. VHS Magnitude Limits

As mentioned before, several objects do not have VHS detections, but this does not mean they do not lie at high-z. Figure 2.13 shows the expected VHS J, H, K_s magnitudes, and the survey limits at 5σ confidence, for a given i DES magnitude in the case of a passively evolving model with redshift between 2 and 5 and an age of 0.1 Gyr (to represent the most common value found for our objects). Our best candidate sources (when available for a given band) are shown as dots with errors. As expected, the majority of points lie below the survey detection limits. The K_s points lying above the relative limit refer to sources with magnitudes in the other bands within the detection limits to which a K_s magnitude was assigned via force-photometry. The difference between the points and the model lines can be accounted for by the varying age, stellar mass and SFH compared to the single model shown here, which should be taken as indicative. We shall use upper limits during model fitting for these non-detections in a forthcoming paper from our team exploiting the whole DES database.

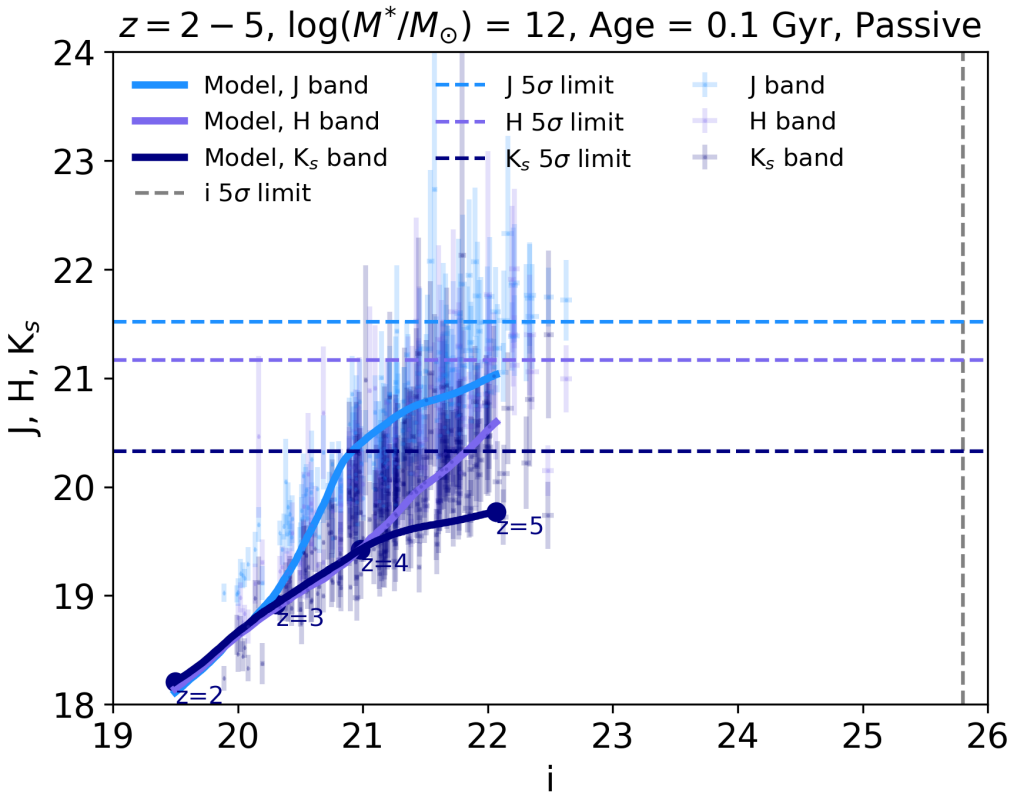

Figure 2.13: Expected J, H, K_s VHS magnitude for given i DES magnitude plotted as solid light blue, purple, and dark blue lines (with 5σ limits shown as dashed lines), respectively, for a passive M05 model with redshift between 2 and 5 and an age of 0.1 Gyr. Best candidate galaxies (for all reddening laws used) are plotted as dots for the available bands of each given source.

2.4.4.4 Age Limits in Photometric Fittings

In our model fitting we set a minimum age of 0.1 Gyr, which is larger than the minimum M05 model age (1 Myr). The setting of this limit is common practice in the literature (e.g. Daddi et al., 2005; Maraston et al., 2010) in order to contain the so-called 'over-shining' effect (Maraston et al., 2010) by which low levels of star formation generate luminosities that are so high that any older populations remain undetected. This effect leads to very low fitted ages, which translates into huge star formation rates and a general underestimation of the stellar mass (see discussion in Maraston et al., 2010). It should be noted that the over-shining effect is a threat mainly for a robust calculation of M^* and not for the photometric redshift, which is regulated by the SED shape. This is exactly what we find when we compare the photometric redshift and stellar masses we derive from a fitting run without an age limit (Figure 2.14) to our results. The plot includes results for all the 606 sources initially selected from the colour selection maps, as black dots, and for our best candidates, as larger symbols. The test shows that changing the age limit has no effect on the derived photometric redshifts (top panel) and little influence on M^* (~ -0.35 dex on average; bottom panel) as far as our best candidates are concerned.

2.4.4.5 Magnitude Saturation Test

Colour magnitude plots g vs $g-r$, r vs $g-r$, r vs $r-i$, and i vs $r-i$ for the full Y3 catalogue matched to the SV COMMODORE sources. Saturation areas correspond to the brightest end of the distributions. Overlaid are *golden sample* galaxies plotted as yellow triangles and the remaining best candidates as red dots. They do not lie at the bottom of the distributions and therefore they are unlikely to be affected by issues related to the saturation limits of the observations.

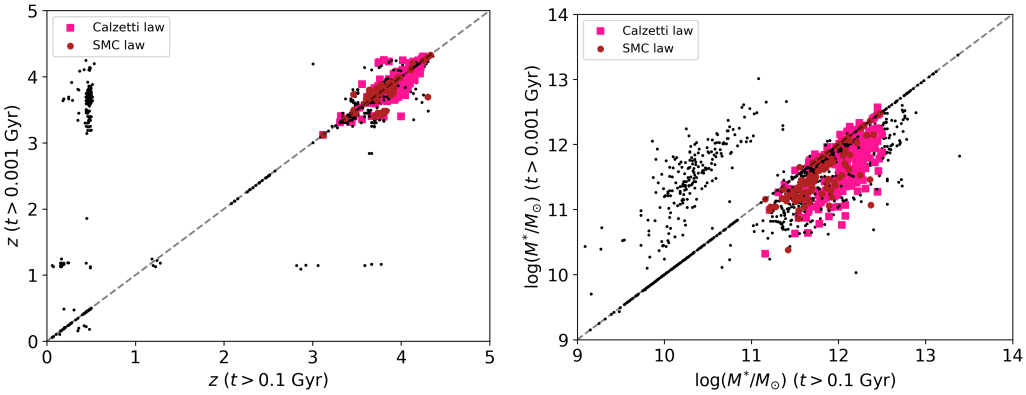

Figure 2.14: Effect of the minimum age allowed in the fitting (0.1 Gyr vs 1 Myr) on photometric redshifts (top panel) and stellar masses (bottom panel) of the 606 $z \sim 4$ selection box high-z candidates (black dots). Best candidates are plotted as dark red circles and deep pink squares depending on the reddening option used in the fitting (SMC law and Calzetti law, respectively). Even though redshift and masses of objects may change, our robust candidates are relatively unaffected.

2.5 Comparison With the Literature

In Section 2.5.1 we re-fit data from Straatman et al. (2014) to assess whether our fitting procedure recover their results. Moreover, we compare the results for our best candidates with recent literature in Section 2.5.2.

2.5.1 Re-fitting Past Literature

As is well known (e.g. Maraston, 2005; Maraston et al., 2006; Pforr et al., 2012) the results of spectro-photometric model fitting to data depend on the adopted stellar population model, the fitting setup, the fitting code, and any assumptions made (e.g. the IMF, the fitting age grid, etc.). In order to compare our results with similar ones obtained in the literature, it is useful to also adopt our fitting framework on literature data. Here we present results for the galaxies from Straatman et al. (2014). One of these objects (ZF-COSMOS-13172) is the spectroscopically confirmed $z = 3.717$

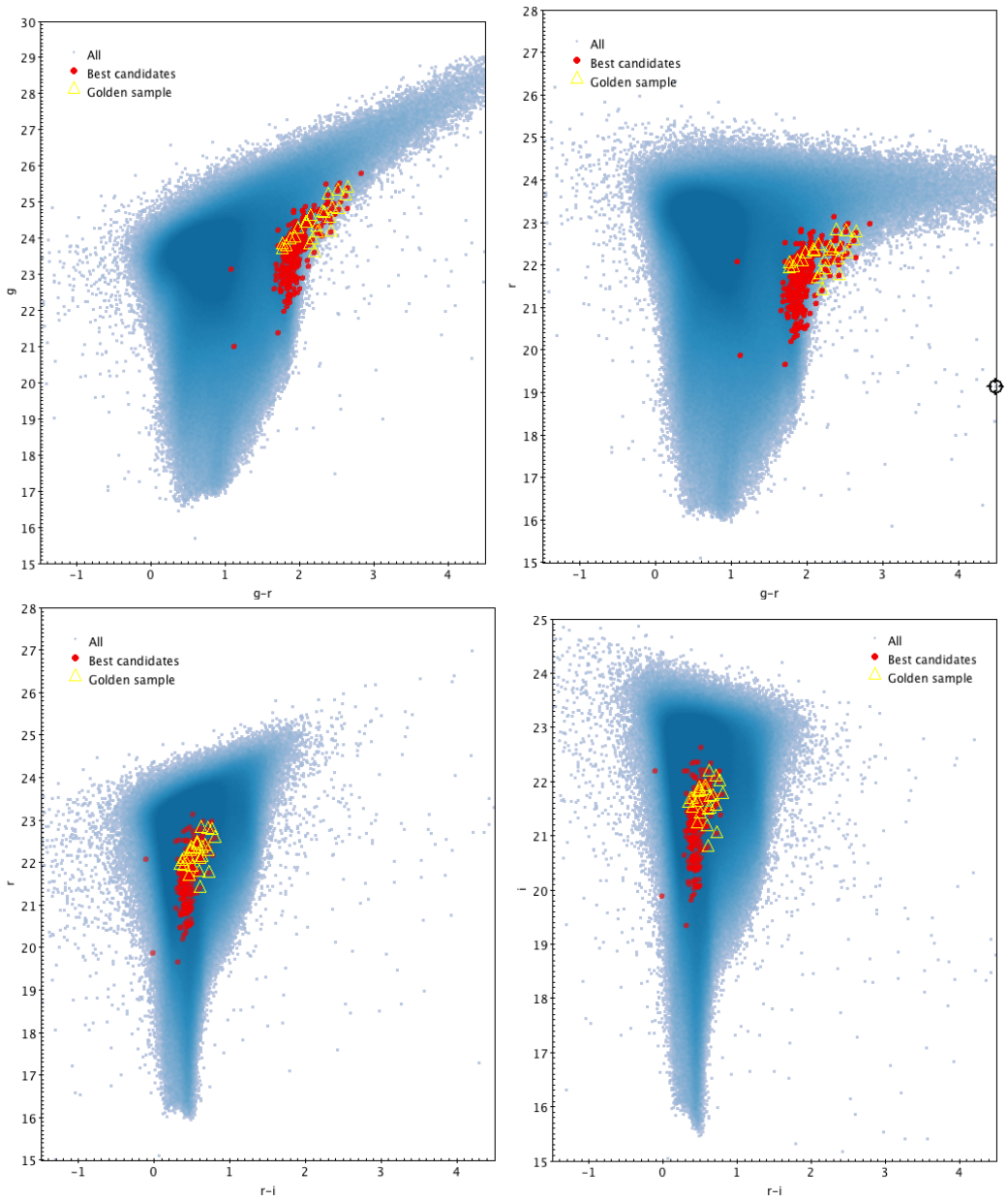

Figure 2.15: Colour magnitude plots g vs $g-r$, r vs $g-r$, r vs $r-i$, and i vs $r-i$ for the full Y3 catalogue matched to the SV COMMODORE sources. Saturation areas correspond to the brightest end of the distributions. The best candidates are plotted as red circles while on top the *golden sample* galaxies are plotted as yellow triangles. They do not lie at the limits of the distributions and therefore are unlikely to be affected by issues related to the saturation limits of the observations.

galaxy published in Glazebrook et al. (2017)[11]. Results are summarised in Table 2.1, which also reports the literature values.

It is important to note that the Straatman et al. (2014) results have been obtained using 36-band photometry (with wavelength range of $3000 - 80000$ $\mathring{A}$) while our DES+VHS combination grants us 8 bands at most. Hence, in order to mimic our fitting, we selected the same bands from the Straatman et al. (2014) database, and therefore the results of Table 2.1 refer to fits with these bands.

We find results that are similar in both photometric redshift and mass. Note that the χ^2_r for most results lie slightly above our adopted cut of $\chi^2_r < 3$ (on the other hand, one object has $\chi^2_r = 0$ as the available photometry is made up of 3 bands out of the 8 we considered and they align with the best fitted model). Overall, however, our method with only a few bands allows us to obtain a similar picture of galaxy evolution at high redshift.

Most interestingly, for the Glazebrook et al. (2017) object we obtain a best solution which includes dust and a younger age than the one reported in their paper. Our result is consistent with Simpson et al. (2017), who find - using ALMA and SCUBA data - dust detection in the same source, thereby questioning the quiescent nature of that galaxy. On the other hand, Schreiber et al. (2018) show that only 3.1 kpc away from that galaxy there is a massive, extremely obscured galaxy that they identify as the origin of the sub-mm emission observed by Simpson et al. (2017). In this work, we have not applied any particular prior on the nature of the galaxy before fitting and we provide fitting solutions with and without dust. These will be useful to potentially perform ALMA follow-ups of our candidates.

2.5.2 Further Comparisons with the Literature

In Figure 2.16 we show the median values of stellar mass and redshift of the 57 galaxies from Spitler et al. (2014), the 7 galaxies by Marsan et al. (2017), the 16 galaxies by Nayyeri et al. (2014), and the 10 galaxies by Merlin

[11]This object is now named ZF-COSMOS-20115 in Glazebrook et al. (2017).

Table 2.1: Properties of the Straatman et al. (2014), 'S14', sample of *quiescent* (according to their own classification) galaxies compared to the values we obtain ('us') using our fitting setup and those bands matching our DES+VHS photometry. For each object we obtain two results according to the assumed reddening option, whose χ^2_r is given in the last column. Note that the Straatman et al. (2014) stellar masses refer to a Chabrier IMF, while ours to a Salpeter IMF. The latter are ~ 0.2 dex larger, hence the Straatman et al. (2014) values should be increased by +0.2 dex to ensure a meaningful comparison with our derived values.

ID	z_{phot}	z_{phot}	$\log_{10}(M^*/M_\odot)$	$\log_{10}(M^*/M_\odot)$	**Age [Gyr]**	**Age [Gyr]**	**Reddening**	χ^2_r
	(S14)	**(us)**	**(S14)**	**(us)**	**(S14)**	**(us)**	**(us)**	**(us)**
ZF-COSMOS-13129	3.81 ± 0.17		11.25		1.58			
		4.65		11.39		0.64	SMC	0.000
		5.28		12.27		0.51	Calzetti	0.000
ZF-COSMOS-13172	3.55 ± 0.06		11.16		0.79			
		2.88		11.85		0.20	SMC	1.693
		4.13		11.82		1.02	Calzetti	4.016
ZF-COSMOS-13414	3.57 ± 0.19		10.64		1.00			
		3.84		10.77		0.64	SMC	4.103
		3.80		11.47		1.28	Calzetti	0.702
ZF-CDFS-5657	3.56 ± 0.07		10.88		1.26			
		2.71		10.50		0.51	SMC	3.786
		2.81		10.76		0.51	Calzetti	3.489
ZF-CDFS-403	3.660 (z_{spec})		11.06		0.79			
		1.76		10.62		1.80	SMC	0.034
		2.42		10.76		0.14	Calzetti	0.000

ID	z_{phot}	z_{phot}	$\log_{10}(M^*/M_\odot)$	$\log_{10}(M^*/M_\odot)$	**Age [Gyr]**	**Age [Gyr]**	**Reddening**	χ^2_r
	(S14)	**(us)**	**(S14)**	**(us)**	**(S14)**	**(us)**	**(us)**	**(us)**
ZF-CDFS-209	3.56 ± 0.05		10.88		0.63			
		2.01		10.83		2.60	SMC	0.054
		2.05		10.53		0.29	Calzetti	0.005
ZF-CDFS-4907	3.46 ± 0.16		10.60		0.40			
		2.89		10.31		0.32	SMC	1.297
		2.89		10.31		0.32	Calzetti	1.297
ZF-CDFS-4719	3.59 ± 0.14		10.65		1.00			
		2.92		10.84		1.68	SMC	0.093
		2.83		10.90		1.43	Calzetti	0.091
ZF-UDS-885	3.99 ± 0.41		10.78		0.40			
		5.42		11.83		0.81	SMC	2.411
		3.95		12.02		1.14	Calzetti	0.410
ZF-UDS-1236	3.58 ± 0.08		10.78		0.50			
		4.27		11.41		0.64	SMC	8.198
		3.45		11.30		0.51	Calzetti	6.397
ZF-UDS-2622	3.77 ± 0.10		10.94		0.63			
		3.81		11.00		0.72	SMC	1.611
		3.87		11.41		0.90	Calzetti	0.962
ZF-UDS-3112	3.53 ± 0.06		10.63		1.26			
		3.99		10.95		0.57	SMC	6.044
		3.99		10.95		0.57	Calzetti	6.044

ID	z_{phot}	z_{phot}	$\log_{10}(M^*/M_\odot)$	$\log_{10}(M^*/M_\odot)$	**Age [Gyr]**	**Age [Gyr]**	**Reddening**	χ^2_r
	(S14)	**(us)**	**(S14)**	**(us)**	**(S14)**	**(us)**	**(us)**	**(us)**
ZF-UDS-5418	3.53 ± 0.07		10.64		0.79			
		3.37		11.00		1.61	SMC	4.306
		3.22		10.91		1.28	Calzetti	2.806
ZF-UDS-6119	4.05 ± 0.27		10.74		0.50			
		3.91		10.84		1.02	SMC	2.040
		4.13		11.48		1.02	Calzetti	1.368
ZF-UDS-9526	3.97 ± 0.18		10.95		0.63			
		2.67		10.33		1.43	SMC	0.128
		2.67		10.33		1.43	Calzetti	0.128
ZF-UDS-10401	3.91 ± 0.38		10.58		0.25			
		3.96		10.62		0.72	SMC	0.013
		3.25		10.64		0.57	Calzetti	0.000
ZF-UDS-10684	3.95 ± 0.48		10.93		1.26			
		3.78		10.51		0.64	SMC	4.681
		3.67		10.90		1.61	Calzetti	4.526
ZF-UDS-11483	3.63 ± 0.32		11.01		1.00			
		1.20		10.25		2.10	SMC	0.000
		1.80		10.45		1.80	Calzetti	0.000

et al. (2018), as a black hexagon, pentagon, triangle and a plus, respectively. The latter two studies focus on what they call 'passive galaxies', while we do not take any particular prior here. For comparison we also plot our best candidates (with the two usual shape and colour schemes for SMC and Calzetti laws) as well as the Straatman et al. (2014) sources as re-fitted by us (as light blue circles and dark blue squares for SMC law and Calzetti law, respectively).

It can be appreciated that our candidates are of typically higher redshifts and stellar masses than these previous studies and expand the envelope of results for high-z massive galaxies.

2.6 Comparison With Model Galaxies

We use the Millennium Simulation Database[12] (volume: $(500Mpc/h)^3$) and extract the number density of galaxies with stellar masses above $\sim 10^{11}$ from different semi-analytical models, at the snapshots corresponding to $z = 3.9$ and $z = 4.1$. We find co-moving densities of $1.6 \times 10^{-5}\mathrm{Mpc}^{-3}$ for the model described in Gonzalez-Perez et al. (2014), $5.2 \times 10^{-7}\mathrm{Mpc}^{-3}$ for model galaxies from Henriques et al. (2015) and $5 \times 10^{-6}\mathrm{Mpc}^{-3}$ for the model described in Lacey et al. (2016). These densities compare to a value of $5 \times 10^{-5}\mathrm{Mpc}^{-3}$ for De Lucia et al. (2006); it is important to note that large density variations for the massive end are found in the literature (e.g. Knebe et al., 2018).

At $z = 3.9$, no galaxies from the Gonzalez-Perez et al. (2014) or Lacey et al. (2016) models have a mass above $10^{11.5}$. The same is true for the model described in Croton et al. (2016)[13]. This lack of galaxies with masses above $10^{11.5} M_{\odot}$ at high redshift is shown in Figure 2.17 for Gonzalez-Perez et al. (2014), while most of our high-redshift candidates have masses above this limit.

Some galaxies from the Henriques et al. (2015) model are indeed expected

[12] http://virgo.dur.ac.uk

[13] https://tao.asvo.org.au/tao/

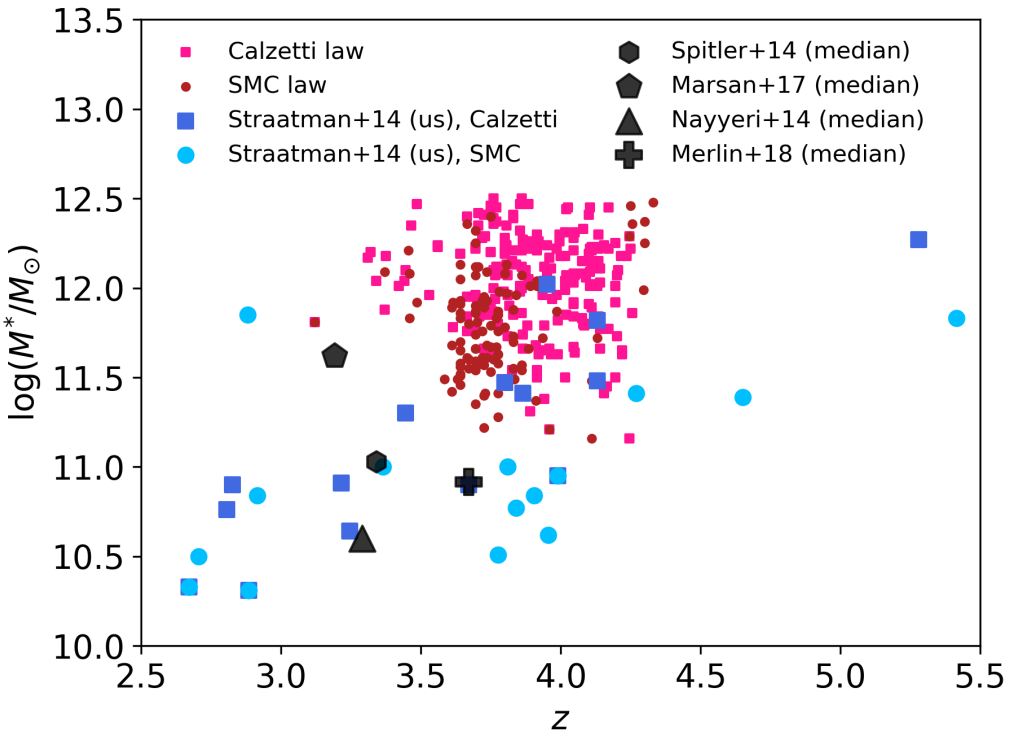

Figure 2.16: Stellar mass vs redshift for our candidates (large symbols for various reddening laws) compared to the median value for 57 galaxies by Spitler et al. (2014) (black hexagon), 7 galaxies by Marsan et al. (2017) (black pentagon), 16 galaxies by Nayyeri et al. (2014) (black triangle), 10 galaxies by Merlin et al. (2018) (black plus), and to the 18 values we obtain for the galaxies by Straatman et al. (2014) with our fitting set-up and their data (blue symbols labelled as Straatman et al. (2014)).

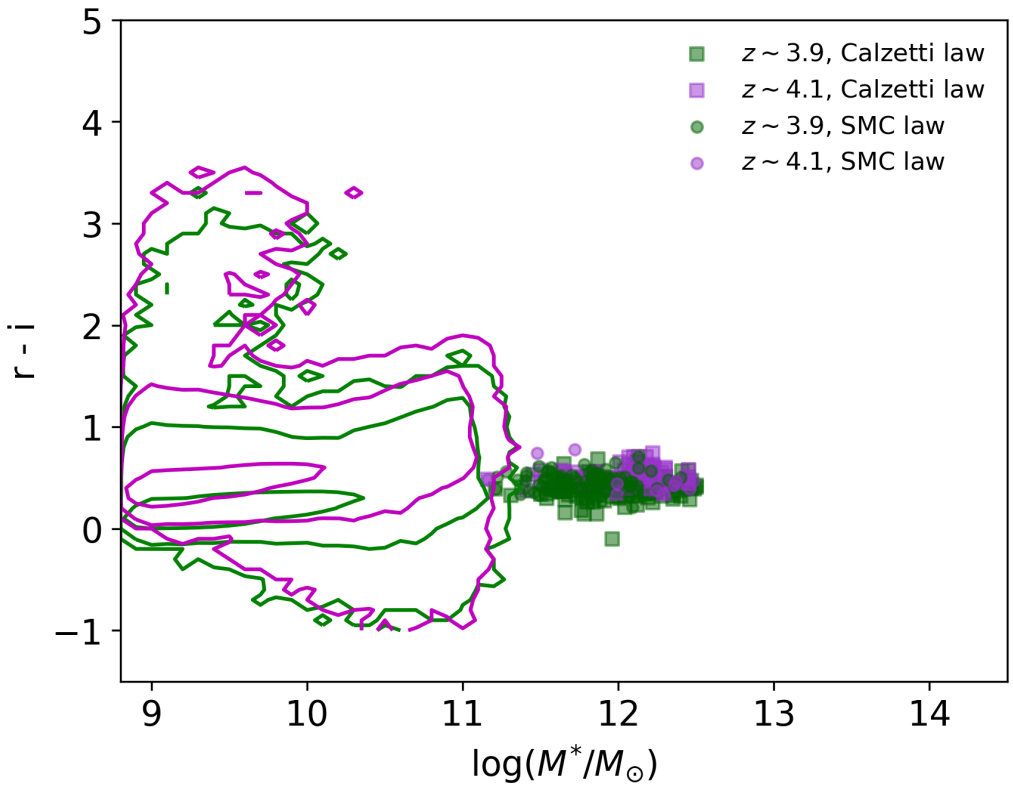

Figure 2.17: Observed-frame $(r - i)$ versus stellar mass for our best candidate galaxies, compared to galaxy distributions at $z \sim 3.9$ and $z \sim 4.1$ (colour-code in green and magenta respectively) from the Gonzalez-Perez et al. (2014) model, assuming the stellar population synthesis model from Maraston (2005). The model galaxies are shown as contours with the outermost one outlining the end of such a distribution, while the best candidates are plotted as scatter plot. Both observed and model galaxies include the effect of dust attenuation. The model stellar masses have been corrected to a Salpeter IMF (Lagos et al., 2014; Lacey et al., 2016) for consistency with our fitting assumptions. No model galaxies are found with masses above $\sim 10^{11.5}$ at these redshifts.

to have masses above $10^{11.5}$ at $z = 3.9$, but they are rare, with a density of $7.3 \times 10^{-9}\mathrm{Mpc}^{-3}$. This last model was designed to match the evolution of the stellar mass function up to $z = 3$ mainly by allowing the reincorporation timescale of wind ejecta to vary with cosmic time. The other two semi-analytical models do not reproduce the observed evolution of the galaxy stellar mass function above $z \sim 1$, predicting a too rapidly evolving high mass end. Moreover, models assuming warm dark matter produce more massive galaxies at high redshifts than standard cold dark matter cosmologies (Wang et al., 2016). Thus, redshift and physical properties of galaxies in place above $z = 2$ provide crucial information to help constrain our understanding of galaxy evolution within a cosmological context. We shall compare number densities in models and data when the DES observations are complete.

In this work we take a first glance at the physical properties - namely, colours vs. stellar mass - of massive galaxies in simulations compared to our best candidates. Figure 2.17 presents the comparison for the Gonzalez-Perez et al. (2014) model run using the version based on the stellar population synthesis model from Maraston (2005). This was chosen as, currently, it is the only model of the five explored that provides magnitudes for the DES bands. The observed-frame $r - i$ colour of the data are consistent with a subset of model galaxies at the appropriate redshift, possibly suggesting compatible star formation histories. The model galaxies have, however, too low a stellar mass with respect to those inferred from the observational data.

As stated above, very few massive model galaxies are found above $z = 3.9$. Thus, these galaxies have the potential to change the way we understand galaxy formation, once their redshifts are spectroscopically confirmed and data for the whole DES survey are analysed.

2.7 Conclusions and Discussion

We have used data from the first three years of Dark Energy Survey (DES) operations together with the Science Verification (SV) catalogue, to probe

the existence of high-redshift ($z \sim 4$), massive ($M \sim 10^{12} M_{\odot}$) galaxies down to the nominal full survey depth, and to study their nature. This analysis was motivated by our previous forecast (D13) according to which DES would be one of the very few surveys (the only one, at time of writing) that has the right combination of area (5000 deg. sq. at completion) and depth ($i = 24.3$) to allow for these rare objects to be detected, should they exist. In turn, these galaxies are key probes of the galaxy formation process within a cosmological framework, as they form from the largest primordial density fluctuations. Their number and characterisation vary substantially between cosmological simulations, and extrapolations of local and intermediate-redshift mass functions predict a large variation in the number density of these objects (see D13, Figure 1). In a similar fashion, DES data have been recently used to search for high-redshift quasars (Banerji et al., 2015b; Reed et al., 2017).

We have applied a rigorous identification method, using theoretical maps as well as visual inspection of ~ 600 potential sources, along with data cleaning (artefacts, error cuts, and star/galaxy separation). We have then performed spectro-photometric template fitting, using a large variety of models and reddening assumptions, to minimise potential biases in the determination of photometric redshifts and galaxy properties. Critical to the model fitting, we extended our DES data g, r, i, z, Y baseline with near-IR J, H, K data from the VHS survey. After model fitting, we further applied other quality cuts in order to extract the most promising sample of high-redshift, massive galaxies, namely: goodness of fit ($\chi^2_r < 3$); unimodal redshift probability distribution function showing a clear high-z solution; physical mass.

Our final result is a sample of 233 galaxies that are $z \sim 4$ candidates, with large stellar masses ($10^{11.5} \leq M/M_{\odot} \leq 10^{12.5}$) and ages of ~ 0.1 Gyr, some of which are on the verge of becoming passive. Their average star formation rates are of the order of thousands of solar masses per year and place them among the most extreme objects found so far (as in Rowan-Robinson et al. (2016)). This number of objects should be regarded as a lower limit due to our very conservative selection. Our best candidates, when paired with our PSF

comparison consideration, constitutes an excellent sample for spectroscopic and ALMA follow-ups.

The properties of our objects make them the most likely progenitors of the most massive elliptical galaxies studied in the local universe (Thomas et al., 2005, 2010). The existence of such a class of mature, massive galaxies in the early universe pose unprecedented constraints to our understanding of galaxy formation and evolution in a cosmological context. An initial test of galaxy formation simulations reveals that galaxies with such large masses are absent in cold dark matter-based cosmologies.

Our work extends the hunt for massive galaxies at $z \sim 4$ by almost an order of magnitude in stellar mass, following the studies performed, for instance, in Straatman et al. (2014), Spitler et al. (2014), Marsan et al. (2017), Nayyeri et al. (2014), and Merlin et al. (2018). Our tests on the Straatman et al. (2014) data also confirm that even though we use a limited amount of photometric bands for the fitting, we obtain results that are similar to those obtained with 36-band photometry or even spectroscopy. This is because in order to constrain a model matching galaxy spectra what is important is the wavelength baseline covered by the data rather than the density of bands over a narrower wavelength span.

We show we are able to recover the properties of one object with a spectroscopic redshift of 3.717 reported by Glazebrook et al. (2017), and in particular we provide solutions including the possible presence of dust.

One is then tempted to push our method to even higher redshifts. Photometric techniques similar to ours have also been used in studies based on the Hubble Frontier Fields (HFF) programme (e.g. Laporte et al., 2016a,b). HFF is a survey aimed at imaging six massive clusters at moderate redshift in order to observe very high-redshift ($z > 7$) galaxies (or proto-galaxies) that are visible because they have been lensed by the foreground clusters. Studies include the discovery of several tens of Lyman-break galaxies at redshifts $z \sim 7 - 11$ (e.g. Zheng et al., 2014; Jauzac et al., 2015; Coe et al., 2015).

Let us finally comment on the number counts of these extreme systems. D13 calculated the predicted galaxy number counts for a variety of approaches, including fully theoretical cosmological simulations (as per the Millennium Simulation), semi-empirical predictions obtained by passively evolving the $z = 0$ and $0.5 < z < 0.7$ published mass functions to higher redshift, available high-z mass functions (Marchesini et al., 2010), and also results from abundance-matching techniques (Behroozi et al., 2013). For example, empirical mass functions do forecast the presence of ~ 7000 galaxies with $\log(M^*/M_\odot) \geq 12.0$ within the whole DES. Of these, ~ 100 will represent true $\log(M^*/M_\odot) \geq 12.0$ systems, with the rest being misidentified due to Eddington bias (e.g. Maraston et al., 2013). In summary, the predicted number counts of D13 (Figure 1) are diverse and, at completion, a survey such as DES will help discriminate among these possibilities at the massive end of the stellar mass function. As the SV-sized data we use here include only ~ 150 deg. sq and because we calculated photometric redshifts that will need to be confirmed spectroscopically, we refrain from probing the precise number counts from D13.

Finally, this manuscript outlines a new method that only uses optical bands (in the context of DES) to identify likely massive high-z galaxies. This will work as a foundation to probe such galaxies using larger and larger photometric datasets that will be completed in the future (such as EUCLID, LSST, etc.).

All the work presented in this chapter is now part of Guarnieri et al. (2019).

Chapter 3

The Galaxy Stellar Mass Function with the Spitzer Extra-Galactic Representative Volume Survey

3.1 Preamble

In this chapter we present the galaxy stellar mass function (GSMF) calculated from $z \sim 4.5$ to the the current epoch for $\sim 750,000$ galaxies from ~ 5 sq. deg. of the Spitzer Extra-galactic Representative Volume Survey. We push the boundaries of what literature achieved by making use of the unique combination of depth (4.5 $\mu m_{AB} = 23.1$) and area (potential of up to ~ 18 sq. deg.). The photometry dataset contains up to 13 bands and allows us to calculate the photometric redshift and physical properties of each individual galaxy. We recover what the literature found in the past and we especially calculate the galaxy stellar mass function with mass bins up to $10^{12.5}$ solar masses, making it the state-of-the-art GSMF results at $z \sim 4.5$. In the massive end at redshift higher than 2 we obtain a steep function placed at the upper end of what obtained before. We also compare our results with

models and investigate the effect of the adopted reddening laws.

3.2 Introduction and Motivation

While mass assembly and structure formation is relatively well understood as far as dark matter (DM) processes are concerned, as part of the ΛCDM model, it is still unclear what governs the formation and evolution of galaxies across cosmic time. In particular, it remains an open question whether the baryonic universe follows a hierarchical structure formation model (Baugh, 2006; White and Frenk, 1991; Kauffmann et al., 1993; Kauffmann and Haehnelt, 2000), tracing the DM halo hosts (e.g.Stringer et al. 2009, Wilman et al. 2013, Zhao et al., 2015, Gu et al. 2016) as it is also replicated by simulations (e.g. De Lucia and Blaizot, 2007; Guo et al., 2011; Furlong et al., 2017, Torrey et al. 2017), or if they rather follow the so-called 'downsizing' paradigm (a term first introduced by Cowie et al. (1996) that predicts massive galaxies to have accumulated most of their masses at early cosmic times (e.g. Cimatti et al., 2006).

One of the most convenient instruments to analyse galaxy mass assembly over the life of the universe is the galaxy stellar mass function (GSMF). Its shape as a function of redshift allows us to determine how galaxy stellar mass forms and evolves. For example, past studies have used the GSMF to try and understand when massive galaxies accrete most of their mass, and whether star formation is driven by local processes or merger events. By looking at how the shape of the GSMF changes with redshift it is possible to start answering these open questions.

Most early studies of the GSMF focused on the $z < 1$ universe (roughly corresponding to the latter half of the lifetime of the universe) as it is the most accessible to optical spectroscopic survey data. Hierarchical ΛCDM models expect the massive end ($\log_{10}(M^*/M_\odot \geq 11.5$)of the GSMF to grow by around 30% (as summarised by Bundy et al. (2017)) from $z \sim 1$ to modern times, but past literature finds little growth over this period (e.g.

Bundy et al., 2006; Pozzetti et al., 2010a; Ilbert et al., 2013a; Moustakas et al., 2013; Muzzin et al., 2013a; Maraston et al., 2013). Mergers have also been excluded as main sources of mass assembly below $z \sim 1$ and cold gas accretion is instead considered to be the main cause (Pozzetti et al., 2010a). Furthermore, it was found that at $z \sim 1$ star formation ceases while it ignites in smaller-mass galaxies, in accordance with 'downsizing' (Bundy et al., 2006, Borch et al. 2006).

Obtaining a complete picture of the GSMF at higher redshifts is more complicated and it is still early to outline a clear empirical consensus on high-z structure formation for baryonic matter. In order to effectively recover the stellar mass of galaxies up to redshift $z \sim 4$, it is first crucial to have a dataset that at least extends to the near-IR, as this allows for a wider wavelength spectrum observed and it can help constrain the photometric fittings (see for example Pforr et al., 2018). Grazian et al. (2015) and Caputi et al. (2015a) managed to do this up to $z \sim 7$ by employing photometric data up to band [4.5 μm]. Grazian et al. (2015)found that the low-mass end of the GSMF evolves slowly and is steeper than the one at low-z, while the massive end does evolve in density. Caputi et al. (2015a) showed that they expect the majority of the most massive galaxies ($\log_{10}(M^*/M_\odot \geq 11$) to have accumulated most of their mass at $z > 1$, with formation redshifts close to $z \sim 6$. However, because of their limited observed area (see next two paragraphs) these two studies could not comment on the high-z, $\log_{10}(M^*/M_\odot \geq 12$ end of the GSMF.

Additionally, the difficulties for higher-redshift studies come from limitations in terms of width and depth of the available surveys. This resulted in past studies mainly focusing on either the massive end (supported by width) or faint end (supported by depth) of the GSMF, with the latter being observable only by space-based telescopes (i.e. the Spitzer Space Telescope or the Hubble Space Telescope) as per the currently available instruments (Grazian et al., 2015).

Given the tough requirements needed to calculate the GSMF at high-z

it became apparent that spectroscopic observations alone (generally used for past studies at $z < 1$) could not suffice and photometric ones were necessary. Grazian et al. (2015) concluded that photometric redshifts only slightly affect the calculation of the GSMF at high redshift (and so does the choice of stellar population models) and therefore they are a useful instrument for this type of task that requires to push the boundaries of area observed and magnitude limits in the infrared part of the electromagnetic spectrum.

In this paper we present the calculation of the GSMF using data from the Spitzer Extragalactic Representative Volume Survey (SERVS). This is a Spitzer-based survey that is in the unique position to offer both wide, i.e. $\sim$ 18 deg^2 (for this work we only use the first $\sim$ 5 deg^2 available, see Section 3.3.2 and 3.3.3 for more details), and relatively deep (i.e. $[4.5\ \mu m] <$ 23.1) photometric data in the infrared (Mauduit et al., 2012). SERVS was designed to be capable to study galaxy environment up to redshift $z \sim 5$, also allowing us to reach similar redshifts for the GSMF. Moreover, the SERVS pipeline offers multi-band photometry spanning from the optical u to the infrared $[4.5\ \mu m]$ band (see Section 2), which makes it suitable to study the GSMF consistently from low redshift up to $z \sim 4.5$. This dataset therefore represents a clear improvement on recent past studies that extend to similarly high redshifts. For instance, Ilbert et al. (2013a) calculated the GSMF up to $z \sim 4$ using $\sim$ 1.5 deg^2 at $K_s < 24.0$, Grazian et al. (2015) did so for redshifts $3.5 < z < 7.5$ with $\sim$ 0.1 deg^2 at a deeper $H < 28.5$, and Caputi et al. (2015a) examined a similar range as Grazian et al. (2015) with $\sim$ 0.8 deg^2 for depth $K_s < 24.8$. It is therefore clear that while we cannot push higher than $z \sim 4.5$ we have already much more width available than previous similar work, with almost three times as much area to become available from the SERVS pipeline in the future. This effectively means that we are able to calculate the GSMF at high-z up to masses $\log(M^*/M_\odot) \sim 12.5$ for the first time.

The additional $\sim$ 13 deg^2 split in 4 additional observed fields observed by the SERVS programme will also allow us in the future to comment more

extensively on the effects of cosmic variance, which the literature suggests potentially being an important factor at redshifts higher than ~ 1.5 (see e.g. Marchesini et al., 2009; Bundy et al., 2017) but that can be mitigated as the observed area increases.

3.3 Method

3.3.1 Overview

We calculated the GSMF up to redshift 4.5 for a 13-band photometric catalogue based on SERVS data and compared our findings to the relevant literature. This redshift upper limit was chosen based on the characteristics of our survey (crucially width and depth, see following two sections), when compared to past studies in order to optimise for the reliability of our results. The data (described in detail in Section 3.3.3) has been fitted to template models (see Section 3.3.4) in order to calculate the photometric redshift as well as the physical properties, among which, crucially, the mass. We then calculated the GSMF and estimated the uncertainties as described in Section 3.3.8 and 3.3.9, respectively.

3.3.2 SERVS

The Spitzer Extragalactic Representative Volume Survey (SERVS) covers a total of ~ 18 sq. deg. in 5 different fields, namely the so-called ELAIS-N1, ELAIS-S1, Lockman Hole, Chandra Deep Field South and XMM-LSS (for brevity, in this work often known simply as XMM).

The survey is based on the [3.6 μm] and [4.5 μm] bands of the Spitzer Space Telescope. The programme was designed to enable galaxy evolution and environmental studies up to $z \sim 5$, and it manages so by combining a relatively large observation area (i.e. 18 sq. deg. in total) and faint magnitude limits (i.e. $[4.5]_{AB} \leq 23.1$). To fulfil this potential the SERVS team and data pipeline have merged the Spitzer data with other ancillary survey data as

described in Section 3.3.3.

Initial data releases simply created the multi-wavelength catalogues necessary to calculate the photometric redshifts and physical properties, but the latest XMM catalogue released (used for this work; Nyland et al., 2017) has also undergone the so-called 'TRACTOR' process, aimed at minimising the risk of blended galaxies, which is especially relevant for high-z studies.

3.3.3 The Photometric Catalogue

The catalogue we used for this work consists in 1,247,954 galaxies being observed in up to 13 photometric bands, spanning a wavelength range going from $\sim$ 3829 $\mathring{A}$ to $\sim$ 45228 $\mathring{A}$ (in the AB-magnitude units). The dataset is created by combining data from the CFHT telescope (u band), Hyper-Supreme Camera (HSC; for bands g, r, i, z, and Y), the VISTA Deep Extragalactic Observations (VIDEO) survey (bands Z, Y, J, H, and K_s), and the SERVS Spitzer bands Ch.1 and Ch.2 (also referred to as [3.6], and [4.5], respectively). The data used here comes uniquely from the SERVS XMM field and it corresponds to a total effective area of 4.9168 squared degrees.

The galaxies are selected using the VIDEO bands and, thus, all sources have at least one non-zero VIDEO band. The detection limit is therefore variable across the VIDEO bands, but the Spitzer Ch.2 is used as an effective limit at AB magnitude of 23.1.

In addition to the photometry, the catalogue also contains one extra column: the so-called 'Ph flag'. This is a flag that indicates whether the photometry of a given galaxy may be affected by systematics such as noisy observational regions in the images or poor photometry quality. Specifically, this flag is raised if the flux density at 4.5 μm is less than 1 μJy, there are fewer than 5 bands among the combination of J, H, Ks, [3.6], [4.5], Y, J, H, [3.6], [4.5], or i, J, H, [3.6], [4.5] at $> 3\sigma$ (in order to ensure a solid photo-z), or if there is a zero or low coverage area in the VIDEO images for a given source. Out of the 1,247,954 galaxies 735,984 ($\sim$ 59%) pass the 'Ph flag' criterium, and these are to be considered to be forming the full list of sources used to finally obtain

the GSMF. As the 'Ph flag' effectively affects the faintest catalogue objects only, which would be well below the GSMF mass limits (see Section 3.3.8.1 for more details), no further considerations are needed to adjust the effective observed area or the count of the total sources when the GSMF is calculated.

3.3.4 The Calculation of the Redshifts and Physical Properties

In order to calculate the GSMF we first need to calculate the photometric redshift and stellar mass of each galaxy in the catalogue described in Section 3.3.3.

This was done using the template-fitting code HyperZ (Bolzonella et al., 2000) combined with ancillary scripts for the calculation of the stellar mass (Daddi et al., 2005; Maraston et al., 2006). HyperZ is described in more detail in Appendix A. For this SERVS-related work we use the same running settings as in our studies with Dark Energy Survey data (see Chapter 2), with the exception except of the maximum allowed redshift, as described below. We report again the full relevant details in the following paragraphs for reference.

HyperZ outputs the photometric redshift, the best-fitting template, and a reduced χ^2 value (χ^2_r) for the best-fitting template, calculated as $\chi^2/(N-1)$, where N is the number of filters. The best-fitting template gives us information of each galaxy's photometric redshift (and associated error), age, star-formation rate (SFR) and history (SFH), metallicity, E(B-V), and absolute magnitude. Using these results, the ancillary scripts then allow us to calculate the stellar mass for each source.

Additionally, a series of input parameters can be modified in order to more finely control the way HyperZ operates. These are: age limits, magnitude limits, redshift range and binning, reddening law, and template setup. We have explored different combinations for fitting and model setup, which we now describe.

Each galaxy spectral energy distribution model (the template) is calcu-

lated assuming a star formation history (SFH, detailing the mode of star formation, e.g. single burst, exponentially-declining star formation, etc.), an age (t parameter, which runs from the start of star formation at $t = 0$ through the galaxy evolution, at logarithmic time steps from 1 Myr to the age of the Universe at the given redshift and assumed cosmology), a chemical composition, and a reddening by dust. Each model is redshifted at various values of redshift and a χ^2 is calculated for each redshifted model.

The redshift range we explored here varied from 0 to 12 in steps of 0.11 (the finest value allowed by HyperZ for such an extended redshift range), consistently for each fitting run. The redshift range is the main difference compared to the running set-up of the DES work (see Chapter 2).

A variegated selection of 32 sets of model spectral energy distributions based on the Maraston (2005) evolutionary population synthesis models (M05) was used at each run, spanning a wide variety of star formation histories (SFHs; as in Maraston et al., 2006). These include single-bursts simple stellar populations, τ (exponentially declining), truncated (constant until an instantaneous decline to zero, to simulate rapid quenching), and constant SFHs, each of them calculated for a grid of 221 ages and four metallicities ranging between 1/5 to twice solar. All the runs were repeated for the option of no reddening as well as for two reddening laws: the so-called 'SMC' law (Prevot et al., 1984; Bouchet et al., 1985) and the well-known 'Calzetti' law (Calzetti et al., 2000). For each the extinction parameter A_V was allowed to vary between 0 and 3, in steps of 0.5. These two reddening laws were selected because they are maximally different among the options offered by HyperZ and they are appropriate for different classes of high-z galaxies. Maraston et al. (2006), by exploring all options in HyperZ, concluded that these two are those identifying the best fits in most cases of $z \sim 2$ galaxies, and that while Calzetti's law is calibrated with starbursts, the SMC seems to be more appropriate for passive galaxies (as also concluded by Kriek and Conroy, 2013). We assumed a Salpeter (1955) IMF for all model options. Furthermore, we used an age cut to retain only solutions older than 0.1 Gyr,

which is commonly used in order to avoid age-dust degeneracy pushing the fits towards low ages. Lastly, we ran the code with loose absolute magnitude limits (i.e. between -12 and -30) in order not to introduce further priors in the fitting process.

3.3.5 Running HyperZ on Large Datasets

When we ran HyperZ for the Dark Energy Survey project, we did so for around 600 galaxies. This means that it was straightforward to run such a code on a local machine in less than 30 minutes, and even when using both the SMC and the Calzetti reddening laws the full running time would amount to no more than one hour.

On the other hand, for this work we needed to fit $\sim 750,000$ galaxy photometries and the workload would have been prohibitive if it was not for the employment of the Sciama cluster supercomputer[1]. Sciama has a total of 3702 cores, each with at least 2 GBs of RAM, and a general HyperZ run requires 3 cores to run properly. Depending on how busy the supercomputer is, it is possible to use up to ~ 750 cores for any given user, meaning that we could run ~ 250 HyperZ processes in parallel at a time. This meant being able to run HyperZ for each reddening law in only ~ 5 hours rather than in ~ 52 days. We can therefore have full results for runs with the SMC and the Calzetti reddening laws in less than a day.

In order to successfully parallelise this task, we created an extensive pipeline to automatically follow the usual steps required to run HyperZ and then to calculate the stellar masses. The pipeline would split the photometric catalogue in 250 smaller datasets and move them in 250 newly created folders on the so-called 'Lustre' storage environment connected to Sciama, via temporary 'stable' directories. This was necessary as the home working directories of Sciama have limited storage and to avoid the risking of crashing the Sciama login node due to the elevate mole of I/O associated to the normal running of HyperZ. The HyperZ and mass calculation ancillary

[1] http://www.sciama.icg.port.ac.uk

script executables along with the stellar population models and the other supplementary files are also copied in each of the 250 directories and a 'jobscript' is launched for each to run the files appropriately. A 'jobscript' is a file that can be submitted to a cluster supercomputer like Sciama to initialise some commands that continue being run in the background even when the user is not currently connected to the server. The first few lines set the parameters for the type of run to be submitted to Sciama. These include the name of the job to run (for reference when checking the status), the resources needed (e.g. number of cores), the username of the account holder, and the maximum 'walltime' (i.e. the number of hours after which the 'jobscript' is automatically killed, to avoid any hanging jobs). The last few lines instead include the normal shell commands, such as changing to correct directories and launching the required executables. The outputs in the 250 different directories are then combined in a single one to represent the full results of the $\sim 750,000$ SERVS galaxies. This process was repeated for both the SMC and the Calzetti reddening laws.

3.3.6 HyperZ Fitting Results

As described in Section 3.3.4, the output results of a HyperZ fitting procedure include multiple physical properties (such as mass, age, SFR, and SFH) for each galaxy as well as its photometric redshift. Moreover, a value of the χ^2_r is calculated for every source in the catalogue. In order to calculate the SERVS GSMF we first combine the HyperZ fitting results using both the SMC and the Calzetti reddening laws by keeping the output values with the lowest χ^2_r for each source. The masses and redshifts found this way are shown in Figure 3.1 as grey dots.

Unlike our DES work, we decided not to make use of the χ^2_r values for this work as it would be otherwise complicated to adjust the observed area, which is a necessary information to calculate the GSMF. Nonetheless, the sources with $\chi^2_r \leq 3$ are highlighted in orange in Figure 3.1. The only cut we perform is to exclude any source above $\log_{10}(M^*/M_\odot = 12.5$ (outlined

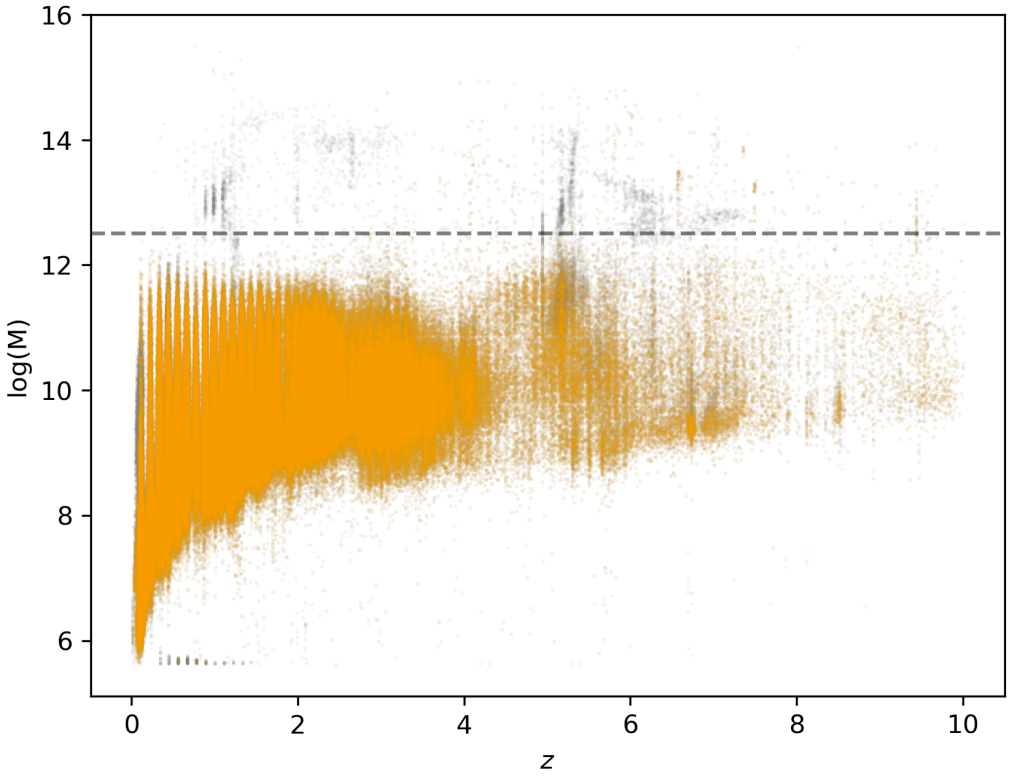

Figure 3.1: Stellar mass M^* (in solar masses units) against redshift for all the SERVS sources fitted using HyperZ. The data plotted here is a combination of results from both the SMC and the Calzetti laws where the solution with the smaller χ^2_r is kept for any given galaxy. The points are plotted initially as grey, and on top the same galaxies with $\chi^2_r \leq 3$ are plotted in orange. A horizontal grey dashed line is plotted at M=12.5 to indicate the threshold above which we deem galaxies to have an unphysical stellar mass and that therefore have been excluded from our GSMF calculations.

by the horizontal dashed grey line), as we deem values higher than that threshold unphysical (these are only $\sim 0.3\%$ of the total number of sources). It can be appreciated that most galaxies above $\log_{10}(M^*/M_\odot) = 12.5$ are grey in Figure 3.1, indicating that their fitting results are less solid. This reinforces the fact that they should not be considered as real galaxies having such extreme mass values as far as the GSMF is concerned.

3.3.7 The $1/V_{max}$ Method

We calculated the GSMF following the commonly used $1/V_{max}$ method (Schmidt, 1968). From this recipe follows that, as reported by Baldry et al. (2008), for each mass bin (ΔM) in each z range, the GSMF value (ϕ) is given by:

$$\phi = \frac{1}{\Delta \log \mathrm{M}*} \sum_i \frac{1}{V_{max}} \omega_i, \tag{3.1}$$

where $\Delta \log \mathrm{M}*$ is the width of the of the given mass bin, V_{max} is the maximum comoving volume accessible by the ith galaxy and ω_i is a weighting associated with every ith galaxy.

This methodology is a relatively straightforward way to calculate the GSMF without the requirement of prior assumptions on the shape of the function, and it is also capable of delivering a normalised result that can be easily compared to literature. On the other hand, a disadvantage of this methodology is that survey-specific clustering may affect in particular the faint-end of the GSMF. While this can a be large source of uncertainty, it should be noted that SERVS is a relatively wide survey, i.e. ~ 18 deg^2 (see Section 3.3.9.3 for more comments on cosmic variance).

3.3.8 The SERVS Galaxy Stellar Mass Function

The calculation of the GSMF in our case has been performed using the Etherington et al. (2017) code, which we modified to accept a catalogue compatible with the SERVS data. In particular, the effective area observed is now directly a single input parameter (calculated by the SERVS data

pipeline) while it used to be estimated by the code, requiring the user to input the number of pixels covered by each galaxy and the sky area corresponding to a single pixel of the DEcam (the camera used for the Dark Energy Survey, the data used by Etherington et al., 2017). The SERVS XMM-field effective area used for this work is 4.9168 sq. deg.

As it follows from Equation 3.1, the input catalogue to feed into the GSMF calculation code requires the mass and z_{phot} of each galaxy as calculated by our HyperZ runs (as highlighted before we use a combination of results from fittings performed with both the SMC and Calzetti reddening laws by using the outputs with lowest χ^2_r for each given source), and a measurement of V_{max}.

The value of the V_{max} depends on z_{min} and z_{max}, which are the minimum and maximum redshifts, respectively, at which each given galaxy could be detected by the survey based on the detection limits. While the value of z_{min} is effectively always set by us to $z = 0.001$ as any galaxy would be observable in the local universe, the value of z_{max} requires further considerations and it is calculated using the HyperZ fitting results of each ith galaxy. The value of z_{max} is estimated by extracting the maximum redshift of a model galaxy with its given SFH and age, according to the same M05 stellar population models utilised for the HyperZ fittings, to have a [4.5] apparent magnitude below the SERVS effective limit of $[4.5]_{AB} = 23.1$. Once z_{min} and z_{max} are obtained these are included in the input catalogue for the GSMF code, which then calculates V_{max} as the comoving volume between the two redshifts.

The cosmology used for this work is the so-called 'concordance cosmology': $\Omega_M = 0.3$ and $\Omega_\Lambda = 0.7$.

3.3.8.1 Completeness and Low-mass Limits

What has not been discussed yet from Equation 3.1 are the values of ω_i, and that is because in our GSMF calculations we make no use of such corrections factors.

Most commonly, ω_i represent completeness factors to adjust the value

of the GSMF, ϕ, by the unobserved fraction of flux for galaxies of a given redshift in a given mass bin due to the limitations of the survey, i.e. the effective magnitude limit. In general, this correction should affect only the low-mass, hence faint, end of the GSMF. In this work we did not attempt to calculate the completeness factors but we instead calculated completeness lower mass limits. These limits would vary for every redshift range considered and indicate the lowest mass bin for every GSMF plot that can be considered 'complete' and therefore the true value of our GSMF.

In order to calculate the low-mass limits we made use of the Pozzetti et al. (2010a) methodology. By employing once again the M05 stellar population models and our HyperZ fittings results, we calculated the mass each galaxy would have if its apparent magnitude matched the survey magnitude limit ($[4.5\ \mu m] = 23.1$) given its z_{phot}, age, and SFH. Pozzetti et al. (2010a) suggests to calculate the low-mass limit as the bottom 20-percentile of the masses calculated, for every GSMF redshift range considered. As it will be appreciated in Section 3.4, where we present the results and we compare them to the literature, this appears a reasonable estimate but we also show the limits corresponding to the bottom 80-percentile as well as the median value.

3.3.9 Uncertainties

Before presenting the SERVS GSMF and comparing it to past literature, it is important to quantify sources of uncertainty on our GSMF calculation. In particular, we calculate uncertainties due to Poisson noise, photometric redshift random errors, and cosmic variance. We now describe in detail how each is estimated.

3.3.9.1 Poisson Uncertainty

The Poisson error, σ_{Poi}, is calculated following the Gehrels 1986 methodology. Starting form the number of galaxies, n, inside a given mass bin for every

redshift range, the Poisson upper limit is given by equation,

$$\lambda_u = n + \sigma\sqrt{n + \frac{3}{4}} + \frac{\sigma^2 + 3}{4}, \tag{3.2}$$

and the Poisson lower limit is given by equation,

$$\lambda_l = n - \sigma\sqrt{n - \frac{1}{4}} + \frac{\sigma^2 - 1}{4}, \tag{3.3}$$

where σ is the confidence level required and therefore set to 1 for our case. The $1-\sigma$ upper and lower errors on n are therefore equivalent to $\lambda_u - n$ and $n - \lambda_l$, respectively. The Poisson errors on the GSMF follows from these by recalculating ϕ using the different values of λ_u and λ_l.

3.3.9.2 Photometric Redshifts Random Uncertainty

In order to estimate the uncertainties due to the photometric redshift random errors, σ_{ran}, the SERVS photometric data was perturbed according to the error and then it was re-fitted with HyperZ and the GSMF re-calculated (for each mass bin of every redshift range considered) 30 times.

In literature the number of realisations is canonically set to 100 (except for example in Ilbert et al. (2013a) that also used 30) as a way to obtain better statistics; here we limit this number to 30 for limitations in computing time. Generally, past studies have used only hundreds or a few thousands of galaxies for their GSMF calculations, while here we attempt the same using almost 1 million sources. In fact, as explained in Section 3.3.5, even taking advantage of a cluster supercomputer like Sciama, we could only limit the running time of a single iteration to ~ 5 hours. This means that to calculate our random errors still required over 6 days of computing time, excluding any overheads and troubleshooting. Also important to note is that to achieve this the pipeline from Section 3.3.5 was extended to use 'jobscript' arrays and to automatically calculate the GSMF for all redshift ranges. These are similar to the classical 'jobscript' files, but have an extra setting that allows to re-run the same 'jobscript' with different parameters. In this case the parameters

used were the number of iteration (1 to 30) and these iterating values were used as input to the Python scripts from Section 3.3.5.

From the values of the GSMF ϕ of these 30 Monte Carlo realisations, we then could estimate the photometric redshift random error, σ_{ran}, as the central 68% of the distribution.

3.3.9.3 Cosmic Variance Uncertainty

Lastly, we also considered the uncertainty due to cosmic variance, σ_{cv}. Usually, this becomes less important as the observed area increases and it is calculated by observing the difference in the GSMF when calculated for different fields.

In our case, as we only have data available for the SERVS XMM field, we could not calculate the cosmic variance uncertainty in the canonical way. We instead made use of the Trenti and Stiavelli (2008) calculator (available online at: http://casa.colorado.edu/ trenti/CosmicVariance.html) to estimate σ_{cv}. This takes as input the redshift range relative to each GSMF calculation, the intrinsic number of galaxies observed, and the chosen cosmology. The output is simply a fractional error on the number count of observed galaxies, which easily translates into the actual cosmic variance error on ϕ.

3.3.9.4 Total Uncertainty

The total error on our GSMF is given by a combination of Poisson, random, and cosmic variance uncertainties. This is given by equation,

$$\sigma_{tot} = \sqrt{\sigma_{Poi}^2 + \sigma_{ran}^2 + \sigma_{cv}^2}. \tag{3.4}$$

This is plotted as a single total error on our GSMF plots (see Section3.4) when comparing our results to literature. Although the choice of errors is not always consistent through literature (for instance cosmic variance is rarely accounted for), the comparisons remain reasonable.

3.4 GSMF Results

We present the GSMF for a series of different redshift bins up to $z \sim 4.5$, which as discussed in Section 3.2 corresponds to the higher limit to which we can conservatively consider SERVS to be capable of delivering accurate results thanks to its combination of width and depth. The redshift ranges presented are: $0.1 < z < 0.2$, $0.2 < z < 0.4$, $0.4 < z < 0.6$, $0.6 < z < 0.8$, $0.8 < z < 1.0$, $1.0 < z < 1.5$, $1.5 < z < 2.5$, $2.5 < z < 3.5$, and $3.5 < z < 4.5$.

All our main results are shown in Figure 3.2. Our GSMF is plotted as dark blue stars. Different literature is plotted with a combination of colours and symbols (errors are plotted only when available in table format or easy to extract from plots on the source manuscripts), based on the different redshift ranges. See legends of Figure 3.2 for the full list and an indication of what type of data and area observed each literature instance used. Our results are also compared to model data simulating the same XMM field and survey limitations (see Section 3.4.1 for more details); this is identified as dark red circles and identified as 'lightcone'. The low-mass limits (see Section 3.3.8.1 are also plotted as vertical lines: dark grey dashed line for the 20-percentile-type limit, black dashed-dotted line for the 80-percentile-type limit, and light grey dotted line for the median-type limit.

Our GSMF results are generally compatible with previous literature across all redshift ranges, with slight differences as described in the next few paragraphs. The literature instances selected are from Muzzin et al. (2013a); Moustakas et al. (2013); Pozzetti et al. (2010a); Baldry et al. (2012); Bundy et al. (2017); Maraston et al. (2013); Marchesini et al. (2009); Caputi et al. (2015a); Grazian et al. (2015); Lee et al. (2011); Stark et al. (2009).

All literature instances have their mass bin positions corrected by IMF and stellar population model choices. We homogenised all data points to our standards, i.e. Salpeter IMF and M05 templates by using the following corrections from Pforr et al. (2018):

$$M_{Salpeter} = M_{Kroupa} + 0.19, \tag{3.5}$$

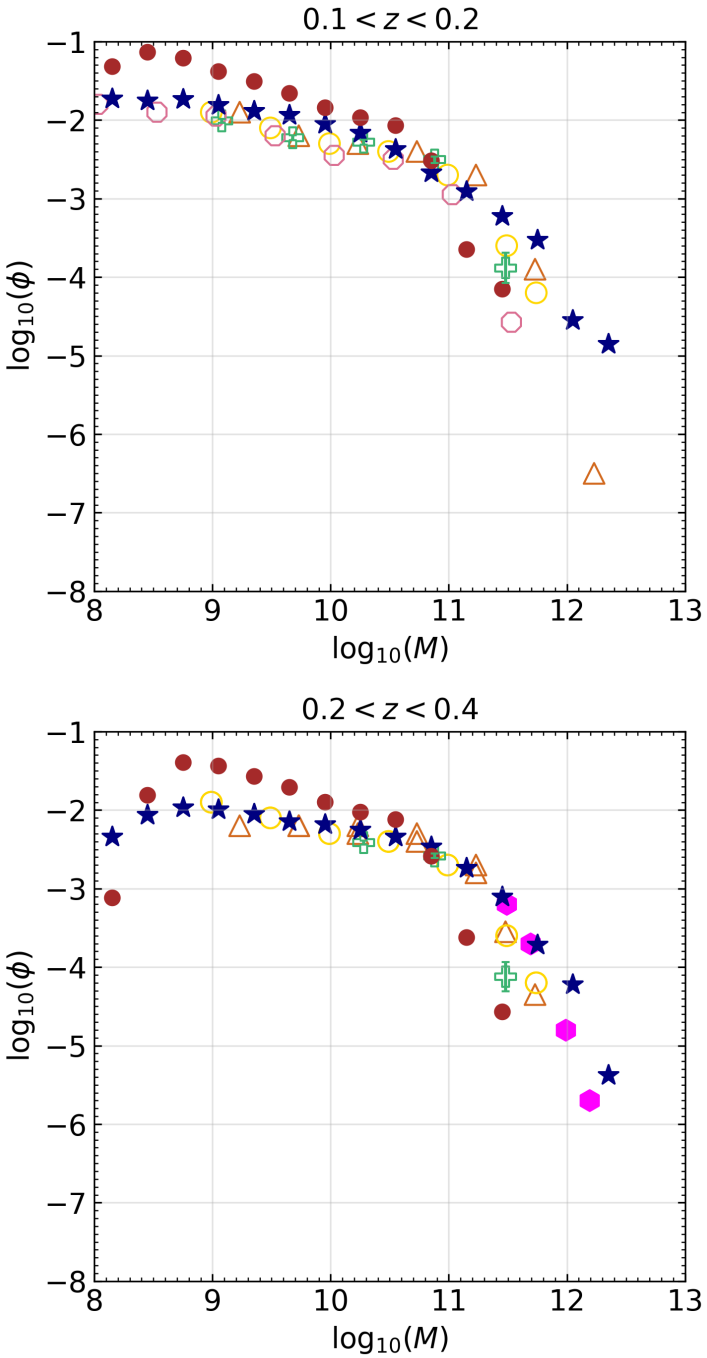

Figure 3.2: This is a figure spanning multiple pages. The full caption is found at the end of the figure.

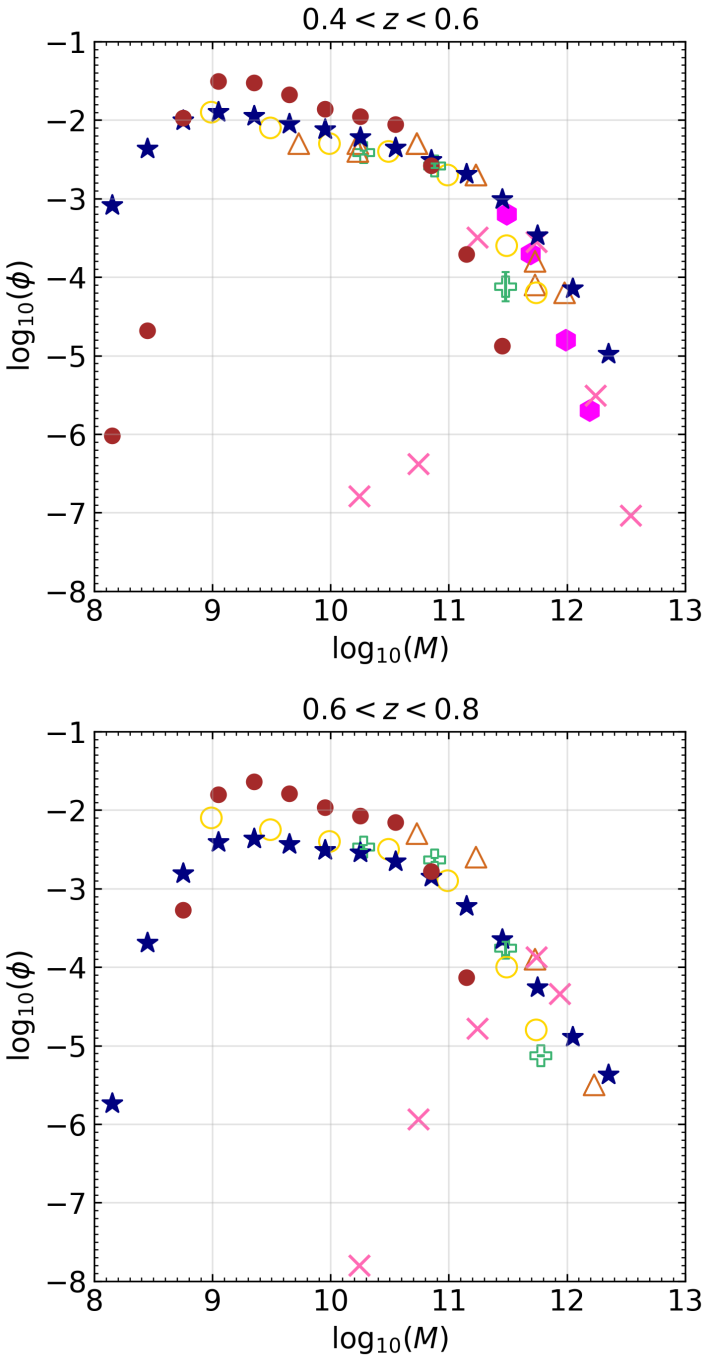

Figure 3.2: This is a figure spanning multiple pages. The full caption is found at the end of the figure.

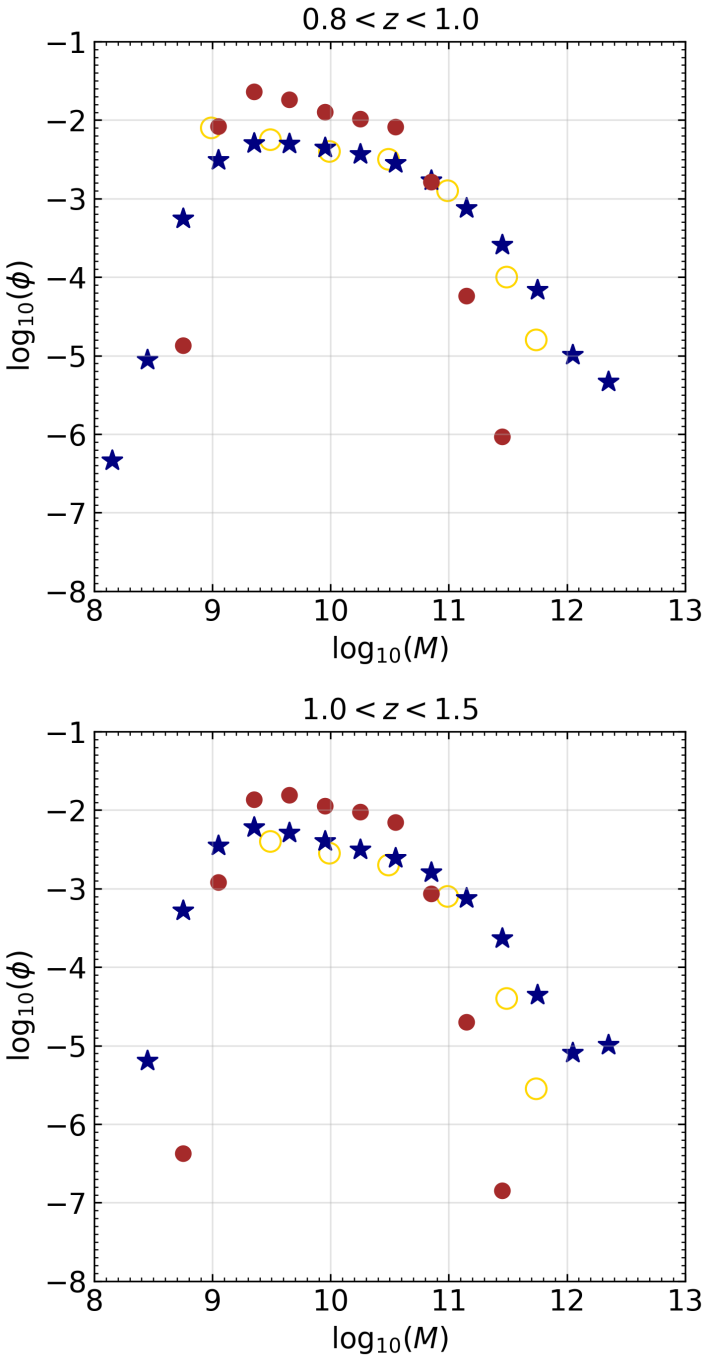

Figure 3.2: This is a figure spanning multiple pages. The full caption is found at the end of the figure.

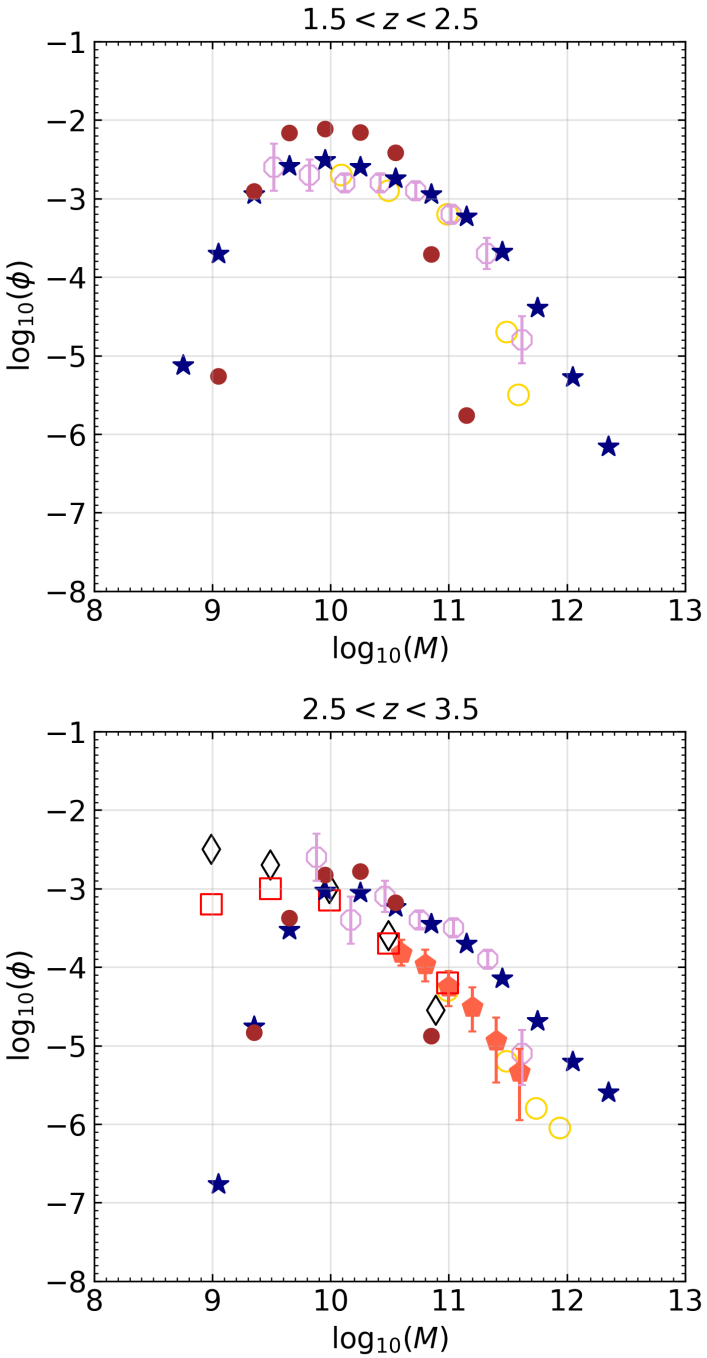

Figure 3.2: This is a figure spanning multiple pages. The full caption is found at the end of the figure.

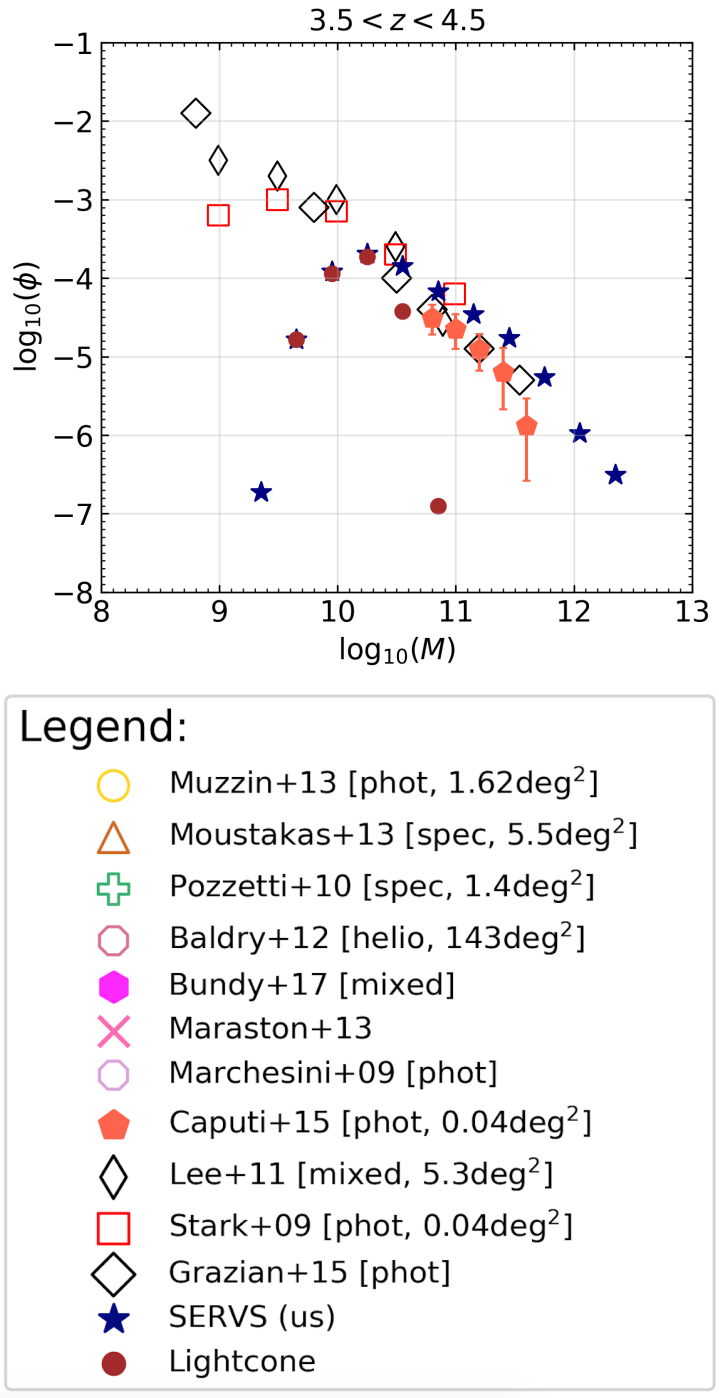

Figure 3.2: This is a figure spanning multiple pages. The full caption is found at the end of the figure.

Figure 3.2: GSMF for redshift ranges (top to bottom panel) $0.1 < z < 0.2$, $0.2 < z < 0.4$, $0.4 < z < 0.6$, $0.6 < z < 0.8$, $0.8 < z < 1.0$, $1.0 < z < 1.5$, $1.5 < z < 2.5$, $2.5 < z < 3.5$, and $3.5 < z < 4.5$. Our GSMF is plotted as dark blue stars. Different literature is plotted with a combination of colours and symbols (errors are plotted only when available in table format or easy to extract from plots on the source manuscripts), based on the different redshift ranges; see legends of Figure 3.2 for the full list and an indication of what type of data and area observed each literature instance used. Our results are also compared to model data simulating the same XMM field and survey limitations (see Section 3.4.1 for more details); this is identified as dark red circles and identified as 'lightcone'. The low-mass limits (see Section 3.3.8.1 are also plotted as vertical lines: dark grey dashed line for the 20-percentile-type limit, black dashed-dotted line for the 80-percentile-type limit, and light grey dotted line for the median-type limit.

$$M_{Salpeter} = M_{Chabrier} + 0.23, \tag{3.6}$$

$$M_{M05} = M_{BC03} - 0.20. \tag{3.7}$$

We find that the massive end of the SERVS GSMF is consistently higher than most literature across all redshift ranges (Marchesini et al. (2009) seems the one that gets closest to us). This could be due to SERVS's unique combination of observed area and depth allowing us to fish the relatively rare massive galaxies at increasingly higher redshifts. No other previous survey had such a large observation area reaching these relatively faint observation limits.

The lower end of SERVS GSMF is generally closer to the literature, even at higher z values, and only in the lowest redshift bins (i.e. from $z \sim 0.1$ to $z \sim 0.6$) our results can be seen to be marginally higher than the rest of the majority of past studies. Moreover, it is interesting to note that in the higher redshift ranges the shape of the GSMF resembles a straight line and we cannot fully appreciate the knee-like part of the curve because of our low-

mass limits. Future surveys that are even deeper than SERVS will be able to better constrain the low-end of the high-z GSMF, ideally also maintaining enough width to explore the massive end as well.

Looking at the low-mass end beyond our low-mass limits, it can be appreciated that all three options of low-mass limits are generally acceptable. However, the median-type and the 80-percentile-type remain clearly more conservative approaches, as the 20-percentile-type is often very close to values of ϕ that seem to have just started to be affected by completeness limitations.

Lastly, it is important to comment on our errors. Often literature values do not have explicit errors and it is incorrect to compare them directly to ours. In fact, rarely past studies consider the full combination of Poisson, random, and cosmic variance uncertainties. Nonetheless, our errors may appear particularly contained. This could be due to the characteristics specific to the data we employ. Precisely, even considering only the XMM field within SERVS we are looking at around 5 sq. deg. for a total of $\sim 800,000$ galaxies, which means that our statistics can indeed be relatively robust. Even in the furthermost massive end, where many literature works have no galaxies or a number below 10, we often have tens of such galaxies making even Poisson contributions small. Similarly, random errors are less affected as the number of galaxies increases and cosmic variance is less of a problem with larger observation areas.

3.4.1 Galaxy Stellar Mass Function for Galaxy Formation Models

Comparison of our GSMF is also performed with models, as briefly mentioned in the previous section. Specifically, we use a dataset from the Lagos et al. (2012) GALFORM model. This dataset was defined by us as a 'lightcone' since it was designed to replicate SERVS-specific observation conditions, such as magnitude limits and area observed. The 'lightcone' has an effective observed area of 18.09 sq. deg. and contains $\sim$ 1.5 million galaxies between redshift 0 and 6.

This data coming from a model, we had all required information available to calculate the GSMF, most importantly the redshift and stellar mass of each model galaxy. The calculation of the GSMF was performed with our usual methodology described earlier. The results are shown in Figure 3.2 as brown circles.

It can be appreciated that, as expected in the literature, the model results recover fewer galaxies in the massive end but more lower-mass galaxies. This behaviour is seen in all redshift ranges considered, from $z \sim 0$ to $z \sim 4.5$.

3.4.2 The SERVS Galaxy Stellar Mass Function in Its Cosmological Context

When we look at galaxy evolution in its cosmological context resulting from the SERVS GSMF calculation we find a mixed and uncertain picture. While the two canonical models of galaxy formation and evolution are the hierarchical ΛCDM and the downsizing paradigm, our results suggest that neither are a complete description of the physical Universe.

It can be seen in Figure 3.3 that the SERVS GSMFs for all redshift ranges appear separate from one another and outline curves mostly parallel to each (while respecting the traditional knee-like GSMF shape). Each redshift range is represented by a solid line of a different colour: dark green for $0.1 < z < 0.2$, light green for $0.2 < z < 0.4$, yellow for $0.4 < z < 0.6$, orange for $0.6 < z < 0.8$, bright red for $0.8 < z < 1.0$, dark red for $1.0 < z < 1.5$, indigo for $1.5 < z < 2.5$, purple for $2.5 < z < 3.5$, and magenta for $3.5 < z < 4.5$.

This behaviour suggests that across cosmic time galaxies form and evolve irrespectively of their inherent stellar mass. The two most followed galaxy formation and evolution models predicted instead that either smaller galaxies form first and then merge to form the most massive ones (hierarchical system) or large gas clouds rapidly collapse to form the most massive galaxies from the start (downsizing).

Moreover, some jumps among the redshift ranges can be perceived. For example, the GSMFs corresponding to the first three redshift ranges (z from

0.1 to 0.6 included) share a similar parameter space in Figure 3.3 and then the GSMFs decrease to occupy again a similar parameter space (for $0.6 \leq z \leq 2.5$). The last two redshift ranges up to $z \sim 4.5$ have a fully parallel evolution. Thus we also note that in terms of evolution starting from $z \sim 4$ the galaxy mass grows by a factor of ~ 10 for most mass bins. It then quickly grows again by a factor of ~ 5 between $z \sim 1$ and $z \sim 0.5$, at which point the evolution seems to slow down to a halt, meaning all three redshift ranges below $z \sim 0.5$ show similar ϕ values.

Even more clearly we can discuss whether our GSMF results follow any of the galaxy formation and evolution paradigms, by plotting the value of ϕ against the redshift for a series of different mass bins. In this case, the mass bins are not the ones used for the normal GSMF calculation, but they all range from a series of mass values (i.e. 9.0, 9.5, 10.1, 10.6, 11.0, 11.3, 11.8) up to M=12.5. This is similar to Figure 7 of Pozzetti et al. (2010a).

In figure 3.4 we can see the results of this visualisation effort. Lines of different colours identify the different mass ranges: dark blue for $M > 9.0$, light blue for $M > 9.5$, green for $M > 10.1$, yellow for $M > 10.6$, purple for $M > 11.0$, red for $M > 11.3$, and brown for $M > 11.8$. The horizontal dashed line indicate the value of ϕ at the lowest redshift available. It can be appreciated, once again, that the mass density of galaxies evolve during the life of the Universe without a particular preference for its absolute value, be it smaller-mass or larger-mass galaxies. Previous literature studies, such as Pozzetti et al. (2010a), had found evidence for downsizing. In a plot of this kind (see again Figure 7 of Pozzetti et al., 2010a) this shows as a flat curve from $z \sim 1$ to the local universe for the most massive ranges and with rising curves for the lower mass ranges. This is because the 'downsizing' paradigm expects the most massive galaxies to have grown the vast majority of their mass in the first half of the age of the Universe (i.e. up to $z \sim 1$), and smaller systems to quickly form in the second half of cosmic time.

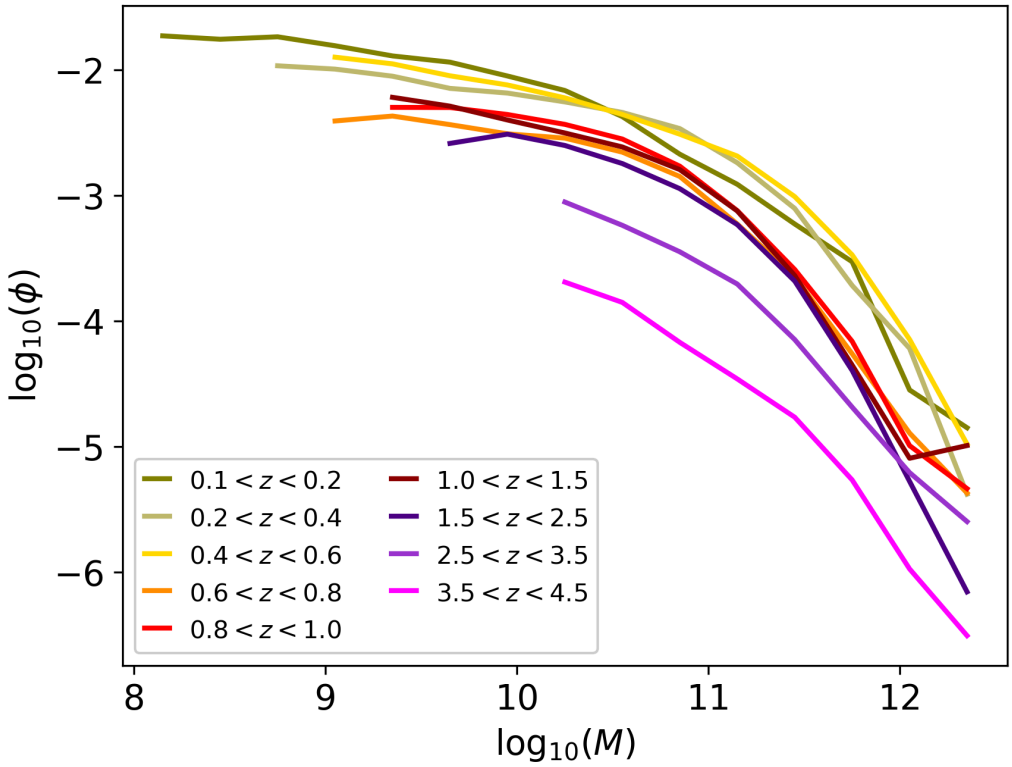

Figure 3.3: The SERVS GSMF for all redshift ranges considered on a single plot. Each redshift range is represented by a solid line of a different colour: dark green for $0.1 < z < 0.2$, light green for $0.2 < z < 0.4$, yellow for $0.4 < z < 0.6$, orange for $0.6 < z < 0.8$, bright red for $0.8 < z < 1.0$, dark red for $1.0 < z < 1.5$, indigo for $1.5 < z < 2.5$, purple for $2.5 < z < 3.5$, and magenta for $3.5 < z < 4.5$.

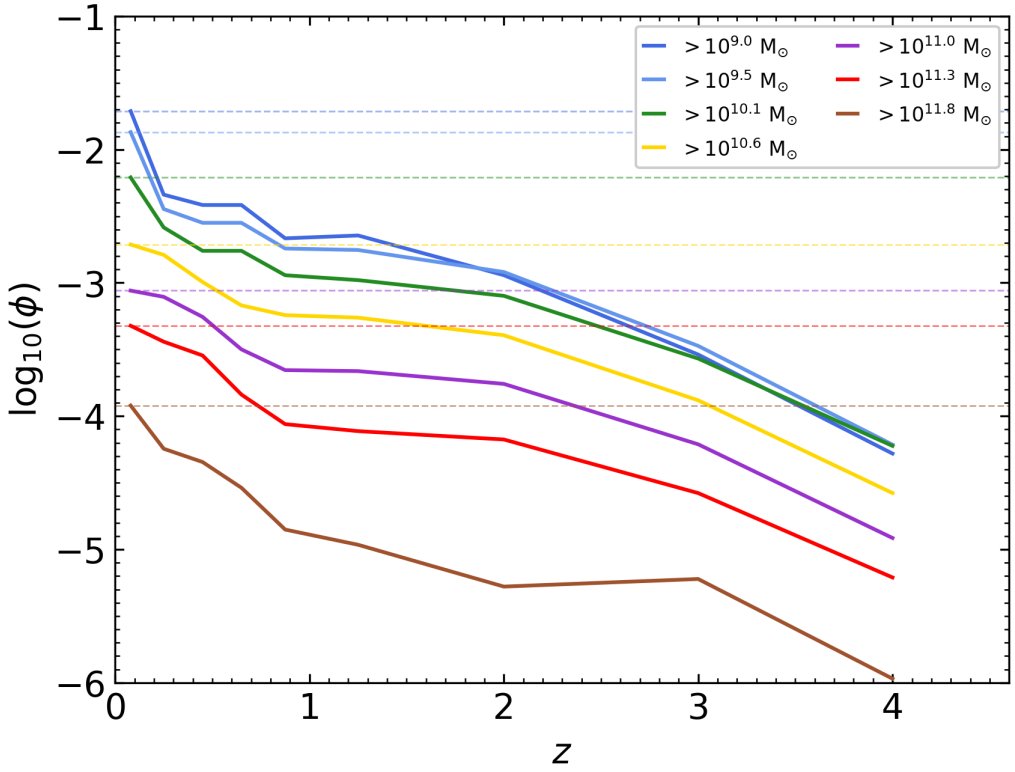

Figure 3.4: The value of ϕ is plotted against the redshift for a series of different mass bins. In this case, the mass bins are not the ones used for the normal GSMF calculation, but they range from a series of mass values (i.e. 9.0, 9.5, 10.1, 10.6, 11.0, 11.3, 11.8) up to M=12.5. This is similar to Figure N of Pozzetti et al. (2010a). Lines of different colours identify the different mass ranges (dark blue for $M > 9.0$, light blue for $M > 9.5$, green for $M > 10.1$, yellow for $M > 10.6$, purple for $M > 11.0$, red for $M > 11.3$, and brown for $M > 11.8$. The horizontal dashed line indicate the value of ϕ at the lowest redshift available. It can be appreciated, once again, that the mass density of galaxies evolve during the life of the Universe without a particular preference for its absolute value, be it smaller-mass or larger-mass galaxies.

3.4.3 The Effects of the Adopted Reddening Laws on the Stellar Mass Function

As explained in Section 3.3.8, the SERVS GSMF presented in Section 3.4 made use of photometric redshift and mass results from a combination of SMC and Calzetti reddening laws, based on lowest χ^2_r for each galaxy.

It is, however, interesting to compare this GSMF solution with what we could get had we only selected a single reddening law. In Figure 3.5 we compare the GSMFs when using SMC-law only data (purple squares), Calzetti-law only data (cyan triangles), and both (i.e. same as in Section 3.3.8; dark blue stars). The redshift ranges selected are the same as usual: $0.1 < z < 0.2$, $0.2 < z < 0.4$, $0.4 < z < 0.6$, $0.6 < z < 0.8$, $0.8 < z < 1.0$, $1.0 < z < 1.5$, $1.5 < z < 2.5$, $2.5 < z < 3.5$, and $3.5 < z < 4.5$.

The plots indicate that overall there is a strong agreement between the outputs calculated with the two reddening laws considered. This means that in general we do not expect our main GSMF results (that uses a combination of the two laws) to be heavily affected by either law and our analysis holds. However, we do note a few differences as described below.

In particular, between redshift 0.2 and 0.4 we observe a slight deviation in the massive end, with the Calzetti law results being almost ten times larger than the SMC result for the largest mass bin. Other differences are clear in the two largest redshift ranges, and especially at $3.5 < z < 4.5$. Here, we find that the SMC-type GSMF is consistently higher than the Calzetti-type results. This means that, were we to use the Calzetti GSMF, our calculation would be closer to the literature findings, and in particular very similar to the work by Marchesini et al. (2009), which did use the Calzetti law as preferred reddening. However, the correction from our combined GSMF (blue stars) is minimal compared to the variation with respect to the SMC law one.

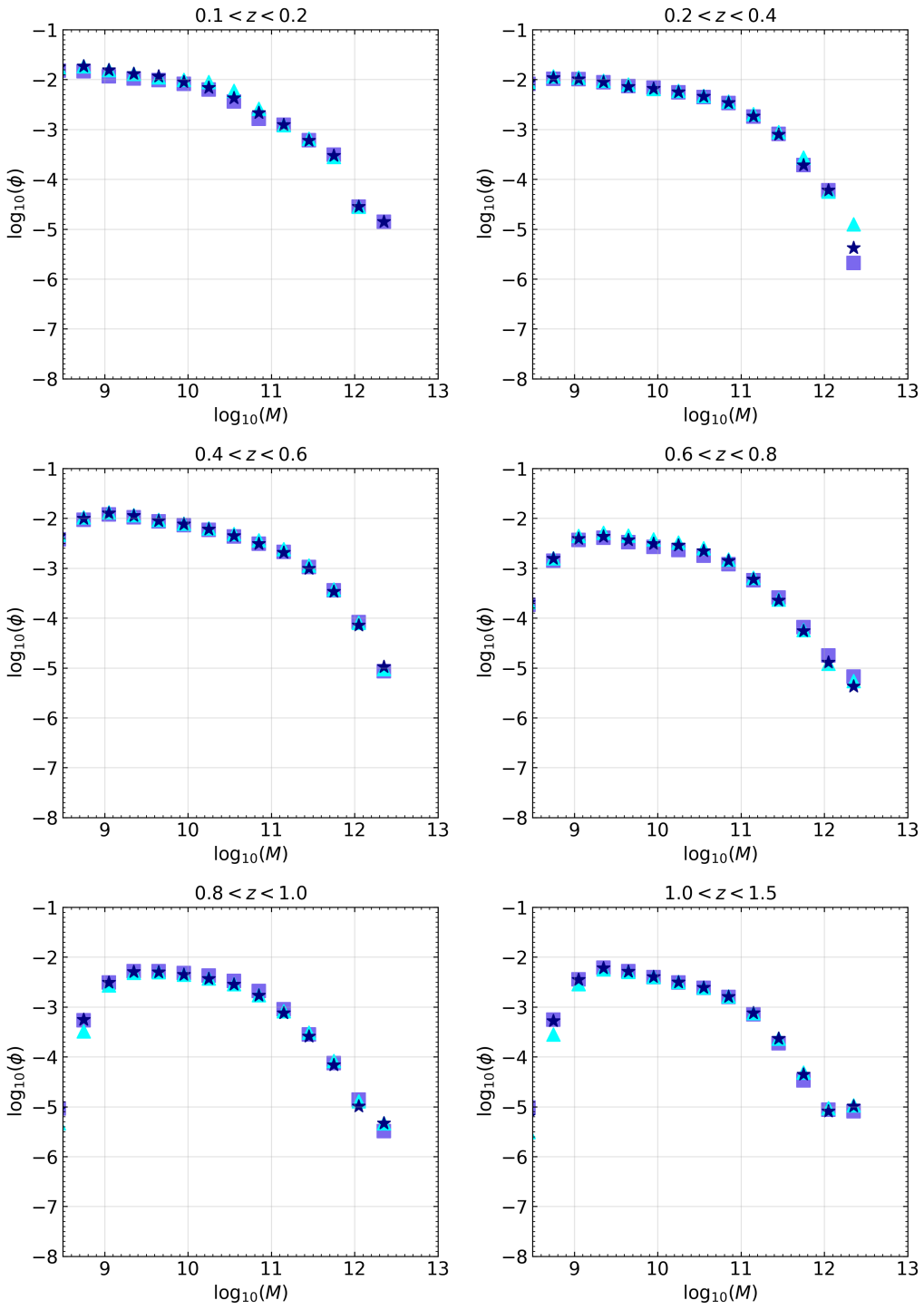

Figure 3.5: This is a figure spanning multiple pages. The full caption is found at the end of the figure.

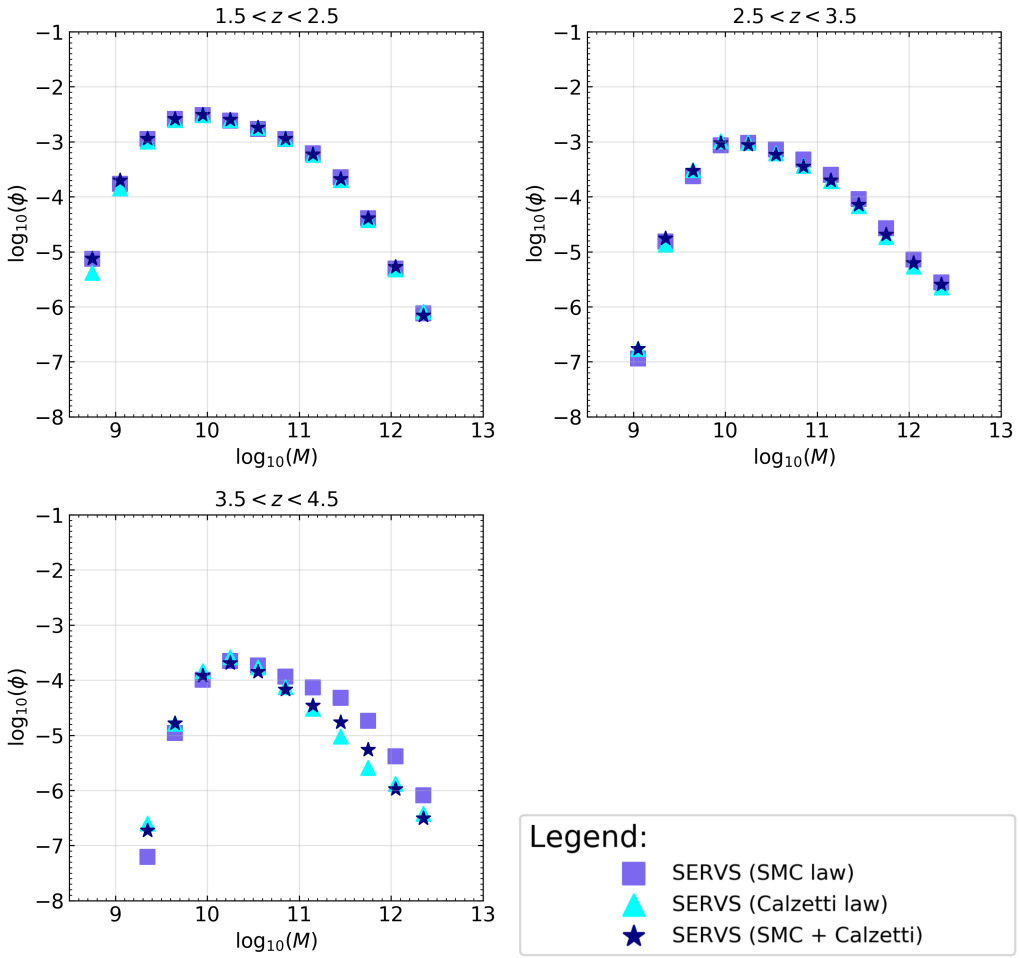

Figure 3.5: Comparison of the SERVS GSMF for the two reddening laws selected, i.e. the SMC reddening law (purple squares) and the Calzetti reddening law (cyan triangles). The main SERVS GSMF calculation (combination of the two reddening laws) is also plotted for comparison as blue stars; this is the same as shown in Figure 3.2. The panels are for the usual redshift ranges used, from top to bottom: $0.1 < z < 0.2$, $0.2 < z < 0.4$, $0.4 < z < 0.6$, $0.6 < z < 0.8$, $0.8 < z < 1.0$, $1.0 < z < 1.5$, $1.5 < z < 2.5$, $2.5 < z < 3.5$, and $3.5 < z < 4.5$.

Chapter 4

The Effect of z_{phot} vs. z_{spec} and the Inference on Downsizing

4.1 Preamble

In this chapter we validate our photometric redshift using a series of tests that investigate the physical properties (stellar mass, age, and dust content) of the galaxies fitted in the previous chapter as well as their photometric redshifts based on the redshift probability distribution functions.

We compare our results with those obtained for a sub-sample of $\sim 40,000$ galaxies with known spectroscopic redshift and we check if the main outliers belong to any particular galaxy population or type.

We also comment and investigate the resulting GSMF calculations in the contexts of photometric and spectroscopic data, while also considering differences between versions of our SERVS dataset and additional photometry for a different SERVS field as well as from the Dark Energy Survey Science Verification programme.

4.2 Photometric Redshift Limitations and Consequences on the Galaxy Stellar Mass Function

The reliability of photometric redshifts has been a matter of discussion for a long time. Generally, spectroscopic redshifts are preferred as they are deemed less prone to misevaluating the true redshift of a given galaxy, but they also have the disadvantage of being more difficult to acquire. As described earlier, this is because the type of observation required (i.e. spectroscopic observations) take a much longer telescope time than the simpler photometric observations. For example, the Dark Energy Survey and the SDSS-III/BOSS are instances of photometric and spectroscopic surveys, respectively, that have a similarly long programme lifetimes. While the former is expected to have observed over 300 million galaxies, the latter obtained spectra for only ~ 1.3 million sources over 5 years.

This translates into an impressive difference factor of ~ 300, meaning that a survey like SERVS that manages to combine a unique set of area observed and depth would simply not be possible with current technology were it planned to be spectroscopic. Our work from Chapter 3 is therefore impossible to replicate with any data programme available as of today, especially if spectroscopic data were deemed essential.

Therefore, it is important to critically analyse any biases originating from potential issues with our photometric redshift calculations. We have calculated random errors deriving from photometric redshifts in Sections 3.3.9.2, but that methodology could not account for potential problems embedded with the data, the stellar population models, or the photometric redshift code utilised.

The best way to analyse this potential issues is to compare our photometric redshift results with spectroscopic redshift measurements for the same galaxies. We do so using the spectroscopic redshifts for ~ 40 thousand of our SERVS galaxies. These spectroscopic measurements were first used in

(Pforr et al., 2018) and come from a series of sources, namely: Le Fevre et al. 2013, Eales et al. 2009, Moncelsi et al. 2011, Cooper et al. 2012, Mao et al. 2012, Coil et al. 2011; Cool et al. 2013, Hsu et al. 2014, Yuan et al. 2015; Childress et al. 2017, Le Fevre et al. 2015; Tasca et al. 2017, Trichas et al. 2009, Abolfathi et al. 2018, Sacchi et al. 2009, Owen & Morrison 2009, Patel et al. 2011, Smail et al. 2008; Simpson et al. 2012, Guzzo & The Vipers Team 2013; Garilli et al. 2014; Scodeggio et al. 2018, Bradshaw et al. 2013; McLure et al. 2013, Liske et al. 2015; and Baldry et al. 2018. The spectroscopic redshifts provided by these sources cannot be independently verified by us, but serve as an effective way to test our results. Pforr et al. (2018) had concluded that if the HyperZ results were cut by χ^2_r and number of bands available for a given source, then the final z_{phot} calculations matched well the available z_{spec}.

We will go through these types of tests, and more, in the following sections.

4.3 Photometry Differences Between Catalogues

Firstly, it is important to visualise how the photometric measurements differ in each of the 13 bands forming the multi-wavelength SERVS catalogues, i.e. the 'TRACTOR' one used by us and the older version utilised by Pforr et al. (2018). We show this in Figure 4.1, where in each panel we plot the photometry of a given band from the 'old' Pforr et al. (2018) catalogue against the 'TRACTOR' one (i.e. ours) as small green dots. This has been done for all the matching sources, which are around two thirds of the ~ 750 thousand galaxies of our TRACTOR catalogue. Wherever one of the bands had photometry missing, these have not been plotted.

It can be appreciated that there are often considerable variations between the two versions of each photometric band, especially as the magnitudes get fainter. For the HSC bands it can also be noticed that some of the brighter sources in the 'old' catalogue have their photometry measured to be fainter in

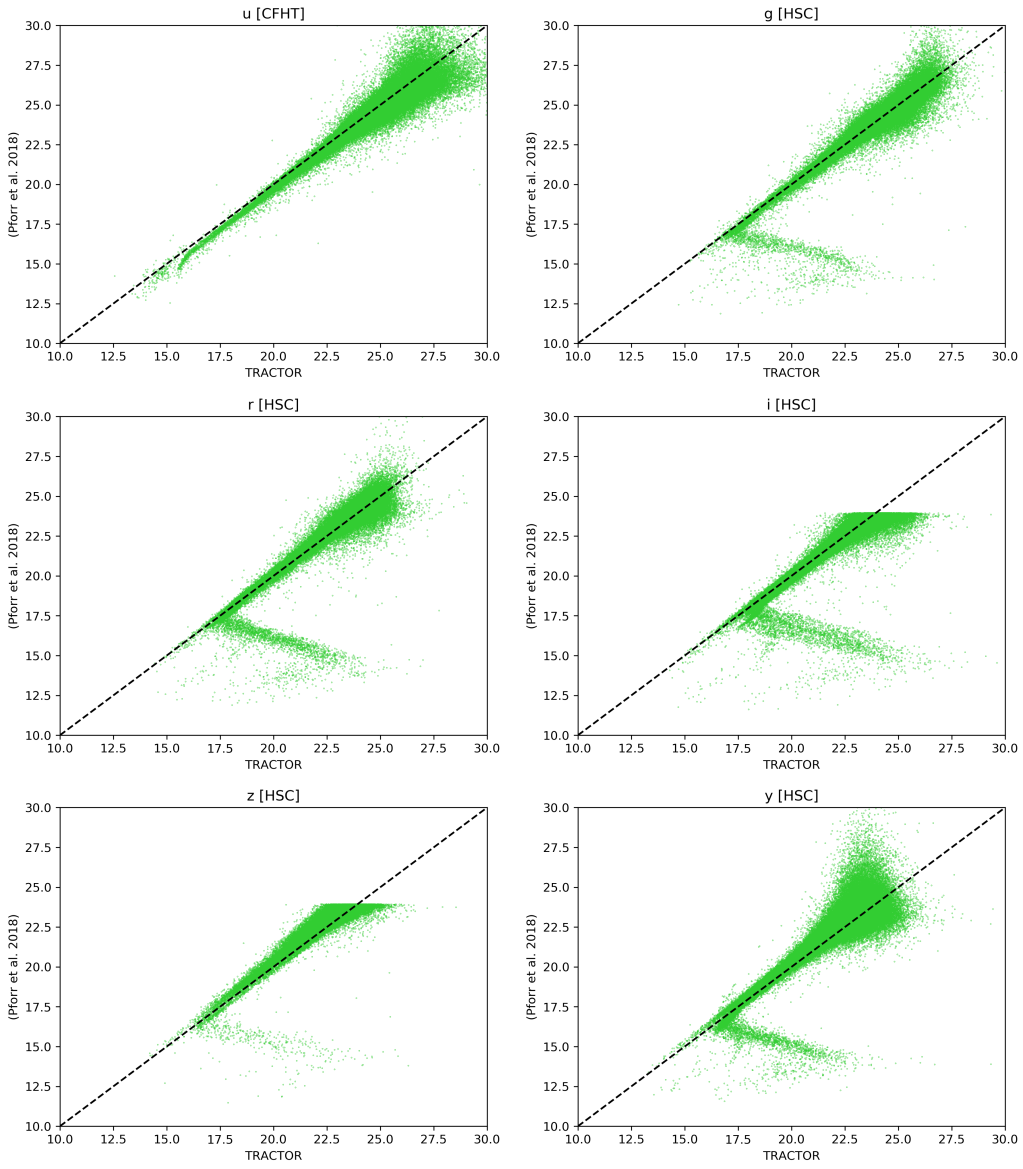

Figure 4.1: This is a figure spanning multiple pages. The full caption is found at the end of the figure.

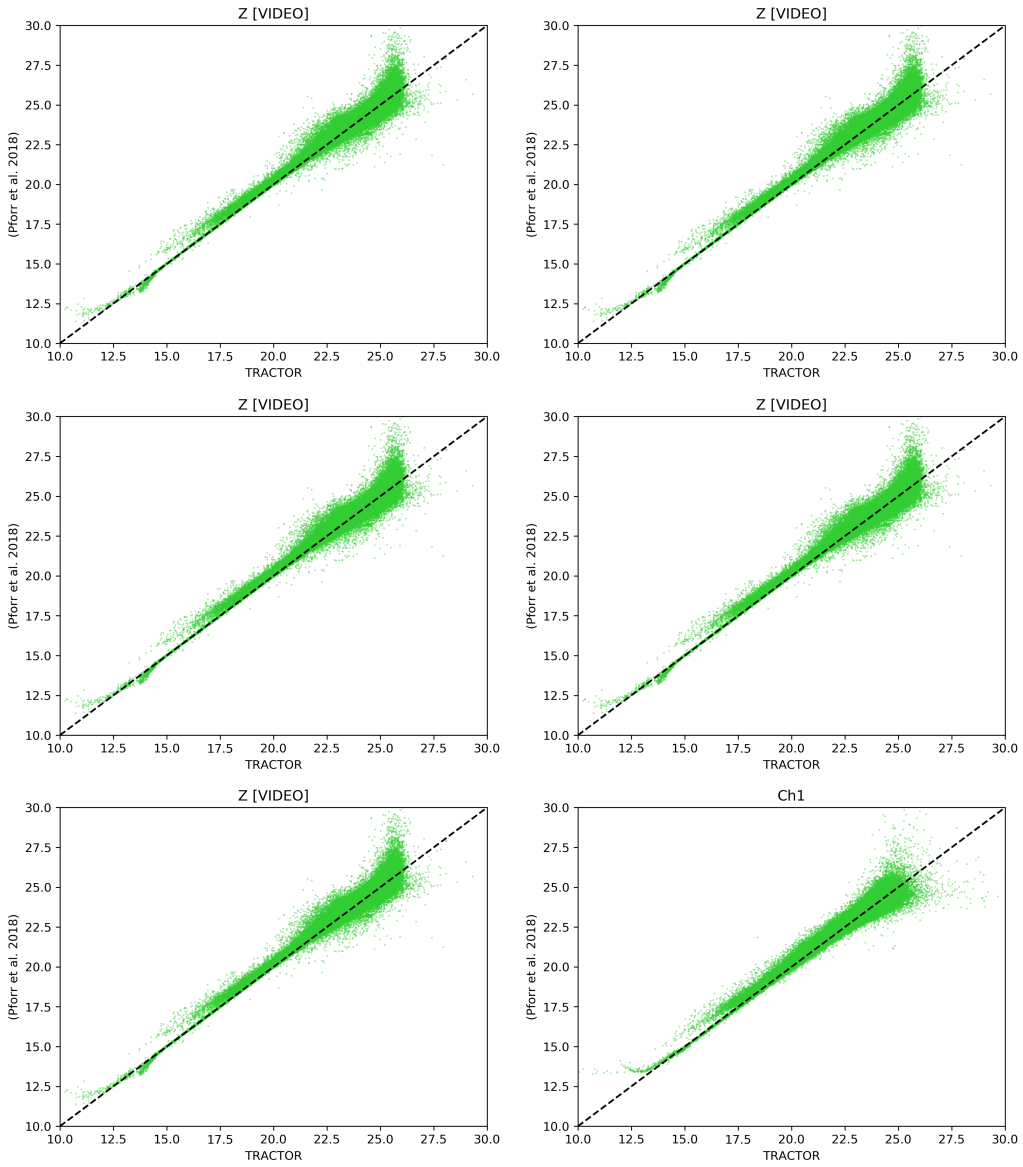

Figure 4.1: This is a figure spanning multiple pages. The full caption is found at the end of the figure.

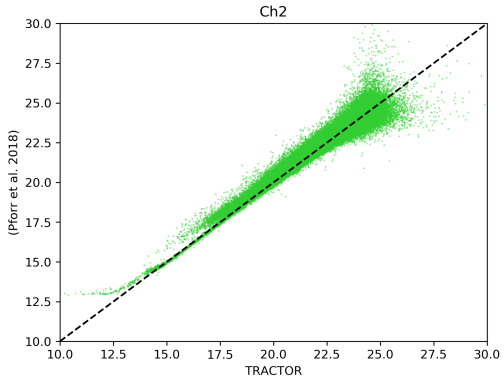

Figure 4.1: For each of the 13 filter used by the multi-wavelength catalogues of SERVS, each panel shows the photometry of a band of the 'old' Pforr et al. (2018) catalogue against the newer one used by us that underwent the 'TRACTOR' procedure. Differences can be noted clearly, especially at the faint ends. The HSC bands also show particularly large differences at the bright ends of the 'old' data, something that will need to be investigated by the data pipeline with regards to the effects on the photometric redshift calculation. Bands missing in any of the catalogues (generally in Pforr et al. 2018, as shown later) are not considered here.

the TRACTOR version. Moreover, the i and z HSC filters show hard edges at the faint ends, which were probably the magnitude limits set artificially by the SERVS data pipeline. Such hard magnitude limits are not present in the TRACTOR catalogue. In fact the effective survey magnitude limit (Ch.2_{AB}) derived from the theoretical limits set by the survey design seems to actually be a conservative lower limit and the data pipeline could push to even fainter magnitudes.

It will be interesting if future studies, along with the SERVS data pipeline, could investigate further the granular effects of such photometric differences to the photometric redshift and physical properties calculation, as we start doing in the following sections. As we described earlier, the way Pforr et al. (2018) managed to clear the outliers and validate the photometric redshift was by looking at the missing bands (as well as the χ^2_r). We will show later that this could be the origin of discrepancies for at least some of the outliers that we are going to analyse in the following sections.

4.4 HyperZ Photometric Redshifts vs. Spectroscopic Redshifts

Here, we present our photometric redshifts against spectroscopic redshifts for the $\sim$ 40000 galaxies from our SERVS sample that have a z_{spec} value. This comparison is presented in Figure 4.2.

The data is plotted as small black dots and we also overlaid in orange the galaxies with a χ^2_r smaller than 3 (one of the cuts we used in our work for DES, see Section 2.4.1). We also annotate the value of the normalised median absolute deviation, σ_{NMAD}, and the fraction of catastrophic outliers, for short Ω, as defined by equations:

$$\sigma_{NMAD} = 1.48 \times median[|\frac{\Delta z - median[\Delta z]}{1 + z_{spec}}|], \tag{4.1}$$

$$\Omega = \frac{count[\frac{\Delta z}{1+z_{spec}} > 5\sigma_{NAMD}]}{count[z_{spec}]} \times 100, \tag{4.2}$$

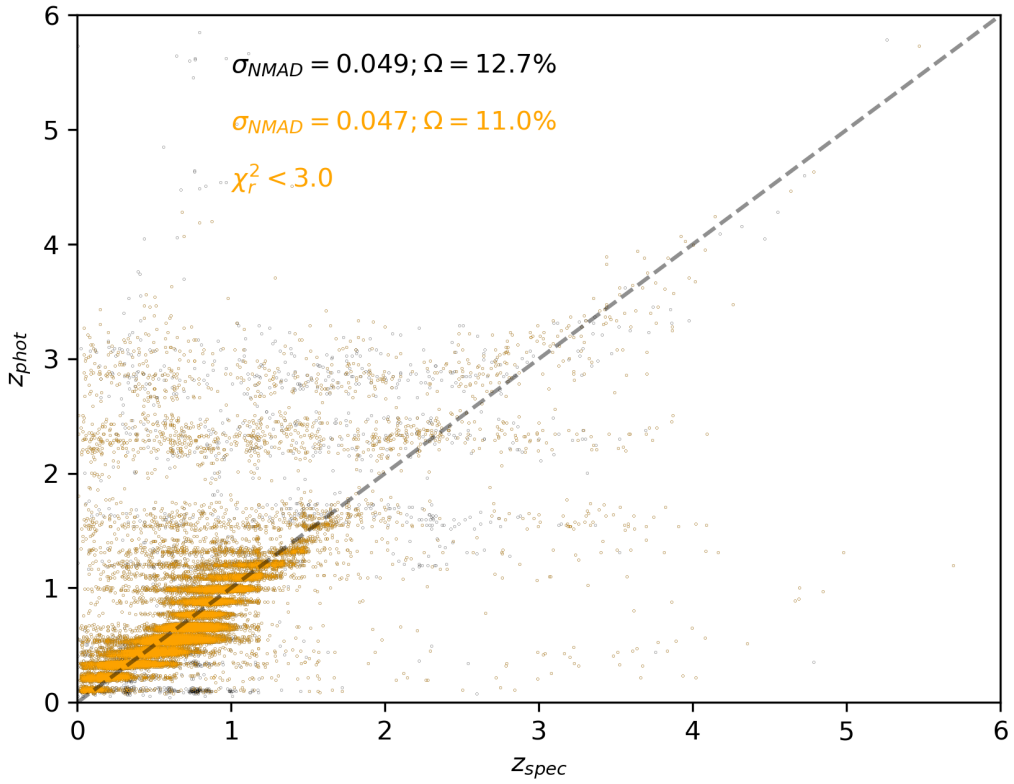

Figure 4.2: Photometric redshift as calculated by us against spectroscopic redshifts for ~ 40 thousand SERVS sources. Points are plotted in black and again in orange for those galaxies whose HyperZ results have $\chi^2_r < 3$.

where Δz is given by $z_{spec} - z_{zphot}$.

We can immediately realise that for our SERVS results the value of χ^2_r is largely irrelevant and the results of σ_{NMAD} and fraction of catastrophic outliers remain similar. Our values of $\sigma_{NMAD} = 0.049$ and $\Omega \sim 13\%$ compare worse than past literature photometric redshift validation reports. As an example, Marchesini et al. (2009) finds values of $\sigma_{NAMD} \sim 0.033$ and $\Omega \sim 4\%$; overall they can still be considered comparable figures. However, the main differences arise as the spectroscopic redshifts increase. The fact that the vast majority of sources here have $z_{spec} < 1.5$ and these end up being plotted on top of one another is to be kept in mind to understand why the calculated σ_{NAMD} and fraction of outliers are, as a whole, overall acceptable.

It it therefore best to analyse this situation in smaller redshift bins, to identify redshift ranges that present the majority of the worse results. We do this by re-creating Figure 4.2, but by annotating values of σ_{NMAD} and Ω for multiple redshift ranges, precisely: $0.0 < z < 1.0$, $1.0 < z < 2.0$, $2.0 < z < 6.0$, $0.0 < z < 0.5$, $0.5 < z < 1.0$, and $0.0 < z < 6.0$. This is shown in Figure 4.3.

We can now quantitively appreciate that our HyperZ-calculated photometric redshifts become particularly unreliable at redshift higher than 2. While we get $\sigma_{NMAD} = 0.049$ and $\Omega = 12.7\%$ over the full redshift range, $0 < z < 6$, we see $\sigma_{NMAD} = 0.126$ and $\Omega = 44.9\%$ at $2 < z < 6$. On the other hand, looking at $1 < z < 2$ we find that the fraction of catastrophic outliers almost doubles compared to the full redshift range as well as to the $z \leq 1$ bins, despite σ_{NMAD} even decreasing marginally (down to 0.042 from 0.049). We could conclude that below $z \sim 2$ the photometric redshifts are good enough for a reliable GSMF calculation, while there are too few $z_{spec} > 2$ sources to conclusively comment on the reliability of high-z results. It is, however, important now to perform further checks on what may be going wrong with our estimations of photometric redshift. It is also still important to keep in mind that the spectroscopic redshifts have not been validated by us, and it is likely that as z_{spec} grows these values become more sensitive to

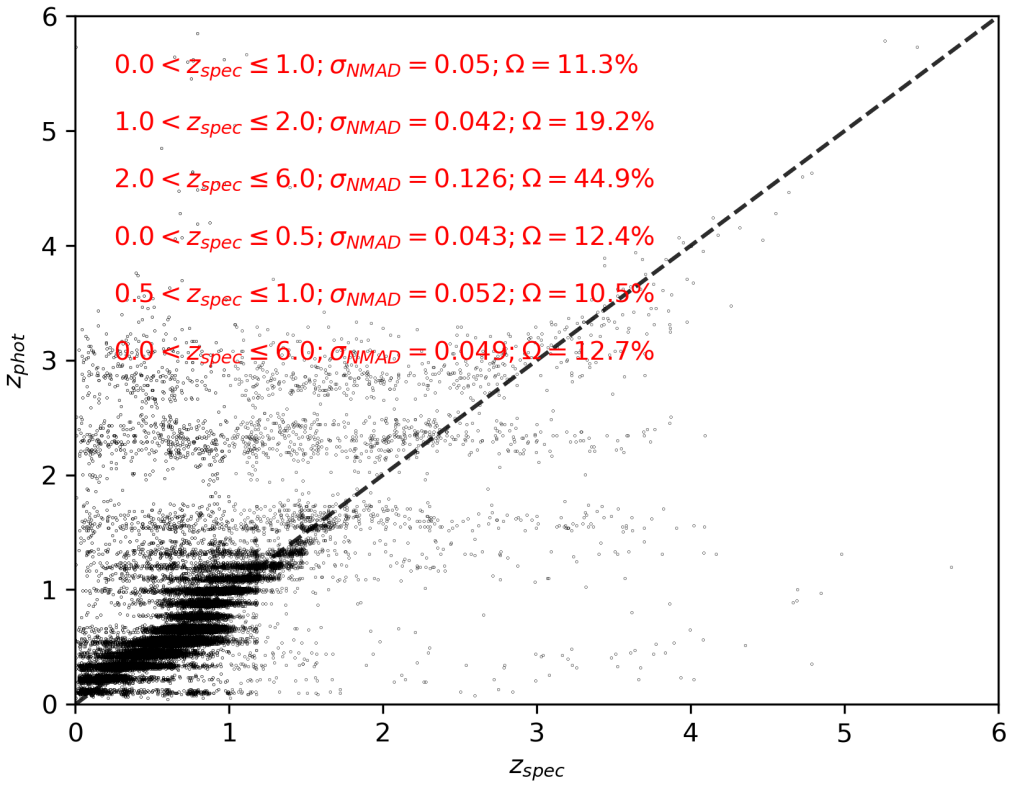

Figure 4.3: Photometric redshift as calculated by us against spectroscopic redshifts for $\sim$ 40 thousand SERVS sources. Points are plotted in black, and in red we annotate values of σ_{NMAD} and Ω for multiple redshift ranges, namely: $0.0 < z < 1.0$, $1.0 < z < 2.0$, $2.0 < z < 6.0$, $0.0 < z < 0.5$, $0.5 < z < 1.0$, and $0.0 < z < 6.0$.

errors due to higher signal to noise ratios.

In the following sections we go through numerous tests to assess the importance of these z_{phot} vs. z_{spec} differences in terms of our GSMF calculation, and to identify their causes and potential steps forward.

4.5 The Nature of Galaxies from the z_{phot} vs. z_{spec} Sample

Firstly, we can try and identify whether galaxies whose photometric redshifts perform particularly poorly when compared to spectroscopic redshifts belong to any particular population. This can be studied replicating Figure 4.2 (excluding the χ^2_r cut) by re-assessing what are our true calculated photometric redshifts, and also by colour-coding galaxies based on their physical properties and HyperZ output results.

4.5.1 z_{phot} vs. z_{spec} by the Photometric Redshift Error

We analyse what the z_{phot} vs. z_{spec} plot looks like if we take into consideration the error on z_{phot}, as estimated by HyperZ. In Figure 4.4 we colour-code in blue the galaxies being part of the bottom 75th percentile in terms on error on the photometric redshift, i.e. the 75% of galaxies with lowest z_{phot} error. The remaining top 25th percentile is plotted in red. We can quickly see that the two groups are extremely compatible and no discerning difference can be appreciated: 0.049 vs. 0.050 for $\sigma_{NMAD} = 0.046$, and 12.5% vs. 13.0% for Ω, respectively.

4.5.2 z_{phot} with Minimum χ^2_r vs. z_{phot} from the Probability Distribution Function

Firstly, as discussed in Section 2.3.3.2 when working with DES data, not always the best z_{phot} results selected by HyperZ are necessarily the most

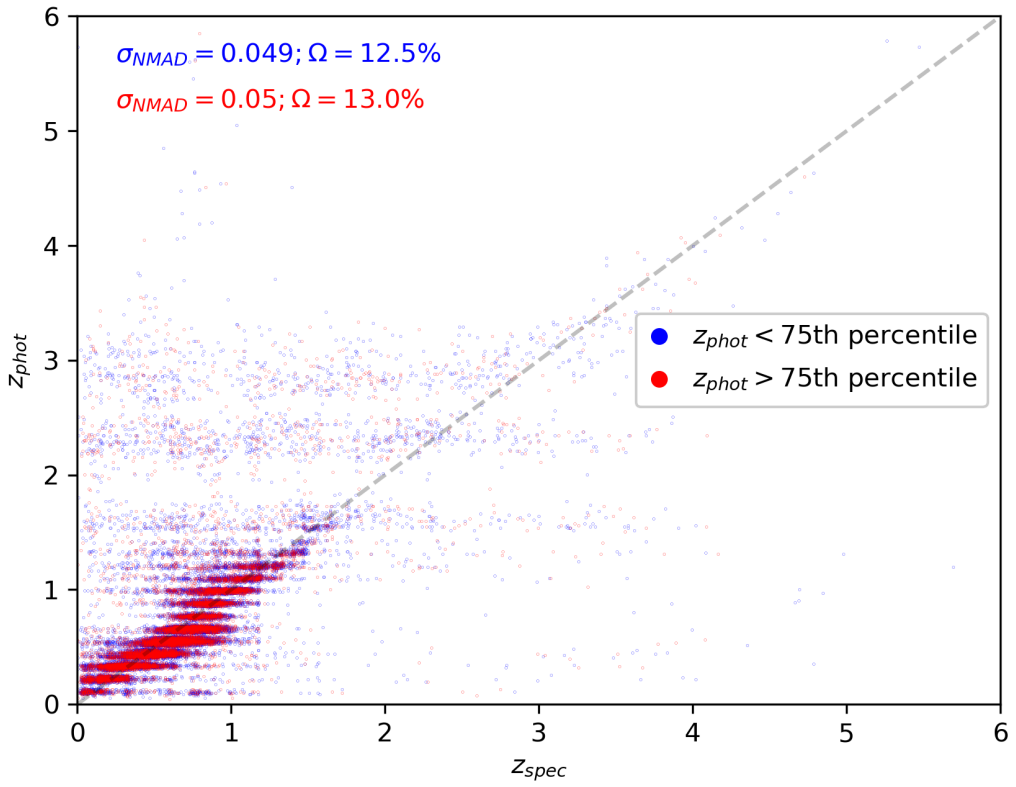

Figure 4.4: Photometric redshift as calculated by us against spectroscopic redshifts for $\sim$ 40 thousand SERVS sources and colour coded by different properties. Here we plot galaxies in the bottom 75th percentile in terms on error on the photometric redshift in blue, and the remaining top 25th percentile in red.

probable. For this, we need to look at the PDF of each source. Originally we did not calculate the PDFs of each source from the $\sim 800,000$ in the SERVS XMM catalogue as this adds computation time and requires more efforts to minimise I/O over the Sciama servers. We then calculated the PDFs by refitting the data using HyperZ and extending our parallelisation pipelines to be more solid and lighter on Sciama's architecture by saving outputs in temporary directories and then iteratively moving that data over to Lustre. In Figure 4.5 we present z_{phot} vs. z_{spec}, where z_{phot} is the most probable photometric redshift according to the PDF of each galaxy, rather than the value output by HyperZ. Overall, results do not change considerably based on the choice of z_{phot} used (σ_{NMAD} and Ω get only marginally worse), indicating this is not the major issue. Note that the data here appears with larger redshift bins as the PDFs are created by HyperZ with a bin size 10 times as large as the one selected as input parameter. The finer calculation of the z_{phot} is performed at a later stage than saving the output files containing the PDFs.

The most probable redshifts are compared to the best-fitted (or lowest χ^2_r) redshifts output automatically by HyperZ for the same galaxies with available spectroscopic data. The former are plotted against the latter in Figure 4.6 (as a density plot for clarity). We find a very good general agreement with less than 4% catastrophic outliers. It is therefore not surprising that Figure 4.5 did not look considerably different to what we obtained when using the default z_{phot} output.

We also make use of the PDFs to exclude galaxies that show multiple local peaks in the PDF, rather than a clear single-peaked distribution. This procedure excludes $\sim 23\%$ of the sources. The result z_{phot} vs. z_{spec} plot is shown in Figure 4.7. The chosen z_{phot} chosen is still the most probable one as found in the PDFs. This choice does not seem to pay off as both σ_{NMAD} and Ω increase compared to the default case.

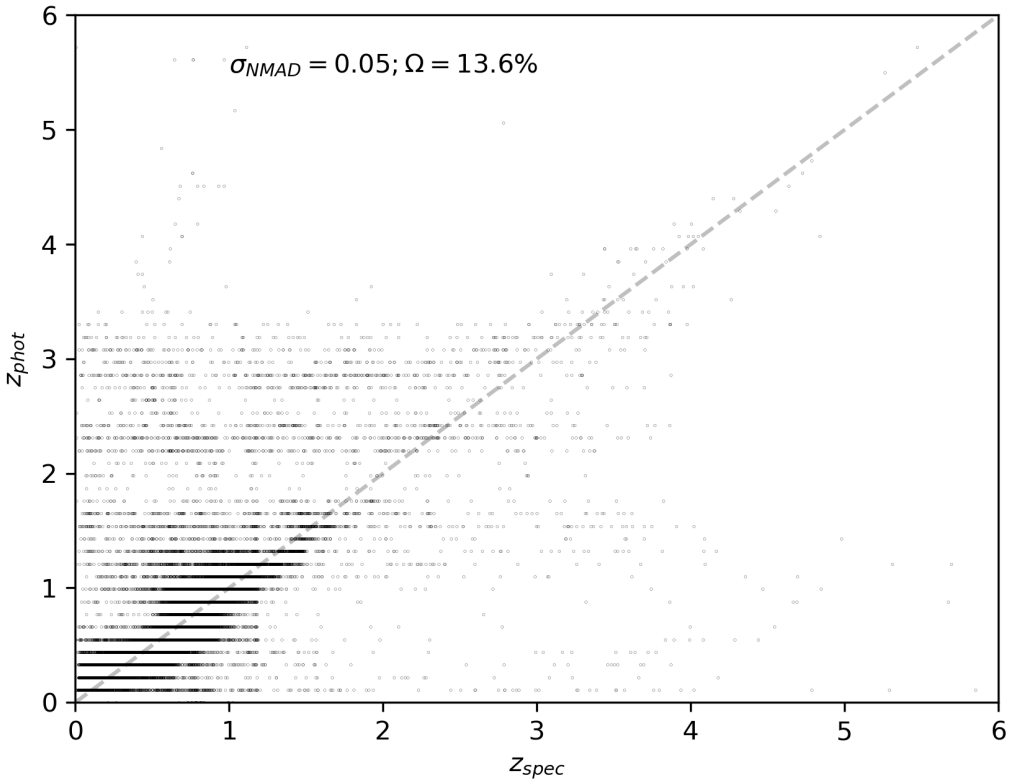

Figure 4.5: z_{phot} vs. z_{spec}, where z_{phot} is the most probable photometric redshift according to the PDF of each galaxy, rather than the value output by HyperZ, output according to the minimum χ^2_r.

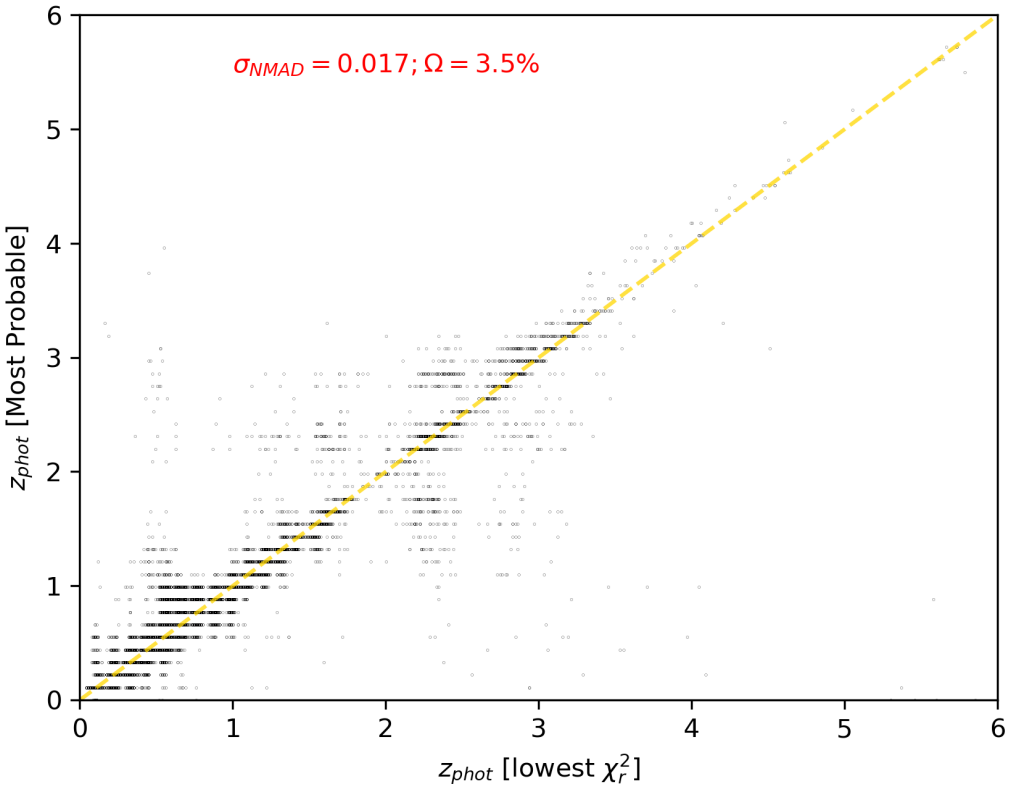
$\sigma_{NMAD} = 0.017; \Omega = 3.5\%$
z_{phot} [Most Probable]
z_{phot} [lowest χ^2_r]
0
1
2
3
4
5
6

Figure 4.6

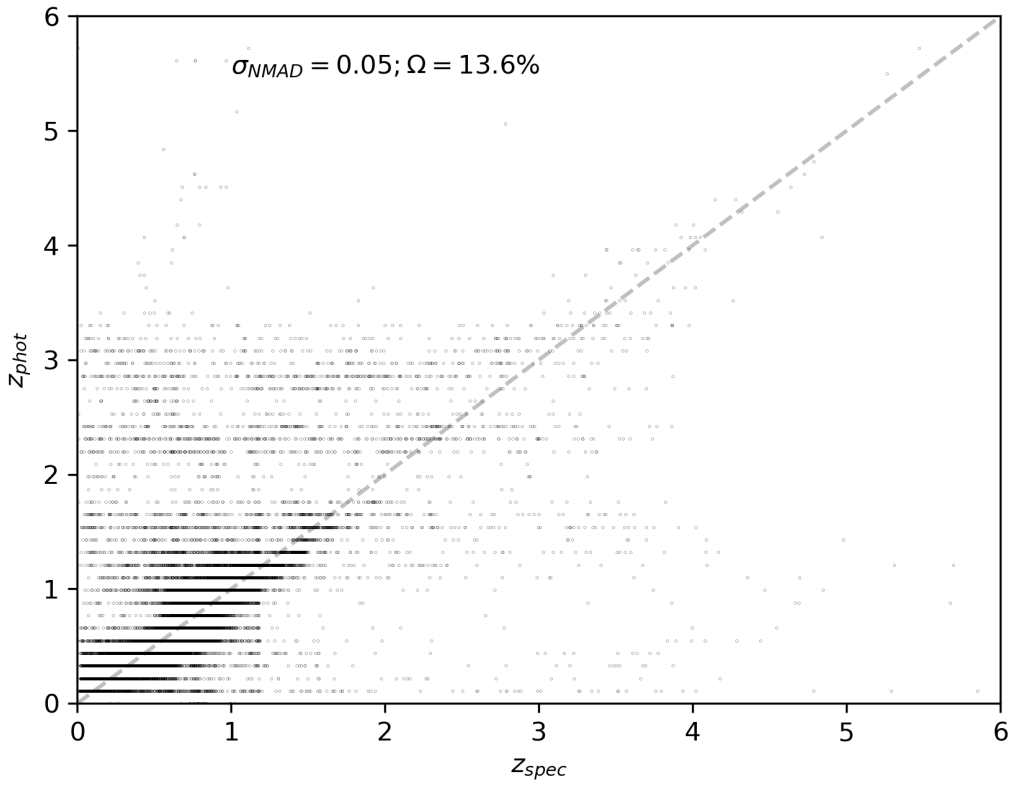

Figure 4.7: z_{phot} vs. z_{spec}, galaxies without a single-peaked PDF have been excluded (leaving $\sim 77\%$ of the original sources).

4.5.3 z_{phot} vs. z_{spec} by Stellar Mass

When we analyse the galaxy properties at large, we observe for instance how the results are divided by mass. In Figure 4.8, we re-plot z_{phot} vs. z_{spec} by representing in blue galaxies with $\log(M) < 11$ and in red galaxies with $\log(M) \geq 11$. We see that smaller-mass galaxies are better fit by HyperZ and catastrophic outlier fractions double from 11.5% to 23% for higher-masses (while σ_{NMAD} shift from 0.049 to 0.059). This however is probably due to the fact the higher the true redshift of a galaxy the more likely they are to have a high mass (because of survey magnitude-limit-related selection effects), and we saw galaxies with high z_{spec} tend to have the most unreliable results. We notice, nonetheless, that the majority of galaxies with high z_{spec} that we indeed manage to classify as such are generally with masses $\log(M) < 11$.

4.5.4 z_{phot} vs. z_{spec} by χ^2_r

We can also re-assess the importance of values of χ^2_r. In Figure 4.9, we colour-code galaxies based on whether their χ^2_r is less than 2 (orange), between 2 and 5 (purple), and above 5 (green). It is clear that the vast majority of galaxies that perform poorly when compared to with their spectroscopic counterparts have $\chi^2_r \geq 5$. This translates into $\sigma_{NMAD} = 0.231$ and $\Omega = 66.9\%$, well above the average value over all sources ($\sigma_{NMAD} = 0.049$ and $\Omega = 12.7\%$). Specifically when we look at high z_{phot} and z_{spec} values we do not see many green points, meaning that the influence of galaxies with χ^2_r above 5 is mainly at lower redshifts and would not fix our reliability at higher redshifts. Moreover, applying cuts based on χ^2_r would complicate our GSMF calculation as it would not be trivial to estimate the correction factors to account for the removed galaxies.

4.5.5 z_{phot} vs. z_{spec} by Dust

Galaxy dust levels are also another important metric to see if it is any specific class of galaxies that we cannot recover photometric redshifts for consistently.

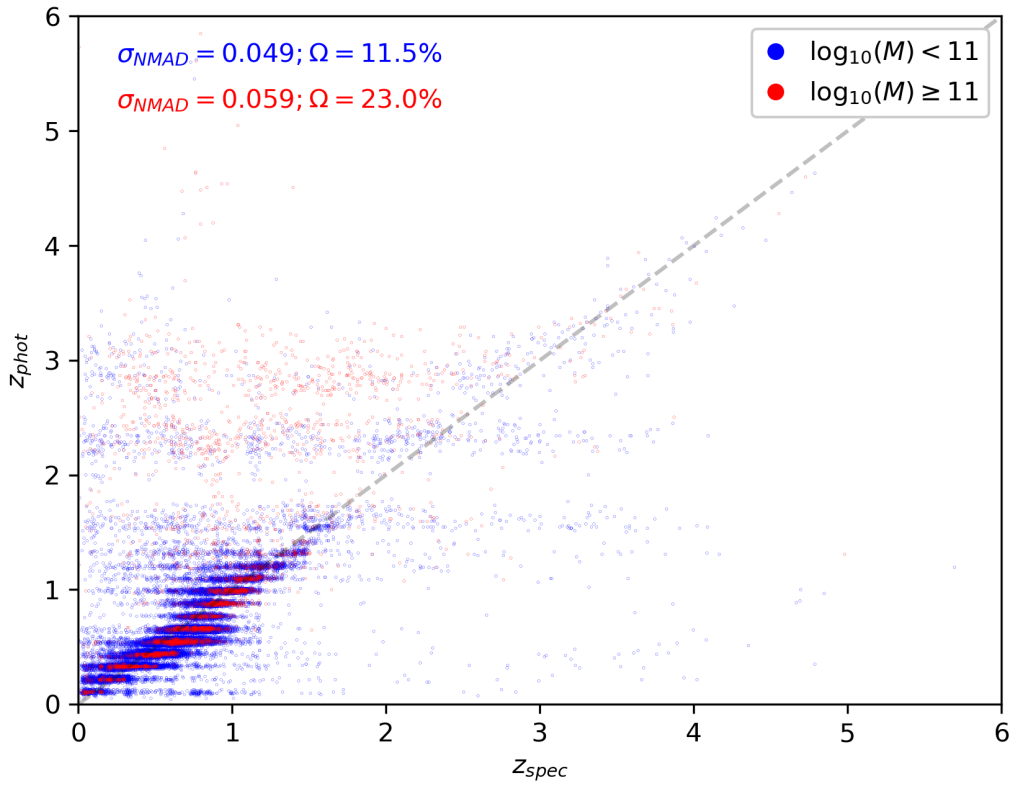

Figure 4.8: Photometric redshift as calculated by us against spectroscopic redshifts for $\sim$ 40 thousand SERVS sources and colour coded by different properties. Here we show in blue galaxies with $\log(M) < 11$ and in red galaxies with $\log(M) \geq 11$, with units of solar mass.

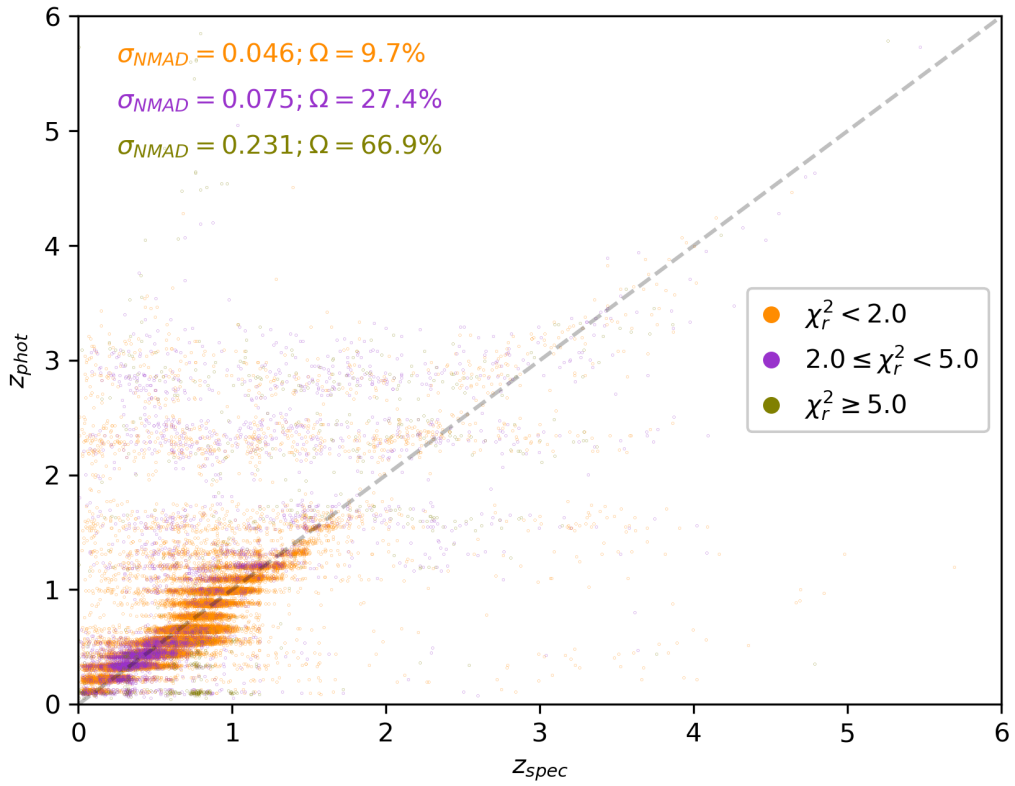

Figure 4.9: Photometric redshift as calculated by us against spectroscopic redshifts for $\sim$ 40 thousand SERVS sources and colour coded by different properties. Here we show in orange galaxies with χ_r^2 less than 2, in purple those with χ_r^2 between 2 and 5, and in green those with χ_r^2 larger than 5.

In Figure 4.10 we plot galaxies with $A_v = 0$ in orange, those with $0 < A_v \leq 1.5$ in purple, and those with $A_v > 1.5$ in green. We see that, by far, the most problematic are those with no reddening found, i.e. $\sigma_{NMAD} = 0.078$ and $\Omega = 30.6\%$ vs. $\sigma_{NMAD} = 0.046$ and $\Omega = 11.7\%$, and $\sigma_{NMAD} = 0.055$ and $\Omega = 9.5\%$ for the other two cases, respectively. On the other hand, the galaxies with $A_v = 0$ appear to be around half of those with an incorrectly high z_{phot} and tend to have correct photometric redshifts for those sources with $z_{spec} > 2$. For this higher-redshift case, it is the galaxies with $0 < A_v \leq 1.5$ that present the majority of wrong photometric redshifts. This mixed picture makes it impossible to discern, in a general way, which galaxies result in poor HyperZ results. We also note that we essentially find no galaxies with $A_v > 1.5$ that have photometric or spectroscopic redshift larger than 2.

4.5.6 z_{phot} vs. z_{spec} by Reddening Law

Highlighting whether a galaxy's z_{phot} and physical properties come from HyperZ results using either the SMC reddening law or the Calzetti one may shed some light on potential biases derived from this type of choice. We identify galaxies coming from the SMC law in blue, and those coming from the Calzetti one in red; see Figure 4.11. We find that the Calzetti law performs clearly worse in general: $\sigma_{NMAD} = 0.067$ vs. 0.0042, and $\Omega = 20.2\%$ vs. 8.5%. At the same time, we find that only the Calzetti law identifies correctly galaxies with high spectroscopic redshift, making the sole use of the SMC law not a viable option.

The full picture, however, should take into consideration the effects due to the χ^2_r selection procedure. When we look at plots of z_{phot} vs. z_{spec} for the HyperZ outputs of the two reddening laws considered individually (see Figure 4.12), we see that the two results tend to be mostly compatible. We find σ_{NMAD} have values of 0.048 and 0.051, and Ω to vary from 13.0% to 12.7%, respectively for the SMC and the Calzetti laws. We can conclude that the differences observed in Figure 4.11 are therefore largely due to χ^2_r selection effects.

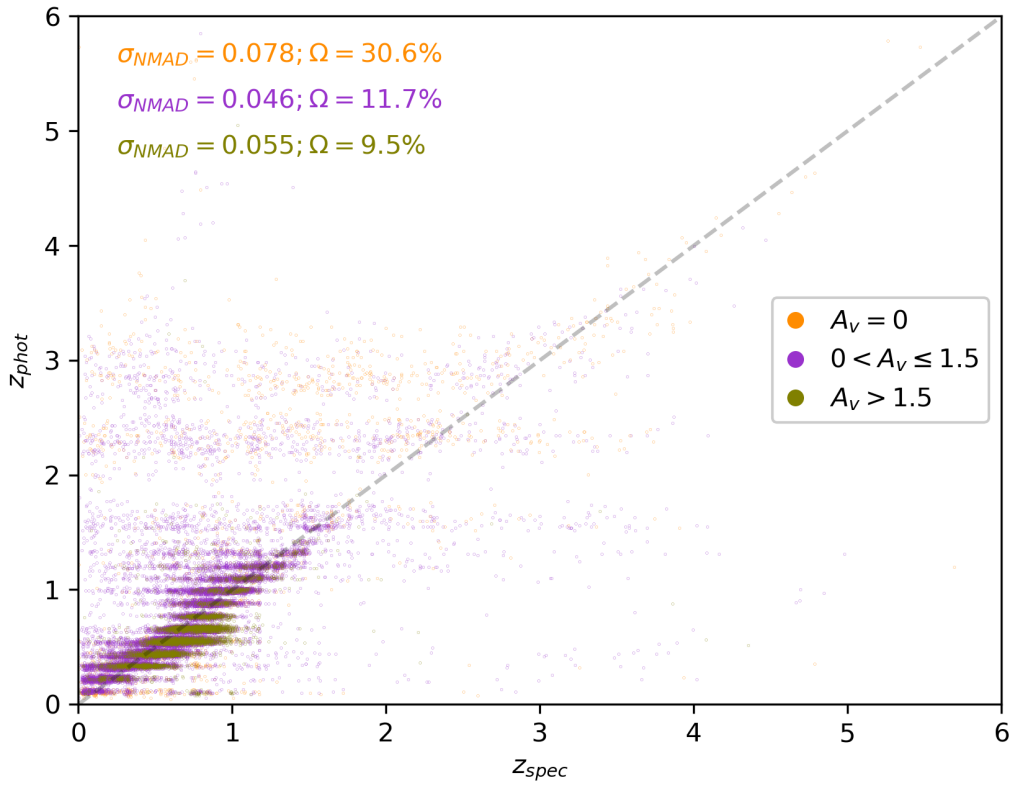

Figure 4.10: Photometric redshift as calculated by us against spectroscopic redshifts for $\sim$ 40 thousand SERVS sources and colour coded by different properties. Here we show galaxies with $A_v = 0$ in orange, those with $0 < A_v \leq 1.5$ in purple, and those with $A_v > 1.5$ in green.

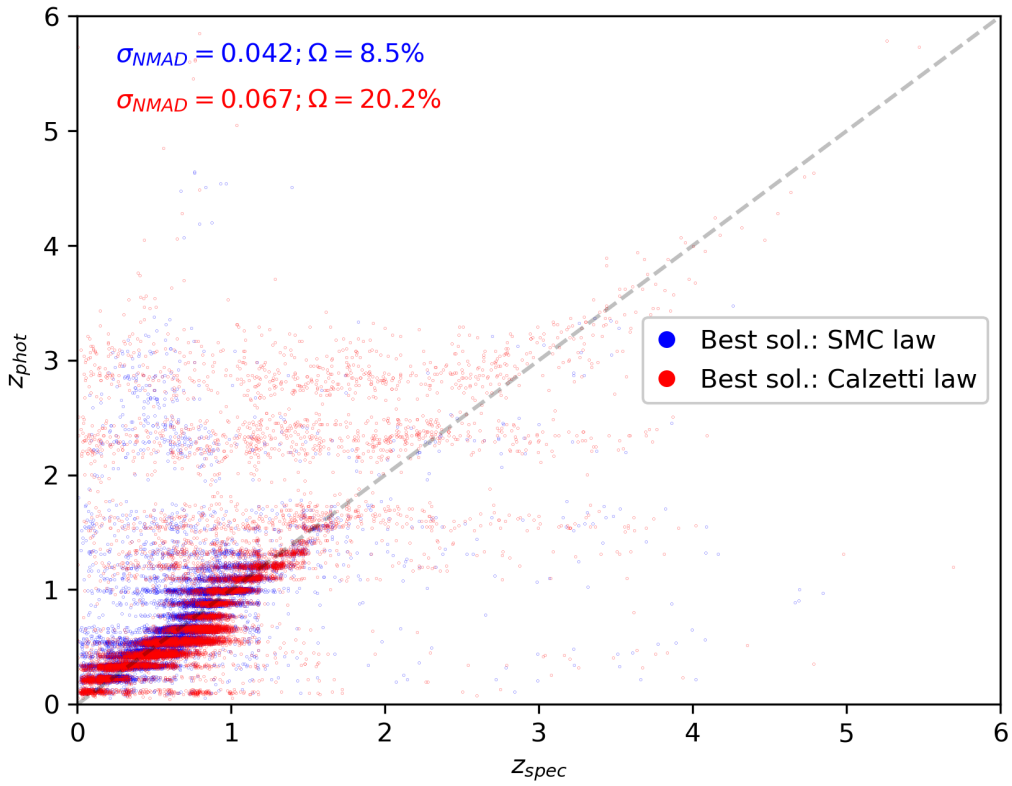

Figure 4.11: Photometric redshift as calculated by us against spectroscopic redshifts for $\sim$ 40 thousand SERVS sources and colour coded by different properties. Here we plot galaxies fitted with the SMC reddening law in blue, and those fitted with the Calzetti law in red.

As discussed and shown in Chapter 3, even when calculating the GSMF for fitting results solely from either of the two reddenings laws, we generally find extremely similar GSMF results.

4.5.7 z_{phot} vs. z_{spec} by Number of Bands and a Comparison with Pforr et al. 2018

Lastly, we check whether the number of photometric bands available that have been fitted using HyperZ has an impact on the photometric redshift results. Along with the χ^2_r, the number of bands was a key factor that Pforr et al. (2018) utilised in order to discard unreliable results.

In Figure 4.13 we plot in orange galaxies with a number of observed bands between 8 and 10 (no galaxy from our catalogue had less than 8), in purple those with either 11 or 12 observed bands, and in green those with all 13 bands observed. We notice that galaxies with fewer than 11 photometric bands start to perform worse consistently, with $\sigma_{NMAD} = 0.068$ and $\Omega = 22.8\%$.

It is important to stress, though, that only 114 galaxies, out of more than 40,000 belong to this poorly performing group. This means that they are largely irrelevant to solve our discrepancies, and the number of filters for our galaxies cannot be used for any particular selection. As we discussed in more detail in Section 4.3, this point raises some questions on the data quality of the photometric catalogue we used. Pforr et al. (2018) used an older version of the SERVS XMM data, and it is apparent that galaxies generally missed many more observed bands, making this feature a good way to discard unreliable results. We can see in Figure 4.14 a plot of z_{phot} vs. z_{spec} using the photometric redshifts from Pforr et al. (2018). We realise that those results, although marginally better than ours ($\sigma_{NMAD} = 0.034$ vs. 0.049, and $\Omega = 11.0\%$ vs. 12.7%), still do not manage to constrain results at high redshifts. On the other hand, by making use of χ^2_r and number of observed filters cuts, Pforr et al. (2018) could validate their results properly. On this front we can conclude that it is possible that the newly created

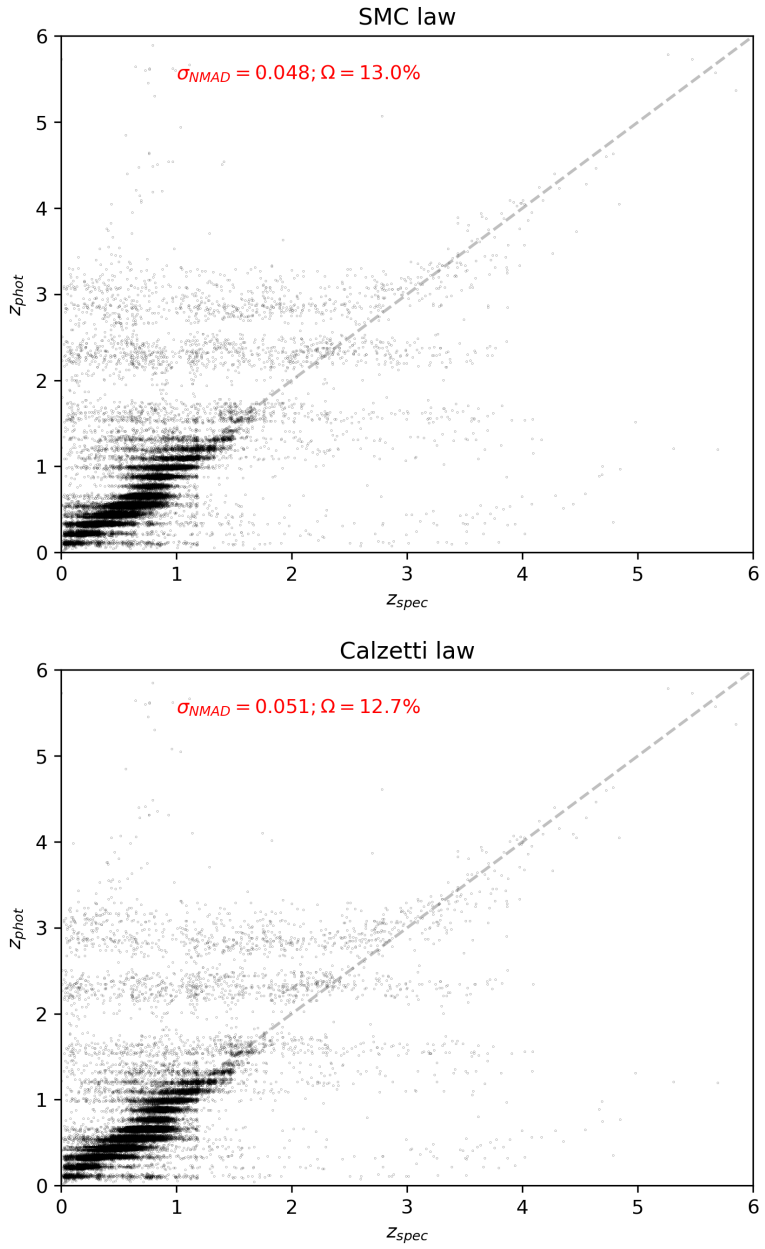

Figure 4.12: z_{phot} vs. z_{spec} plots for the results obtained with the SMC reddening law (top panel) and the Calzetti reddening law (bottom panel). The performance of the two reddening laws is extremely similar, meaning that what could be observed in Figure 4.11 was largely due to χ^2_r-related selection effects.

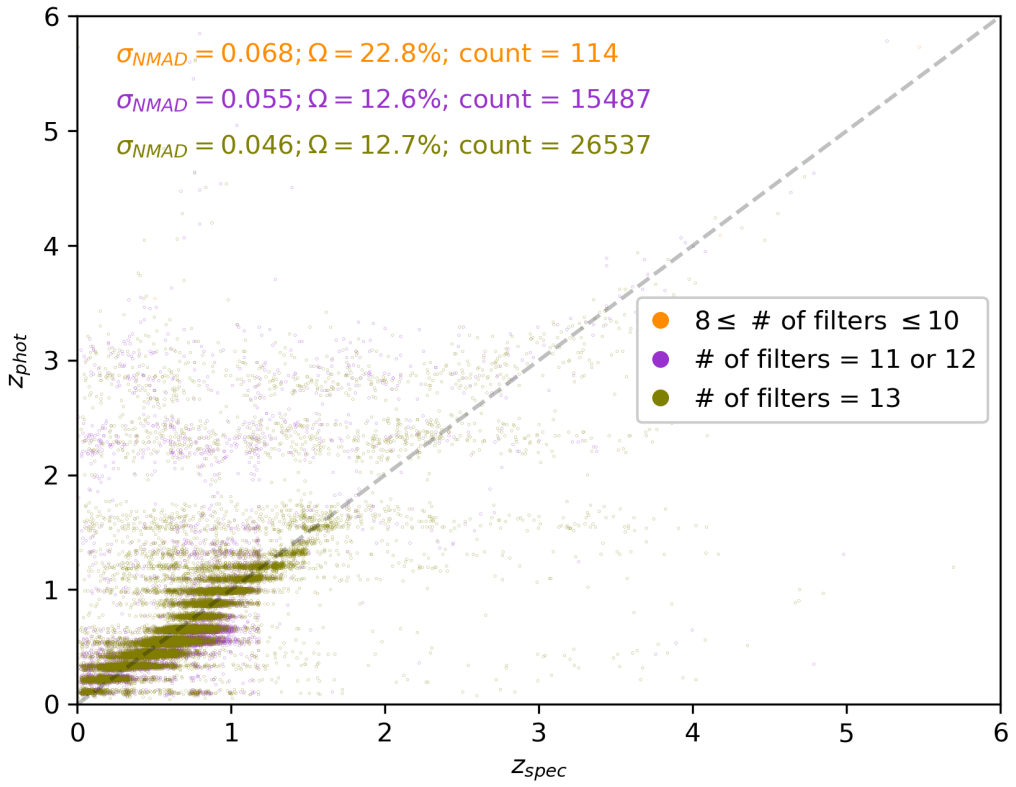

Figure 4.13: Photometric redshift as calculated by us against spectroscopic redshifts for $\sim$ 40 thousand SERVS sources and colour coded by different properties. Here we show in orange galaxies with a number of observed bands between 8 and 10 (no galaxy had less than 8), in purple those with either 11 or 12 observed bands, and in green those with all 13 bands observed

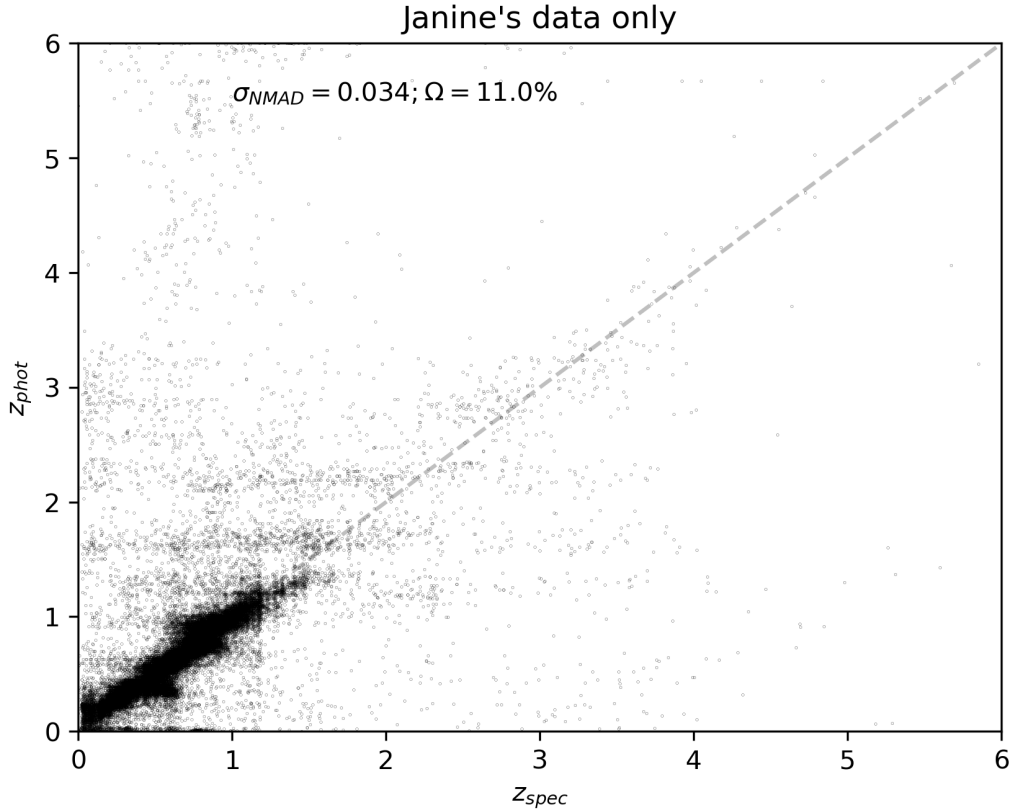

Figure 4.14: Photometric redshift as calculated by Pforr et al. (2018) against spectroscopic redshifts for ~ 40 thousand SERVS XMM sources. The values of σ_{NMAD} and Ω are also annotated.

SERVS XMM catalogue does not allow us to obtain a higher number of reliable results despite the improvements related to the de-blending of high-z sources. Moreover, this very data pre-processing makes it harder to remove seemingly incorrect results by using empirical cuts unlike Pforr et al. (2018) could do. Note that the HyperZ redshift bin size in Pforr et al. (2018) is finer than in our case because they fitted galaxies up to $z = 6$, while we did so up to $z = 12$ to avoid implicit priors; this is why the z_{phot} vs. z_{spec} plot using Pforr et al. (2018) data shows a smoother distribution.

Moreover, if for the same sources we plot the photometric redshift calculated by us against the one obtained by Pforr et al. (2018), as shown in

Figure 4.15 (plotted as density), we see a large disparity. Here we note that we are plotting against each other the full catalogues ($\sim 800,000$ sources), meaning that visually it is expected that the figure appears less clean. However, not only the value of σ_{NMAD} (i.e. 0.179), but especially the $\sim 26\%$ of catastrophic outliers (here a Ω has a slightly different meaning than when z_{spec} are considered) indicate that the photometric catalogues are different enough to artificially create high levels of unreliable results. It is important to remember that Pforr et al. (2018) also used HyperZ with M05 models and similar settings. This strengthen the argument that the cause of problems originate with the photometric data.

In the next sections we will discuss further whether these uncertainties on the quality of the photometric redshifts can have an impact on our results of the GSMF.

4.6 The Spectroscopic Galaxy Stellar Mass Function

It is important to understand what type of GSMF we can obtain when using only galaxies with spectroscopic redshifts. We calculate the spectroscopic GSMF for the available galaxies with $z_{spec} \leq 1$, i.e. 90% of the $\sim 40,000$ total sample. We do this following the exact same procedure described in Section 3.3.8. The only difference is that, as we already have known redshifts, we utilise HyperZ-spec (see Section A.5 for more details) to simply calculate the physical properties of the galaxies, crucially the mass. Parallelisation on Sciama was used here as well, which required some tweaks to our pipeline to accept HyperZ-spec executables and parameter files. The GSMF was also then derived in the exact same way as described for our normal SERVS GSMF.

For our analysis the most informative plots are the one showing all the GSMFs over multiple redshift bins up to $z = 1$ (above this limit we do not have much spectroscopic data) and the one similar to the figure from

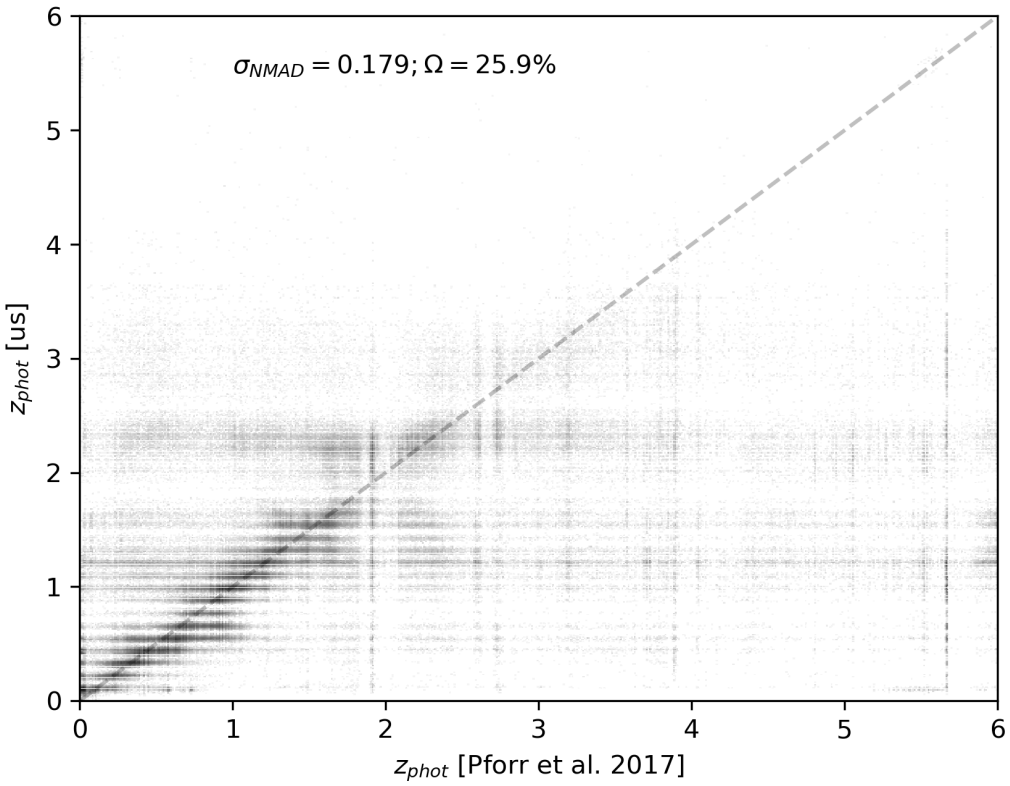

Figure 4.15: Photometric redshift as calculated by us against those calculated by Pforr et al. (2018) for the vast majority of the $\sim 800,000$ SERVS XMM sources. The values of σ_{NMAD} and Ω are also annotated. For clarity, this figure has been created as a density plot.

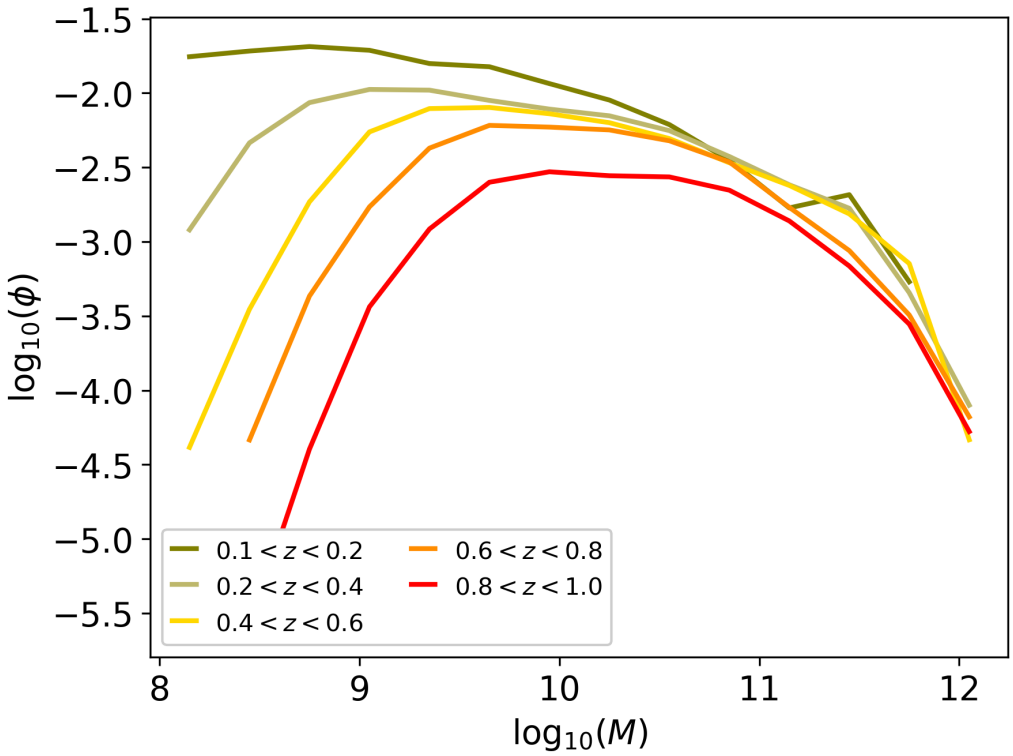

Figure 4.16: The SERVS GSMF for the spectroscopic sources for all redshift ranges considered below $z = 1$ on a single plot. Each redshift range is represented by a solid line of a different colour: dark green for $0.1 < z < 0.2$, light green for $0.2 < z < 0.4$, yellow for $0.4 < z < 0.6$, orange for $0.6 < z < 0.8$, and bright red for $0.8 < z < 1.0$.

Pozzetti et al. (2010a) showing ϕ vs. z for a series of mass ranges. The former is presented in Figure 4.16 while the latter is found in Figure 4.17.

These two can be compared to our photometric results from Figure 3.3 and 3.4, respectively. What we can infer is that the massive end of all redshift ranges does not evolve; this is clear in Figure 4.16 and in the most massive bin of Figure 4.17. This picture seems to support the 'downsizing' paradigm, though when we focus our attention to the four redshift ranges up to $z = 0.8$ we tend to see little evolution at all masses, except for the least massive end where completion can play a role as well.

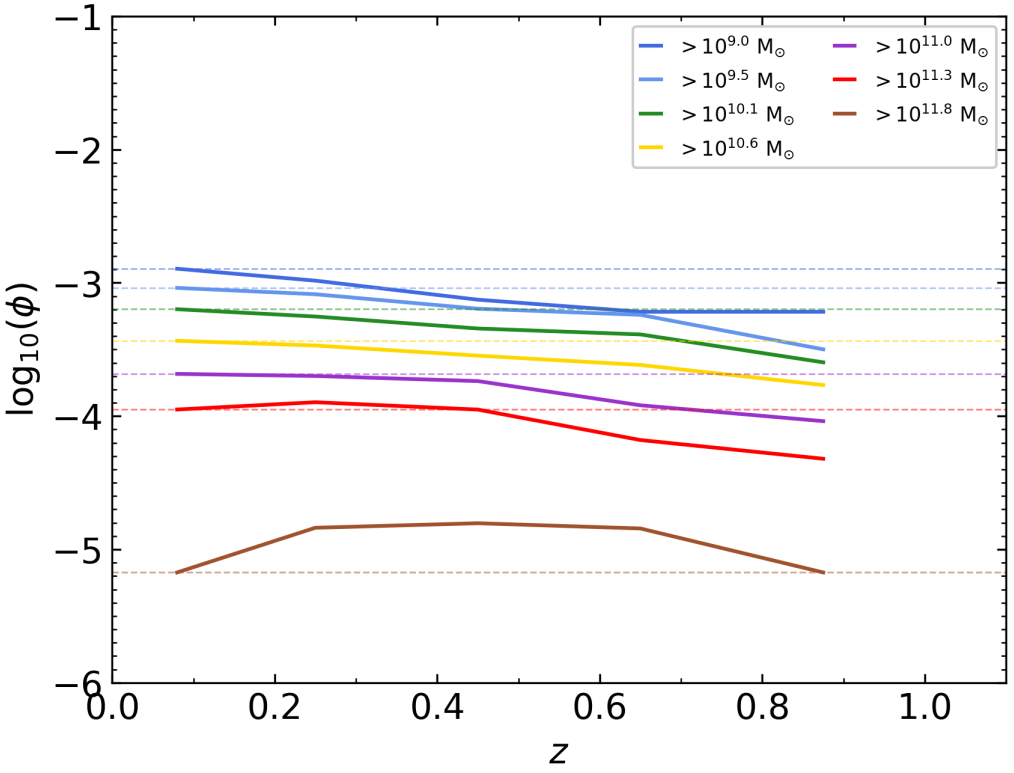

Figure 4.17: The value of ϕ is plotted against the redshift for a series of different mass bins for the results obtained by fitting the sample of galaxies with a spectroscopic redshift using HyperZ-spec. In this case, the mass bins are not the ones used for the normal GSMF calculation, but they range from a series of mass values (i.e. 9.0, 9.5, 10.1, 10.6, 11.0, 11.3, 11.8) up to M=12.5. This is similar to Figure 7 of Pozzetti et al. (2010a). Lines of different colours identify the different mass ranges (dark blue for $M > 9.0$, light blue for $M > 9.5$, green for $M > 10.1$, yellow for $M > 10.6$, purple for $M > 11.0$, red for $M > 11.3$, and brown for $M > 11.8$. The horizontal dashed line indicate the value of ϕ at the lowest redshift available.

It is important to reiterate that we could not independently verify the spectroscopic redshifts and, even more importantly, there could selection effects on the spectroscopic sample available. This means that the distribution we are seeing here may not correspond to what the physical universe looks like nor, crucially, to what SERVS would observe based on its experimental design. It may therefore be that the downsizing we see in Figure 4.16 and 4.17 is due to, for example, the fact that as redshift increases we can still manage to observe high-mass galaxies while we miss other ones that are less massive. That would be because the spectroscopic data may come from observing sessions that did not aim to push the magnitude limit boundaries as much as SERVS.

We also briefly compare the masses calculated for the spectroscopic data using their z_{spec} values with the masses we originally calculated from the z_{phot}. The comparison is shown in Figure 4.18, with the stellar mass calculated from spectroscopic redshifts is on the x-axis and the stellar mass coming from the photometric redshift is on the y-axis. Note that here only galaxies with $z_{spec} < 1$ are considered. It is interesting to note that the matching is generally very good, with less than 2% of catastrophic outliers. This may suggest that we can recover stellar masses generally better than photometric redshifts despite using the same templates and photometric redshift code for the two methodologies.

In order to further investigate the effects of these findings we compare the GSMF results from Figure 3.3 with the plot we would obtain when using our photometric outputs for only the galaxies with a spectroscopic equivalent. This check will not necessarily allow us to comment with specific physical conclusions, but it will enable us to verify whether using photometric redshifts may result in a wildly different picture of the GSMF. We can see the result of this exercise in Figure 4.19.

Clearly, we do not manage to recover the spectroscopic GSMF results successfully. The lowest redshift bin ($0.1 < z < 0.2$) also seems particularly affected and it seems to be missing a prominent fraction of the mid-mass

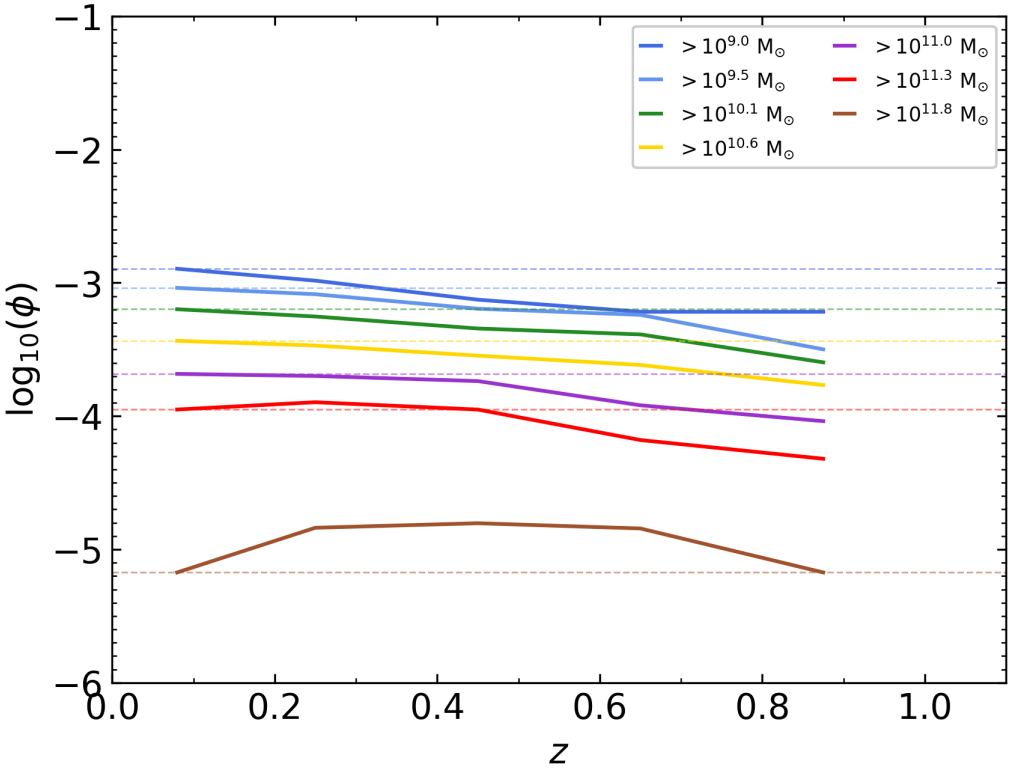

Figure 4.18: The stellar masses calculated from the photometric redshift against those calculated from the spectroscopic redshifts. The sources shown are all those for which we have spectroscopic data available and where $z_{spec} < 1$. The generally very good agreement may suggest that we can recover stellar masses better than photometric redshifts.

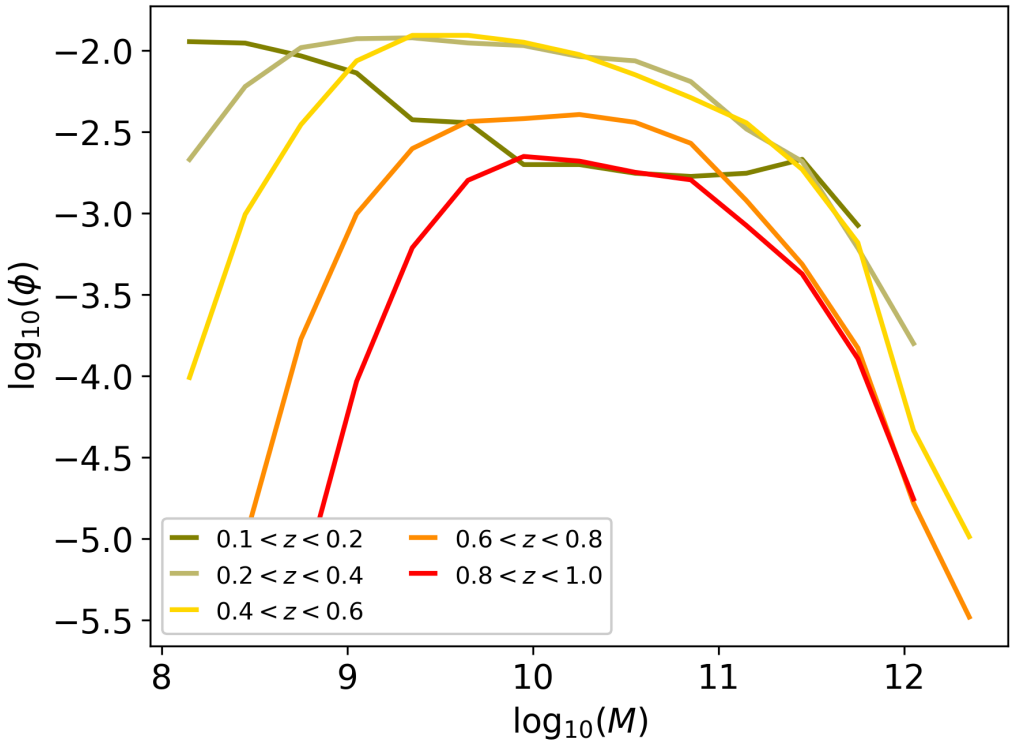

Figure 4.19: The SERVS GSMF for the spectroscopic sources but using our photometric calculations for all redshift ranges considered below $z = 1$ on a single plot. Each redshift range is represented by a solid line of a different colour: dark green for $0.1 < z < 0.2$, light green for $0.2 < z < 0.4$, yellow for $0.4 < z < 0.6$, orange for $0.6 < z < 0.8$, and bright red for $0.8 < z < 1.0$.

galaxies. It is unclear what is happening here, but it could be a hint of some selection process being in the background of the spectroscopic data. As described earlier, this could be due to the spectroscopic redshift z_{spec} values being often incorrect or to issues related to our photometric redshift calculation, e.g. issues with the code, the models, or the photometric data.

We test the reliability of the photometric code and stellar population models in the following section, by re-fitting all the data using an independent photometric redshift code called EAZY and their different template set.

4.6.1 The GSMF of SERVS Obtained with EAZY

4.6.1.1 EAZY Photometric Redshifts

To test the impact of the choice of photometric redshift code and fitting templates, we now replicate the work performed in Chapter 3 by re-calculating the z_{phot}, the stellar masses, and eventually the GSMF for our SERVS XMM catalogue using EAZY (Brammer et al., 2008).

This code works in a similar way as HyperZ by taking input photometric data and by making usage of a parameter file to set the fitting settings. By default the code has a set of five templates created combining PEGASE models and a calibration set of synthetic photometry derived from semi-analytical models. EAZY then combines them during the fitting process and creates hybrid templates to calculate the photometric redshifts of the input galaxies. Also, by default, EAZY uses priors to prefer solutions that it deems more likely based on the semi-analytical models. When we ran EAZY we switched off these priors as we did not want our calculations to be influenced by any assumptions (our HyperZ run made no use of such priors).

We first calculated the EAZY photometric redshifts for all $\sim 800,000$ SERVS sources belonging to our catalogue. We then calculated their masses using HyperZ-spec, as EAZY cannot estimate physical properties because it uses hybrid templates. It is important to note that the combined templates may not be physical stellar population models. While EAZY is fast enough

to calculate the z_{phot} values for the whole catalogue in less than 5 hours on its own, the mass calculation done by refitting the galaxies with HyperZ-spec required, as we have seen earlier, tweaks to our Sciama parallelisation pipeline.

We can start by comparing the photometric redshift calculated by EAZY with the spectroscopic values. We show this in Figure 4.20. We find that EAZY results have a $\sigma_{NMAD} = 0.047$ and $\Omega = 13.8\%$; the former value is only marginally better than what we found with HyperZ ($\sigma_{NMAD} = 0.049$), and on the other hand the fraction of catastrophic outliers is slightly worse, i.e. $\Omega = 12.7\%$.

We can also verify how the EAZY photometric redshifts directly compare with those calculated using HyperZ. In Figure 4.21 we plot the EAZY z_{phot} against the HyperZ z_{phot} for the sources that also have a spectroscopic redshift. We immediately see that overall the agreement between the two is good, with just a few tens of candidates being categorised as high-redshift by either code while the other one suggests otherwise. We find $\sigma_{NMAD} = 0.035$ and $\Omega = 8.0\%$, values that are similar to those found by Marchesini et al. (2009), when comparing to z_{spec}, to successfully verify their photometric redshifts. This suggests that the choice of code or fitting templates here is irrelevant to the quality of the results. This once again points to the high likelihood that the problems originate from a defective SERVS dataset or badly-estimated z_{spec}.

4.6.1.2 The EAZY Galaxy Stellar Mass Function

Even though the EAZY results do not appear to solve the z_{spec} validation problems, subtle changes in the photometric redshifts can easily translate in large GSMF variations. We therefore also present the GSMF calculated using the EAZY z_{phot} values (and associated stellar masses).

We plot the stellar mass function for the usual redshift ranges ($0.1 < z < 0.2$, $0.2 < z < 0.4$, $0.4 < z < 0.6$, $0.6 < z < 0.8$, $0.8 < z < 1.0$, $1.0 < z < 1.5$, $1.5 < z < 2.5$, $2.5 < z < 3.5$, and $3.5 < z < 4.5$) selected using EAZY

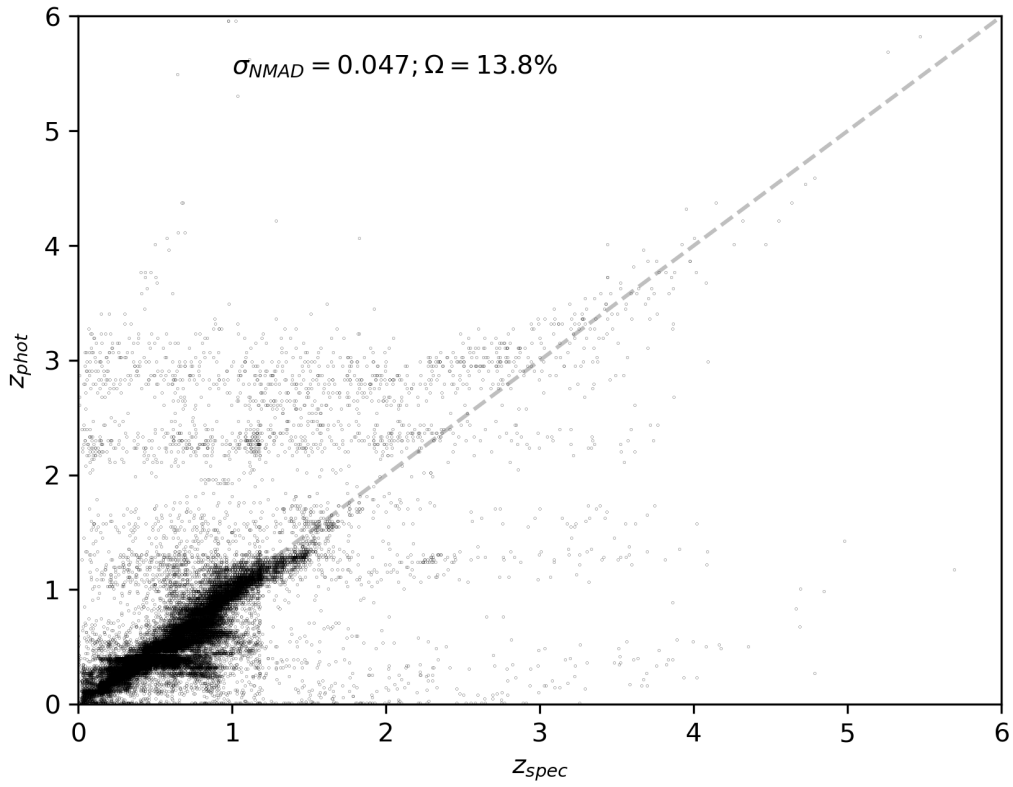

Figure 4.20: The photometric redshifts calculated using the EAZY code and stellar population combination are plotted against the spectroscopic redshifts. The results include values of $\sigma_{NMAD} = 0.047$ and $\Omega = 13.8\%$, both indicating similar outputs as the ones calculated by HyperZ with M05 stellar populations models. This may indicate that the issues lie with either the photometric data or the reliability of the z_{spec} values.

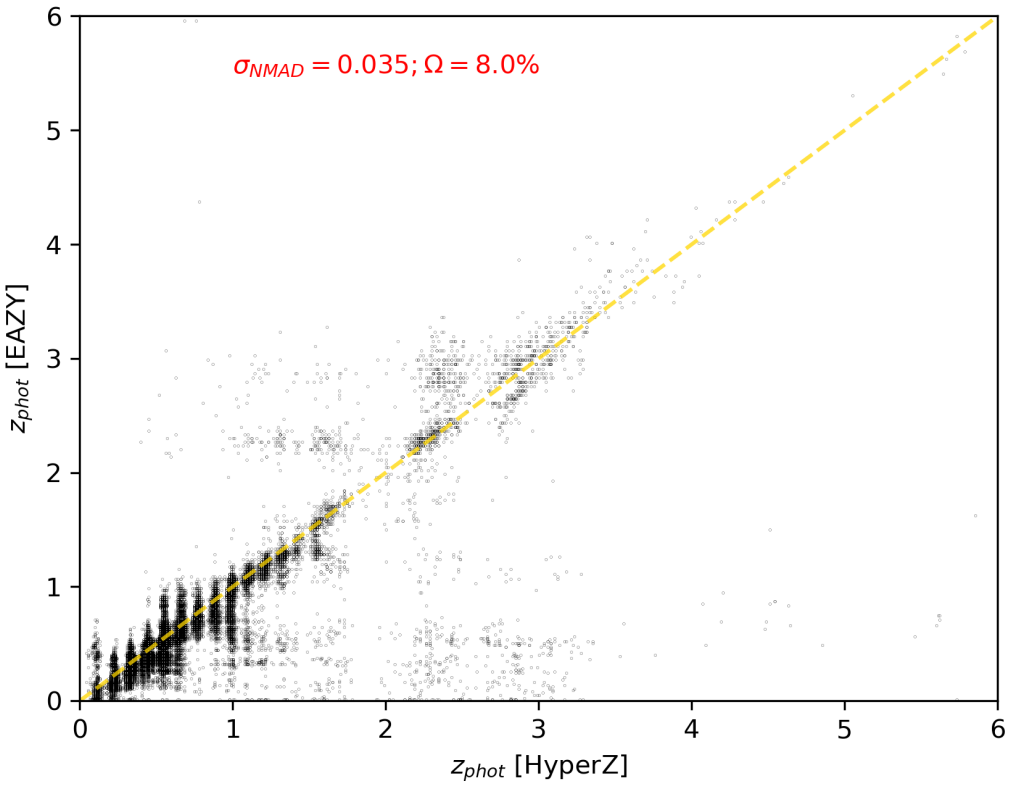

Figure 4.21: The photometric redshifts calculated by EAZY are plotted against the ones estimated by HyperZ. The agreement is overall good ($\sigma_{NMAD} = 0.035$ and $\Omega = 8.0\%$) and only a few tens of galaxies are estimated to be at high redshift by either code, while the other suggests otherwise.

results in Figure 4.22. We can compare this with what we obtained using the photometric redshifts coming from HyperZ (Figure 3.2) as well as what obtained using the spectroscopic data (Figure 4.16). We find that the EAZY GSMF remains similar to what got with HyperZ fittings. This means we cannot recover, the 'downsizing'-like behaviour obtained with spectroscopic data (see Figure 4.16). Like in the original HyperZ case, the EAZY GSMF has been calculated using the full SERVS XMM data sample that expands well further than the spectroscopic data available. As said earlier, we cannot therefore exclude yet the possibility that what we found using only galaxies with a z_{spec} is only a selection effect, even ignoring the possibility the some of the spectroscopic values are incorrect in the first place.

It is also interesting to directly compare the EAZY and HyperZ stellar mass functions. We present in Figure 4.23 a series of panel plots for the usual redshifts ranges showing the two side by side. HyperZ data is plotted as blue stars, while EAZY data is shown as red circles. What can be observed is that, as already noted, the two types of GSMF are extremely similar. The mid-mass bins tend to be almost identical, with only slight exceptions at high redshift. Although minor, the main differences are registered in the low-mass, the high-mass ends, or both. In particular, at the lowest redshift bins ($z \leq 0.4$) EAZY seems to recover slightly more low-mass galaxies, diminishing the gap that HyperZ had with the SERVS model 'lightcone'. EAZY also seems to overestimate, compared to HyperZ, the number of massive galaxies until $z \sim 1.5$. At higher redshifts the massive ends are instead very similar and the main divergences are obtained at lower masses, $M \sim 10.5$

Lastly, we take a quick look at what we obtain when re-creating the Pozzetti et al. (2010a) style plot with the EAZY calculation results. This can be seen in Figure 4.24. As for the case of HyperZ, we find a mixed-bag picture showing parallel evolution across cosmic time of all mass bins. We only note an apparent clustering, potentially an artefact of the EAZY fitting procedure, at $z \sim 0.5$ for all mass bins.

The results are similar even when looking only at galaxies with a spectro-

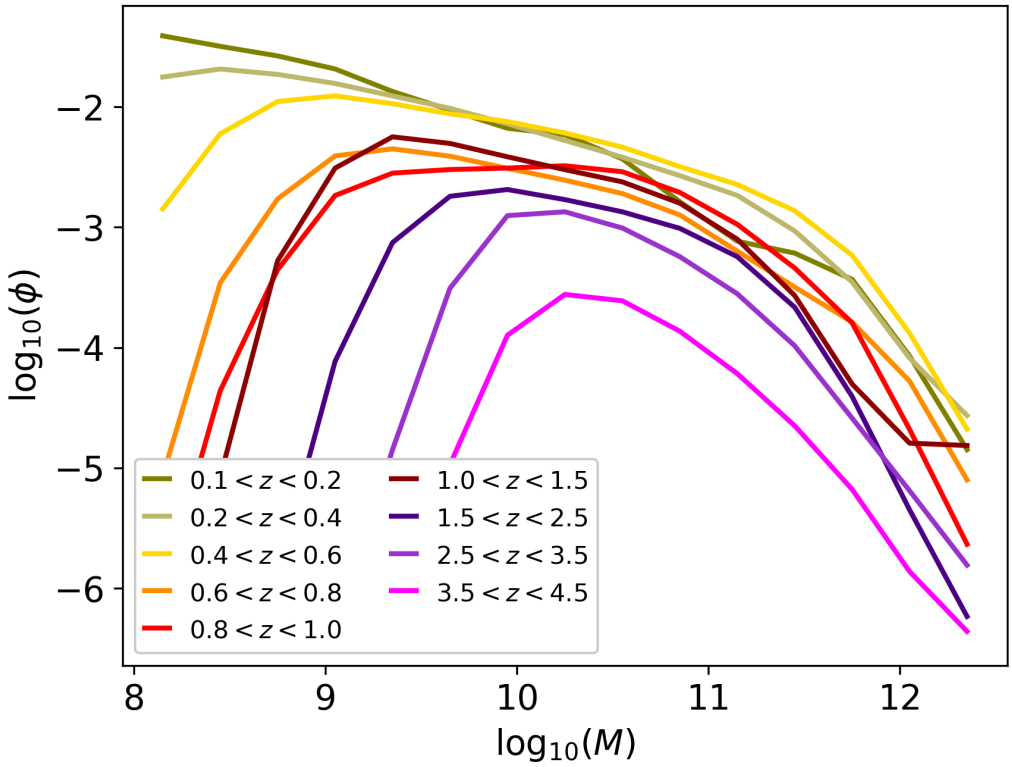

Figure 4.22: The SERVS GSMF for all redshift ranges considered on a single plot using the photometric redshifts calculated with EAZY. Each redshift range is represented by a solid line of a different colour: dark green for $0.1 < z < 0.2$, light green for $0.2 < z < 0.4$, yellow for $0.4 < z < 0.6$, orange for $0.6 < z < 0.8$, bright red for $0.8 < z < 1.0$, dark red for $1.0 < z < 1.5$, indigo for $1.5 < z < 2.5$, purple for $2.5 < z < 3.5$, and magenta for $3.5 < z < 4.5$.

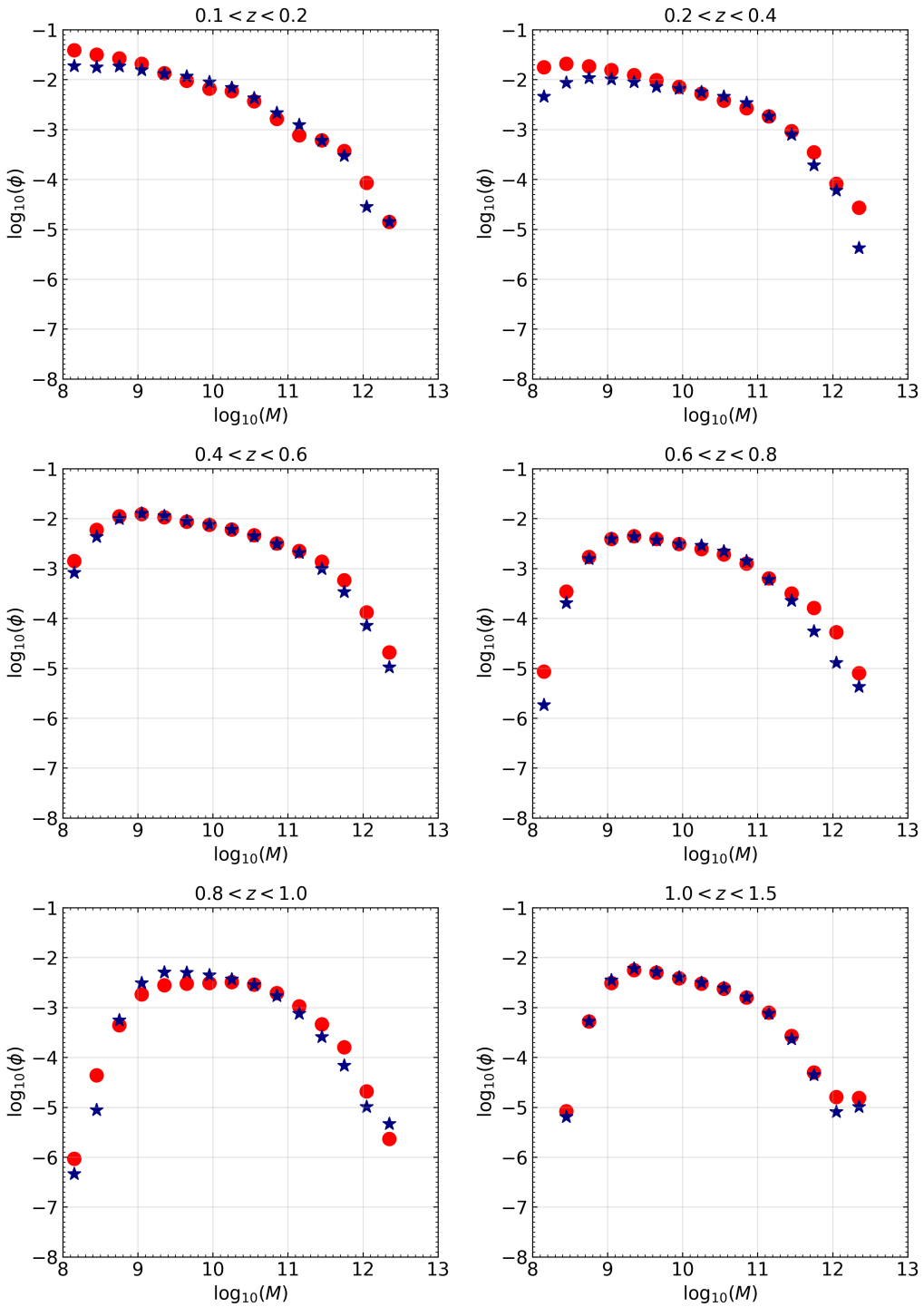

Figure 4.23: This is a figure spanning multiple pages. The full caption is found at the end of the figure.

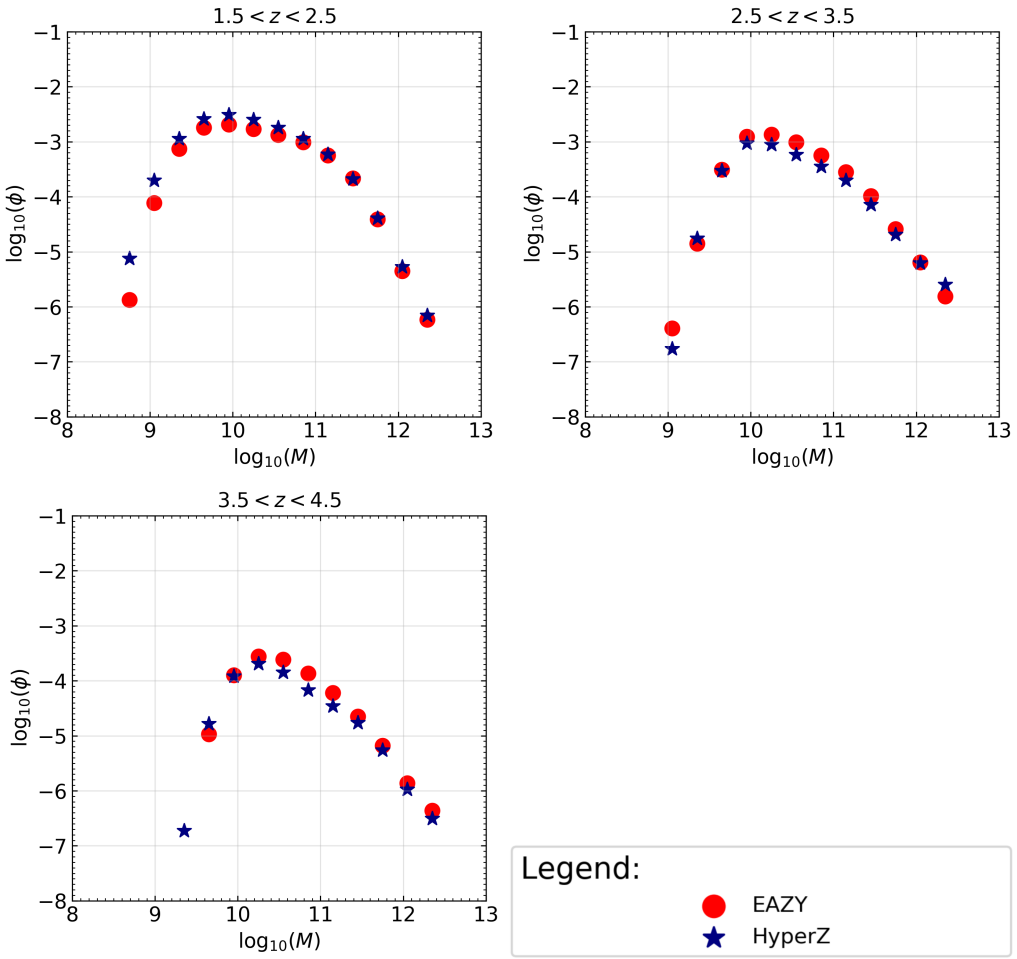

Figure 4.23: GSMF comparing HyperZ results with those obtained using EAZY for redshift ranges (top to bottom panel) $0.1 < z < 0.2$, $0.2 < z < 0.4$, $0.4 < z < 0.6$, $0.6 < z < 0.8$, $0.8 < z < 1.0$, $1.0 < z < 1.5$, $1.5 < z < 2.5$, $2.5 < z < 3.5$, and $3.5 < z < 4.5$. Data is plotted as blue stars for HyperZ and as red circles for EAZY. The results tend to be similar and they are clearly compatible with only minor differences at the low-mass and high-mass ends.

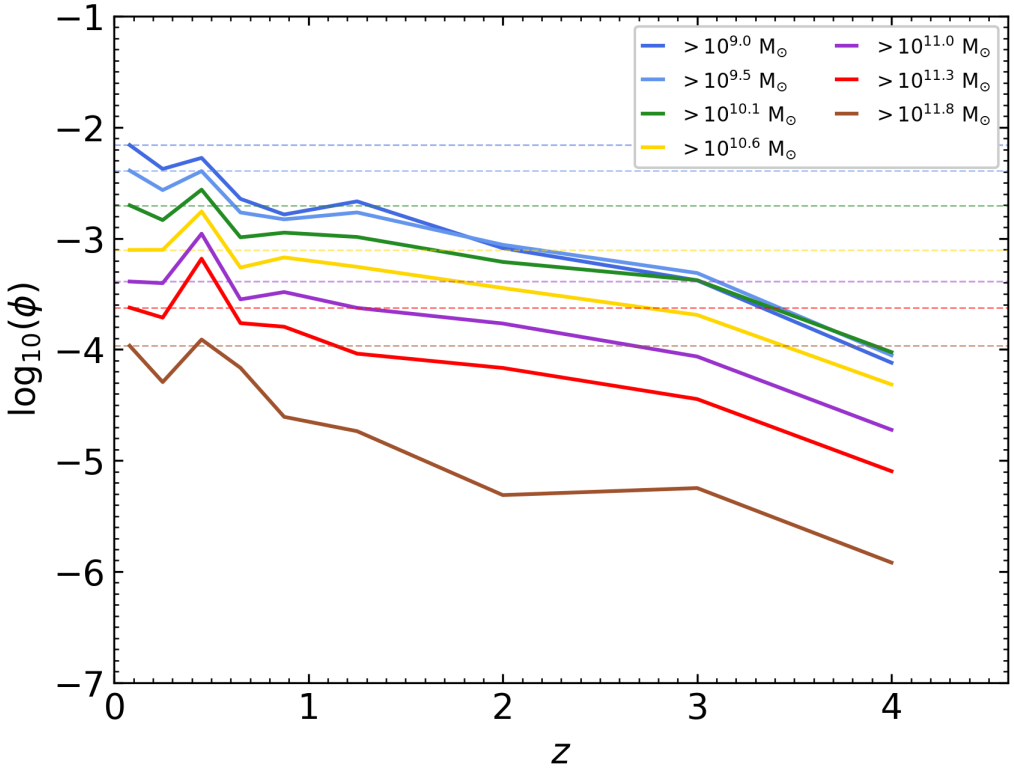

Figure 4.24: The value of ϕ, as calculated with EAZY photometric redshifts, is plotted against the redshift for a series of different mass bins. In this case, the mass bins are not the ones used for the normal GSMF calculation, but they range from a series of mass values (i.e. 9.0, 9.5, 10.1, 10.6, 11.0, 11.3, 11.8) up to M=12.5. This is similar to Figure 7 ofPozzetti et al. (2010a). Lines of different colours identify the different mass ranges (dark blue for $M > 9.0$, light blue for $M > 9.5$, green for $M > 10.1$, yellow for $M > 10.6$, purple for $M > 11.0$, red for $M > 11.3$, and brown for $M > 11.8$. The horizontal dashed line indicate the value of ϕ at the lowest redshift available.

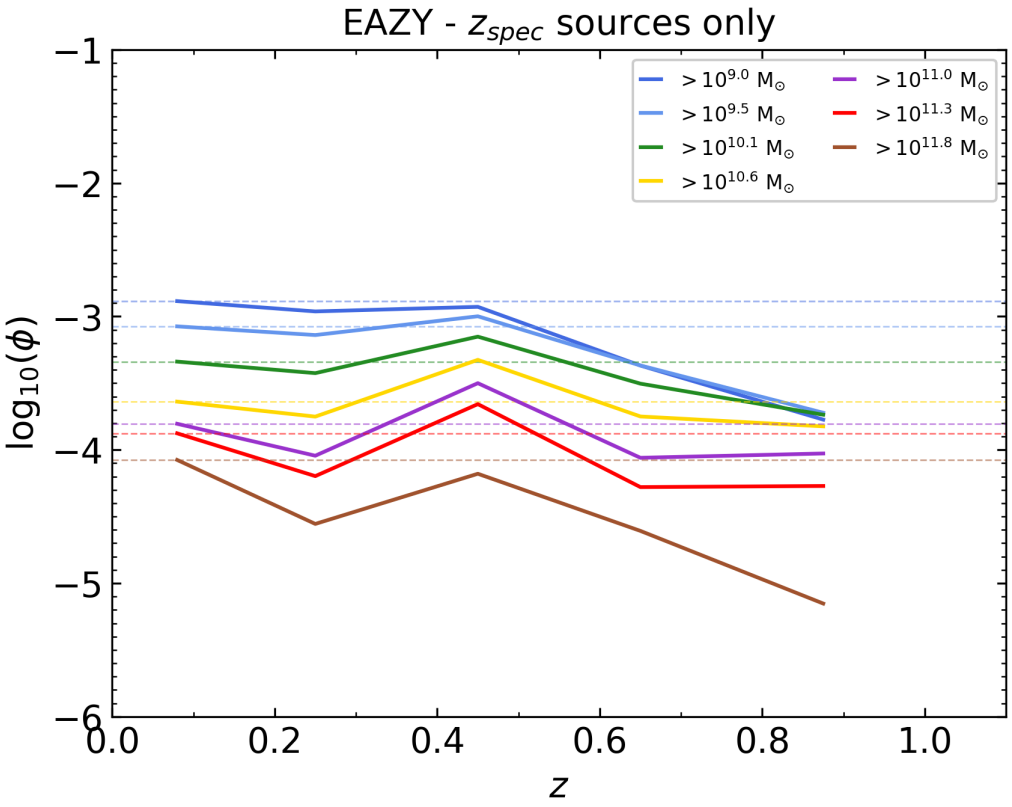

Figure 4.25: As Figure 4.24, but limited to galaxies with a known spectroscopic redshift.

scopic observation equivalent. See Figure 4.25 for the same plot again limited to sources that have a known z_{spec} (limited at $z < 1$). The same behaviour as above is found and we do not recover what was shown in Figure 4.17.

4.7 How Good Is z_{spec} for z_{phot} Outliers?

Some of the outliers in the original z_{phot} vs. z_{spec} plot have been analysed in more detail. By outliers, here these are defined as those galaxies that have $z_{phot} \geq 2$ and $z_{spec} \leq 1$ in Figure 4.2.

We plotted the PDFs and photometric fittings of these in order to verify whether any specific patterns could be identified in order to understand where

the fitting procedure could be going wrong. Both the PDFs and the fittings are of the same types as those used in Chapter 2 to analyse candidates from the Dark Energy Survey.

Along with these two types of plots, we also show fittings created with HyperZ-spec by fixing the redshift according to the spectroscopic values.

We show these results for two example galaxies (identified as 16371 and 10257) in Figure 4.26. Each column has a results for a different object, and each row represents the PDF, the fit, and the spec-type fit, respectively. As in the Dark Energy Survey project, the PDF is shown in red with a vertical red line indicating the best solution For the two fittings the data is plotted as red circles with errors, the model points matched to the telescope response function adjusted model are the template fluxes and are plotted as blue squares, and in the background the best-fit model is plotted as a solid black line.

We can appreciate that, indeed, the canonical fittings get a better result fit and χ^2_r. When looking at the spec-type fittings it seems that the models struggle to find any good matches, reinforcing the idea that some of the z_{spec} data may be compromised unless unaccounted emission lines play a major role.

Also to note is that that despite being outliers, most of these galaxies have single-peaked PDFs (like the one on the left side of Figure 4.26). The example on the right with a double peaked PDF is rarer and is shown for completeness.

4.8 The Galaxy Stellar Mass Function of Other Fields

We also tested our GSMF methodology by using different data coming from surveys or fields unlike our SERVS XMM. For these we did not have spectroscopic redshifts, but it was a way to test whether results would support 'downsizing', hierarchical galaxy formation and evolution, or the hybrid we

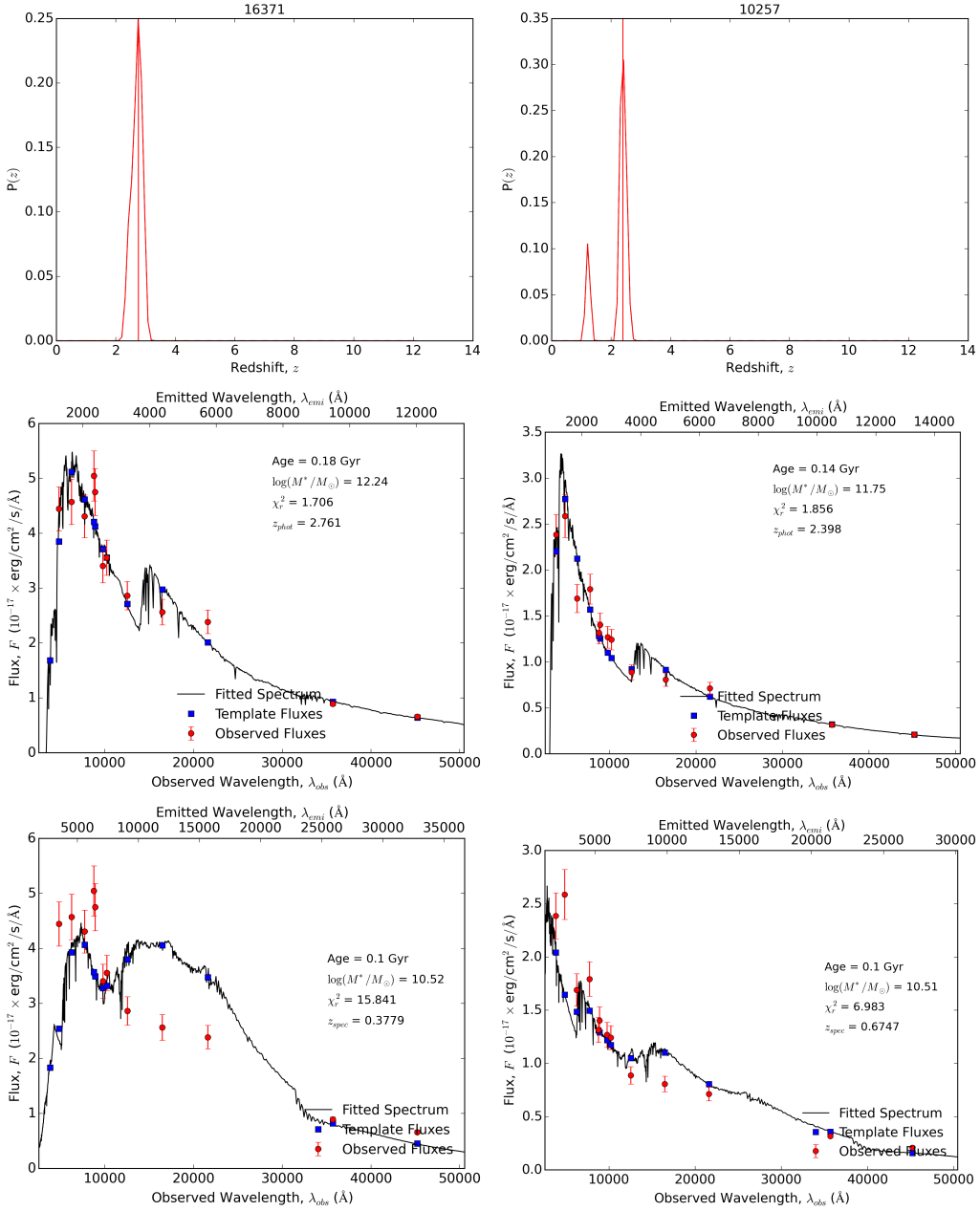

Figure 4.26: PDFs (top row), fittings (middle row), and fittings with fixed z_{spec} (bottom row) for two outlier galaxies, namely 16371 (left column) and 10257 (right column). Outliers are defined as galaxies that have $z_{phot} \geq 2$ and $z_{spec} \leq 1$ in Figure 4.2.

find for SERVS XMM of a parallel evolution. We do this using both the SERVS Lockman Hole as well as Dark Energy Survey data from the science verification programme.

4.8.1 The SERVS GSMF in the Lockman Hole

We calculated the photometric redshift and stellar masses, and eventually the GSMF of SERVS data corresponding to the 'Lockman Hole' observation field using the same procedure as described earlier. This dataset contains $\sim 950,000$ sources and has not undergone a TRACTOR-like process yet, meaning it is from a data release equivalent to the SERVS XMM data used by Pforr et al. (2018). The precise observed area in this case is unknown and therefore the y-axis scaling is to be considered arbitrary and it is not relevant for the aim of this test.

Given the size of the sample here, once again we had to make use of a modified version of our Sciama parallelisation pipeline in order to keep running times reasonably short.

As a summary result, we show the GSMF for different redshift bins up to $z \sim 1$ in Figure 4.27. We find results[1] that certainly do not match what we had found with the spectroscopic sample, and in this case hierarchical structure formation seems even preferred. This implies that the parallel-like galaxy evolution does not seem to be an effect of our fitting procedure or GSMF calculation.

We do not draw further conclusions as we did not have spectroscopic redshifts for validation and our primary aim was to simply check whether our procedure would replicate similar results to any of the instances we have analysed earlier, which does not seem to be the case.

[1]Note any GSMF lines interrupted are simply due to some limitations of the GSMF calculation code when encountering values such as zeros or above certain thresholds. For the scope of this test with Lockman Hole data, it was not important to upgrade the code to be able to deal with these types of input.

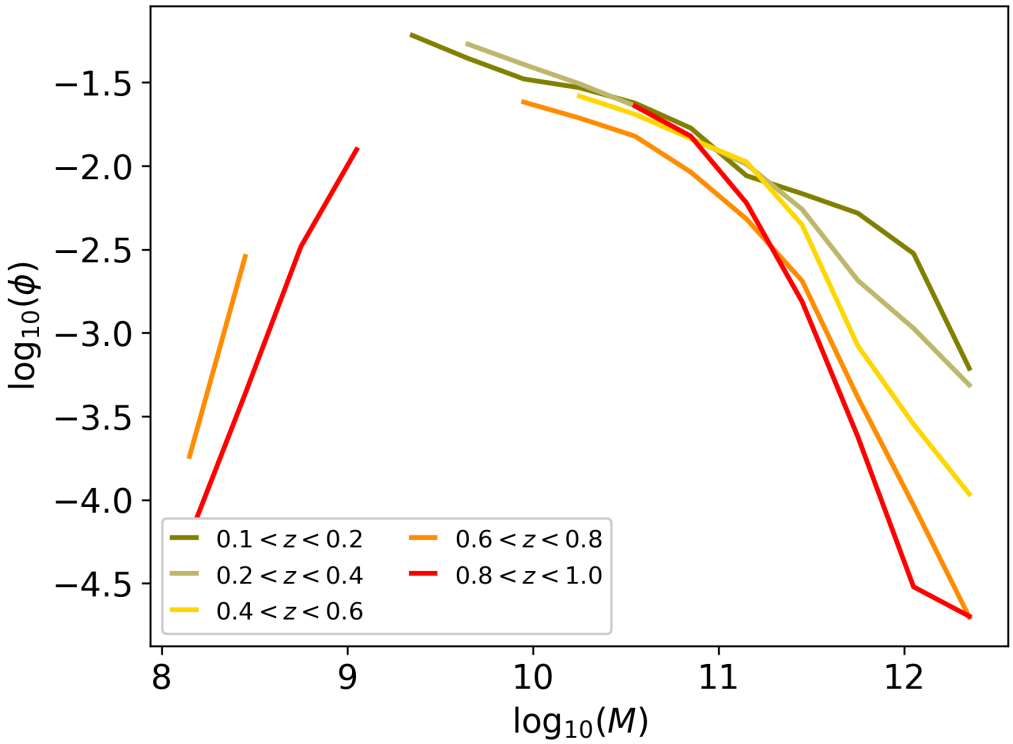

Figure 4.27: The GSMF for the usual redshift ranges up to $z \sim 1$. The data used here comes from the Lockman Hole catalogue of SERVS, a dataset that has not undergone the TRACTOR procedure. Results do not seem to replicate any of our previous findings and instead hint at hierarchical galaxy formation.

4.8.2 The Dark Energy Survey Stellar Mass Function

Lastly, we also perform a test similar to the one shown in Section 4.8.1, but using data from the Science Verification programme of the Dark Energy Survey for an observed area of ~ 150 sq. deg. (the precise area not important for this test either).

In this case the photometric redshifts were calculated by a machine learning algorithm developed by the DES data pipeline (see Section 2.3.2.1). The masses were instead calculated by the COMMODORE team (see again Section 2.3.2.1) following a methodology similar to ours by using HyperZ and M05 models.

We then calculated the GSMF up to redshift ~ 1 ourselves following our usual procedure. Results are shown in Figure 4.28 and once again show a mixed bag output with little indication of replicating past results. The global picture with these data suggests some inverse-hierarchical paradigm with massive galaxies increasingly remaining undetected since $z \sim 1$. We do not comment further on scientific results using these data as our analysis did not explore further details.

Final remarks and conclusions relative to the work performed on SERVS data (previous and current chapter) are found in Chapter 6.

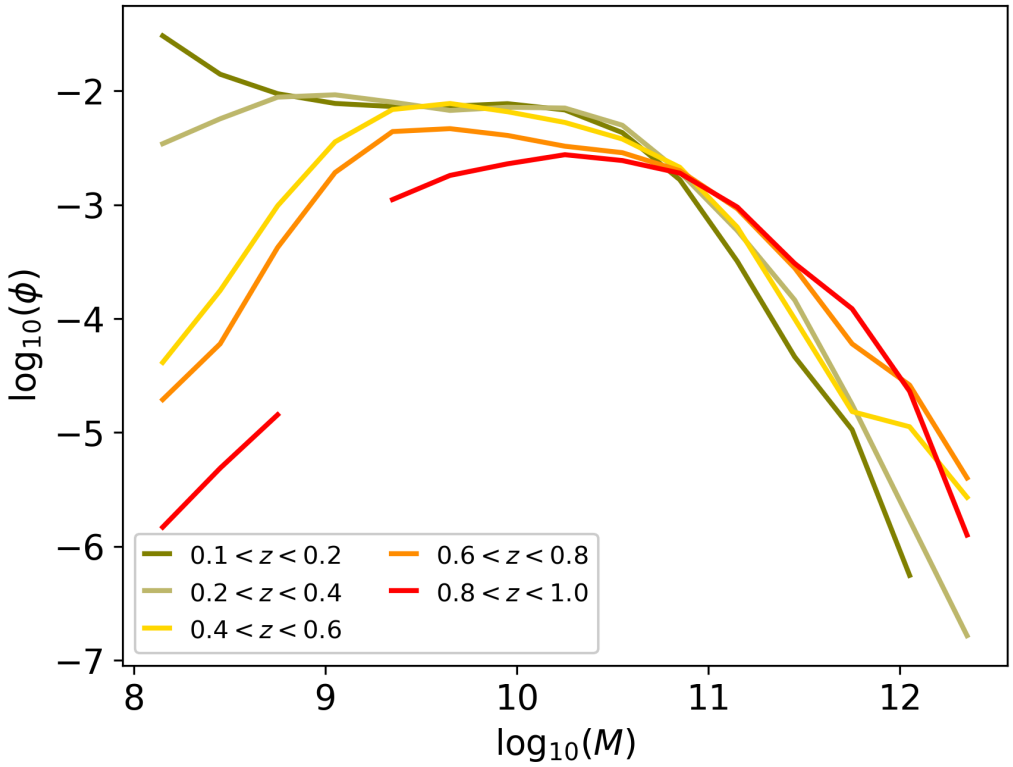

Figure 4.28: The GSMF for the usual redshift ranges up to $z \sim 1$. The data used here comes from the Science Verification programme of the Dark Energy Survey ($\sim$ 150 sq. deg.). Here the photometric redshifts were calculated by a machine learning algorithm developed by the DES data pipeline while the masses were estimated by the COMMODORE team following a methodology similar to ours by using HyperZ and M05 models.

Chapter 5

Additional Work and Related Publications

In addition to the two main projects involving DES and SERVS data described so far, other minor works contribute to this thesis.

As we suggested in Chapter 2, the obvious next step after finding candidates for $z \sim 4$ massive galaxies was to verify our results spectroscopically. We collaborated with Thiago Signorini Goncalves from the Federal University of Rio de Janeiro in order to submit a short proposal for the spectroscopic observation of three of our candidates using the Gemini fast-turnaround proposal format. In order to follow the format's requirements we aimed to minimise observation time by focusing on detecting emission lines. In particular, I wrote the scientific justification, which was also revised by my collaborators, and I identified the visible best candidates given the telescope and programme requirements (i.e. location in the sky and time of the year). We successfully obtained time in May 2018, and over the following summer the data was collected. Thiago is undergoing data reduction and analysis at the moment of writing this chapter. The long timescales for the data analysis is mostly due to difficulties in reducing the data properly to obtain clear spectra. This could be because the observed galaxies are fainter than expected and not showing any clear emission line, or due to technical chal-

lenges. We hope that future spectroscopic programmes or other astronomers' research will also allow a comprehensive review of our candidates.

Still related to DES, I was part of the overview paper of the collaboration that focused on non Dark Energy projects (Abbott et al. 2016). This was because it included a description of the work done for Chapter 2, which at that time was in preparation.

Thanks to the expertise developed with fitting photometric data with HyperZ, I could also contribute to the works of Lacy et al. (2018) and of Lonoce et al. (*sub.*).

For the former paper I fitted and calculated stellar masses for 165 galaxies located within SERVS fields observed with the Gemini South Adaptive Optics Imager (GSAOI). The fittings were produced by running HyperZ-spec (and stellar mass ancillary script) with redshifts calculated by the collaborators using EAZY. The reddening options used were the Calzetti law as well as by imposing no reddening. The results are summarised in the histogram shown in Figure 5.1 (red for the Calzetti law fittings and in black for the no-reddening case).

For Lonoce et al. (*sub.*), I fitted four galaxies with known spectroscopic redshift to calculate their physical properties. These sources had up to 16 observed photometric bands and they all had $z_{spec} > 1.4$. The fitting results are shown in Figure 5.2 for the four sources, and their stellar masses and age are annotated on the plots along with the spectroscopic redshifts and ID numbers. The legend is the same as the fittings shown in the previous chapters.

Lastly, I could calculate the physical properties of the spectroscopically confirmed $z = 9.11$ source from Hashimoto et al. (2018). Given its high redshift, it was particularly interesting to determine its age. We found it to be 0.14 Gyr. On the other hand, if we let the redshift free we could recover a solution that has $z_{phot} = 9.39$ and age 0.29 Gyr. It is particularly important to notice that we manage to recover a similar redshift, even this high, using 10 photometric bands (5 of which being upper limits). The age difference found

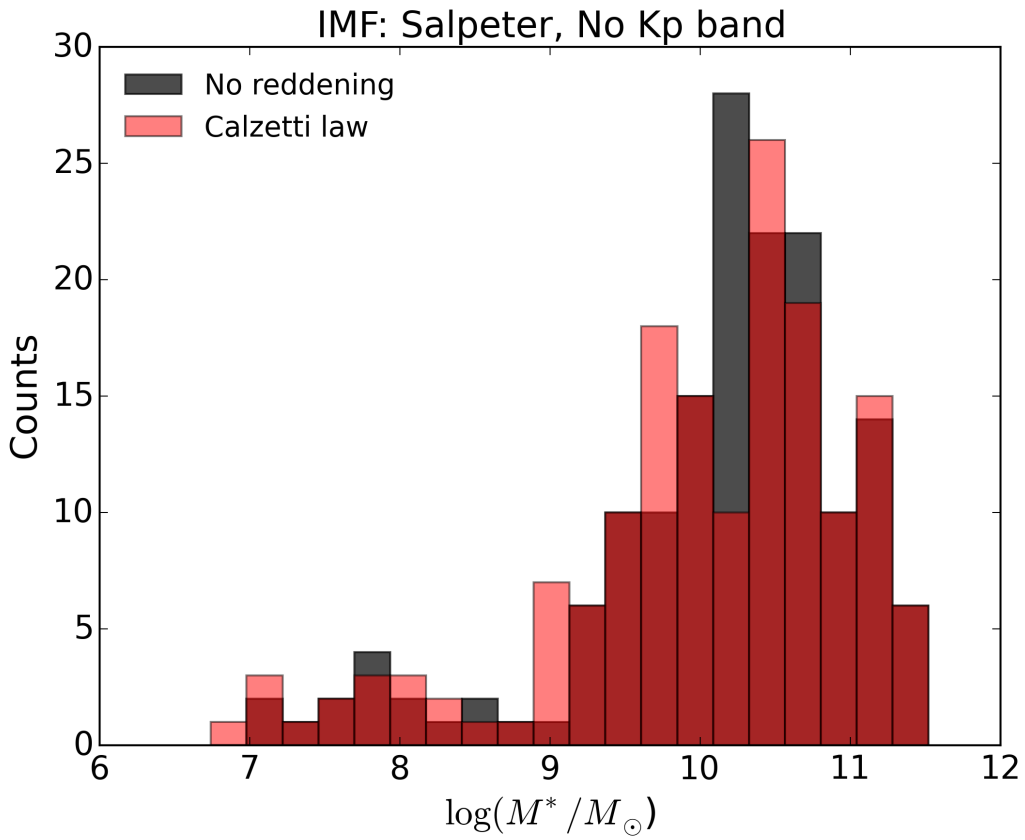

Figure 5.1: Distribution of stellar mass in solar units for the 165 galaxies imaged with the GSAOI and calculated by me by fitting them using HyperZ-spec and the ancillary script.

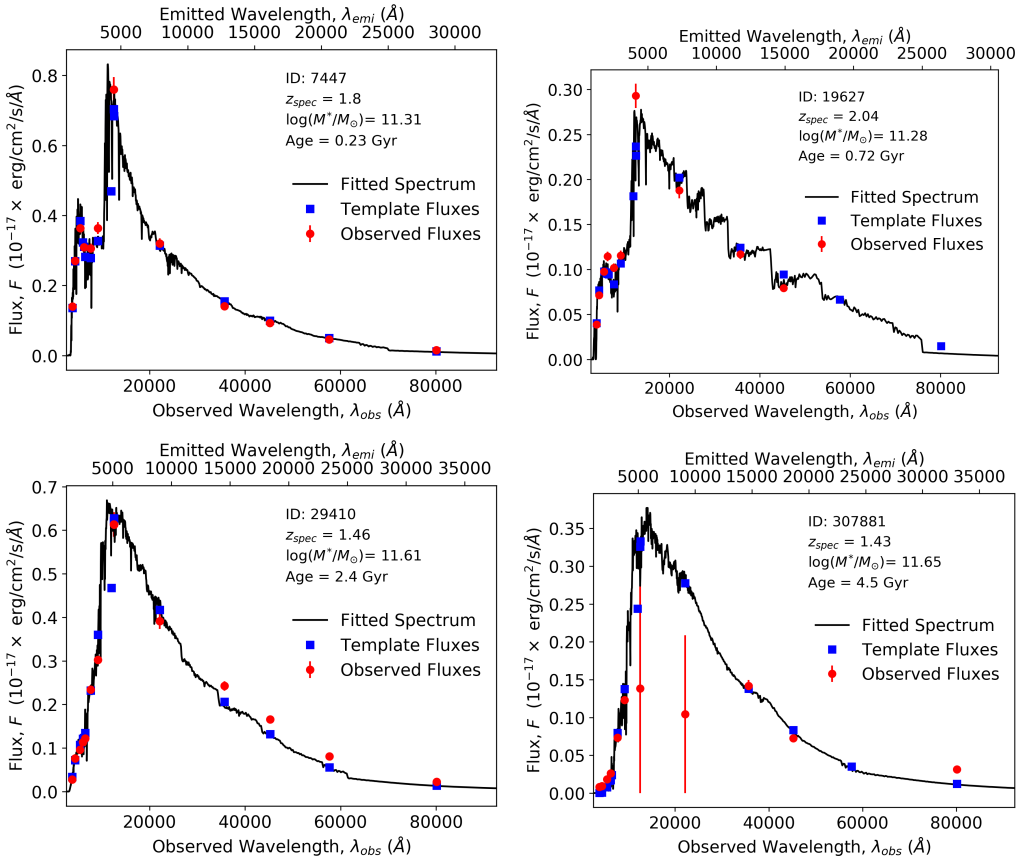

Figure 5.2: The four fitting results for the galaxies with spectroscopic redshifts analysed in Lonoce et al., *sub.* These galaxies have up to 16 distinct bands and all their spectroscopic redshift are above 1.4. The calculated stellar mass and age are annotated on the plots along with z_{spec} and ID numbers.

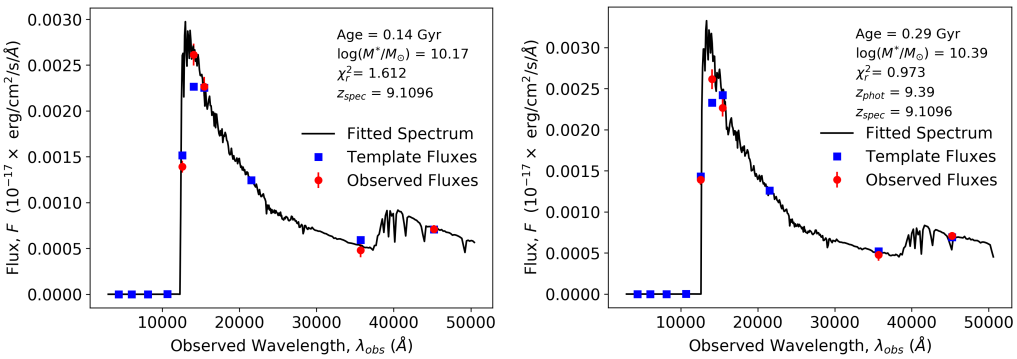

Figure 5.3: The data of the $z_{spec} = 9.11$ Hashimoto et al. 2018 galaxy fitted using HyperZ-spec (left panel) and HyperZ with redshift let free (right panel). This allowed us to calculate the age and stellar mass of the galaxy and also successfully test that we can the photometric procedure can replicate closely spectroscopic measurements even at such high redshifts.

for the two cases (0.15 Gyr) is relatively high given the age of the university at such high redshift ($\sim$ 0.5 Gyr). The two fittings corresponding to both the spectroscopic and the photometric runs are shown in Figure 5.3, on the left-hand and right-hand panels, respectively. The observed flux marker is not plotted for bands with upper limits and the legend is the same as in previous chapters.

Chapter 6

Summary and Conclusions

In this thesis the work of the last 3.5 years related to my PhD has been described. This focused on some of the central open question in extra-galactic astrophysics. We focused on trying to better understand what type of galaxies inhabit the high-redshift universe and how their distribution change over cosmic time. In order to contribute answering these questions, we followed two main branches of work, and in both we aimed to push the limits of what is possible with current telescope technology and existing survey data.

We started by using the large wealth of photometric data offered by the Dark Energy Survey to identify candidates for $z \sim 4$ massive galaxies. This was accomplished starting from a dataset that included several million sources and ultimately identifying 233 strong candidates. Despite this dataset being aimed at cosmological studies, the large statistics and the relatively high depth of the survey allowed us to follow up on the D13 theoretical predictions, claiming that DES would be the first survey to be capable of detecting such massive and high-z galaxies, should they exist. We used real DES data for the first time to produce colour-colour selection maps that helped us prioritise the sources most likely to be the high-z and massive galaxies that we were looking for. We firstly performed extensive cleaning to remove artefacts and sources that were not actually galaxies, such as stars or satellite trails. This way we could fit the initially selected ~ 600 sources using

the photometric redshift code HyperZ and the M05 stellar population models. This fitting procedure allowed us to calculate the photometric redshift and physical properties, including the stellar mass, age, and star formation history for each galaxy. We could also visualise the fittings of each object to better get a sense of the problem at hand. Additional output results, such as the χ^2_r and probability distribution functions, allowed us to perform a series of extra cuts to identify the very best candidates as a sample of 233 galaxies. We look forward to future work where our team or other researchers will be able to verify what fraction of these is really high-z and massive. We began this work with an initial small proposal using the Gemini telescope, which observed 3 of our best candidates. The data is currently under reduction and we hope to have complete results soon.

In a similar way to DES, we made use of data from SERVS to calculate the galaxy stellar mass function up to $z \sim 4.5$ with unprecedented statistics. Our work totalled around 750 thousand galaxies over $\sim$ 5 sq. deg., with a potential of further $\sim$ 13 sq. deg. once the other fields have fully undergone data pre-processing. The management of exponentially larger datasets was only possible by making use of our resident supercomputer. In fact, an important part of the efforts were spent developing the correct pipelines to run HyperZ and calculate the GSMF in a reasonable amount of time. We find results largely consistent with past literature and we manage to push the massive end at high-z to $\sim 10^{12.5}$ solar masses, where we seem to find a wealth of massive galaxies that had remained undetected until today. In terms of the galaxy evolution and formation models, our work does not seem to favour neither hierarchical galaxy formation nor downsizing, but rather a hybrid paradigm. Indeed, we find that massive and little-massive galaxies co-evolve across cosmic time.

In order to be confident of these conclusions on the work done with SERVS data, we tried to find sources to verify our photometric redshifts. We used a sample of over 40 thousand galaxies that was previously utilised by Pforr et al. (2018) for their work. Overall, we found a performance in terms of

σ_{NMAD} and fraction of catastrophic outliers that is worse than what usually seen in the literature, such as in Pforr et al. (2018), i.e. $\sigma_{NMAD} = 0.049$ against $\sigma_{NMAD} = 0.038$. Especially at redshifts higher than 2 the fraction of catastrophic outliers become the majority, but the absolute number of available spectroscopic data is very low and therefore our statistics less certain. It was important to notice that Pforr et al. (2018) managed to remove the worse outliers from their results by selecting sources according to χ^2_r and number of available bands. It was not possible to do the same in our case due to the usage of a new SERVS data release that, while de-blending mostly high-z sources, also optimises photometry extraction from the fainter filters, making the above cuts impossible to implement. We performed several tests to investigate whether a particular class of galaxies is responsible for the majority of the outliers, but we could not find any promising leads. We found that the GSMF calculated from spectroscopic sources points clearly to downsizing, but it is unclear if this is due to selection effects. When we replicated our GSMF work with other SERVS datasets or even DES data with redshifts calculated with a machine learning technique, we could not replicate the spectroscopic results, adding to the uncertainty of what we are finding. Further to this, we also tested using different stellar population models and photometric redshift calculation code (i.e. EAZY), but we reconstructed results similar to our original ones. This suggests that the problems may lie in the newly released SERVS data, and the pipeline should revisit their methodology and further verify the photometry measurements. At the same time, the impossibility of independently verifying the spectroscopic results suggests that the best path forward is to proceed with the publication of the SERVS work, while clearly outlining the limitations that are inherent to the photometric process.

Lastly, we briefly summarised in Chapter 5 some extra work that has been done to support other collaborators by making use of the photometric fitting skills refined so far.

Appendix A

HyperZ

A.1 Introduction

HyperZ is a spectral energy distribution (SED) fitting code aimed at calculating the photometric redshift of galaxies using photometric data as the observational input. It was written in Fortran 77 and first published as part of Bolzonella et al. 2000. These types of codes compare photometric data to stellar population models in order to estimate the redshift of a given galaxy, and potentially other physical properties. This procedure is particularly useful to derive insights from large photometric datasets that due to their size could not have been performed with spectroscopic instruments (because of costs and time limitations). This is particularly common with large cosmological surveys like the Dark Energy Survey, but also those aimed at galaxy evolution studies like SERVS (both surveys being the main datasets used for the work presented in this thesis).

HyperZ uses a simple χ-minimisation technique to find the best-fitted stellar population model (also referred to as template) to any input galaxy photometry instance. The equation governing the fitting procedure is the following:

$$\chi^2(z) = \sum_{i=1}^{N_{filters}} \left(\frac{F_{obs,i} - b \times F_{temp,i}(z)}{\sigma_i} \right), \tag{A.1}$$

where, for a given galaxy, $F_{obs,i}$ is its observed flux (for the ith filter), σ_i is its relative error, $F_{temp,i}$ is the template flux (model flux adjusted by response function of the telescope camera, which varies for each filter), b is a normalisation constant, and $N_{filters}$ is the number of observed filters (or photometric bands) that each object has as input.

The selection of templates is part of the user inputs and throughout our work we predominantly utilised the Maraston 2005 (M05) stellar population models. Lastly, it is interesting to note that unlike other codes like EAZY (see Section 4.6.1), the HyperZ creators decided not to include any priors in the fitting procedure to avoid any unexpected behaviour when dealing with exotic or poorly-understood sources.

A.2 Running Procedure

In order to to run HyperZ successfully a series of files are required. Most importantly, the photometric data is necessary, including errors for each filter utilised. This can be in both flux and apparent magnitude format. Any missing band or band that was too faint to get a photometric measurement can have its photometry and error set to 99.0 or 0.0, respectively. The executable is clearly also crucial and it contains the ready-to-run code and fitting algorithm. The 'parameter file' is the main file to edit to adjust the fitting settings. These are several and they are described in the following section along with details on other supplementary files referenced within the 'parameter file'.

A.2.1 The Parameter File

The 'parameter file' contains a series of instruction to adjust the settings for the HyperZ fittings. The most important and relevant settings that can be tweaked include the redshift range, the redshifts steps, the reddening law selected (we used both the SMC law and the Calzetti law), the minimum and maximum dust absorption values (A_v), the minimum and maximum

absolute magnitude limits (in order to impose any priors on the physicality of the fittings results), and finally an age-check flag to constrain the results to be younger than the age of the Universe at a given redshift. Another crucial element that can be chosen here is the IMF.

Moreover, other minor technical details can be adjusted, such as indicating the format of the input photometric catalogue, the desired format and filename structure of the output files, and the preferred cosmology.

Lastly, the 'parameter file' requires to list the paths to further supplementary files to aid the fitting procedure of HyperZ. These include the paths to the photometric catalogue, the selected stellar population models, the telescope camera filter response functions, and the spectrum of the star Vega for normalisation purposes.

A.3 HyperZ Outputs

At the end of the fitting procedure multiple output files are created.

The '.zphot' file includes the main results, crucially the photometric redshift for each fitted galaxy corresponding to the best-fit model (minimum χ^2). Additionally, it reports the reduced χ^2 value (calculated by HyperZ as the χ^2 divided by the number of fitted filters), the χ^2-related probability, the age of the galaxy, its A_v extinction, the absolute magnitude in one of the bands fitted, and different photometric redshift confidence levels (upper and lower limits for levels 68%, 90%, and 99%). Also importantly, this file contains the reference number of the best-fitted model from which it is possible to obtain the star formation history type and the metallicity.

Other outputs include the template fluxes (as described earlier the best-fit model data points at the wavelengths used by the photometric data filters and adjusted by the telescope camera response function), and the best-fit model data in the same units. Moreover, a '.spe' file for each galaxy is created and it contains the photometric data and relative error in flux format compatible to the template fluxes and best-fit model for easy plotting.

Lastly, each fitted galaxy obtains an associated '.p' that contains the probability distribution function for the given source. This is created by summing all associated probabilities of all used templates. This means that it is possible that the best-fitted result reported in the '.zphot' file is not the most probable. This happens when worse-fitted models have same or very similar redshifts and their probabilities sum together to present a more probable solution. The information from this file can therefore be used for further analysis, as we have done for both our work using DES and SERVS data.

A.4 Calculating the Stellar Mass from HyperZ Outputs

HyperZ does not directly calculate the stellar mass of the fitted galaxies. In order to do this an ancillary script is used (Daddi et al., 2005; Maraston et al., 2006). This code reads in the *.zphot* output file, crucially the information of photometric redshift, age, star formation history, metallicity, and absolute magnitude of one the fitted bands, and compares these values to the templates selected to estimate the stellar mass. This step is very quick and even when using large datasets it rarely requires any parallelisation.

This script requires to edit the running settings by modifying another 'parameter file'. This file contains adjustable parameters to insert, including the type of HyperZ code (i.e. the canonical HyperZ or its 'spec' version, see following section), the number of fitted sources and templates, the types of SEDs, the reddening law, and the chosen cosmology.

It is important to notice that the stellar mass calculation is possible in this case due to the fact that HyperZ calculates the fitting results by extracting these from the best-fit model only. Other photometric redshift codes like EAZY (see again Section 4.6.1) often combine the templates during the fitting process making it impossible to disentangle the stellar mass calculation procedure a posteriori.

A.5 HyperZ-spec

In some cases, codes like HyperZ are not primarily used to calculate the photometric redshift of galaxies, but rather their physical properties. This could be especially if the redshift is already known, generally because calculated from spectroscopic observations and in some cases because calculated with other scripts, such machine learning algorithms.

If the redshift is known, a modified version of HyperZ can be used and it is known as 'HyperZ-spec'.

This is operated in a very similar way as the canonical version of HyperZ. The input and output files as well as the 'parameter file' are almost identical. The main difference lies simply in the catalogue. This one should still contain the photometric data and errors but with an extra column containing the redshift of each galaxy source. The output files obviously do not include the '.p' files that contain the redshift probability distribution function.

The stellar mass can be calculated using the same ancillary script described in Section A.4. The only required change is to indicate the correct HyperZ version used, i.e. HyperZ-spec, in the ancillary script 'parameter file'.

Appendix B

Complete Results from The Dark Energy Survey Project

B.1 Fitting Results for the Best Candidates

Here we provide the stellar population properties and photometric redshift for all best candidate galaxies. As usual, fits are performed for two reddening options: SMC law and Calzetti law.

Table B.1: Properties of the best candidates for the SMC law case, from left to right: object ID, z_{phot}, χ^2_r, stellar mass M^*, absolute magnitude, age, star formation history, metallicity, the number σ's used to estimate potential AGN contamination, photometric redshift found by fitting DES only bands, redshift from the DES pipeline, extinction as $E(B-V)$). Errors refer to the 99% confidence level.

ID	z_{phot}	χ^2_r	$\log_{10}(M^*/M_\odot)$	**Abs. Mag.** (i)	**Age (Gyr)**	**SFH**	**[Z/H] ($Z_\odot$)**	σ_{AGN}	$z_{DESonly}$	z_{BPZ}	**E (B-V)**
100600870	$3.67^{+0.16}_{-0.23}$	1.224	$11.8^{+0.03}_{-0.0}$	-27.02	0.1	$t_{trunc} = 1.0$	1	0.16	3.37	0.38	0.18
102002089	$3.77^{+0.47}_{-0.3}$	2.019	$11.28^{+0.71}_{-0.06}$	-25.63	0.1	$t_{trunc} = 1.0$	2	5.59	3.37	0.51	0.18
102009403	$3.64^{+0.19}_{-0.19}$	1.578	$11.7^{+0.02}_{-0.01}$	-26.69	0.1	$t_{trunc} = 1.0$	2	1.71	4.25	0.35	0.18
102009835	$3.77^{+0.17}_{-0.1}$	1.632	$11.83^{+0.0}_{-0.05}$	-27.01	0.1	$t_{trunc} = 0.1$	2	10.86	2.47	0.47	0.18
102009849	$3.73^{+0.23}_{-0.14}$	1.007	$11.93^{+0.04}_{-0.25}$	-27.24	0.1	$t_{trunc} = 0.1$	2	12.22	3.58	0.47	0.18
102031864	$3.77^{+0.16}_{-0.14}$	1.978	$11.67^{+0.01}_{-0.07}$	-26.6	0.1	$t_{trunc} = 0.1$	2	3.34	2.48	0.5	0.18
132987082	$3.7^{+0.14}_{-0.26}$	1.522	$11.57^{+0.42}_{-0.02}$	-26.54	0.1	CONSTANT	1/2	7.21	2.52	0.37	0.18
133572897	$3.46^{+0.12}_{-0.08}$	1.792	$12.21^{+0.05}_{-0.04}$	-27.52	0.11	$t_{trunc} = 0.1$	2	1.77	3.48	0.49	0.18
136067262	$3.73^{+0.12}_{-0.16}$	2.073	$12.09^{+0.0}_{-0.24}$	-27.66	0.1	$t_{trunc} = 0.1$	2	15.27	2.54	0.4	0.18
137806706	$3.78^{+0.55}_{-0.28}$	0.338	$11.98^{+0.21}_{-0.17}$	-26.6	0.4	$t_{trunc} = 0.3$	1	0.06	3.69	0.49	0.0
164738198	$3.67^{+0.16}_{-0.19}$	2.642	$12.36^{+0.28}_{-0.01}$	-27.76	0.29	$t_{trunc} = 1.0$	2	19.48	2.39	0.49	0.18
287114376	$3.73^{+0.26}_{-0.32}$	1.54	$11.89^{+0.27}_{-0.13}$	-26.76	0.13	$e^{-t/0.1\ \mathrm{Gyr}}$	2	2.52	3.4	0.41	0.18
396223342	$3.69^{+0.11}_{-0.26}$	0.891	$11.59^{+0.04}_{-0.02}$	-26.59	0.1	$t_{trunc} = 1.0$	1/2	4.44	3.34	0.37	0.18
396276124	$3.69^{+0.18}_{-0.26}$	1.022	$11.66^{+0.02}_{-0.23}$	-26.66	0.1	$t_{trunc} = 0.1$	1	2.61	3.45	0.48	0.18
397300605	$3.83^{+0.09}_{-0.3}$	2.084	$11.73^{+0.02}_{-0.0}$	-26.93	0.1	CONSTANT	1/2	7.77	3.25	0.47	0.18
397303505	$3.69^{+0.15}_{-0.32}$	1.604	$11.54^{+0.01}_{-0.27}$	-26.29	0.11	$t_{trunc} = 1.0$	1	4.8	3.4	0.49	0.18
397554368	$3.71^{+0.35}_{-0.28}$	1.366	$12.12^{+0.0}_{-0.44}$	-27.23	0.29	SSP	1/5	3.19	2.5	0.37	0.0
397764328	$3.77^{+0.13}_{-0.27}$	2.321	$11.58^{+0.02}_{-0.04}$	-26.4	0.1	CONSTANT	2	4.27	4.3	0.54	0.18
397885462	$3.8^{+0.2}_{-0.56}$	0.709	$11.78^{+0.4}_{-0.04}$	-26.18	0.18	$t_{trunc} = 0.1$	2	1.74	3.34	0.5	0.0

ID	z_{phot}	χ^2_r	$\log_{10}(M^*/M_\odot)$	Abs. Mag. (i)	Age (Gyr)	SFH	[Z/H] ($Z_\odot$)	σ_{AGN}	$z_{DESonly}$	z_{BPZ}	E (B-V)
398107560	$3.67^{+0.25}_{-0.2}$	1.0	$11.61^{+0.03}_{-0.2}$	-26.46	0.1	$t_{trunc} = 0.1$	2	3.3	3.34	0.45	0.18
399804681	$3.86^{+0.21}_{-0.48}$	1.764	$11.54^{+0.02}_{-0.3}$	-26.28	0.1	$t_{trunc} = 0.1$	2	1.88	2.49	0.5	0.18
399842053	$3.72^{+0.16}_{-0.25}$	0.946	$11.61^{+0.01}_{-0.03}$	-26.48	0.1	CONSTANT	2	5.7	4.28	0.43	0.18
399842613	$4.11^{+0.15}_{-0.48}$	1.443	$11.48^{+0.0}_{-0.38}$	-26.15	0.1	$t_{trunc} = 1.0$	2	0.36	3.31	0.59	0.18
400998781	$3.64^{+0.23}_{-0.17}$	0.863	$11.52^{+0.04}_{-0.08}$	-26.23	0.1	$t_{trunc} = 0.1$	2	2.2	2.53	0.47	0.18
401003476	$3.86^{+0.18}_{-0.41}$	0.666	$12.07^{+0.07}_{-0.71}$	-26.72	1.02	$t_{trunc} = 1.0$	2	1.37	2.48	0.39	0.0
404788215	$3.61^{+0.19}_{-0.2}$	1.098	$11.68^{+0.03}_{-0.02}$	-26.65	0.1	$t_{trunc} = 1.0$	2	4.63	2.51	0.43	0.18
404798117	$3.46^{+0.38}_{-0.13}$	0.929	$12.08^{+0.26}_{-0.13}$	-27.31	0.11	$t_{trunc} = 0.1$	1/5	16.39	3.42	0.48	0.18
404886634	$3.72^{+0.15}_{-0.3}$	1.837	$11.76^{+0.02}_{-0.21}$	-26.92	0.1	$t_{trunc} = 0.1$	1	6.63	3.45	0.47	0.18
404907811	$3.61^{+0.32}_{-0.26}$	1.542	$11.89^{+0.54}_{-0.04}$	-26.86	0.23	$e^{-t/1.0\ \mathrm{Gyr}}$	1/2	6.14	4.22	0.36	0.18
405937444	$3.64^{+0.19}_{-0.2}$	1.272	$11.83^{+0.01}_{-0.02}$	-27.02	0.1	$t_{trunc} = 1.0$	2	11.74	3.42	0.42	0.18
408135057	$3.77^{+0.23}_{-0.17}$	1.411	$11.41^{+0.04}_{-0.07}$	-25.97	0.1	$t_{trunc} = 0.1$	2	0.64	3.5	0.48	0.18
408311797	$3.83^{+0.1}_{-0.19}$	2.208	$11.88^{+0.05}_{-0.01}$	-27.15	0.1	CONSTANT	2	9.19	2.52	0.48	0.18
409127588	$3.77^{+0.21}_{-0.48}$	1.367	$11.85^{+0.41}_{-0.09}$	-26.38	0.11	SSP	2	4.41	3.45	0.52	0.0
411491335	$3.69^{+0.23}_{-0.17}$	1.521	$12.32^{+0.19}_{-0.08}$	-27.84	0.13	$e^{-t/0.1\ \mathrm{Gyr}}$	2	27.57	3.19	0.43	0.18
411500732	$3.73^{+0.31}_{-0.24}$	2.43	$11.4^{+0.41}_{-0.03}$	-25.93	0.1	$t_{trunc} = 1.0$	2	0.7	3.4	0.46	0.18
412637681	$3.61^{+0.19}_{-0.25}$	2.309	$11.42^{+0.4}_{-0.01}$	-26.06	0.1	CONSTANT	1	0.49	2.48	0.46	0.18
414233666	$3.8^{+0.15}_{-0.3}$	2.121	$12.08^{+0.01}_{-0.21}$	-27.71	0.1	$t_{trunc} = 0.1$	1	11.09	3.29	0.46	0.18
414237423	$3.73^{+0.41}_{-0.29}$	1.102	$11.61^{+0.77}_{-0.22}$	-26.45	0.1	$t_{trunc} = 0.1$	2	2.3	3.58	0.43	0.18
417565185	$3.64^{+0.22}_{-0.23}$	1.051	$11.51^{+0.04}_{-0.27}$	-26.22	0.1	$t_{trunc} = 1.0$	2	1.49	2.5	0.39	0.18
431455424	$3.81^{+0.2}_{-0.24}$	1.217	$12.13^{+0.12}_{-0.09}$	-27.04	0.13	SSP	2	14.07	3.67	0.64	0.0
431827017	$3.77^{+0.16}_{-0.16}$	0.764	$11.83^{+0.04}_{-0.28}$	-27.01	0.1	$t_{trunc} = 0.1$	2	9.63	3.34	0.49	0.18
434401854	$3.69^{+0.14}_{-0.29}$	1.31	$12.25^{+0.08}_{-0.06}$	-27.82	0.16	$e^{-t/1.0\ \mathrm{Gyr}}$	1	29.43	3.42	0.44	0.18
444147103	$3.69^{+0.2}_{-0.36}$	1.289	$11.56^{+0.35}_{-0.38}$	-26.41	0.1	$t_{trunc} = 0.1$	1	4.9	3.42	0.46	0.18
470611726	$3.69^{+0.23}_{-0.47}$	1.081	$11.35^{+0.04}_{-0.29}$	-25.8	0.1	$t_{trunc} = 0.1$	2	7.27	2.5	0.5	0.18

ID	z_{phot}	χ^2_r	$\log_{10}(M^*/M_\odot)$	Abs. Mag. (i)	Age (Gyr)	SFH	[Z/H] ($Z_\odot$)	σ_{AGN}	$z_{DESonly}$	z_{BPZ}	E (B-V)
470971747	$4.25^{+0.11}_{-0.89}$	0.739	$12.36^{+0.04}_{-0.85}$	-27.54	0.45	$e^{-t/0.1\ \mathrm{Gyr}}$	2	2.36	2.56	0.28	0.0
471600124	$3.94^{+0.49}_{-0.37}$	0.544	$11.72^{+0.36}_{-0.42}$	-26.17	0.32	$t_{trunc} = 0.3$	2	2.32	3.31	0.49	0.0
471985468	$3.64^{+0.14}_{-0.21}$	2.193	$12.13^{+0.07}_{-0.1}$	-27.32	0.11	$t_{trunc} = 0.1$	2	10.29	2.54	0.54	0.18
473133985	$3.67^{+0.22}_{-0.22}$	2.112	$11.6^{+0.43}_{-0.01}$	-26.52	0.1	$t_{trunc} = 1.0$	1	7.56	3.58	0.38	0.18
473136272	$3.64^{+0.17}_{-0.18}$	1.491	$11.91^{+0.03}_{-0.06}$	-27.16	0.1	$e^{-t/0.3\ \mathrm{Gyr}}$	2	11.56	2.52	0.41	0.18
473140970	$3.69^{+0.11}_{-0.27}$	1.047	$11.74^{+0.03}_{-0.01}$	-26.95	0.1	$t_{trunc} = 1.0$	1/2	9.56	3.34	0.42	0.18
473404298	$4.3^{+0.11}_{-0.14}$	0.554	$12.37^{+0.04}_{-0.2}$	-27.57	0.45	$e^{-t/0.1\ \mathrm{Gyr}}$	2	0.43	3.58	0.47	0.0
473408311	$3.75^{+0.16}_{-0.28}$	1.53	$11.79^{+0.39}_{-0.04}$	-27.08	0.1	$t_{trunc} = 0.1$	1/2	8.66	3.65	0.44	0.18
473411673	$3.69^{+0.22}_{-0.24}$	1.016	$11.54^{+0.02}_{-0.26}$	-26.28	0.1	$t_{trunc} = 1.0$	2	5.69	3.58	0.45	0.18
473496203	$4.3^{+0.08}_{-0.84}$	0.53	$12.25^{+0.37}_{-0.73}$	-26.98	1.28	$e^{-t/1.0\ \mathrm{Gyr}}$	2	0.37	3.05	0.38	0.0
473498930	$3.64^{+0.21}_{-0.18}$	0.992	$11.93^{+0.01}_{-0.01}$	-27.26	0.1	$t_{trunc} = 1.0$	2	20.72	3.42	0.41	0.18
473503196	$3.83^{+0.28}_{-0.18}$	0.835	$11.49^{+0.03}_{-0.26}$	-26.15	0.1	$t_{trunc} = 0.1$	2	3.37	3.5	0.59	0.18
473511031	$3.64^{+0.2}_{-0.16}$	1.643	$11.58^{+0.05}_{-0.07}$	-26.39	0.1	$t_{trunc} = 0.1$	2	1.92	2.44	0.41	0.18
473512115	$3.89^{+0.2}_{-0.34}$	2.122	$12.01^{+0.33}_{-0.37}$	-26.91	0.32	$t_{trunc} = 0.3$	2	3.44	3.58	0.43	0.0
473515263	$3.63^{+0.22}_{-0.2}$	1.616	$11.49^{+0.02}_{-0.01}$	-26.18	0.1	$t_{trunc} = 1.0$	2	2.27	3.4	0.45	0.18
473519025	$3.75^{+0.41}_{-0.35}$	1.318	$11.53^{+0.76}_{-0.36}$	-26.25	0.1	$t_{trunc} = 0.1$	2	0.81	3.4	0.5	0.18
473520285	$3.64^{+0.2}_{-0.21}$	1.199	$11.56^{+0.03}_{-0.02}$	-26.35	0.1	$t_{trunc} = 1.0$	2	3.35	3.42	0.38	0.18
473521671	$3.48^{+0.62}_{-0.13}$	1.08	$11.92^{+0.35}_{-0.16}$	-26.8	0.11	$t_{trunc} = 0.1$	2	2.5	3.45	0.58	0.18
473528868	$3.88^{+0.26}_{-0.48}$	0.686	$11.66^{+0.36}_{-0.12}$	-26.03	0.32	$t_{trunc} = 0.3$	2	1.9	3.59	0.5	0.0
473530252	$3.92^{+0.27}_{-0.31}$	1.431	$12.04^{+0.24}_{-0.36}$	-26.97	0.32	$t_{trunc} = 0.3$	2	0.76	3.5	0.46	0.0
477008049	$4.25^{+0.08}_{-0.17}$	0.681	$12.46^{+0.03}_{-0.22}$	-27.78	0.45	$e^{-t/0.1\ \mathrm{Gyr}}$	2	4.79	3.34	0.51	0.0
477008438	$3.77^{+0.19}_{-0.21}$	2.679	$11.63^{+0.01}_{-0.02}$	-26.52	0.1	$t_{trunc} = 1.0$	2	4.99	3.31	0.45	0.18
480339250	$3.86^{+0.25}_{-0.53}$	1.089	$11.57^{+0.03}_{-0.27}$	-26.37	0.1	$t_{trunc} = 0.1$	2	6.05	3.4	0.55	0.18
480995070	$3.75^{+0.16}_{-0.16}$	1.823	$11.67^{+0.0}_{-0.34}$	-26.62	0.1	$t_{trunc} = 0.1$	2	7.03	2.52	0.43	0.18
481350973	$3.67^{+0.28}_{-0.26}$	0.967	$11.55^{+0.86}_{-0.32}$	-26.48	0.1	$t_{trunc} = 1.0$	1/2	5.37	4.25	0.4	0.18

ID	z_{phot}	χ^2_r	$\log_{10}(M^*/M_\odot)$	Abs. Mag. (i)	Age (Gyr)	SFH	[Z/H] ($Z_\odot$)	σ_{AGN}	$z_{DESonly}$	z_{BPZ}	E (B-V)
482208365	$3.69^{+0.16}_{-0.21}$	1.481	$11.86^{+0.04}_{-0.08}$	-27.03	0.1	$e^{-t/0.3\ \mathrm{Gyr}}$	2	13.71	2.5	0.44	0.18
483918716	$3.64^{+0.45}_{-0.48}$	1.28	$11.65^{+0.47}_{-0.02}$	-26.21	0.16	$e^{-t/0.1\ \mathrm{Gyr}}$	1/2	0.5	3.45	0.43	0.18
489254835	$3.83^{+0.37}_{-0.49}$	1.73	$11.55^{+0.75}_{-0.29}$	-26.31	0.1	$t_{trunc} = 0.1$	2	4.53	3.42	0.48	0.18
490704656	$3.73^{+0.68}_{-0.35}$	1.209	$11.22^{+1.12}_{-0.27}$	-25.49	0.1	$t_{trunc} = 1.0$	2	0.75	3.4	0.51	0.18
494789087	$3.96^{+0.48}_{-0.38}$	1.445	$11.21^{+0.55}_{-0.1}$	-25.38	0.11	$t_{trunc} = 0.1$	2	0.73	2.63	0.4	0.0
494790027	$3.83^{+0.31}_{-0.19}$	1.281	$11.7^{+0.6}_{-0.08}$	-26.22	0.14	$t_{trunc} = 0.1$	2	3.18	2.58	0.52	0.0
494790169	$4.29^{+0.12}_{-0.62}$	0.598	$11.99^{+0.35}_{-0.11}$	-26.76	0.29	$e^{-t/0.1\ \mathrm{Gyr}}$	2	1.53	3.98	0.42	0.0
494792459	$4.11^{+0.36}_{-0.34}$	1.167	$11.16^{+1.68}_{-0.65}$	-25.27	0.11	$t_{trunc} = 0.1$	2	0.36	3.08	0.44	0.0
494793098	$3.98^{+0.29}_{-0.25}$	0.383	$11.87^{+0.25}_{-0.11}$	-26.55	0.32	$t_{trunc} = 0.3$	2	0.33	4.0	0.48	0.0
494800805	$4.25^{+0.1}_{-1.22}$	0.196	$12.29^{+0.26}_{-0.5}$	-27.19	0.81	$e^{-t/0.3\ \mathrm{Gyr}}$	2	0.64	3.15	0.39	0.0
494801634	$3.37^{+0.5}_{-0.3}$	0.437	$12.09^{+0.1}_{-0.01}$	-27.08	0.45	$t_{trunc} = 0.3$	1/5	0.95	3.56	0.35	0.0
495323159	$3.91^{+0.42}_{-0.31}$	1.903	$11.37^{+0.68}_{-0.08}$	-25.66	0.14	$t_{trunc} = 0.1$	1/5	0.54	2.65	0.41	0.0
495342175	$3.64^{+0.2}_{-0.23}$	2.408	$11.46^{+0.38}_{-0.27}$	-26.09	0.1	$t_{trunc} = 1.0$	2	0.81	2.46	0.4	0.18
495566911	$3.12^{+0.21}_{-0.15}$	0.438	$11.81^{+0.03}_{-0.11}$	-26.12	0.16	SSP	2	0.56	4.29	0.54	0.0
497171956	$3.72^{+0.24}_{-0.11}$	1.868	$11.93^{+0.04}_{-0.05}$	-27.26	0.1	$t_{trunc} = 0.1$	2	6.9	3.56	0.44	0.18
501217876	$3.69^{+0.16}_{-0.22}$	1.175	$11.87^{+0.01}_{-0.03}$	-27.11	0.1	CONSTANT	2	14.42	2.5	0.42	0.18
501218097	$3.84^{+0.11}_{-0.29}$	1.961	$11.96^{+0.09}_{-0.35}$	-26.78	0.32	$t_{trunc} = 0.3$	2	5.96	3.61	0.38	0.0
501524910	$3.92^{+0.25}_{-0.46}$	1.41	$12.01^{+0.36}_{-0.12}$	-26.91	0.32	$t_{trunc} = 0.3$	2	4.02	3.53	0.4	0.0
501577492	$3.69^{+0.15}_{-0.14}$	1.59	$12.12^{+0.01}_{-0.07}$	-27.73	0.1	$t_{trunc} = 0.1$	2	34.62	2.5	0.45	0.18
503984762	$3.77^{+0.27}_{-0.28}$	0.479	$11.76^{+0.36}_{-0.1}$	-26.28	0.32	$t_{trunc} = 0.3$	2	0.27	2.54	0.38	0.0
504038042	$3.73^{+0.22}_{-0.12}$	1.172	$11.95^{+0.04}_{-0.06}$	-27.3	0.1	$t_{trunc} = 0.1$	2	10.92	3.29	0.48	0.18
504056183	$3.76^{+0.18}_{-0.53}$	1.519	$11.6^{+0.0}_{-0.32}$	-26.51	0.1	$t_{trunc} = 0.1$	1	5.42	3.27	0.43	0.18
504194446	$3.77^{+0.25}_{-0.09}$	2.009	$11.87^{+0.03}_{-0.05}$	-27.1	0.1	$t_{trunc} = 0.1$	2	9.77	3.4	0.48	0.18
504330828	$3.58^{+0.11}_{-0.21}$	2.148	$11.49^{+0.03}_{-0.03}$	-26.32	0.1	CONSTANT	1/2	4.25	2.45	0.35	0.18
505028285	$3.69^{+0.26}_{-0.13}$	1.048	$11.9^{+0.04}_{-0.06}$	-27.18	0.1	$t_{trunc} = 0.1$	2	17.04	3.56	0.47	0.18

ID	z_{phot}	χ^2_r	$\log_{10}(M^*/M_\odot)$	**Abs. Mag.** (i)	**Age (Gyr)**	**SFH**	**[Z/H] ($Z_\odot$)**	σ_{AGN}	$z_{DESonly}$	z_{BPZ}	**E (B-V)**
506017320	$3.77^{+0.19}_{-0.14}$	0.719	$11.63^{+0.03}_{-0.07}$	-26.5	0.1	$t_{trunc} = 0.1$	2	4.07	3.37	0.49	0.18
506345182	$3.73^{+0.44}_{-0.47}$	1.044	$11.41^{+0.78}_{-0.31}$	-25.97	0.1	$t_{trunc} = 0.1$	2	1.09	3.4	0.53	0.18
506534457	$3.64^{+0.18}_{-0.13}$	1.484	$11.86^{+0.03}_{-0.06}$	-27.08	0.1	$t_{trunc} = 0.1$	2	8.97	2.49	0.4	0.18
506537406	$3.73^{+0.24}_{-0.24}$	1.615	$11.57^{+0.03}_{-0.25}$	-26.35	0.1	$t_{trunc} = 0.1$	2	4.12	2.61	0.5	0.18
507681715	$3.81^{+0.62}_{-0.41}$	1.395	$11.97^{+0.88}_{-0.04}$	-26.65	0.36	$t_{trunc} = 0.3$	1	5.25	2.56	0.41	0.0
507785363	$3.46^{+0.72}_{-0.18}$	0.872	$11.83^{+0.33}_{-0.08}$	-26.56	0.13	$t_{trunc} = 0.1$	1/2	0.67	2.64	0.48	0.18
507791066	$3.62^{+0.17}_{-0.21}$	1.08	$11.92^{+0.16}_{-0.1}$	-27.13	0.11	$e^{-t/0.1\ \mathrm{Gyr}}$	1/2	10.98	4.25	0.47	0.18
507791331	$3.75^{+0.19}_{-0.21}$	1.514	$12.4^{+0.12}_{-0.07}$	-27.95	0.14	$e^{-t/0.1\ \mathrm{Gyr}}$	2	30.31	2.5	0.48	0.18
507810919	$3.69^{+0.15}_{-0.31}$	1.282	$11.66^{+0.01}_{-0.27}$	-26.67	0.1	$t_{trunc} = 0.1$	1	9.6	2.55	0.41	0.18
507820438	$3.64^{+0.19}_{-0.2}$	0.78	$12.05^{+0.04}_{-0.08}$	-27.47	0.11	$e^{-t/1.0\ \mathrm{Gyr}}$	2	18.39	4.28	0.42	0.18
508601732	$4.13^{+0.16}_{-0.15}$	1.847	$11.72^{+0.05}_{-0.07}$	-26.74	0.1	$t_{trunc} = 0.1$	2	5.08	3.53	0.65	0.18
618652137	$3.7^{+0.17}_{-0.24}$	0.918	$11.81^{+0.0}_{-0.27}$	-27.05	0.1	$t_{trunc} = 0.1$	1	4.1	3.5	0.45	0.18
618663972	$3.69^{+0.21}_{-0.2}$	1.575	$12.07^{+0.13}_{-0.03}$	-27.31	0.11	$e^{-t/0.1\ \mathrm{Gyr}}$	2	8.83	3.53	0.52	0.18
618664093	$3.73^{+0.13}_{-0.31}$	1.132	$11.68^{+0.0}_{-0.25}$	-26.81	0.1	$t_{trunc} = 0.1$	1/2	1.29	3.4	0.47	0.18
618664306	$4.33^{+0.08}_{-0.12}$	1.867	$12.48^{+0.23}_{-0.16}$	-27.93	0.36	$e^{-t/0.1\ \mathrm{Gyr}}$	2	1.62	3.25	0.41	0.0

Table B.2: As in Table B.1, but for the Calzetti-type reddening.

ID	z_{phot}	χ^2_r	$\log_{10}(M^*/M_\odot)$	**Abs. Mag.** (i)	**Age (Gyr)**	**SFH**	**[Z/H] ($Z_\odot$)**	σ_{AGN}	$z_{DESonly}$	z_{BPZ}	**E (B-V)**
100669215	$3.87^{+0.39}_{-0.38}$	0.863	$11.74^{+0.25}_{-0.28}$	-26.5	0.1	$t_{trunc} = 0.1$	2	0.04	2.65	0.47	0.25
102002089	$4.22^{+0.12}_{-0.44}$	1.209	$11.65^{+0.04}_{-0.02}$	-26.26	0.1	$t_{trunc} = 0.1$	2	5.59	3.31	0.51	0.25
102009403	$4.05^{+0.13}_{-0.38}$	2.106	$12.07^{+0.02}_{-0.33}$	-27.33	0.1	$t_{trunc} = 0.1$	2	1.71	3.75	0.35	0.25
102031864	$4.01^{+0.28}_{-0.19}$	2.487	$12.31^{+0.4}_{-0.01}$	-27.6	0.1	$t_{trunc} = 1.0$	2	3.34	3.58	0.5	0.37
105765488	$4.1^{+0.24}_{-0.47}$	1.199	$12.19^{+0.44}_{-0.28}$	-27.29	0.1	$t_{trunc} = 0.1$	2	2.41	2.56	0.51	0.37
115286147	$3.96^{+0.31}_{-0.32}$	0.35	$11.63^{+0.15}_{-0.0}$	-26.23	0.1	$t_{trunc} = 1.0$	2	0.66	3.25	0.43	0.25
132987082	$3.98^{+0.22}_{-0.21}$	0.733	$11.96^{+0.08}_{-0.04}$	-27.03	0.1	$t_{trunc} = 0.1$	2	7.21	3.64	0.37	0.25
133076071	$3.56^{+0.75}_{-0.25}$	0.926	$12.23^{+0.6}_{-0.02}$	-26.75	0.1	SSP	2	1.9	3.4	0.49	0.25
133575827	$4.11^{+0.18}_{-0.22}$	1.165	$12.23^{+0.33}_{-0.05}$	-27.4	0.1	$t_{trunc} = 0.1$	2	11.06	3.31	0.5	0.37
133592684	$3.81^{+0.65}_{-0.48}$	0.023	$12.07^{+0.62}_{-0.2}$	-26.65	0.13	$t_{trunc} = 0.1$	2	1.18	3.71	0.51	0.25
133755647	$3.73^{+0.63}_{-0.45}$	0.404	$12.41^{+0.13}_{-0.18}$	-27.14	0.18	$e^{-t/0.1\ \mathrm{Gyr}}$	2	0.38	3.75	0.33	0.37
133779875	$4.13^{+0.2}_{-0.51}$	0.978	$12.11^{+0.33}_{-0.25}$	-27.08	0.1	$t_{trunc} = 0.1$	2	4.32	3.64	0.52	0.37
133785852	$3.69^{+0.57}_{-0.38}$	0.773	$11.77^{+0.47}_{-0.03}$	-26.26	0.1	CONSTANT	2	1.44	2.46	0.46	0.37
134036466	$3.96^{+0.3}_{-0.34}$	0.829	$12.17^{+0.48}_{-0.26}$	-27.24	0.1	$t_{trunc} = 0.1$	2	1.73	3.73	0.51	0.37
134797801	$4.04^{+0.29}_{-0.76}$	1.2	$11.67^{+0.37}_{-0.17}$	-26.33	0.1	$t_{trunc} = 0.1$	2	0.82	3.15	0.48	0.25
135449486	$3.73^{+0.56}_{-0.54}$	0.707	$11.9^{+0.25}_{-0.12}$	-26.57	0.1	$t_{trunc} = 1.0$	2	2.37	3.25	0.4	0.37
135756581	$4.02^{+0.19}_{-0.2}$	0.85	$12.44^{+0.18}_{-0.01}$	-27.93	0.1	$t_{trunc} = 1.0$	2	2.51	3.35	0.53	0.37
135760809	$3.75^{+0.19}_{-0.31}$	0.731	$12.2^{+0.3}_{-0.08}$	-27.32	0.1	$t_{trunc} = 0.1$	2	1.05	3.69	0.45	0.37
135856576	$3.64^{+0.31}_{-0.32}$	1.148	$12.19^{+0.54}_{-0.03}$	-27.31	0.1	$e^{-t/0.3\ \mathrm{Gyr}}$	1	0.4	3.64	0.42	0.37
135857162	$3.86^{+0.32}_{-0.43}$	1.097	$12.0^{+0.09}_{-0.06}$	-26.82	0.1	CONSTANT	2	0.05	3.45	0.39	0.37
136034648	$4.01^{+0.37}_{-0.53}$	0.488	$11.5^{+0.52}_{-0.07}$	-25.88	0.1	$t_{trunc} = 0.1$	2	0.39	3.79	0.42	0.25
137552954	$3.8^{+0.31}_{-0.36}$	1.028	$12.21^{+0.19}_{-0.02}$	-27.36	0.1	CONSTANT	2	1.72	3.4	0.41	0.37
137650861	$3.44^{+0.61}_{-0.08}$	0.733	$12.1^{+0.66}_{-0.04}$	-26.95	0.11	$t_{trunc} = 0.1$	2	1.76	3.4	0.42	0.25
137806706	$3.94^{+0.53}_{-0.43}$	0.234	$12.12^{+0.27}_{-0.3}$	-26.84	0.32	$t_{trunc} = 0.3$	2	0.06	3.94	0.49	0.12

ID	z_{phot}	χ^2_r	$\log_{10}(M^*/M_\odot)$	Abs. Mag. (i)	Age (Gyr)	SFH	[Z/H] ($Z_\odot$)	σ_{AGN}	$z_{DESonly}$	z_{BPZ}	E (B-V)
164738777	$3.69^{+0.53}_{-0.53}$	0.571	$12.22^{+0.15}_{-0.46}$	-26.8	0.23	$e^{-t/0.1\ \mathrm{Gyr}}$	2	1.85	2.38	0.51	0.25
285308599	$3.81^{+0.6}_{-0.52}$	0.176	$11.9^{+0.58}_{-0.01}$	-26.46	0.11	$t_{trunc} = 0.1$	2	0.37	2.58	0.4	0.25
287114376	$4.0^{+0.31}_{-0.27}$	1.173	$12.3^{+0.31}_{-0.01}$	-27.57	0.1	$t_{trunc} = 1.0$	2	2.52	3.33	0.41	0.37
287127591	$3.67^{+0.64}_{-0.42}$	0.138	$11.95^{+0.41}_{-0.09}$	-26.68	0.1	$t_{trunc} = 0.1$	2	1.94	3.73	0.4	0.37
289328303	$4.01^{+0.29}_{-0.39}$	0.6	$12.04^{+0.37}_{-0.1}$	-26.91	0.1	$t_{trunc} = 0.1$	2	0.3	2.52	0.45	0.37
289329064	$4.2^{+0.18}_{-0.45}$	0.744	$12.01^{+0.35}_{-0.23}$	-26.86	0.1	$t_{trunc} = 1.0$	2	2.4	3.69	0.54	0.37
290792079	$3.42^{+0.85}_{-0.2}$	1.864	$12.01^{+0.69}_{-0.14}$	-26.74	0.11	$t_{trunc} = 0.1$	2	2.83	3.42	0.36	0.25
395017226	$3.69^{+0.35}_{-0.33}$	0.435	$12.23^{+0.39}_{-0.07}$	-27.34	0.1	$e^{-t/0.3\ \mathrm{Gyr}}$	2	2.96	3.4	0.41	0.37
395746810	$4.04^{+0.26}_{-0.29}$	0.244	$12.28^{+0.35}_{-0.0}$	-27.54	0.1	$t_{trunc} = 1.0$	2	8.31	3.25	0.45	0.37
396223342	$4.04^{+0.17}_{-0.18}$	0.557	$11.92^{+0.32}_{-0.34}$	-26.95	0.1	$t_{trunc} = 0.3$	2	4.44	3.44	0.37	0.25
396276124	$3.85^{+0.32}_{-0.18}$	0.701	$12.32^{+0.36}_{-0.01}$	-27.63	0.1	$t_{trunc} = 1.0$	2	2.61	3.42	0.48	0.37
396551822	$3.77^{+0.54}_{-0.38}$	0.231	$12.07^{+0.06}_{-0.03}$	-27.01	0.1	$t_{trunc} = 1.0$	2	1.27	3.29	0.47	0.37
397300605	$4.14^{+0.15}_{-0.13}$	1.197	$12.03^{+0.4}_{-0.02}$	-27.23	0.1	$t_{trunc} = 1.0$	2	7.77	3.29	0.47	0.25
397303505	$3.8^{+0.34}_{-0.34}$	1.263	$12.19^{+0.18}_{-0.02}$	-27.29	0.1	CONSTANT	2	4.8	3.4	0.49	0.37
397554368	$3.77^{+0.54}_{-0.33}$	0.717	$12.12^{+0.41}_{-0.05}$	-27.09	0.11	$t_{trunc} = 0.1$	1	3.19	3.61	0.37	0.25
397885462	$4.14^{+0.22}_{-0.67}$	0.569	$12.11^{+0.53}_{-0.18}$	-27.08	0.1	$t_{trunc} = 0.1$	2	1.74	3.29	0.5	0.37
398107560	$3.91^{+0.29}_{-0.21}$	0.699	$12.25^{+0.13}_{-0.04}$	-27.46	0.1	CONSTANT	2	3.3	3.4	0.45	0.37
399842613	$4.25^{+0.15}_{-0.16}$	1.231	$12.22^{+0.45}_{-0.02}$	-27.37	0.1	$t_{trunc} = 0.1$	2	0.36	3.32	0.59	0.37
401003476	$3.86^{+0.42}_{-0.53}$	0.44	$12.0^{+0.19}_{-0.34}$	-26.54	0.16	$e^{-t/0.1\ \mathrm{Gyr}}$	2	1.37	3.4	0.39	0.25
401582291	$3.7^{+0.6}_{-0.46}$	0.259	$11.91^{+0.35}_{-0.04}$	-26.49	0.11	$t_{trunc} = 0.1$	2	2.58	2.46	0.4	0.25
404760121	$3.88^{+0.33}_{-0.28}$	0.224	$11.79^{+0.43}_{-0.3}$	-26.63	0.1	$t_{trunc} = 0.1$	2	4.56	3.61	0.4	0.25
404798494	$3.92^{+0.17}_{-0.1}$	0.823	$12.02^{+0.04}_{-0.05}$	-27.2	0.1	$t_{trunc} = 0.1$	2	7.32	3.34	0.44	0.25
404907811	$3.72^{+0.42}_{-0.32}$	0.664	$12.28^{+0.21}_{-0.02}$	-27.52	0.1	$e^{-t/1.0\ \mathrm{Gyr}}$	2	6.14	3.4	0.36	0.37
405529691	$3.71^{+0.43}_{-0.31}$	0.264	$12.42^{+0.12}_{-0.12}$	-27.72	0.11	$e^{-t/0.3\ \mathrm{Gyr}}$	2	7.91	3.42	0.41	0.37
405537460	$4.2^{+0.18}_{-0.84}$	0.301	$12.07^{+0.52}_{-0.11}$	-26.99	0.1	$t_{trunc} = 0.1$	2	7.74	3.39	0.59	0.37

ID	z_{phot}	χ^2_r	$\log_{10}(M^*/M_\odot)$	Abs. Mag. (i)	Age (Gyr)	SFH	[Z/H] ($Z_\odot$)	σ_{AGN}	$z_{DESonly}$	z_{BPZ}	E (B-V)
405539533	$3.8^{+0.35}_{-0.37}$	0.246	$12.2^{+0.19}_{-0.03}$	-27.33	0.1	$t_{trunc} = 1.0$	2	2.12	3.45	0.46	0.37
405686502	$3.99^{+0.32}_{-0.38}$	0.789	$11.63^{+0.15}_{-0.34}$	-26.22	0.1	$t_{trunc} = 1.0$	2	1.33	3.25	0.41	0.25
405937444	$4.04^{+0.12}_{-0.14}$	1.5	$12.21^{+0.03}_{-0.35}$	-27.67	0.1	$t_{trunc} = 0.1$	2	11.74	3.4	0.42	0.25
406039218	$3.76^{+0.37}_{-0.17}$	1.012	$12.5^{+0.15}_{-0.0}$	-28.09	0.1	$t_{trunc} = 1.0$	2	22.07	3.42	0.39	0.37
406366767	$3.44^{+0.86}_{-0.25}$	0.957	$12.04^{+0.25}_{-0.0}$	-26.82	0.11	$t_{trunc} = 0.1$	2	0.03	3.29	0.43	0.25
407630148	$3.88^{+0.38}_{-0.34}$	0.985	$12.05^{+0.16}_{-0.02}$	-26.95	0.1	CONSTANT	2	2.07	3.37	0.53	0.37
408132796	$3.76^{+0.4}_{-0.33}$	1.048	$12.36^{+0.48}_{-0.09}$	-27.71	0.1	$t_{trunc} = 0.1$	2	4.01	3.34	0.46	0.37
408135057	$4.08^{+0.24}_{-0.24}$	1.633	$12.08^{+0.42}_{-0.02}$	-27.02	0.1	$t_{trunc} = 1.0$	2	0.64	3.75	0.48	0.37
409127588	$4.11^{+0.21}_{-0.63}$	1.095	$12.14^{+0.35}_{-0.23}$	-27.18	0.1	$t_{trunc} = 1.0$	2	4.41	3.48	0.52	0.37
410163990	$4.11^{+0.22}_{-0.49}$	0.959	$12.22^{+0.26}_{-0.23}$	-27.38	0.1	$t_{trunc} = 0.1$	2	0.52	2.51	0.54	0.37
411500732	$4.17^{+0.13}_{-0.28}$	1.938	$11.77^{+0.03}_{-0.31}$	-26.57	0.1	$t_{trunc} = 0.1$	2	0.7	3.37	0.46	0.25
411502452	$3.94^{+0.28}_{-0.42}$	0.828	$11.96^{+0.46}_{-0.32}$	-27.06	0.1	$t_{trunc} = 0.1$	2	2.72	3.4	0.41	0.25
412637681	$3.94^{+0.26}_{-0.47}$	1.938	$11.79^{+0.44}_{-0.29}$	-26.61	0.1	$t_{trunc} = 0.1$	2	0.49	2.48	0.46	0.25
414173316	$3.67^{+0.5}_{-0.2}$	0.421	$11.76^{+0.31}_{-0.0}$	-26.56	0.1	CONSTANT	2	2.24	3.4	0.34	0.25
414235028	$4.04^{+0.29}_{-0.61}$	0.151	$12.08^{+0.46}_{-0.19}$	-27.07	0.16	CONSTANT	2	8.39	3.29	0.35	0.25
414237423	$4.0^{+0.31}_{-0.3}$	0.331	$12.26^{+0.17}_{-0.01}$	-27.48	0.1	$t_{trunc} = 1.0$	2	2.3	3.46	0.43	0.37
414248322	$3.8^{+0.48}_{-0.27}$	0.397	$12.08^{+0.12}_{-0.04}$	-27.06	0.1	$t_{trunc} = 0.3$	1/5	4.73	3.67	0.45	0.37
415246403	$3.79^{+0.37}_{-0.35}$	1.017	$11.98^{+0.35}_{-0.02}$	-26.79	0.1	CONSTANT	2	0.17	2.46	0.49	0.37
417446833	$3.86^{+0.51}_{-0.46}$	0.283	$12.12^{+0.39}_{-0.23}$	-26.77	0.13	$t_{trunc} = 0.1$	2	0.43	3.65	0.57	0.25
417565001	$3.83^{+0.13}_{-0.34}$	2.192	$11.86^{+0.03}_{-0.28}$	-26.8	0.1	$t_{trunc} = 0.1$	2	2.01	2.42	0.37	0.25
417565185	$3.83^{+0.41}_{-0.33}$	0.801	$12.21^{+0.08}_{-0.02}$	-27.35	0.1	CONSTANT	2	1.49	3.77	0.39	0.37
417579802	$3.83^{+0.41}_{-0.48}$	0.281	$12.41^{+0.46}_{-0.04}$	-27.52	0.1	$t_{trunc} = 0.1$	2	6.89	3.5	0.51	0.49
429617726	$3.92^{+0.33}_{-0.26}$	0.289	$12.3^{+0.44}_{-0.29}$	-27.56	0.1	$t_{trunc} = 0.1$	2	5.91	3.34	0.46	0.37
431449768	$3.76^{+0.4}_{-0.37}$	0.636	$12.1^{+0.07}_{-0.03}$	-27.07	0.1	$t_{trunc} = 1.0$	2	3.77	3.4	0.34	0.37
431455424	$3.81^{+0.53}_{-0.24}$	1.217	$12.13^{+0.27}_{-0.09}$	-27.04	0.13	SSP	2	14.07	3.42	0.64	0.0

ID	z_{phot}	χ^2_r	$\log_{10}(M^*/M_\odot)$	Abs. Mag. (i)	Age (Gyr)	SFH	[Z/H] ($Z_\odot$)	σ_{AGN}	$z_{DESonly}$	z_{BPZ}	E (B-V)
444147103	$3.87^{+0.34}_{-0.39}$	0.609	$12.23^{+0.18}_{-0.04}$	-27.39	0.1	$t_{trunc} = 1.0$	2	4.9	3.44	0.46	0.37
444182193	$3.89^{+0.3}_{-0.41}$	0.76	$12.26^{+0.39}_{-0.22}$	-27.47	0.1	$t_{trunc} = 0.1$	2	9.0	3.64	0.43	0.37
446501990	$4.24^{+0.17}_{-0.23}$	0.934	$12.18^{+0.36}_{-0.03}$	-27.27	0.1	$t_{trunc} = 1.0$	2	2.7	3.88	0.5	0.37
465281154	$4.13^{+0.2}_{-0.44}$	0.128	$11.84^{+0.52}_{-0.36}$	-26.75	0.1	$t_{trunc} = 0.1$	2	8.61	3.4	0.39	0.25
470611726	$3.88^{+0.38}_{-0.5}$	0.538	$12.04^{+0.27}_{-0.06}$	-26.93	0.1	$t_{trunc} = 0.1$	2	7.27	3.64	0.5	0.37
470971747	$3.83^{+0.52}_{-0.46}$	0.57	$12.39^{+0.0}_{-0.28}$	-27.22	1.02	$t_{trunc} = 1.0$	1	2.36	2.54	0.28	0.12
471106730	$4.11^{+0.27}_{-0.82}$	0.184	$12.09^{+0.02}_{-0.1}$	-26.62	0.29	$e^{-t/0.3\ \mathrm{Gyr}}$	2	0.54	3.38	0.42	0.25
471394809	$3.88^{+0.42}_{-0.46}$	0.932	$12.22^{+0.0}_{-0.25}$	-26.89	0.32	$e^{-t/0.3\ \mathrm{Gyr}}$	2	4.72	3.81	0.4	0.25
471566339	$3.71^{+0.3}_{-0.27}$	0.576	$11.84^{+0.38}_{-0.04}$	-26.75	0.1	$t_{trunc} = 0.1$	2	5.77	2.46	0.29	0.25
471600124	$4.14^{+0.26}_{-0.51}$	0.213	$11.77^{+0.3}_{-0.28}$	-26.36	0.14	CONSTANT	2	2.32	3.25	0.49	0.25
471612288	$3.92^{+0.33}_{-0.45}$	0.448	$11.63^{+0.39}_{-0.31}$	-26.21	0.1	$t_{trunc} = 0.1$	2	0.92	3.29	0.39	0.25
471703164	$3.83^{+0.43}_{-0.46}$	0.273	$11.54^{+0.26}_{-0.19}$	-26.0	0.1	CONSTANT	2	0.51	3.46	0.36	0.25
473133985	$4.01^{+0.18}_{-0.28}$	0.903	$11.99^{+0.16}_{-0.29}$	-27.11	0.1	$t_{trunc} = 0.1$	2	7.56	3.58	0.38	0.25
473140970	$3.96^{+0.19}_{-0.09}$	0.896	$12.11^{+0.29}_{-0.28}$	-27.43	0.1	$t_{trunc} = 0.1$	2	9.56	3.43	0.42	0.25
473404298	$3.85^{+0.53}_{-0.45}$	0.14	$11.98^{+0.42}_{-0.15}$	-26.76	0.1	$e^{-t/1.0\ \mathrm{Gyr}}$	2	0.43	3.69	0.47	0.37
473408311	$4.08^{+0.14}_{-0.13}$	0.674	$12.15^{+0.26}_{-0.28}$	-27.51	0.1	$t_{trunc} = 0.1$	2	8.66	3.65	0.44	0.25
473411673	$4.1^{+0.15}_{-0.33}$	0.533	$11.91^{+0.26}_{-0.35}$	-26.91	0.1	$t_{trunc} = 0.1$	2	5.69	3.61	0.45	0.25
473496203	$4.16^{+0.22}_{-0.55}$	0.383	$11.41^{+0.51}_{-0.16}$	-26.07	0.1	$t_{trunc} = 0.1$	1	0.37	3.05	0.38	0.12
473498930	$4.05^{+0.13}_{-0.08}$	1.032	$12.31^{+0.03}_{-0.04}$	-27.91	0.1	$t_{trunc} = 0.1$	2	20.72	3.53	0.41	0.25
473503196	$4.13^{+0.23}_{-0.25}$	0.547	$12.15^{+0.43}_{-0.01}$	-27.19	0.1	$t_{trunc} = 1.0$	2	3.37	3.31	0.59	0.37
473511031	$3.86^{+0.34}_{-0.19}$	1.458	$12.21^{+0.36}_{-0.04}$	-27.36	0.1	CONSTANT	2	1.92	2.44	0.41	0.37
473512115	$4.11^{+0.18}_{-0.29}$	1.324	$12.01^{+0.51}_{-0.37}$	-27.16	0.1	$t_{trunc} = 0.1$	2	3.44	3.62	0.43	0.25
473514761	$4.2^{+0.14}_{-0.47}$	1.842	$12.25^{+0.23}_{-0.45}$	-27.03	0.72	$e^{-t/1.0\ \mathrm{Gyr}}$	2	3.02	3.15	0.46	0.12
473515047	$3.81^{+0.41}_{-0.37}$	0.625	$12.35^{+0.03}_{-0.15}$	-27.31	0.26	$e^{-t/0.3\ \mathrm{Gyr}}$	2	3.13	3.4	0.37	0.25
473515263	$4.08^{+0.17}_{-0.16}$	0.998	$11.8^{+0.16}_{-0.01}$	-26.65	0.1	CONSTANT	2	2.27	3.34	0.45	0.25

ID	z_{phot}	χ^2_r	$\log_{10}(M^*/M_\odot)$	Abs. Mag. (i)	Age (Gyr)	SFH	[Z/H] ($Z_\odot$)	σ_{AGN}	$z_{DESonly}$	z_{BPZ}	E (B-V)
473519025	$4.01^{+0.29}_{-0.31}$	0.714	$12.18^{+0.15}_{-0.02}$	-27.27	0.1	$t_{trunc} = 1.0$	2	0.81	3.46	0.5	0.37
473520285	$3.8^{+0.37}_{-0.18}$	1.077	$12.24^{+0.34}_{-0.0}$	-27.44	0.1	CONSTANT	2	3.35	3.4	0.38	0.37
473520601	$4.14^{+0.19}_{-0.38}$	0.503	$12.23^{+0.22}_{-0.1}$	-27.41	0.1	$t_{trunc} = 1.0$	2	2.05	3.55	0.56	0.37
473521671	$4.13^{+0.14}_{-0.18}$	0.866	$12.3^{+0.02}_{-0.03}$	-27.57	0.1	$t_{trunc} = 0.1$	2	2.5	3.45	0.58	0.37
473528868	$4.05^{+0.31}_{-0.57}$	0.208	$11.64^{+0.37}_{-0.31}$	-26.24	0.1	$t_{trunc} = 0.1$	2	1.9	3.63	0.5	0.25
473530252	$4.11^{+0.22}_{-0.26}$	0.371	$12.02^{+0.82}_{-0.3}$	-27.2	0.1	$t_{trunc} = 0.1$	2	0.76	3.75	0.46	0.25
473532585	$4.04^{+0.22}_{-0.31}$	0.523	$11.91^{+0.43}_{-0.35}$	-26.91	0.1	$t_{trunc} = 0.1$	2	0.78	3.33	0.43	0.25
476998818	$3.76^{+0.38}_{-0.37}$	1.496	$12.39^{+0.07}_{-0.27}$	-27.81	0.1	$t_{trunc} = 1.0$	2	8.94	3.46	0.33	0.37
477008049	$3.8^{+0.52}_{-0.58}$	0.339	$12.28^{+0.2}_{-0.13}$	-27.18	0.2	CONSTANT	1	4.79	3.45	0.51	0.37
477008438	$4.2^{+0.08}_{-0.14}$	2.353	$11.92^{+0.03}_{-0.02}$	-26.95	0.1	CONSTANT	2	4.99	3.29	0.45	0.25
479472291	$3.83^{+0.49}_{-0.52}$	0.957	$11.85^{+0.57}_{-0.05}$	-26.44	0.1	$t_{trunc} = 0.1$	2	0.38	2.4	0.56	0.37
479999051	$3.46^{+0.81}_{-0.06}$	0.255	$12.35^{+0.43}_{-0.12}$	-27.57	0.11	$t_{trunc} = 0.1$	2	3.53	3.4	0.36	0.25
480008436	$3.48^{+0.82}_{-0.2}$	0.365	$12.47^{+0.67}_{-0.15}$	-27.89	0.11	$t_{trunc} = 0.1$	2	10.76	3.29	0.41	0.25
480339250	$4.13^{+0.19}_{-0.53}$	0.613	$12.3^{+0.53}_{-0.07}$	-27.57	0.1	$t_{trunc} = 0.1$	2	6.05	3.34	0.55	0.37
481065880	$3.87^{+0.43}_{-0.29}$	1.102	$12.27^{+0.31}_{-0.01}$	-27.51	0.1	$t_{trunc} = 1.0$	2	4.82	2.64	0.5	0.37
481350973	$3.97^{+0.33}_{-0.35}$	0.275	$11.94^{+0.39}_{-0.34}$	-26.98	0.1	$t_{trunc} = 0.1$	2	5.37	3.64	0.4	0.25
481989803	$3.76^{+0.62}_{-0.47}$	0.543	$12.0^{+0.59}_{-0.03}$	-26.71	0.11	$t_{trunc} = 0.1$	2	3.48	3.29	0.43	0.25
481994767	$4.2^{+0.25}_{-0.63}$	0.245	$11.5^{+0.54}_{-0.25}$	-25.89	0.1	$t_{trunc} = 0.1$	2	0.98	3.49	0.51	0.25
482001634	$3.88^{+0.38}_{-0.56}$	1.609	$12.04^{+0.01}_{-0.29}$	-26.44	0.32	$e^{-t/0.3\ \mathrm{Gyr}}$	2	0.04	3.34	0.44	0.25
483918716	$4.11^{+0.25}_{-0.83}$	0.701	$12.45^{+0.06}_{-0.38}$	-27.28	0.64	$e^{-t/1.0\ \mathrm{Gyr}}$	2	0.5	3.37	0.43	0.25
489254835	$4.11^{+0.25}_{-0.39}$	0.866	$12.21^{+0.42}_{-0.11}$	-27.34	0.1	$t_{trunc} = 1.0$	2	4.53	3.75	0.48	0.37
490689649	$4.1^{+0.11}_{-0.33}$	1.02	$12.41^{+0.07}_{-0.1}$	-27.88	0.11	$e^{-t/0.1\ \mathrm{Gyr}}$	2	23.72	3.25	0.42	0.25
490704656	$4.17^{+0.21}_{-0.71}$	0.896	$12.45^{+0.13}_{-0.38}$	-27.31	0.45	$e^{-t/0.3\ \mathrm{Gyr}}$	2	0.75	3.29	0.51	0.25
492431224	$4.17^{+0.19}_{-0.8}$	0.868	$12.22^{+0.74}_{-0.05}$	-27.36	0.1	$t_{trunc} = 0.1$	2	7.22	3.29	0.54	0.37
492605523	$3.77^{+0.33}_{-0.12}$	0.595	$11.8^{+0.36}_{-0.27}$	-26.64	0.1	$t_{trunc} = 0.1$	2	5.57	3.75	0.41	0.25

ID	z_{phot}	χ^2_r	$\log_{10}(M^*/M_\odot)$	**Abs. Mag.** (i)	**Age (Gyr)**	**SFH**	**[Z/H] ($Z_\odot$)**	σ_{AGN}	$z_{DESonly}$	z_{BPZ}	**E (B-V)**
493212188	$4.08^{+0.18}_{-0.37}$	0.799	$11.83^{+0.32}_{-0.34}$	-26.72	0.1	$t_{trunc} = 0.1$	2	3.81	3.5	0.4	0.25
493739755	$4.21^{+0.21}_{-0.45}$	0.94	$12.1^{+0.43}_{-0.24}$	-27.07	0.1	$t_{trunc} = 0.3$	2	4.09	3.15	0.5	0.37
493882026	$3.69^{+0.4}_{-0.46}$	0.421	$11.96^{+0.19}_{-0.14}$	-26.71	0.1	$e^{-t/1.0\ \mathrm{Gyr}}$	2	1.0	2.46	0.44	0.37
494789087	$3.96^{+0.48}_{-0.38}$	1.445	$11.21^{+0.55}_{-0.1}$	-25.38	0.11	$t_{trunc} = 0.1$	2	0.73	2.63	0.4	0.0
494790027	$4.04^{+0.35}_{-0.38}$	1.06	$11.84^{+0.36}_{-0.05}$	-26.62	0.11	$t_{trunc} = 0.1$	2	3.18	2.58	0.52	0.12
494790169	$4.08^{+0.32}_{-0.39}$	0.243	$11.79^{+0.55}_{-0.06}$	-26.66	0.1	CONSTANT	1/5	1.53	3.96	0.42	0.25
494790792	$3.95^{+0.44}_{-0.65}$	0.243	$12.24^{+0.38}_{-0.05}$	-27.49	0.1	$t_{trunc} = 0.1$	1	4.72	3.26	0.5	0.37
494791393	$3.75^{+0.61}_{-0.4}$	0.724	$11.65^{+0.14}_{-0.21}$	-25.82	0.13	SSP	2	0.52	3.4	0.59	0.0
494792459	$4.25^{+0.2}_{-0.42}$	0.761	$11.16^{+1.67}_{-0.63}$	-25.36	0.1	$t_{trunc} = 0.1$	2	0.36	3.15	0.44	0.12
494793098	$4.02^{+0.4}_{-0.32}$	0.179	$11.85^{+0.34}_{-0.1}$	-26.65	0.11	$t_{trunc} = 0.1$	2	0.33	3.81	0.48	0.12
494793167	$4.09^{+0.24}_{-0.47}$	0.229	$11.8^{+0.38}_{-0.35}$	-26.64	0.1	$t_{trunc} = 0.1$	2	2.53	3.75	0.41	0.25
494800805	$4.25^{+0.1}_{-1.22}$	0.196	$12.29^{+0.26}_{-0.5}$	-27.19	0.81	$e^{-t/0.3\ \mathrm{Gyr}}$	2	0.64	3.15	0.39	0.0
494801634	$3.34^{+0.53}_{-0.26}$	0.373	$12.04^{+0.61}_{-0.06}$	-26.95	0.1	SSP	1/2	0.95	3.44	0.35	0.12
495323159	$3.92^{+0.41}_{-0.48}$	1.814	$11.5^{+0.22}_{-0.07}$	-25.9	0.11	$t_{trunc} = 0.1$	1/5	0.54	2.65	0.41	0.12
495325646	$3.74^{+0.58}_{-0.45}$	0.378	$11.85^{+0.25}_{-0.16}$	-26.45	0.1	$t_{trunc} = 1.0$	2	0.18	3.29	0.48	0.37
495342175	$3.75^{+0.29}_{-0.25}$	1.587	$12.2^{+0.38}_{-0.05}$	-27.32	0.1	$t_{trunc} = 0.1$	2	0.81	2.46	0.4	0.37
495508558	$4.25^{+0.11}_{-0.18}$	1.819	$11.86^{+0.4}_{-0.06}$	-26.79	0.1	$t_{trunc} = 0.3$	2	0.02	3.29	0.39	0.25
495566911	$3.12^{+0.21}_{-0.15}$	0.438	$11.81^{+0.03}_{-0.11}$	-26.12	0.16	SSP	2	0.56	4.29	0.54	0.0
496787409	$4.14^{+0.23}_{-0.49}$	0.246	$11.77^{+0.53}_{-0.34}$	-26.58	0.1	$t_{trunc} = 0.1$	2	4.22	3.19	0.45	0.25
497171956	$4.16^{+0.1}_{-0.08}$	0.851	$12.24^{+0.04}_{-0.29}$	-27.75	0.1	$t_{trunc} = 0.1$	2	6.9	3.75	0.44	0.25
497174314	$3.94^{+0.47}_{-0.89}$	0.17	$11.38^{+0.92}_{-0.15}$	-25.58	0.11	$t_{trunc} = 0.1$	1	1.76	2.56	0.59	0.12
498898550	$3.67^{+0.56}_{-0.34}$	0.39	$11.84^{+0.25}_{-0.02}$	-26.42	0.1	$t_{trunc} = 1.0$	2	2.18	2.44	0.41	0.37
499908069	$3.37^{+0.85}_{-0.21}$	0.565	$11.88^{+0.25}_{-0.14}$	-26.41	0.11	$t_{trunc} = 0.1$	2	0.89	3.42	0.41	0.25
499909599	$4.14^{+0.26}_{-0.47}$	0.595	$11.66^{+0.36}_{-0.35}$	-26.29	0.1	$t_{trunc} = 0.1$	2	2.04	3.21	0.43	0.25
500048125	$3.75^{+0.64}_{-0.45}$	0.585	$11.87^{+0.83}_{-0.18}$	-26.37	0.13	SSP	2	2.17	3.25	0.49	0.0

ID	z_{phot}	χ^2_r	$\log_{10}(M^*/M_\odot)$	Abs. Mag. (i)	Age (Gyr)	SFH	[Z/H] ($Z_\odot$)	σ_{AGN}	$z_{DESonly}$	z_{BPZ}	E (B-V)
500110571	$3.99^{+0.26}_{-0.55}$	0.655	$11.82^{+0.36}_{-0.32}$	-26.7	0.1	$t_{trunc} = 0.1$	2	3.83	3.71	0.41	0.25
500571685	$3.38^{+0.88}_{-0.09}$	0.985	$12.18^{+0.08}_{-0.28}$	-27.17	0.11	$t_{trunc} = 0.1$	2	14.94	3.26	0.4	0.25
500910602	$4.22^{+0.15}_{-0.55}$	0.558	$11.63^{+0.6}_{-0.09}$	-26.23	0.1	$t_{trunc} = 0.1$	2	1.08	3.25	0.51	0.25
501218097	$4.11^{+0.22}_{-0.14}$	0.666	$11.89^{+0.43}_{-0.02}$	-26.89	0.1	$t_{trunc} = 1.0$	2	5.96	3.6	0.38	0.25
501511673	$4.2^{+0.13}_{-0.37}$	0.806	$11.73^{+0.04}_{-0.4}$	-26.46	0.1	$t_{trunc} = 0.1$	2	0.23	3.25	0.49	0.25
501524910	$4.13^{+0.2}_{-0.32}$	0.38	$12.01^{+0.42}_{-0.36}$	-27.17	0.1	$t_{trunc} = 0.1$	2	4.02	3.79	0.4	0.25
501665859	$3.91^{+0.37}_{-0.48}$	1.302	$11.68^{+0.42}_{-0.0}$	-26.4	0.1	$t_{trunc} = 0.1$	1/5	2.39	2.65	0.29	0.25
502431214	$3.67^{+0.28}_{-0.29}$	0.805	$12.4^{+0.24}_{-0.01}$	-27.8	0.1	$e^{-t/1.0\ \mathrm{Gyr}}$	2	7.24	3.67	0.42	0.37
502433292	$3.92^{+0.33}_{-0.39}$	1.378	$12.21^{+0.38}_{-0.04}$	-27.35	0.1	$t_{trunc} = 1.0$	2	4.44	3.4	0.45	0.37
502449004	$3.71^{+0.11}_{-0.18}$	2.397	$12.35^{+0.05}_{-0.0}$	-27.69	0.1	CONSTANT	2	5.02	2.46	0.45	0.37
503482151	$3.68^{+0.59}_{-0.32}$	0.318	$11.95^{+0.08}_{-0.0}$	-26.71	0.1	CONSTANT	2	5.9	3.7	0.46	0.37
503811408	$3.88^{+0.28}_{-0.13}$	0.809	$12.47^{+0.22}_{-0.06}$	-28.0	0.1	$t_{trunc} = 0.1$	2	11.55	3.34	0.47	0.37
503973856	$4.03^{+0.29}_{-0.61}$	1.435	$12.45^{+0.77}_{-0.01}$	-27.93	0.1	$t_{trunc} = 0.1$	2	3.56	3.35	0.61	0.37
503973990	$3.73^{+0.38}_{-0.37}$	0.86	$11.66^{+0.41}_{-0.14}$	-26.3	0.1	$t_{trunc} = 0.1$	2	2.25	2.4	0.56	0.25
503984762	$3.81^{+0.3}_{-0.46}$	0.301	$11.73^{+0.05}_{-0.26}$	-26.37	0.11	$t_{trunc} = 0.1$	2	0.27	2.54	0.38	0.12
503985134	$3.85^{+0.4}_{-0.39}$	0.257	$12.01^{+0.12}_{-0.23}$	-26.84	0.1	$t_{trunc} = 0.1$	2	0.82	3.48	0.48	0.37
504051667	$4.0^{+0.24}_{-0.64}$	1.718	$12.18^{+0.54}_{-0.25}$	-27.06	0.26	CONSTANT	2	1.42	3.25	0.39	0.25
504056183	$3.92^{+0.33}_{-0.25}$	0.944	$12.26^{+0.18}_{-0.01}$	-27.48	0.1	$t_{trunc} = 1.0$	2	5.42	3.4	0.43	0.37
504194446	$4.21^{+0.09}_{-0.26}$	1.142	$12.18^{+0.05}_{-0.38}$	-27.59	0.1	$t_{trunc} = 0.1$	2	9.77	3.48	0.48	0.25
504330828	$3.86^{+0.14}_{-0.1}$	1.841	$11.86^{+0.02}_{-0.37}$	-26.8	0.1	$t_{trunc} = 0.1$	2	4.25	2.45	0.35	0.25
504394690	$3.56^{+0.59}_{-0.29}$	1.649	$12.24^{+0.61}_{-0.1}$	-27.31	0.11	$t_{trunc} = 0.1$	2	1.57	3.34	0.37	0.25
504825888	$4.04^{+0.28}_{-0.38}$	0.31	$12.03^{+0.22}_{-0.19}$	-26.89	0.18	$t_{trunc} = 0.3$	2	1.46	3.3	0.37	0.25
505013250	$3.86^{+0.3}_{-0.16}$	1.22	$12.5^{+0.0}_{-0.0}$	-28.07	0.1	$t_{trunc} = 1.0$	2	12.17	3.35	0.46	0.37
505018776	$3.31^{+0.65}_{-0.29}$	0.523	$12.17^{+0.75}_{-0.13}$	-26.68	0.23	$t_{trunc} = 0.1$	1/5	0.29	2.48	0.42	0.25
505028285	$4.13^{+0.11}_{-0.32}$	0.528	$12.22^{+0.36}_{-0.35}$	-27.68	0.1	$t_{trunc} = 0.1$	2	17.04	3.48	0.47	0.25

ID	z_{phot}	χ^2_r	$\log_{10}(M^*/M_\odot)$	Abs. Mag. (i)	Age (Gyr)	SFH	[Z/H] ($Z_\odot$)	σ_{AGN}	$z_{DESonly}$	z_{BPZ}	E (B-V)
506153545	$3.96^{+0.32}_{-0.59}$	1.414	$11.66^{+0.38}_{-0.29}$	-26.29	0.1	$t_{trunc} = 0.1$	2	2.61	3.29	0.38	0.25
506329583	$3.77^{+0.6}_{-0.45}$	0.399	$11.94^{+0.87}_{-0.25}$	-26.72	0.11	$t_{trunc} = 0.1$	1/2	1.72	2.56	0.4	0.25
506345182	$4.02^{+0.29}_{-0.53}$	0.485	$12.07^{+0.39}_{-0.13}$	-27.01	0.1	$t_{trunc} = 1.0$	2	1.09	3.4	0.53	0.37
506383847	$4.17^{+0.3}_{-0.55}$	0.3	$11.45^{+0.76}_{-0.18}$	-25.95	0.1	$t_{trunc} = 0.1$	1/2	4.16	3.12	0.5	0.25
506534457	$3.86^{+0.1}_{-0.15}$	1.624	$12.49^{+0.05}_{-0.01}$	-28.06	0.1	CONSTANT	2	8.97	2.49	0.4	0.37
506537406	$3.98^{+0.35}_{-0.25}$	1.501	$12.22^{+0.05}_{-0.01}$	-27.37	0.1	CONSTANT	2	4.12	2.59	0.5	0.37
506572275	$3.81^{+0.44}_{-0.35}$	0.905	$12.24^{+0.59}_{-0.1}$	-27.42	0.1	$t_{trunc} = 0.1$	2	2.15	3.75	0.49	0.37
506589633	$3.73^{+0.39}_{-0.29}$	0.252	$12.29^{+0.27}_{-0.08}$	-27.53	0.1	$t_{trunc} = 0.1$	2	0.77	2.55	0.43	0.37
506646930	$3.62^{+0.37}_{-0.17}$	0.67	$11.78^{+0.36}_{-0.01}$	-26.62	0.1	$t_{trunc} = 1.0$	2	13.77	3.83	3.5	0.25
506674710	$3.92^{+0.35}_{-0.6}$	0.793	$11.54^{+0.4}_{-0.05}$	-26.0	0.1	$t_{trunc} = 0.1$	2	4.77	3.29	0.45	0.25
506674855	$3.75^{+0.46}_{-0.33}$	0.231	$11.91^{+0.12}_{-0.24}$	-26.43	0.14	$e^{-t/0.1\ \mathrm{Gyr}}$	2	4.12	2.48	0.35	0.25
506674909	$3.53^{+0.22}_{-0.58}$	2.948	$11.96^{+0.04}_{-0.62}$	-26.35	0.81	$e^{-t/0.3\ \mathrm{Gyr}}$	2	4.29	3.31	0.41	0.0
506675198	$3.95^{+0.19}_{-0.1}$	1.455	$12.07^{+0.17}_{-0.05}$	-27.31	0.1	$t_{trunc} = 0.1$	2	13.62	3.3	0.39	0.25
507681715	$3.81^{+0.57}_{-0.37}$	1.116	$11.96^{+0.59}_{-0.04}$	-26.72	0.13	$t_{trunc} = 0.1$	2	5.25	2.56	0.41	0.12
507691551	$3.87^{+0.36}_{-0.43}$	0.75	$11.66^{+0.16}_{-0.05}$	-26.3	0.1	$e^{-t/1.0\ \mathrm{Gyr}}$	2	3.45	3.34	0.38	0.25
507780409	$3.84^{+0.16}_{-0.4}$	0.874	$12.13^{+0.15}_{-0.07}$	-27.07	0.13	$e^{-t/0.1\ \mathrm{Gyr}}$	2	1.67	3.65	0.36	0.25
507785363	$3.88^{+0.58}_{-0.44}$	0.37	$12.1^{+0.57}_{-0.29}$	-26.95	0.11	$t_{trunc} = 0.1$	2	0.67	2.64	0.48	0.25
507791066	$3.75^{+0.41}_{-0.21}$	0.553	$12.42^{+0.22}_{-0.02}$	-27.88	0.1	CONSTANT	2	10.98	3.7	0.47	0.37
507791530	$3.77^{+0.53}_{-0.31}$	0.702	$12.45^{+0.08}_{-0.02}$	-27.62	0.1	$t_{trunc} = 0.3$	2	2.4	2.6	0.54	0.49
507803985	$3.83^{+0.35}_{-0.38}$	0.62	$12.15^{+0.19}_{-0.03}$	-27.21	0.1	CONSTANT	2	1.63	3.5	0.4	0.37
507810919	$3.77^{+0.21}_{-0.21}$	0.563	$12.37^{+0.09}_{-0.04}$	-27.73	0.1	$t_{trunc} = 0.1$	2	9.6	2.55	0.41	0.37
508217521	$3.89^{+0.37}_{-0.73}$	0.38	$11.31^{+0.4}_{-0.18}$	-25.41	0.1	$t_{trunc} = 0.1$	2	1.41	3.4	0.45	0.25
618652137	$3.85^{+0.3}_{-0.18}$	0.711	$12.47^{+0.19}_{-0.0}$	-28.01	0.1	CONSTANT	2	4.1	3.34	0.45	0.37
618654757	$3.94^{+0.35}_{-0.27}$	0.554	$11.65^{+0.16}_{-0.02}$	-26.28	0.1	$t_{trunc} = 1.0$	2	0.64	3.27	0.43	0.25
618660654	$3.77^{+0.38}_{-0.19}$	1.199	$12.12^{+0.19}_{-0.0}$	-27.45	0.1	$t_{trunc} = 1.0$	2	27.05	3.37	0.27	0.25

ID	z_{phot}	χ^2_r	$\log_{10}(M^*/M_\odot)$	**Abs. Mag.** (i)	**Age (Gyr)**	**SFH**	**[Z/H] ($Z_\odot$)**	σ_{AGN}	$z_{DESonly}$	z_{BPZ}	**E (B-V)**
618664093	$4.08^{+0.14}_{-0.42}$	0.811	$12.33^{+0.11}_{-0.02}$	-27.45	0.26	CONSTANT	2	1.29	3.34	0.47	0.25
618664306	$4.09^{+0.25}_{-0.24}$	0.964	$12.06^{+0.25}_{-0.02}$	-27.38	0.1	$t_{trunc} = 0.1$	1	1.62	3.21	0.41	0.25
618667069	$3.75^{+0.2}_{-0.45}$	1.662	$12.46^{+0.1}_{-0.24}$	-27.48	0.14	$e^{-t/0.1\ \mathrm{Gyr}}$	2	0.76	2.42	0.49	0.37
618667272	$3.32^{+0.94}_{-0.05}$	2.294	$12.2^{+0.67}_{-0.03}$	-27.14	0.14	$t_{trunc} = 0.1$	2	0.4	3.29	0.4	0.12

B.2 Photometry of All Candidates

The full DES+VHS photometry, and RA and Dec coordinates (J2000) are provided for all galaxies matching the best candidate criteria.

Table B.3: Photometry for all galaxies matching the best candidate criteria (as in Section 2.4.1).

ID	RA	Dec	g	r	i	z	Y	J	H	K_s
100600870	342.30182	-45.078395	22.6555 ± 0.0389	20.8248 ± 0.0107	20.4152 ± 0.0091	20.0676 ± 0.017	20.0109 ± 0.0434	19.5742 ± 0.1168	///	19.1676 ± 0.1954
100669215	342.03479	-44.585222	23.4434 ± 0.0705	21.6989 ± 0.0216	21.3218 ± 0.0203	21.1502 ± 0.0362	20.8496 ± 0.1093	20.3986 ± 0.2289	///	20.0326 ± 0.2853
102002089	342.83733	-44.098439	24.601 ± 0.1949	22.4569 ± 0.0323	21.8981 ± 0.0313	21.4884 ± 0.0422	21.5888 ± 0.1419	22.069 ± 0.6841	///	20.7842 ± 0.5095
102009403	342.92415	-44.216238	23.0138 ± 0.0534	21.1502 ± 0.0133	20.7563 ± 0.0117	20.3417 ± 0.0217	20.2165 ± 0.0552	20.2064 ± 0.2059	///	19.8197 ± 0.4318
102009835	342.78469	-44.222644	23.2401 ± 0.0574	21.2488 ± 0.0128	20.7316 ± 0.0108	20.3393 ± 0.0172	20.0885 ± 0.0449	19.9653 ± 0.1708	///	19.5771 ± 0.301
102009849	343.07164	-44.222642	22.9057 ± 0.0415	20.9317 ± 0.0096	20.4301 ± 0.0082	20.0647 ± 0.0132	19.9559 ± 0.0384	19.5375 ± 0.1272	///	18.8814 ± 0.1611
102031864	342.67377	-44.586054	23.7029 ± 0.0824	21.6185 ± 0.0158	21.166 ± 0.0131	20.6985 ± 0.0243	20.559 ± 0.069	20.3562 ± 0.1998	///	20.0655 ± 0.3812
105765488	343.14792	-44.73924	24.547 ± 0.186	22.2931 ± 0.0307	21.679 ± 0.0248	21.3457 ± 0.0381	20.9561 ± 0.1048	20.5069 ± 0.2779	///	19.9714 ± 0.3972
115286147	346.7354	-54.15315	23.6712 ± 0.072	21.8732 ± 0.0187	21.5055 ± 0.0216	21.2711 ± 0.0271	21.2205 ± 0.1017	21.0654 ± 0.3385	20.4333 ± 0.3563	20.7988 ± 0.5508
132987082	352.71081	-56.175512	23.1963 ± 0.0604	21.3267 ± 0.0138	20.936 ± 0.0128	20.6552 ± 0.0213	20.4853 ± 0.0558	20.4962 ± 0.3287	20.2877 ± 0.326	19.9255 ± 0.2908
133076071	352.25228	-54.44832	25.4926 ± 0.3086	23.1365 ± 0.0578	22.627 ± 0.0485	22.0704 ± 0.0467	22.0912 ± 0.182	21.7161 ± 0.3706	20.9951 ± 0.3085	///
133572897	352.63464	-55.347821	23.438 ± 0.0723	21.2476 ± 0.0132	20.6824 ± 0.0148	20.2945 ± 0.0123	20.1462 ± 0.0443	19.777 ± 0.1121	19.3033 ± 0.1181	18.9962 ± 0.1502
133575827	352.67649	-55.400238	24.4783 ± 0.198	22.2043 ± 0.0323	21.6132 ± 0.0291	21.1491 ± 0.0318	21.1862 ± 0.1105	20.9814 ± 0.3641	19.8677 ± 0.2136	19.8708 ± 0.2773
133592684	351.76774	-55.706425	25.4775 ± 0.4146	22.9885 ± 0.0455	22.3547 ± 0.054	22.0122 ± 0.066	21.8248 ± 0.1865	21.5672 ± 0.4797	21.0576 ± 0.3478	///
133755647	351.91336	-53.493204	24.4042 ± 0.1861	22.4897 ± 0.039	22.062 ± 0.0436	21.6709 ± 0.0432	21.4716 ± 0.129	21.6099 ± 0.414	20.5935 ± 0.3413	///
133779875	352.71218	-56.397366	24.934 ± 0.265	22.5784 ± 0.0335	21.9448 ± 0.0276	21.5152 ± 0.0376	21.2576 ± 0.0928	21.511 ± 0.4189	20.7446 ± 0.4251	20.2463 ± 0.3848
133785852	352.18188	-56.500569	24.3457 ± 0.1665	22.4928 ± 0.0368	22.2019 ± 0.0372	21.7933 ± 0.0578	21.7324 ± 0.1663	21.8538 ± 0.528	21.3977 ± 0.4754	///
134036466	352.37636	-53.819372	24.223 ± 0.1449	22.1393 ± 0.0323	21.605 ± 0.0203	21.27 ± 0.028	21.0453 ± 0.0917	20.2741 ± 0.2098	20.7209 ± 0.4705	19.8545 ± 0.29
134797801	353.7305	-54.894179	24.0588 ± 0.1346	22.1215 ± 0.0328	21.6522 ± 0.0369	21.4115 ± 0.051	21.437 ± 0.1785	20.5483 ± 0.2525	20.1579 ± 0.2536	20.4186 ± 0.3508
135449486	353.25806	-53.740368	24.0972 ± 0.1317	22.256 ± 0.0245	21.8684 ± 0.025	21.5708 ± 0.037	21.5983 ± 0.1506	20.6018 ± 0.2768	///	20.2794 ± 0.3621
135756581	353.7427	-55.810608	23.3406 ± 0.0691	21.3252 ± 0.023	20.8207 ± 0.0213	20.3921 ± 0.0167	20.3421 ± 0.0519	19.7828 ± 0.2156	19.4258 ± 0.1912	19.1619 ± 0.1735
135760809	353.74692	-55.88496	23.588 ± 0.0759	21.7434 ± 0.025	21.3865 ± 0.0304	20.9549 ± 0.0351	20.8349 ± 0.0815	20.1222 ± 0.2272	20.1289 ± 0.2668	19.4991 ± 0.2475
135856576	353.29081	-55.221638	23.1259 ± 0.0632	21.434 ± 0.018	21.1319 ± 0.0191	20.8609 ± 0.029	20.729 ± 0.0756	19.8682 ± 0.1669	20.0908 ± 0.2622	19.2495 ± 0.1864
135857162	353.45976	-55.233363	24.1318 ± 0.1085	22.1671 ± 0.0264	21.7816 ± 0.0302	21.3856 ± 0.0349	21.3156 ± 0.1054	21.1737 ± 0.4544	20.1333 ± 0.2346	20.3493 ± 0.3292
136034648	353.68277	-54.057979	24.4399 ± 0.123	22.5119 ± 0.0313	22.0482 ± 0.027	21.8656 ± 0.0407	21.7545 ± 0.1699	21.1021 ± 0.258	21.1659 ± 0.4415	21.0203 ± 0.4616
136067262	352.86591	-54.565938	22.4776 ± 0.0329	20.5077 ± 0.0077	20.055 ± 0.0083	19.7252 ± 0.0083	19.4739 ± 0.0236	19.1608 ± 0.0844	18.8353 ± 0.0815	18.5181 ± 0.0889
137552954	354.14324	-53.680157	23.4352 ± 0.0772	21.5577 ± 0.0173	21.2035 ± 0.0199	20.7824 ± 0.0228	20.7397 ± 0.0852	20.0006 ± 0.1948	20.2114 ± 0.36	19.6497 ± 0.3023
137650861	354.24639	-55.389564	23.5837 ± 0.0773	21.779 ± 0.0219	21.4551 ± 0.0323	21.0314 ± 0.0309	21.049 ± 0.0851	20.508 ± 0.2074	20.1826 ± 0.2531	19.5486 ± 0.1901
137806706	354.36219	-54.375504	24.7472 ± 0.2121	22.5005 ± 0.0355	21.8507 ± 0.0285	21.5693 ± 0.0312	21.4401 ± 0.1208	21.9481 ± 0.6971	20.7374 ± 0.3222	19.7515 ± 0.2184
164738198	358.90161	-54.818986	22.4492 ± 0.0527	20.5963 ± 0.0152	20.1956 ± 0.0165	19.776 ± 0.0202	19.3846 ± 0.0736	19.1157 ± 0.1568	19.3069 ± 0.2075	18.3731 ± 0.189
164738777	358.75276	-54.83057	23.8034 ± 0.1519	22.1184 ± 0.0473	21.8647 ± 0.0596	21.4598 ± 0.0756	21.0705 ± 0.2825	21.2516 ± 0.4482	20.556 ± 0.3502	19.8052 ± 0.2597
285308599	14.414781	-48.804004	24.7676 ± 0.2334	22.7232 ± 0.0415	22.2136 ± 0.0395	21.9378 ± 0.073	21.5997 ± 0.178	21.3909 ± 0.3709	21.1189 ± 0.4607	///
287114376	15.20774	-49.788143	23.6629 ± 0.1105	21.6639 ± 0.0206	21.1472 ± 0.0223	20.6945 ± 0.021	20.6482 ± 0.0625	21.0043 ± 0.4252	20.005 ± 0.3234	19.3694 ± 0.2374
287127591	14.834417	-50.057703	24.0709 ± 0.101	22.278 ± 0.0287	21.8705 ± 0.0376	21.5943 ± 0.0422	21.3773 ± 0.1198	20.9281 ± 0.2765	20.8242 ± 0.4541	///
289328303	14.893991	-48.693727	24.7251 ± 0.169	22.5617 ± 0.0361	21.9878 ± 0.0314	21.6397 ± 0.0474	21.367 ± 0.106	20.7427 ± 0.3011	20.8539 ± 0.3599	20.3699 ± 0.439
289329064	15.312428	-48.706967	25.0449 ± 0.2507	22.6631 ± 0.0372	22.0102 ± 0.0359	21.6065 ± 0.0423	21.4101 ± 0.1157	20.875 ± 0.3671	21.2675 ± 0.5009	20.5554 ± 0.3884

ID	RA	Dec	g	r	i	z	Y	J	H	K_s
290792079	16.25137	-49.77414	23.7461 ± 0.0919	21.9562 ± 0.0302	21.6583 ± 0.038	21.1624 ± 0.0467	21.4474 ± 0.189	21.039 ± 0.3194	20.3046 ± 0.3015	///
395017226	74.586265	-58.313936	23.2962 ± 0.0743	21.5345 ± 0.0202	21.1771 ± 0.0232	20.8012 ± 0.0234	20.7718 ± 0.0792	20.3102 ± 0.1374	///	19.4084 ± 0.2242
395746810	74.445041	-44.532828	23.8575 ± 0.1305	21.7522 ± 0.0161	21.198 ± 0.0142	20.8371 ± 0.0216	20.752 ± 0.0812	20.2545 ± 0.2339	///	19.5169 ± 0.2744
396223342	73.654576	-53.700542	23.1074 ± 0.0432	21.3073 ± 0.0138	20.8929 ± 0.0132	20.5505 ± 0.0186	20.5346 ± 0.0786	20.1705 ± 0.299	20.0543 ± 0.3993	19.9464 ± 0.416
396276124	74.967618	-48.454857	23.2672 ± 0.0618	21.3685 ± 0.0149	20.9423 ± 0.0173	20.58 ± 0.0236	20.4901 ± 0.0503	20.1177 ± 0.1443	///	19.5708 ± 0.2546
396551822	75.118785	-56.433087	23.7063 ± 0.0999	21.866 ± 0.029	21.4662 ± 0.0184	21.1487 ± 0.0288	21.0696 ± 0.1015	20.9235 ± 0.3866	///	20.0047 ± 0.3445
397300605	74.061341	-51.962462	23.0718 ± 0.0482	21.1513 ± 0.0107	20.6845 ± 0.0113	20.2851 ± 0.0154	20.281 ± 0.0626	20.3177 ± 0.3422	20.6818 ± 0.6108	19.4903 ± 0.3249
397303505	74.450771	-52.010571	23.4739 ± 0.0603	21.6514 ± 0.0155	21.2691 ± 0.0192	20.7807 ± 0.0235	20.8044 ± 0.0696	20.791 ± 0.3929	20.2137 ± 0.3405	19.739 ± 0.3198
397554368	75.356969	-50.873063	23.7775 ± 0.0869	21.8318 ± 0.0203	21.4502 ± 0.0201	21.1724 ± 0.0298	20.9651 ± 0.097	20.4776 ± 0.2366	21.1366 ± 0.7077	19.2596 ± 0.2286
397764328	74.890797	-52.347374	23.5908 ± 0.0918	21.6711 ± 0.0211	21.2131 ± 0.0219	20.6847 ± 0.0255	20.5936 ± 0.0656	20.8524 ± 0.2944	19.809 ± 0.257	20.0628 ± 0.3292
397885462	73.562242	-59.48389	24.9502 ± 0.2252	22.5626 ± 0.0249	21.9313 ± 0.0258	21.5111 ± 0.0346	21.5167 ± 0.1147	21.4336 ± 0.469	///	20.1094 ± 0.3602
398107560	74.313676	-51.699346	23.5493 ± 0.0617	21.6321 ± 0.014	21.1804 ± 0.0144	20.7587 ± 0.0196	20.6536 ± 0.0679	20.6748 ± 0.27	20.1912 ± 0.3498	19.5987 ± 0.2567
399804681	74.814022	-51.10434	24.2284 ± 0.1626	22.166 ± 0.0331	21.604 ± 0.0277	21.032 ± 0.0389	20.9641 ± 0.1101	///	21.3539 ± 0.8698	19.7706 ± 0.38
399842053	74.771454	-51.68691	23.36 ± 0.0647	21.5027 ± 0.0156	21.0551 ± 0.0165	20.6205 ± 0.0208	20.5097 ± 0.0549	20.2867 ± 0.2367	20.8851 ± 0.7733	19.7016 ± 0.3453
399842613	75.053674	-51.696081	24.9501 ± 0.2206	22.4861 ± 0.029	21.746 ± 0.0226	21.2557 ± 0.0297	21.2596 ± 0.1008	///	20.7158 ± 0.4189	20.3271 ± 0.3888
400998781	75.100601	-45.683346	23.7645 ± 0.0918	21.839 ± 0.0178	21.3687 ± 0.0167	21.0268 ± 0.0233	20.7628 ± 0.0704	20.4275 ± 0.2373	20.5278 ± 0.3386	20.3169 ± 0.5816
401003476	75.35966	-45.76118	23.9154 ± 0.1235	22.0856 ± 0.0308	21.7697 ± 0.0271	21.4402 ± 0.0393	21.3884 ± 0.164	21.2846 ± 0.302	21.2964 ± 0.5372	19.9379 ± 0.3416
401582291	64.467562	-58.898214	24.5483 ± 0.2288	22.5131 ± 0.0473	22.1264 ± 0.0501	21.7576 ± 0.0536	21.5444 ± 0.2075	21.5302 ± 0.4591	///	20.1246 ± 0.2651
404760121	64.736812	-59.604299	23.3602 ± 0.0617	21.5514 ± 0.0183	21.2555 ± 0.0152	20.9841 ± 0.0219	20.8746 ± 0.0889	20.624 ± 0.3042	///	20.0661 ± 0.3319
404788215	65.0661	-60.109331	22.9465 ± 0.0545	21.1413 ± 0.0128	20.7484 ± 0.0107	20.4236 ± 0.012	20.2369 ± 0.0494	20.0363 ± 0.2626	///	19.5802 ± 0.3211
404798117	64.63269	-60.275175	22.7971 ± 0.0477	20.9261 ± 0.0108	20.5082 ± 0.0075	20.134 ± 0.0088	20.0712 ± 0.0445	19.6986 ± 0.2053	///	18.7474 ± 0.1934
404798494	64.735582	-60.281503	22.8486 ± 0.0472	21.0882 ± 0.0127	20.7222 ± 0.0085	20.3916 ± 0.0104	20.3547 ± 0.0532	19.866 ± 0.1715	///	19.65 ± 0.3155
404886634	75.115868	-53.892735	23.0517 ± 0.0705	21.1583 ± 0.015	20.7596 ± 0.0158	20.2935 ± 0.0149	20.2824 ± 0.0602	19.5284 ± 0.1803	19.7741 ± 0.3507	19.1199 ± 0.1798
404907811	74.805477	-54.223115	23.1039 ± 0.0568	21.3026 ± 0.0133	20.9829 ± 0.0146	20.5729 ± 0.0189	20.5462 ± 0.0627	20.219 ± 0.2805	20.2028 ± 0.3399	19.1973 ± 0.2258
405529691	65.117284	-47.215187	22.9859 ± 0.0566	21.2186 ± 0.0135	20.8256 ± 0.0128	20.476 ± 0.0285	20.4139 ± 0.061	19.9611 ± 0.1815	///	19.0709 ± 0.2174
405537460	65.478563	-47.338487	25.2986 ± 0.3594	22.7805 ± 0.0411	22.0764 ± 0.0386	21.6464 ± 0.0506	21.6283 ± 0.1684	21.2757 ± 0.4063	///	20.0457 ± 0.3743
405539533	65.116222	-47.369926	23.4267 ± 0.0564	21.6028 ± 0.0149	21.1819 ± 0.0171	20.8571 ± 0.0257	20.7523 ± 0.0766	20.2255 ± 0.1939	///	19.6028 ± 0.3283
405686502	65.164352	-52.879981	23.7051 ± 0.0819	21.9415 ± 0.0233	21.5463 ± 0.0237	21.2429 ± 0.0309	21.4574 ± 0.1453	///	20.9149 ± 0.6179	20.5062 ± 0.5354
405937444	62.975669	-50.249041	22.6574 ± 0.0422	20.8067 ± 0.0097	20.4151 ± 0.0095	20.0197 ± 0.0116	19.9339 ± 0.0373	19.7463 ± 0.132	19.2522 ± 0.1818	19.134 ± 0.2049
406039218	62.191626	-50.576468	22.6071 ± 0.0332	20.7808 ± 0.0105	20.3524 ± 0.0092	20.0607 ± 0.0132	19.991 ± 0.0418	19.424 ± 0.1381	19.2638 ± 0.1886	18.9398 ± 0.1777
406366767	64.496811	-51.686919	23.7201 ± 0.1058	21.9184 ± 0.0252	21.5077 ± 0.0268	21.1835 ± 0.0334	21.4243 ± 0.1671	///	20.0413 ± 0.2778	19.8268 ± 0.2729
407630148	64.861041	-57.074594	24.0186 ± 0.1351	22.1055 ± 0.0429	21.6619 ± 0.0326	21.2322 ± 0.038	21.2625 ± 0.1413	21.4115 ± 0.552	///	20.2885 ± 0.4175
408132796	75.087803	-58.98511	23.2578 ± 0.0719	21.3597 ± 0.0177	20.952 ± 0.0188	20.5829 ± 0.022	20.5814 ± 0.0786	19.8598 ± 0.1492	///	19.1699 ± 0.221
408135057	75.239132	-59.018159	24.3785 ± 0.1205	22.3252 ± 0.023	21.7784 ± 0.025	21.3381 ± 0.0293	21.1517 ± 0.0868	21.5292 ± 0.4326	///	20.5262 ± 0.4663
408311797	76.370391	-51.127227	22.9456 ± 0.0566	21.0052 ± 0.0147	20.5265 ± 0.012	20.0224 ± 0.0178	19.8377 ± 0.0435	19.7207 ± 0.2125	19.8212 ± 0.3157	19.3971 ± 0.2453
409127588	76.164078	-53.361555	24.6746 ± 0.3113	22.1943 ± 0.0363	21.6538 ± 0.0346	21.1917 ± 0.0454	21.2397 ± 0.1598	21.0225 ± 0.3155	///	20.0819 ± 0.398
410163990	76.409332	-51.657022	24.5772 ± 0.1976	22.2201 ± 0.0338	21.6152 ± 0.0272	21.2317 ± 0.0394	20.9677 ± 0.0847	21.2381 ± 0.6188	20.2781 ± 0.3549	20.0919 ± 0.495
411491335	76.457981	-51.875177	22.439 ± 0.0278	20.5167 ± 0.007	20.0393 ± 0.0058	19.5733 ± 0.0087	19.5696 ± 0.0314	19.1866 ± 0.1195	18.7518 ± 0.1313	18.4397 ± 0.1378
411500732	76.42265	-52.014029	24.104 ± 0.1255	22.0469 ± 0.0223	21.5737 ± 0.021	21.1512 ± 0.0331	21.0509 ± 0.0991	22.7368 ± 1.9292	20.8167 ± 0.5139	20.8872 ± 0.6996

ID	RA	Dec	g	r	i	z	Y	J	H	K_s
411502452	76.547769	-52.041829	23.0166 ± 0.0598	21.2702 ± 0.0143	20.893 ± 0.0146	20.5077 ± 0.0256	20.538 ± 0.0825	20.0929 ± 0.2539	20.1879 ± 0.361	19.6299 ± 0.3589
412637681	77.509814	-55.587338	23.4912 ± 0.0853	21.7185 ± 0.0212	21.3535 ± 0.0247	20.9935 ± 0.0281	20.7794 ± 0.0752	21.2144 ± 0.3166	///	20.3509 ± 0.5627
414173316	77.759211	-54.51745	22.6755 ± 0.0334	21.1531 ± 0.0118	20.9737 ± 0.014	20.7169 ± 0.0233	20.725 ± 0.083	20.7809 ± 0.3979	20.3158 ± 0.3934	20.1399 ± 0.3997
414233666	77.141751	-52.204417	22.4313 ± 0.035	20.4623 ± 0.0082	20.0013 ± 0.0073	19.5652 ± 0.0116	19.5786 ± 0.03	19.0301 ± 0.1276	18.7956 ± 0.1321	18.4607 ± 0.1602
414235028	77.228654	-52.228478	23.1905 ± 0.0504	21.3496 ± 0.0125	20.9219 ± 0.0111	20.6251 ± 0.0199	20.5805 ± 0.0544	20.4523 ± 0.2887	20.1747 ± 0.3567	///
414237423	77.311045	-52.267314	23.7765 ± 0.0811	21.723 ± 0.0165	21.2099 ± 0.0133	20.8681 ± 0.0229	20.7274 ± 0.0637	20.5735 ± 0.2637	20.3744 ± 0.4091	19.5854 ± 0.2725
414248322	77.450892	-52.451427	23.4408 ± 0.0635	21.6418 ± 0.0184	21.2592 ± 0.0181	21.0471 ± 0.0299	20.968 ± 0.0853	20.3269 ± 0.235	20.4217 ± 0.3819	19.7555 ± 0.3024
415246403	76.845921	-57.960174	23.9919 ± 0.1117	22.1305 ± 0.0279	21.7255 ± 0.0302	21.4194 ± 0.0404	21.0415 ± 0.1004	21.0782 ± 0.321	///	20.347 ± 0.3444
417446833	78.683303	-55.542744	25.3732 ± 0.2964	22.9691 ± 0.0373	22.3065 ± 0.0362	21.8995 ± 0.0516	21.6686 ± 0.1419	21.5122 ± 0.5379	///	20.2202 ± 0.4242
417565001	78.514677	-59.118784	23.1326 ± 0.0993	21.292 ± 0.0256	21.1465 ± 0.0298	20.7002 ± 0.0366	20.586 ± 0.0808	20.4386 ± 0.2725	///	19.7768 ± 0.3142
417565185	78.042549	-59.12149	23.503 ± 0.079	21.6217 ± 0.0196	21.2055 ± 0.0206	20.8387 ± 0.0271	20.6695 ± 0.099	20.7859 ± 0.3845	///	19.9382 ± 0.3777
417579802	78.892568	-59.302243	25.0052 ± 0.2943	22.689 ± 0.0433	22.1223 ± 0.0446	21.6426 ± 0.0533	21.5012 ± 0.1415	21.0526 ± 0.2719	///	19.722 ± 0.253
429617726	80.073587	-60.616957	23.7366 ± 0.1092	21.7555 ± 0.0241	21.2501 ± 0.0228	20.8693 ± 0.0338	20.8168 ± 0.1043	20.2875 ± 0.1685	///	19.511 ± 0.2726
431449768	80.455728	-58.88703	23.6336 ± 0.0945	21.786 ± 0.0229	21.4117 ± 0.0223	21.0735 ± 0.0398	21.0377 ± 0.1018	20.4183 ± 0.1879	///	19.975 ± 0.3288
431455424	81.597737	-58.959126	24.6513 ± 0.2397	21.8823 ± 0.0227	21.1749 ± 0.0156	20.7796 ± 0.0256	20.6714 ± 0.0717	20.0864 ± 0.2123	///	19.3482 ± 0.2785
431827017	81.354041	-58.057944	23.2026 ± 0.0476	21.2471 ± 0.011	20.7517 ± 0.0115	20.3163 ± 0.0167	20.152 ± 0.0392	19.8805 ± 0.1737	///	19.1435 ± 0.2499
434401854	82.755855	-59.110482	22.1099 ± 0.0321	20.2853 ± 0.008	19.8901 ± 0.0083	19.4465 ± 0.0112	19.3971 ± 0.029	19.025 ± 0.0832	///	18.2387 ± 0.1132
444147103	85.376884	-58.940568	23.5463 ± 0.0735	21.6129 ± 0.0154	21.192 ± 0.0154	20.818 ± 0.0267	20.775 ± 0.0862	20.1796 ± 0.2493	///	19.7918 ± 0.3938
444182193	85.110945	-59.440915	23.7537 ± 0.0926	21.8281 ± 0.0205	21.3662 ± 0.0227	20.8868 ± 0.0312	20.7948 ± 0.0928	20.6415 ± 0.2817	///	19.5198 ± 0.3014
446501990	85.426451	-59.886883	24.6979 ± 0.188	22.3271 ± 0.0229	21.6196 ± 0.0219	21.2602 ± 0.0285	21.088 ± 0.0768	20.4715 ± 0.2061	///	20.2923 ± 0.4367
465281154	88.694639	-60.880289	23.8226 ± 0.1104	21.8313 ± 0.0213	21.328 ± 0.0163	20.9986 ± 0.0192	20.9853 ± 0.0918	20.7884 ± 0.3129	///	20.0238 ± 0.4269
470611726	68.015452	-57.726539	24.4208 ± 0.1593	22.3445 ± 0.0275	21.8636 ± 0.0288	21.4757 ± 0.0426	21.2412 ± 0.1197	21.3266 ± 0.3366	///	20.1595 ± 0.4922
470971747	68.208929	-46.413716	24.0987 ± 0.1243	22.224 ± 0.0271	21.7986 ± 0.0315	21.5484 ± 0.0447	21.2657 ± 0.1219	21.8636 ± 0.639	20.633 ± 0.2853	///
471106730	67.806799	-48.09239	24.4546 ± 0.1494	22.5018 ± 0.0334	22.012 ± 0.0311	21.6765 ± 0.0431	21.6995 ± 0.1584	21.3476 ± 0.4082	///	20.3634 ± 0.414
471394809	68.225794	-49.845339	23.7923 ± 0.1258	22.0831 ± 0.0333	21.7222 ± 0.0397	21.3568 ± 0.0477	21.2234 ± 0.1538	21.5166 ± 0.3726	21.6085 ± 0.7613	19.8777 ± 0.3553
471566339	67.791747	-55.696441	22.863 ± 0.0353	21.2469 ± 0.0107	20.9837 ± 0.0153	20.8102 ± 0.02	20.5601 ± 0.0619	20.3447 ± 0.2166	///	19.7623 ± 0.3429
471600124	67.869581	-50.51476	24.1376 ± 0.1269	22.1467 ± 0.0252	21.6436 ± 0.0243	21.3571 ± 0.0396	21.4194 ± 0.1494	21.4962 ± 0.5654	20.9746 ± 0.5645	20.2412 ± 0.4441
471612288	68.709632	-50.703145	23.8449 ± 0.0823	22.0712 ± 0.0192	21.7054 ± 0.0212	21.3864 ± 0.0332	21.3935 ± 0.1154	20.763 ± 0.2999	20.8055 ± 0.3421	20.5186 ± 0.4057
471703164	67.76219	-58.42731	23.5709 ± 0.0907	21.937 ± 0.0255	21.6394 ± 0.0294	21.3997 ± 0.0499	21.4529 ± 0.1611	21.0869 ± 0.3356	///	20.9197 ± 0.611
471985468	68.102795	-51.605856	23.9431 ± 0.1032	21.7663 ± 0.0198	21.1723 ± 0.0183	20.6454 ± 0.0214	20.3563 ± 0.0652	20.0749 ± 0.2601	20.1773 ± 0.435	19.3967 ± 0.2487
473133985	68.278612	-59.221893	23.1876 ± 0.0564	21.2676 ± 0.0179	20.918 ± 0.0184	20.5623 ± 0.0208	20.4779 ± 0.0616	20.3628 ± 0.3244	///	19.8854 ± 0.3629
473136272	68.511645	-59.258768	22.6157 ± 0.0438	20.757 ± 0.0124	20.394 ± 0.0159	19.9438 ± 0.0164	19.811 ± 0.0456	19.567 ± 0.179	///	19.0002 ± 0.236
473140970	68.018102	-59.326386	22.7329 ± 0.0328	20.9469 ± 0.0087	20.5496 ± 0.01	20.171 ± 0.0128	20.1362 ± 0.0353	19.9709 ± 0.2354	///	19.3725 ± 0.273
473404298	69.190285	-53.57752	24.2228 ± 0.1205	22.2758 ± 0.0231	21.8083 ± 0.0265	21.5149 ± 0.0354	21.3414 ± 0.1081	21.1183 ± 0.349	20.9943 ± 0.4442	///
473408311	68.154396	-53.640567	22.899 ± 0.0414	20.9924 ± 0.0089	20.5245 ± 0.0097	20.2577 ± 0.0128	20.1052 ± 0.0392	20.1029 ± 0.2052	19.4351 ± 0.2472	19.3967 ± 0.3048
473411673	68.342642	-53.697237	23.5694 ± 0.0761	21.6306 ± 0.0165	21.1501 ± 0.0169	20.8434 ± 0.0221	20.7352 ± 0.0698	20.2406 ± 0.282	20.0624 ± 0.311	20.1277 ± 0.4122
473496203	68.212594	-52.534274	23.1208 ± 0.0483	21.32 ± 0.0153	20.948 ± 0.019	20.8536 ± 0.0234	20.8906 ± 0.103	20.7444 ± 0.28	20.0464 ± 0.3494	20.3174 ± 0.4628
473498930	68.254197	-52.584789	22.4382 ± 0.0244	20.5714 ± 0.0071	20.137 ± 0.0061	19.7813 ± 0.0081	19.7027 ± 0.0285	19.4225 ± 0.1614	19.1099 ± 0.1822	18.9732 ± 0.1685
473503196	68.909139	-52.659906	24.4077 ± 0.1486	22.2416 ± 0.0277	21.6304 ± 0.0284	21.2237 ± 0.0288	21.119 ± 0.1047	20.9983 ± 0.3423	21.0803 ± 0.6356	20.1595 ± 0.3725

ID	RA	Dec	g	r	i	z	Y	J	H	K_s
473511031	68.753934	-52.795529	23.6007 ± 0.0809	21.6237 ± 0.0185	21.257 ± 0.0227	20.8359 ± 0.0276	20.6099 ± 0.1122	20.218 ± 0.2205	20.4341 ± 0.418	19.9327 ± 0.3162
473512115	68.849081	-52.81743	23.3463 ± 0.0571	21.3662 ± 0.0129	20.9137 ± 0.0147	20.6 ± 0.0171	20.4476 ± 0.0603	20.854 ± 0.3506	19.6202 ± 0.273	19.7195 ± 0.3539
473514761	68.69552	-52.864257	23.4876 ± 0.0658	21.6858 ± 0.0173	21.2713 ± 0.0206	20.9585 ± 0.0238	21.2592 ± 0.1275	21.4338 ± 0.6027	20.0219 ± 0.2868	20.1094 ± 0.3443
473515047	68.696452	-52.86959	22.9084 ± 0.0388	21.2686 ± 0.012	20.9422 ± 0.0151	20.6508 ± 0.0177	20.6624 ± 0.0729	19.9769 ± 0.2377	20.3863 ± 0.507	19.3123 ± 0.2227
473515263	68.722423	-52.873137	23.5003 ± 0.0656	21.6486 ± 0.0165	21.2154 ± 0.0192	20.8589 ± 0.0212	20.8558 ± 0.0863	20.8481 ± 0.4468	20.0665 ± 0.2988	20.8256 ± 0.7838
473519025	69.1008	-52.936476	24.0393 ± 0.1012	21.9567 ± 0.0205	21.4533 ± 0.0223	21.0557 ± 0.0245	20.9363 ± 0.0906	21.27 ± 0.5549	20.5077 ± 0.3753	19.7921 ± 0.3149
473520285	69.096087	-52.956492	23.3578 ± 0.069	21.4833 ± 0.0169	21.1118 ± 0.02	20.6784 ± 0.0245	20.6302 ± 0.0854	20.2812 ± 0.2525	20.1506 ± 0.3385	19.8298 ± 0.3216
473520601	68.931326	-52.962545	24.3092 ± 0.177	22.0243 ± 0.0249	21.4266 ± 0.0275	21.0256 ± 0.0279	20.8627 ± 0.1009	20.5927 ± 0.3115	20.1106 ± 0.3451	19.9529 ± 0.4215
473521671	69.128687	-52.981234	24.3187 ± 0.1436	22.0736 ± 0.0243	21.4911 ± 0.0283	20.9878 ± 0.0247	20.8696 ± 0.0906	20.6394 ± 0.3011	20.1737 ± 0.4037	19.8794 ± 0.3939
473528868	68.674413	-53.097801	24.1166 ± 0.1223	22.2099 ± 0.028	21.7669 ± 0.0328	21.4741 ± 0.0407	21.3384 ± 0.1279	21.5962 ± 0.6845	21.1738 ± 0.5239	20.4126 ± 0.4157
473530252	68.665468	-53.118678	23.326 ± 0.0575	21.3349 ± 0.0126	20.8245 ± 0.0183	20.5805 ± 0.0171	20.5111 ± 0.0568	20.0143 ± 0.1948	19.8325 ± 0.2459	19.5137 ± 0.2643
473532585	68.669534	-53.155561	23.4498 ± 0.0613	21.5327 ± 0.0145	21.1079 ± 0.0173	20.79 ± 0.0206	20.7767 ± 0.072	20.4669 ± 0.3203	19.8571 ± 0.2716	19.9781 ± 0.4112
476998818	80.775198	-56.96095	22.9227 ± 0.0728	21.0226 ± 0.0221	20.6496 ± 0.0176	20.3897 ± 0.0232	20.3291 ± 0.1019	19.5362 ± 0.1445	///	19.0818 ± 0.2283
477008049	80.723353	-57.106877	23.8122 ± 0.0925	21.9787 ± 0.0233	21.5891 ± 0.0195	21.2365 ± 0.0342	21.2065 ± 0.1147	21.1477 ± 0.4207	///	19.56 ± 0.2348
477008438	81.047966	-57.113178	23.4808 ± 0.0706	21.5231 ± 0.016	21.0241 ± 0.0144	20.5601 ± 0.0207	20.5961 ± 0.0637	20.4656 ± 0.2417	///	20.9803 ± 1.057
479472291	72.171121	-45.288854	24.7652 ± 0.2445	22.7269 ± 0.0468	22.3355 ± 0.0494	21.8283 ± 0.0716	21.6033 ± 0.2091	21.7642 ± 0.4696	21.3982 ± 0.5541	///
479999051	72.528332	-52.87657	23.0289 ± 0.0458	21.1696 ± 0.0115	20.8216 ± 0.0123	20.464 ± 0.0166	20.4292 ± 0.0546	20.0697 ± 0.2392	19.643 ± 0.2247	///
480008436	72.410619	-53.037279	22.7515 ± 0.0367	20.9045 ± 0.0097	20.5081 ± 0.0099	20.1442 ± 0.0134	20.1127 ± 0.0436	19.7786 ± 0.2444	19.1614 ± 0.1861	///
480339250	72.299325	-53.204044	24.2994 ± 0.1888	22.0722 ± 0.0321	21.4702 ± 0.0296	20.9923 ± 0.0313	20.999 ± 0.1264	20.3812 ± 0.2839	20.3993 ± 0.2756	///
480995070	73.093464	-60.584365	23.6004 ± 0.0912	21.6301 ± 0.0165	21.1455 ± 0.0187	20.7126 ± 0.0206	20.4067 ± 0.0573	20.2847 ± 0.1411	///	19.7413 ± 0.379
481065880	72.101555	-48.944222	23.4708 ± 0.0812	21.4922 ± 0.0152	20.9918 ± 0.0149	20.8064 ± 0.0195	20.5594 ± 0.0635	20.2096 ± 0.1334	///	19.4956 ± 0.1879
481350973	72.813908	-47.600626	23.1958 ± 0.0612	21.3706 ± 0.0158	20.9589 ± 0.0182	20.6744 ± 0.0213	20.5618 ± 0.0759	20.5647 ± 0.3233	///	19.9526 ± 0.5323
481989803	72.120899	-45.61534	24.4427 ± 0.1475	22.4001 ± 0.0324	21.9192 ± 0.0285	21.5902 ± 0.0425	21.6684 ± 0.1651	20.8491 ± 0.2714	20.8164 ± 0.3249	///
481994767	71.896784	-45.687727	24.8643 ± 0.2282	22.7831 ± 0.0452	22.2127 ± 0.0404	21.9062 ± 0.0618	21.8439 ± 0.2125	21.8744 ± 0.5399	22.007 ± 0.7345	///
482001634	72.307954	-45.794599	24.2255 ± 0.1234	22.5135 ± 0.0314	22.1931 ± 0.0315	21.7569 ± 0.0548	22.0476 ± 0.2355	21.3845 ± 0.3144	21.9101 ± 0.6719	///
482208365	73.320644	-51.189418	22.8554 ± 0.0359	20.9531 ± 0.0099	20.5427 ± 0.0095	20.1552 ± 0.014	20.0031 ± 0.0415	19.931 ± 0.2528	19.1732 ± 0.209	19.2358 ± 0.2245
483918716	72.085462	-48.777383	24.1798 ± 0.1091	22.2827 ± 0.0232	21.8386 ± 0.0258	21.435 ± 0.0344	21.4798 ± 0.1145	21.4635 ± 0.3782	///	19.9161 ± 0.3324
489254835	69.13225	-55.548991	24.316 ± 0.1564	22.0218 ± 0.0194	21.4483 ± 0.0165	21.0965 ± 0.0303	20.9006 ± 0.0864	20.7104 ± 0.2035	///	20.0555 ± 0.3584
490689649	69.699465	-50.470457	22.724 ± 0.0556	20.7901 ± 0.0101	20.3348 ± 0.0047	20.0119 ± 0.0048	19.9312 ± 0.0311	19.5759 ± 0.1132	19.2226 ± 0.1444	18.8934 ± 0.1221
490704656	69.206037	-50.70402	24.5856 ± 0.2029	22.52 ± 0.0384	22.0135 ± 0.0387	21.5827 ± 0.0518	21.7259 ± 0.2148	21.752 ± 0.5469	21.1371 ± 0.3792	///
492431224	72.971578	-53.024726	24.6768 ± 0.2208	22.3423 ± 0.0348	21.7108 ± 0.0311	21.2272 ± 0.0405	21.3848 ± 0.1612	20.7611 ± 0.382	20.2978 ± 0.2511	///
492605523	69.282253	-53.006647	23.105 ± 0.0616	21.4524 ± 0.0268	21.1915 ± 0.0238	20.8579 ± 0.0313	20.7097 ± 0.098	20.472 ± 0.3439	20.775 ± 0.4058	19.9658 ± 0.326
493212188	73.272104	-47.599847	23.6873 ± 0.0792	21.7956 ± 0.0184	21.3344 ± 0.0192	20.9807 ± 0.0258	20.8355 ± 0.1045	20.6709 ± 0.4332	///	20.5957 ± 0.685
493739755	70.668823	-48.194975	24.8323 ± 0.2236	22.4769 ± 0.0337	21.7691 ± 0.0326	21.4422 ± 0.0406	21.3932 ± 0.1217	20.491 ± 0.2117	///	20.4062 ± 0.5695
493882026	73.756147	-47.923077	23.8901 ± 0.1064	22.0808 ± 0.024	21.7685 ± 0.0306	21.4226 ± 0.0387	21.246 ± 0.1024	20.6618 ± 0.3157	///	19.9958 ± 0.4409
494789087	69.898546	-46.782506	23.8557 ± 0.1356	21.9308 ± 0.0361	21.5423 ± 0.0289	21.5443 ± 0.0481	21.1287 ± 0.1132	22.0732 ± 0.8393	///	21.0469 ± 0.8443
494790027	70.402136	-46.796962	24.138 ± 0.1352	21.864 ± 0.0236	21.3387 ± 0.02	21.1324 ± 0.0258	20.8994 ± 0.0731	20.6496 ± 0.3046	///	20.2624 ± 0.3745
494790169	70.575727	-46.798513	23.2371 ± 0.0465	21.3858 ± 0.0118	20.941 ± 0.0128	20.8265 ± 0.0172	20.7429 ± 0.0526	20.5034 ± 0.1831	///	20.0217 ± 0.4448
494790792	70.118141	-46.809179	23.7461 ± 0.0968	21.758 ± 0.026	21.2542 ± 0.0242	20.9573 ± 0.0278	20.8978 ± 0.0929	20.3048 ± 0.2452	///	19.3178 ± 0.2806

ID	RA	Dec	g	r	i	z	Y	J	H	K_s
494791393	70.545803	-46.818298	25.8019 ± 0.5094	22.9725 ± 0.0505	22.3344 ± 0.0364	21.9215 ± 0.0508	22.0782 ± 0.2109	21.7367 ± 0.5105	///	20.8025 ± 0.6156
494792459	70.361105	-46.834652	24.2656 ± 0.1335	22.2795 ± 0.0298	21.7942 ± 0.0307	21.6362 ± 0.0434	21.7176 ± 0.1596	20.8556 ± 0.2748	///	22.1288 ± 1.8666
494793098	70.361899	-46.84422	23.9821 ± 0.1053	21.8222 ± 0.0204	21.2755 ± 0.0197	21.0539 ± 0.0263	20.9669 ± 0.0823	20.8774 ± 0.2682	///	20.2478 ± 0.5222
494793167	70.322957	-46.845463	23.8321 ± 0.0829	21.8795 ± 0.0192	21.387 ± 0.0206	21.1299 ± 0.0252	20.9922 ± 0.0774	20.6869 ± 0.2351	///	20.3403 ± 0.5394
494800805	70.223709	-46.969603	23.3453 ± 0.0791	21.6088 ± 0.0224	21.2646 ± 0.0233	21.1833 ± 0.0371	21.3461 ± 0.1833	20.9634 ± 0.4222	///	19.9742 ± 0.3398
494801634	70.204006	-46.984426	23.108 ± 0.0641	21.3465 ± 0.018	21.1355 ± 0.0166	20.9708 ± 0.0236	20.926 ± 0.0767	20.3121 ± 0.2086	///	19.2022 ± 0.2093
495323159	65.394135	-46.057881	23.4555 ± 0.0678	21.7668 ± 0.0197	21.4263 ± 0.0244	21.433 ± 0.0555	21.0016 ± 0.0969	20.7891 ± 0.3456	21.5235 ± 0.9513	20.8319 ± 0.6251
495325646	65.413155	-46.101938	24.1823 ± 0.1228	22.4046 ± 0.038	22.001 ± 0.0336	21.6707 ± 0.0519	21.7598 ± 0.2104	///	21.7652 ± 1.3242	20.4605 ± 0.5438
495342175	65.087082	-46.3792	23.6315 ± 0.0661	21.7161 ± 0.017	21.3624 ± 0.0171	21.0386 ± 0.0259	20.6991 ± 0.0633	20.9568 ± 0.4498	20.768 ± 0.6159	19.9356 ± 0.4688
495508558	64.591881	-57.810162	24.0085 ± 0.1786	21.734 ± 0.0197	21.1739 ± 0.0263	20.8205 ± 0.0317	21.0451 ± 0.1696	20.2084 ± 0.1872	///	20.4662 ± 0.4553
495566911	70.276529	-48.286447	24.379 ± 0.1996	22.23 ± 0.0356	21.6714 ± 0.0325	21.6571 ± 0.0625	21.791 ± 0.2094	20.9532 ± 0.3595	///	19.9958 ± 0.3845
496787409	63.374087	-59.79275	24.0008 ± 0.1195	22.0032 ± 0.0246	21.4945 ± 0.0205	21.1897 ± 0.033	21.2715 ± 0.1553	20.727 ± 0.2958	///	20.0388 ± 0.3226
497171956	65.710748	-58.418902	22.884 ± 0.0491	20.8448 ± 0.0097	20.3696 ± 0.0094	20.0618 ± 0.0114	19.9096 ± 0.0327	19.6361 ± 0.1176	///	18.9846 ± 0.1623
497174314	64.973407	-58.457378	24.4577 ± 0.1761	22.5676 ± 0.0456	22.1586 ± 0.0487	21.9922 ± 0.0904	21.7573 ± 0.2387	22.3304 ± 0.8953	///	20.7245 ± 0.5142
498898550	65.712873	-59.065758	24.0901 ± 0.1197	22.2997 ± 0.0353	21.9947 ± 0.0433	21.6648 ± 0.0426	21.4354 ± 0.136	21.5185 ± 0.5076	///	20.4729 ± 0.408
499908069	65.468426	-47.534492	23.8878 ± 0.0981	22.1885 ± 0.0242	21.9058 ± 0.0318	21.5545 ± 0.0485	21.6761 ± 0.1802	21.0946 ± 0.2938	///	20.1886 ± 0.3185
499909599	65.492297	-47.55904	24.3098 ± 0.1254	22.2842 ± 0.0236	21.7533 ± 0.0253	21.4982 ± 0.0397	21.6327 ± 0.1549	20.8654 ± 0.2354	///	20.4361 ± 0.4379
500048125	66.429253	-56.267392	24.9981 ± 0.311	22.4494 ± 0.026	21.7672 ± 0.0244	21.3979 ± 0.0352	21.466 ± 0.1457	20.7618 ± 0.3188	///	19.8518 ± 0.3352
500110571	70.92143	-58.350365	23.5309 ± 0.0876	21.6786 ± 0.0192	21.2638 ± 0.0178	20.9827 ± 0.0324	20.7802 ± 0.0892	20.4678 ± 0.2583	///	20.3056 ± 0.5442
500571685	65.734516	-47.379303	23.1512 ± 0.0701	21.4725 ± 0.018	21.1271 ± 0.0229	20.7555 ± 0.0351	20.9316 ± 0.1251	20.5235 ± 0.2618	///	19.4581 ± 0.2056
500910602	71.460323	-46.202889	24.5877 ± 0.1886	22.4886 ± 0.0312	21.914 ± 0.0343	21.5586 ± 0.0428	21.6458 ± 0.1791	21.7584 ± 0.4942	20.7106 ± 0.3438	20.6049 ± 0.5369
501217876	66.041527	-52.819775	22.6725 ± 0.0419	20.8092 ± 0.0101	20.3847 ± 0.0101	19.9921 ± 0.0153	19.8369 ± 0.0438	20.0441 ± 0.3983	19.1979 ± 0.2433	19.0833 ± 0.2217
501218097	65.762156	-52.821932	23.3563 ± 0.0535	21.4202 ± 0.0166	20.969 ± 0.0122	20.7017 ± 0.0207	20.5805 ± 0.0659	///	20.7299 ± 0.4663	20.3083 ± 0.5642
501511673	67.243745	-60.378716	24.3018 ± 0.1113	22.2241 ± 0.0241	21.6714 ± 0.0206	21.2992 ± 0.0242	21.3162 ± 0.1111	20.6496 ± 0.2486	///	20.9327 ± 0.8991
501524910	66.697138	-60.5957	23.3954 ± 0.0716	21.3984 ± 0.0152	20.8981 ± 0.0123	20.6364 ± 0.0167	20.5033 ± 0.0732	19.9998 ± 0.2457	///	19.5555 ± 0.2512
501577492	65.529485	-57.087743	22.2891 ± 0.0412	20.4103 ± 0.0083	19.9915 ± 0.0091	19.5186 ± 0.0116	19.3548 ± 0.0362	19.0141 ± 0.0798	///	18.6395 ± 0.1814
501665859	71.672277	-47.591956	23.1878 ± 0.0515	21.4964 ± 0.0157	21.1655 ± 0.0188	21.1146 ± 0.0246	20.8241 ± 0.0756	20.7005 ± 0.2542	///	20.1931 ± 0.3165
502431214	65.942299	-46.553076	22.7071 ± 0.0379	20.9606 ± 0.0099	20.6372 ± 0.0112	20.2516 ± 0.0176	20.1892 ± 0.0442	19.9818 ± 0.1994	19.2778 ± 0.1497	19.0157 ± 0.1745
502433292	66.409402	-46.568465	23.6993 ± 0.0929	21.727 ± 0.0198	21.2826 ± 0.0206	20.8858 ± 0.0303	20.9898 ± 0.115	20.1812 ± 0.2583	19.8842 ± 0.263	19.974 ± 0.3567
502449004	65.844648	-46.707587	22.8891 ± 0.0412	21.0685 ± 0.0131	20.7778 ± 0.0151	20.474 ± 0.0207	20.146 ± 0.0553	19.8829 ± 0.12	///	19.5314 ± 0.3161
503482151	66.649327	-58.546895	23.8134 ± 0.1008	22.062 ± 0.0256	21.6794 ± 0.0291	21.3887 ± 0.0404	21.189 ± 0.1058	21.1799 ± 0.2995	///	20.2835 ± 0.3403
503811408	70.787127	-52.978216	23.2053 ± 0.0594	21.28 ± 0.0135	20.8055 ± 0.0143	20.3545 ± 0.0178	20.2962 ± 0.055	20.1231 ± 0.2981	19.3309 ± 0.218	19.1173 ± 0.2316
503973856	71.227329	-44.778327	23.6823 ± 0.1294	21.5272 ± 0.0331	20.9504 ± 0.0298	20.6236 ± 0.0319	20.6429 ± 0.1169	19.6565 ± 0.1644	///	18.9792 ± 0.2099
503973990	71.217655	-44.780499	23.3519 ± 0.0959	21.6747 ± 0.0375	21.5158 ± 0.0491	21.1546 ± 0.0515	21.0994 ± 0.1777	21.2706 ± 0.4969	///	20.2714 ± 0.3984
503984762	71.018342	-44.948031	23.7379 ± 0.0742	21.7577 ± 0.0188	21.4376 ± 0.0183	21.2233 ± 0.0361	21.0102 ± 0.0878	20.9198 ± 0.3497	///	19.8396 ± 0.354
503985134	71.013934	-44.953898	24.331 ± 0.1115	22.389 ± 0.023	21.9089 ± 0.023	21.5687 ± 0.041	21.4623 ± 0.127	20.7513 ± 0.2782	///	20.2006 ± 0.3825
504038042	71.39045	-52.049047	22.8125 ± 0.0375	20.8787 ± 0.0102	20.4005 ± 0.0098	19.9239 ± 0.012	19.8667 ± 0.0352	19.8114 ± 0.2304	19.2146 ± 0.1916	18.9377 ± 0.1799
504051667	72.349051	-52.272785	23.322 ± 0.0564	21.5095 ± 0.0165	21.0965 ± 0.0145	20.8096 ± 0.0196	20.8302 ± 0.064	19.9785 ± 0.2024	19.7234 ± 0.2235	19.7586 ± 0.2747
504056183	71.339025	-52.34761	23.5642 ± 0.0655	21.6291 ± 0.018	21.1479 ± 0.0177	20.7422 ± 0.0222	20.8139 ± 0.0927	20.1137 ± 0.2159	///	19.504 ± 0.2264

ID	RA	Dec	g	r	i	z	Y	J	H	K_s
504194446	66.099016	-51.118123	23.2181 ± 0.0612	21.0982 ± 0.0136	20.5919 ± 0.0111	20.255 ± 0.0145	20.0988 ± 0.0477	19.7879 ± 0.2517	19.4747 ± 0.2418	19.3972 ± 0.2774
504330828	67.145378	-50.373978	23.1291 ± 0.047	21.4316 ± 0.0119	21.097 ± 0.0127	20.813 ± 0.02	20.5226 ± 0.0553	20.6876 ± 0.3383	20.9076 ± 0.58	19.8315 ± 0.3205
504394690	66.525615	-49.260798	23.4748 ± 0.084	21.5242 ± 0.0237	21.1626 ± 0.0202	20.7947 ± 0.022	20.8201 ± 0.1049	19.8222 ± 0.1774	///	19.3278 ± 0.2493
504825888	66.295589	-60.190845	23.4268 ± 0.0619	21.5766 ± 0.0192	21.1377 ± 0.0204	20.8464 ± 0.0219	20.8598 ± 0.0862	20.3412 ± 0.2711	///	19.793 ± 0.2894
505013250	72.080434	-51.480723	22.8535 ± 0.0334	20.9016 ± 0.0095	20.4941 ± 0.0088	20.1545 ± 0.0115	20.0737 ± 0.0361	19.4464 ± 0.185	19.2072 ± 0.1731	19.0424 ± 0.1933
505018776	71.922491	-51.553863	24.6871 ± 0.151	22.8295 ± 0.0404	22.481 ± 0.0474	22.1188 ± 0.0708	21.8956 ± 0.1942	///	20.1492 ± 0.2341	19.7364 ± 0.3091
505028285	72.117204	-51.713201	22.8788 ± 0.0383	20.914 ± 0.0103	20.4363 ± 0.0104	20.0759 ± 0.0153	19.9913 ± 0.0502	19.7034 ± 0.2184	19.5768 ± 0.2826	19.0487 ± 0.2171
506017320	70.104975	-51.684777	23.7955 ± 0.0866	21.7769 ± 0.0226	21.2558 ± 0.0231	20.8174 ± 0.0265	20.6396 ± 0.0907	20.352 ± 0.255	20.2845 ± 0.3382	19.886 ± 0.2878
506153545	71.440457	-48.468766	23.8422 ± 0.0748	22.0488 ± 0.0183	21.6804 ± 0.0228	21.2587 ± 0.0364	21.3952 ± 0.0943	21.1499 ± 0.3377	///	20.2704 ± 0.3557
506329583	66.656908	-51.464977	23.8578 ± 0.1753	22.0277 ± 0.0259	21.6374 ± 0.0301	21.468 ± 0.0503	21.1333 ± 0.136	21.0297 ± 0.3731	20.9004 ± 0.4895	///
506345182	66.967637	-55.747027	24.3794 ± 0.1524	22.2277 ± 0.0236	21.7105 ± 0.0249	21.3227 ± 0.0318	21.2297 ± 0.1161	21.075 ± 0.3798	///	20.231 ± 0.475
506383847	71.82706	-49.119781	24.5496 ± 0.1903	22.52 ± 0.034	21.9882 ± 0.0337	21.8294 ± 0.049	21.8817 ± 0.2167	21.1532 ± 0.3435	///	20.7714 ± 0.4408
506534457	66.516394	-59.392889	22.8638 ± 0.0421	20.9491 ± 0.0089	20.5583 ± 0.0132	20.1807 ± 0.0111	19.9464 ± 0.0325	19.7133 ± 0.1204	///	19.0525 ± 0.1728
506537406	67.81106	-59.441728	23.8835 ± 0.108	21.8331 ± 0.0224	21.2802 ± 0.024	21.0069 ± 0.0313	20.6972 ± 0.0676	20.7452 ± 0.2988	///	20.0631 ± 0.4094
506572275	67.113463	-56.408528	23.6338 ± 0.0742	21.7324 ± 0.019	21.2609 ± 0.0186	20.9633 ± 0.0232	20.8565 ± 0.0851	19.8368 ± 0.2241	///	19.4777 ± 0.352
506589633	67.51748	-56.684982	23.3492 ± 0.0663	21.5182 ± 0.0151	21.0862 ± 0.0146	20.7987 ± 0.0234	20.5561 ± 0.077	20.2118 ± 0.2368	///	19.4276 ± 0.3205
506646930	70.326828	-50.439845	22.5345 ± 0.035	21.0373 ± 0.0109	20.8922 ± 0.0076	20.6646 ± 0.0092	20.5195 ± 0.0734	20.5782 ± 0.2394	20.1755 ± 0.3336	20.3265 ± 0.4575
506674710	70.499013	-50.804827	24.0668 ± 0.111	22.2647 ± 0.0309	21.9204 ± 0.0175	21.5804 ± 0.0188	21.7134 ± 0.1519	20.9526 ± 0.3146	///	20.5681 ± 0.3619
506674855	70.492258	-50.807343	23.6095 ± 0.0811	21.9397 ± 0.0226	21.6659 ± 0.0135	21.4152 ± 0.0157	21.2002 ± 0.104	21.2213 ± 0.4521	///	20.1676 ± 0.3064
506674909	70.483191	-50.807614	22.6307 ± 0.0341	21.71 ± 0.0187	21.8107 ± 0.0162	21.5835 ± 0.019	22.261 ± 0.2839	20.7457 ± 0.3673	///	20.1191 ± 0.3587
506675198	70.515975	-50.811698	22.8002 ± 0.04	21.0193 ± 0.0105	20.6184 ± 0.0057	20.322 ± 0.0062	20.3049 ± 0.0482	19.5661 ± 0.1436	19.7694 ± 0.2368	19.4277 ± 0.2112
507681715	67.217708	-53.525888	24.1343 ± 0.2575	21.8899 ± 0.0466	21.3924 ± 0.0455	21.2145 ± 0.0623	20.7942 ± 0.1663	20.4294 ± 0.2097	20.8157 ± 0.4821	///
507691551	68.038665	-53.69669	23.405 ± 0.0675	21.6883 ± 0.0188	21.4028 ± 0.0239	21.1287 ± 0.0322	21.2214 ± 0.1073	20.6715 ± 0.2216	///	20.4637 ± 0.4587
507780409	67.850037	-52.458756	23.0356 ± 0.0385	21.3203 ± 0.0121	21.0019 ± 0.0121	20.7608 ± 0.0172	20.6037 ± 0.0508	19.8961 ± 0.2066	20.0266 ± 0.3041	19.5255 ± 0.2173
507785363	67.470004	-52.559327	24.4789 ± 0.13	22.3368 ± 0.027	21.7613 ± 0.0222	21.4934 ± 0.0299	21.2488 ± 0.0884	20.6533 ± 0.3225	20.6363 ± 0.4087	///
507791066	67.361423	-52.654125	22.777 ± 0.0355	20.9881 ± 0.0115	20.5918 ± 0.0103	20.2706 ± 0.0138	20.1095 ± 0.0426	20.2512 ± 0.2678	19.6486 ± 0.2564	18.9594 ± 0.1986
507791331	67.519725	-52.659509	22.5887 ± 0.0331	20.5847 ± 0.0091	20.0805 ± 0.0075	19.7081 ± 0.0098	19.4835 ± 0.028	19.2903 ± 0.1538	18.7168 ± 0.1575	18.3319 ± 0.1223
507791530	67.159439	-52.661824	24.3771 ± 0.1232	22.2965 ± 0.0274	21.7254 ± 0.0219	21.3829 ± 0.0295	21.0487 ± 0.0816	20.8737 ± 0.337	20.3442 ± 0.4227	19.78 ± 0.3309
507803985	67.325717	-52.880165	23.6147 ± 0.0647	21.7564 ± 0.018	21.3175 ± 0.0159	21.0028 ± 0.018	20.8713 ± 0.0692	20.516 ± 0.2842	19.8374 ± 0.2882	20.1467 ± 0.4506
507810919	66.8646	-52.989845	23.2527 ± 0.0481	21.3523 ± 0.0131	20.9483 ± 0.0126	20.631 ± 0.0177	20.4023 ± 0.0505	20.0732 ± 0.2434	19.9002 ± 0.3387	19.4536 ± 0.3144
507820438	67.1093	-53.141275	22.2814 ± 0.0225	20.4405 ± 0.0068	20.0207 ± 0.007	19.6673 ± 0.0072	19.5324 ± 0.0272	19.2047 ± 0.1324	18.9817 ± 0.1372	18.647 ± 0.1656
508217521	69.432208	-58.182331	24.6135 ± 0.1574	22.8099 ± 0.0352	22.486 ± 0.0399	22.1762 ± 0.0578	22.3086 ± 0.2506	21.7479 ± 0.2708	///	21.4014 ± 0.7731
508601732	69.941686	-51.027099	24.8183 ± 0.329	22.1654 ± 0.0476	21.3868 ± 0.0203	20.8769 ± 0.0232	20.6581 ± 0.0926	20.7992 ± 0.3906	19.6832 ± 0.2352	19.9412 ± 0.3366
618652137	358.88296	-54.30947	22.8707 ± 0.0532	21.0181 ± 0.0112	20.5872 ± 0.0106	20.1606 ± 0.0143	20.085 ± 0.0485	19.9487 ± 0.2035	19.8445 ± 0.3877	18.9431 ± 0.1907
618654757	358.67695	-54.356158	23.549 ± 0.137	21.8112 ± 0.0272	21.4459 ± 0.0274	21.1584 ± 0.0431	21.2514 ± 0.1468	21.0447 ± 0.3029	20.8919 ± 0.477	21.2233 ± 1.0699
618660654	359.14404	-54.461467	22.0072 ± 0.0258	20.3997 ± 0.0077	20.1682 ± 0.009	19.8417 ± 0.0127	19.8875 ± 0.0355	19.6534 ± 0.1604	20.4625 ± 0.7439	19.1208 ± 0.2385
618663972	358.73193	-54.517818	22.8714 ± 0.045	20.9306 ± 0.0113	20.5016 ± 0.0106	20.0363 ± 0.0137	20.0142 ± 0.037	19.4945 ± 0.1769	19.2994 ± 0.1598	18.8724 ± 0.155
618664093	359.04338	-54.519852	23.1158 ± 0.0456	21.2542 ± 0.0124	20.818 ± 0.0123	20.4231 ± 0.0171	20.4425 ± 0.0485	19.9913 ± 0.1884	19.9082 ± 0.4418	19.3846 ± 0.2939
618664306	359.09017	-54.523087	22.9282 ± 0.0433	21.0268 ± 0.0135	20.5623 ± 0.0124	20.2491 ± 0.0187	20.3538 ± 0.0456	19.8083 ± 0.1913	20.1177 ± 0.5618	19.2618 ± 0.2835

ID	RA	Dec	g	r	i	z	Y	J	H	K_s
618667069	358.8217	-54.567628	23.8333 ± 0.1179	21.8771 ± 0.0233	21.5924 ± 0.0206	21.0456 ± 0.0259	20.9855 ± 0.105	20.6079 ± 0.323	20.1235 ± 0.4174	19.4716 ± 0.2758
618667272	358.80469	-54.571019	23.2565 ± 0.0703	21.2546 ± 0.0138	20.8998 ± 0.0135	20.4648 ± 0.0184	20.735 ± 0.1075	19.8864 ± 0.2031	19.8565 ± 0.2992	19.0797 ± 0.2255

Appendix C

UPR16 Ethics Form and Ethics Committee Letter

The following pages include the required UPR16 Ethics Form properly filled and the letter of the Ethics Committee confirming the favourable opinion.

FORM UPR16

Research Ethics Review Checklist

Please include this completed form as an appendix to your thesis (see the Research Degrees Operational Handbook for more information

UNIVERSITY OF PORTSMOUTH

Postgraduate Research Student (PGRS) Information			**Student ID:**	788652
PGRS Name:	Pierandrea Guarnieri			
Department:	Institute of Cosmology and Gravitation (Tech)	**First Supervisor:**	Prof. Claudia Maraston	
Start Date: (or progression date for Prof Doc students)	1st October 2015			
Study Mode and Route:	Part-time ☐ Full-time ☑	MPhil ☐ PhD ☑	MD ☐ Professional Doctorate ☐	

Title of Thesis:	Galaxy Evolution at High Redshift Exploiting Large Galaxy Surveys
Thesis Word Count: (excluding ancillary data)	35429

If you are unsure about any of the following, please contact the local representative on your Faculty Ethics Committee for advice. Please note that it is your responsibility to follow the University's Ethics Policy and any relevant University, academic or professional guidelines in the conduct of your study

Although the Ethics Committee may have given your study a favourable opinion, the final responsibility for the ethical conduct of this work lies with the researcher(s).

UKRIO Finished Research Checklist:
(If you would like to know more about the checklist, please see your Faculty or Departmental Ethics Committee rep or see the online version of the full checklist at: http://www.ukrio.org/what-we-do/code-of-practice-for-research/)

a) Have all of your research and findings been reported accurately, honestly and within a reasonable time frame?	YES ☑ NO ☐
b) Have all contributions to knowledge been acknowledged?	YES ☑ NO ☐
c) Have you complied with all agreements relating to intellectual property, publication and authorship?	YES ☑ NO ☐
d) Has your research data been retained in a secure and accessible form and will it remain so for the required duration?	YES ☑ NO ☐
e) Does your research comply with all legal, ethical, and contractual requirements?	YES ☑ NO ☐

Candidate Statement:

I have considered the ethical dimensions of the above named research project, and have successfully obtained the necessary ethical approval(s)

Ethical review number(s) from Faculty Ethics Committee (or from NRES/SCREC):	68CB-0D78-A019-2A46-5840-7461-8369-A749

If you have *not* submitted your work for ethical review, and/or you have answered 'No' to one or more of questions a) to e), please explain below why this is so:

Signed *(PGRS)*:	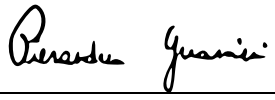	**Date:** 29th March 2019

University of Portsmouth

Certificate of Ethics Review

Project Title:	Galaxy Evolution at High Redshift
User ID:	788652
Name:	Pierandrea Guarnieri
Application Date:	23/09/2016 10:34:09

You must download your certificate, print a copy and keep it as a record of this review.

It is your responsibility to adhere to the University Ethics Policy and any Department/School or professional guidelines in the conduct of your study including relevant guidelines regarding health and safety of researchers and University Health and Safety Policy.

It is also your responsibility to follow University guidance on Data Protection Policy:

- General guidance for all data protection issues
- University Data Protection Policy

You are reminded that as a University of Portsmouth Researcher you are bound by the UKRIO Code of Practice for Research; any breach of this code could lead to action being taken following the University's Procedure for the Investigation of Allegations of Misconduct in Research.

Any changes in the answers to the questions reflecting the design, management or conduct of the research over the course of the project must be notified to the Faculty Ethics Committee. **Any changes that affect the answers given in the questionnaire, not reported to the Faculty Ethics Committee, will invalidate this certificate.**

This ethical review should not be used to infer any comment on the academic merits or methodology of the project. If you have not already done so, you are advised to develop a clear protocol/proposal and ensure that it is independently reviewed by peers or others of appropriate standing. A favourable ethical opinion should not be perceived as permission to proceed with the research; there might be other matters of governance which require further consideration including the agreement of any organisation hosting the research.

GovernanceChecklist
A1-BriefDescriptionOfProject: My project involves studying galaxy evolution, with a special focus on high redshift objects. I have worked so far using data from the Dark Energy Survey that allowed me to find strong candidates for very massive high redshift (z~4) galaxies that, despite very rare, were expected to be found with this survey for the first time (thanks to its size, 5 million galaxies used by me and 300 million at completion, and depth). The next steps will include using data from the deeper SERVS observation program (with around 650 thousand galaxies) to calculate their redshifts and study their mass functions (redshifts will vary from low values to even higher than 4).

During the development of my project so far a series of additional skills have also been acquired, such as presentation and coding ones (as well as others that include for example time management, project management, team work, planning). Additionally, so far, some outreach activities were performed, posters were presented (GRADnet Summer School), and short talks were given (DES Collaboration Meeting at Stanford, SERVS Collaboration Meeting at Marseille Laboratory of Astrophysics, and the Faculty Conference in Portsmouth).
A2-Faculty: Technology
A3-VoluntarilyReferToFEC: No
A5-AlreadyExternallyReviewed: No
B1-HumanParticipants: No
HumanParticipantsDefinition
B2-HumanParticipantsConfirmation: Yes
C6-SafetyRisksBeyondAssessment: No
SafetyRisksBeyondAssessmentWarning
D2-PhysicalEcologicalDamage: No
PhysicalEcologicalDamageWarning
D4-HistoricalOrCulturalDamage: No
HistoricalOrCulturalDamageWarning
E1-ContentiousOrIllegal: No
ContentiousOrIllegalWarning
E2-SociallySensitiveIssues: No
SociallySensitiveWarning
F1-InvolvesAnimals: No
InvolvesAnimalsWarning
F2-HarmfulToThirdParties: No
HarmfulToThirdPartiesWarning
G1-ConfirmReadEthicsPolicy: Confirmed
G2-ConfirmReadUKRIOCodeOfPractice: Confirmed
G3-ConfirmReadConcordatToSupportResearchIntegrity: Confirmed
G4-ConfirmedCorrectInformation: Confirmed

Bibliography

T. M. C. Abbott et al. The Dark Energy Survey Data Release 1. *ArXiv e-prints*, Jan. 2018.

I. K. Baldry et al. On the galaxy stellar mass function, the mass-metallicity relation and the implied baryonic mass function. *MNRAS*, 388:945–959, Aug 2008. doi: 10.1111/j.1365-2966.2008.13348.x.

I. K. Baldry et al. Galaxy And Mass Assembly (GAMA): the galaxy stellar mass function at $z <; 0.06$. *MNRAS*, 421:621–634, Mar 2012. doi: 10.1111/j.1365-2966.2012.20340.x.

M. Banerji et al. Photometric redshifts for the Dark Energy Survey and VISTA and implications for large-scale structure. *MNRAS*, 386:1219–1233, May 2008. doi: 10.1111/j.1365-2966.2008.13095.x.

M. Banerji et al. Combining Dark Energy Survey Science Verification data with near-infrared data from the ESO VISTA Hemisphere Survey. *MNRAS*, 446:2523–2539, Jan. 2015a. doi: 10.1093/mnras/stu2261.

M. Banerji et al. Heavily reddened type 1 quasars at $z > 2$ - I. Evidence for significant obscured black hole growth at the highest quasar luminosities. *MNRAS*, 447:3368–3389, Mar. 2015b. doi: 10.1093/mnras/stu2649.

C. M. Baugh. A primer on hierarchical galaxy formation: the semi-analytical approach. *Reports on Progress in Physics*, 69:3101–3156, Dec 2006. doi: 10.1088/0034-4885/69/12/R02.

P. S. Behroozi et al. The Average Star Formation Histories of Galaxies in Dark Matter Halos from z = 0-8. *ApJ*, 770:57, June 2013. doi: 10.1088/0004-637X/770/1/57.

E. F. Bell et al. The Optical and Near-Infrared Properties of Galaxies. I. Luminosity and Stellar Mass Functions. *The Astrophysical Journal Supplement Series*, 149:289–312, Dec 2003. doi: 10.1086/378847.

M. Bolzonella, J.-M. Miralles, and R. Pelló. Photometric redshifts based on standard SED fitting procedures. *A&A*, 363:476–492, Nov. 2000.

P. Bouchet et al. The visible and infrared extinction law and the gas-to-dust ratio in the Small Magellanic Cloud. *A&A*, 149:330–336, Aug. 1985.

G. B. Brammer, P. G. van Dokkum, and P. Coppi. EAZY: A Fast, Public Photometric Redshift Code. *ApJ*, 686:1503–1513, Oct. 2008. doi: 10.1086/591786.

K. Bundy et al. The Mass Assembly History of Field Galaxies: Detection of an Evolving Mass Limit for Star-Forming Galaxies. *ApJ*, 651:120–141, Nov 2006. doi: 10.1086/507456.

K. Bundy et al. The Stripe 82 Massive Galaxy Project. III. A Lack of Growth among Massive Galaxies. *ApJ*, 851:34, Dec 2017. doi: 10.3847/1538-4357/aa9896.

D. Calzetti et al. The Dust Content and Opacity of Actively Star-forming Galaxies. *ApJ*, 533:682–695, Apr. 2000. doi: 10.1086/308692.

K. I. Caputi et al. The Nature of Extremely Red H - [4.5] > 4 Galaxies Revealed with SEDS and CANDELS. *ApJ*, 750:L20, May 2012. doi: 10.1088/2041-8205/750/1/L20.

K. I. Caputi et al. Spitzer Bright, UltraVISTA Faint Sources in COSMOS: The Contribution to the Overall Population of Massive Galaxies at z = 3-7. *ApJ*, 810:73, Sep 2015a. doi: 10.1088/0004-637X/810/1/73.

K. I. Caputi et al. Spitzer Bright, UltraVISTA Faint Sources in COSMOS: The Contribution to the Overall Population of Massive Galaxies at z = 3-7. *ApJ*, 810:73, Sept. 2015b. doi: 10.1088/0004-637X/810/1/73.

A. Cimatti, E. Daddi, and A. Renzini. Mass downsizing and "top-down" assembly of early-type galaxies. *A&A*, 453:L29–L33, July 2006. doi: 10.1051/0004-6361:20065155.

A. Cimatti et al. Old galaxies in the young Universe. *Nature*, 430:184–187, July 2004. doi: 10.1038/nature02668.

D. Coe, L. Bradley, and A. Zitrin. Frontier Fields: High-redshift Predictions and Early Results. *ApJ*, 800:84, Feb. 2015. doi: 10.1088/0004-637X/800/2/84.

C. J. Conselice et al. The properties and evolution of a K-band selected sample of massive galaxies at $z \sim 0.4 - 2$ in the Palomar/DEEP2 survey. *MNRAS*, 381:962–986, Nov. 2007. doi: 10.1111/j.1365-2966.2007.12316.x.

L. L. Cowie and A. J. Barger. An Integrated Picture of Star Formation, Metallicity Evolution, and Galactic Stellar Mass Assembly. *ApJ*, 686:72-116, Oct. 2008. doi: 10.1086/591176.

L. L. Cowie, A. Songaila, and A. J. Barger. Evidence for a Gradual Decline in the Universal Rest-Frame Ultraviolet Luminosity Density for Z ¡ 1. *AJ*, 118:603–612, Aug. 1999. doi: 10.1086/300959.

L. L. Cowie et al. New Insight on Galaxy Formation and Evolution From Keck Spectroscopy of the Hawaii Deep Fields. *AJ*, 112:839, Sept. 1996. doi: 10.1086/118058.

N. J. G. Cross et al. The VISTA Science Archive. *A&A*, 548:A119, Dec. 2012. doi: 10.1051/0004-6361/201219505.

D. J. Croton et al. Semi-Analytic Galaxy Evolution (SAGE): Model Calibration and Basic Results. *ApJS*, 222:22, Feb. 2016. doi: 10.3847/0067-0049/222/2/22.

E. Daddi et al. Passively Evolving Early-Type Galaxies at $1.4 < z < 2.5$ in the Hubble Ultra Deep Field. *ApJ*, 626:680–697, June 2005. doi: 10.1086/430104.

L. J. M. Davies et al. Detecting massive galaxies at high redshift using the Dark Energy Survey. *MNRAS*, 434:296–312, Sept. 2013. doi: 10.1093/mnras/stt1018.

K. S. Dawson et al. The Baryon Oscillation Spectroscopic Survey of SDSS-III. *AJ*, 145:10, Jan. 2013. doi: 10.1088/0004-6256/145/1/10.

G. De Lucia and J. Blaizot. The hierarchical formation of the brightest cluster galaxies. *MNRAS*, 375:2–14, Feb. 2007. doi: 10.1111/j.1365-2966.2006.11287.x.

G. De Lucia et al. The formation history of elliptical galaxies. *MNRAS*, 366:499–509, Feb. 2006. doi: 10.1111/j.1365-2966.2005.09879.x.

L. S. Douglas et al. Photometric selection of $z \sim 5$ Lyman break galaxies in the ESO Remote Galaxy Survey. *MNRAS*, 400:561–574, Dec. 2009. doi: 10.1111/j.1365-2966.2009.15482.x.

A. Dressler. Galaxy morphology in rich clusters - Implications for the formation and evolution of galaxies. *ApJ*, 236:351–365, Mar. 1980. doi: 10.1086/157753.

O. J. Eggen, D. Lynden-Bell, and A. R. Sandage. Evidence from the motions of old stars that the Galaxy collapsed. *ApJ*, 136:748, Nov. 1962. doi: 10.1086/147433.

J. Etherington et al. Environmental dependence of the galaxy stellar mass function in the Dark Energy Survey Science Verification Data. *MNRAS*, 466:228–247, Apr. 2017. doi: 10.1093/mnras/stw3069.

S. M. Faber et al. Galaxy Luminosity Functions to $z \sim 1$ from DEEP2 and COMBO-17: Implications for Red Galaxy Formation. *ApJ*, 665:265–294, Aug. 2007. doi: 10.1086/519294.

M. Furlong et al. Size evolution of normal and compact galaxies in the EAGLE simulation. *MNRAS*, 465:722–738, Feb 2017. doi: 10.1093/mnras/stw2740.

K. Glazebrook et al. A massive, quiescent galaxy at redshift of z=3.717. *ArXiv e-prints*, Feb. 2017.

D. Goddard et al. SDSS-IV MaNGA: Spatially resolved star formation histories in galaxies as a function of galaxy mass and type. *MNRAS*, 466: 4731–4758, Apr. 2017. doi: 10.1093/mnras/stw3371.

V. Gonzalez-Perez et al. Massive, red galaxies in a hierarchical universe - I. Counts of extremely red objects and basic properties. *MNRAS*, 398: 497–514, Sept. 2009. doi: 10.1111/j.1365-2966.2009.14397.x.

V. Gonzalez-Perez et al. How sensitive are predicted galaxy luminosities to the choice of stellar population synthesis model? *MNRAS*, 439:264–283, Mar. 2014. doi: 10.1093/mnras/stt2410.

A. Grazian et al. The galaxy stellar mass function at 3.5 $\leq$z $\leq$ 7.5 in the CANDELS/UDS, GOODS-South, and HUDF fields. *A&A*, 575:A96, Mar 2015. doi: 10.1051/0004-6361/201424750.

P. Guarnieri et al. Candidate massive galaxies at $z \sim 4$ in the Dark Energy Survey. *MNRAS*, 483:3060–3081, Mar 2019. doi: 10.1093/mnras/sty3305.

Q. Guo et al. From dwarf spheroidals to cD galaxies: simulating the galaxy population in a ΛCDM cosmology. *MNRAS*, 413:101–131, May 2011. doi: 10.1111/j.1365-2966.2010.18114.x.

Y. Guo. UV Snapshot of Low-redshift Massive Star-forming Galaxies: Searching for the Analogs of High-redshift Clumpy Galaxies. HST Proposal, Oct. 2013.

T. Hashimoto et al. The onset of star formation 250 million years after the Big Bang. *Nature*, 557:392–395, May 2018. doi: 10.1038/s41586-018-0117-z.

B. M. B. Henriques, S. D. M. White, P. A. Thomas, R. Angulo, Q. Guo, G. Lemson, V. Springel, and R. Overzier. Galaxy formation in the Planck cosmology - I. Matching the observed evolution of star formation rates, colours and stellar masses. *MNRAS*, 451:2663–2680, Aug. 2015. doi: 10.1093/mnras/stv705.

B. Hoyle et al. Dark Energy Survey Year 1 Results: Redshift distributions of the weak lensing source galaxies. *ArXiv e-prints*, Aug. 2017.

O. Ilbert et al. Mass assembly in quiescent and star-forming galaxies since $z \sim 4$ from UltraVISTA. *A&A*, 556:A55, Aug 2013a. doi: 10.1051/0004-6361/201321100.

O. Ilbert et al. Mass assembly in quiescent and star-forming galaxies since $z \sim 4$ from UltraVISTA DR1 in the COSMOS field. In L. Cambresy, F. Martins, E. Nuss, and A. Palacios, editors, *SF2A-2013: Proceedings of the Annual meeting of the French Society of Astronomy and Astrophysics*, pages 545–548, Nov. 2013b.

M. Jauzac et al. Hubble Frontier Fields: a high-precision strong-lensing analysis of the massive galaxy cluster Abell 2744 using ∼ 180 multiple images. *MNRAS*, 452:1437–1446, Sept. 2015. doi: 10.1093/mnras/stv1402.

G. Kauffmann and M. Haehnelt. A unified model for the evolution of galaxies and quasars. *MNRAS*, 311:576–588, Jan 2000. doi: 10.1046/j.1365-8711.2000.03077.x.

G. Kauffmann et al. The Formation and Evolution of Galaxies Within Merging Dark Matter Haloes. *MNRAS*, 264:201, Sept. 1993. doi: 10.1093/mnras/264.1.201.

E. J. Kim et al. A hybrid ensemble learning approach to star-galaxy classification. *MNRAS*, 453:507–521, Oct. 2015. doi: 10.1093/mnras/stv1608.

A. Knebe et al. Cosmic CARNage I: on the calibration of galaxy formation models. *MNRAS*, 475:2936–2954, Apr. 2018. doi: 10.1093/mnras/stx3274.

M. Kriek and C. Conroy. The Dust Attenuation Law in Distant Galaxies: Evidence for Variation with Spectral Type. *ApJ*, 775:L16, Sept. 2013. doi: 10.1088/2041-8205/775/1/L16.

M. Kriek et al. A massive, quiescent, population II galaxy at a redshift of 2.1. *Nature*, 540:248–251, Dec. 2016. doi: 10.1038/nature20570.

C. G. Lacey et al. A unified multiwavelength model of galaxy formation. *MNRAS*, 462:3854–3911, Nov. 2016. doi: 10.1093/mnras/stw1888.

M. Lacy et al. A Subarcsecond Near-infrared View of Massive Galaxies at $z > 1$ with Gemini Multi-conjugate Adaptive Optics. *ApJ*, 864:8, Sep 2018. doi: 10.3847/1538-4357/aad27d.

C. d. P. Lagos et al. Predictions for the CO emission of galaxies from a coupled simulation of galaxy formation and photon-dominated regions. *MNRAS*, 426:2142–2165, Nov 2012. doi: 10.1111/j.1365-2966.2012.21905.x.

C. D. P. Lagos et al. Which galaxies dominate the neutral gas content of the Universe? *MNRAS*, 440:920–941, May 2014. doi: 10.1093/mnras/stu266.

N. Laporte et al. Young Galaxy Candidates in the Hubble Frontier Fields. III. MACS J0717.5+3745. *ApJ*, 820:98, Apr. 2016a. doi: 10.3847/0004-637X/820/2/98.

N. Laporte et al. Photometric and Spectroscopic analysis of lensed reionising sources at the frontier of the Universe. In C. Reylé, J. Richard, L. Cambrésy, M. Deleuil, E. Pécontal, L. Tresse, and I. Vauglin, editors, *SF2A-2016: Proceedings of the Annual meeting of the French Society of Astronomy and Astrophysics*, pages 411–415, Dec. 2016b.

K.-S. Lee et al. The Average Physical Properties and Star Formation Histories of the UV-brightest Star-forming Galaxies at z ˜3.7. *ApJ*, 733:99, Jun 2011. doi: 10.1088/0004-637X/733/2/99.

I. Lonoce et al. Old age and supersolar metallicity in a massive $z \sim 1.4$ early-type galaxy from VLT/X-Shooter spectroscopy. *MNRAS*, 454:3912–3919, Dec. 2015. doi: 10.1093/mnras/stv2150.

C. Mancini et al. Searching for massive galaxies at $z > 3.5$ in GOODS-North. *A&A*, 500:705–723, June 2009. doi: 10.1051/0004-6361/200810630.

C. Maraston. Evolutionary population synthesis: models, analysis of the ingredients and application to high-z galaxies. *MNRAS*, 362:799–825, Sept. 2005. doi: 10.1111/j.1365-2966.2005.09270.x.

C. Maraston et al. Evidence for TP-AGB Stars in High-Redshift Galaxies, and Their Effect on Deriving Stellar Population Parameters. *ApJ*, 652: 85–96, Nov. 2006. doi: 10.1086/508143.

C. Maraston et al. Star formation rates and masses of $z \sim 2$ galaxies from multicolour photometry. *MNRAS*, 407:830–845, Sept. 2010. doi: 10.1111/j.1365-2966.2010.16973.x.

C. Maraston et al. Stellar masses of SDSS-III/BOSS galaxies at $z \sim 0.5$ and constraints to galaxy formation models. *MNRAS*, 435:2764–2792, Nov. 2013. doi: 10.1093/mnras/stt1424.

D. Marchesini et al. The Evolution of the Stellar Mass Function of Galaxies from z = 4.0 and the First Comprehensive Analysis of its Uncertainties: Evidence for Mass-Dependent Evolution. *ApJ*, 701:1765–1796, Aug 2009. doi: 10.1088/0004-637X/701/2/1765.

D. Marchesini et al. Measuring the Rest-Frame UV Properties and the Number Density of Massive Galaxies at $3 < z < 4$. NOAO Proposal, Aug. 2010.

Z. C. Marsan et al. A Spectroscopic Follow-up Program of Very Massive Galaxies at $3 < z < 4$: Confirmation of Spectroscopic Redshifts, and a High Fraction of Powerful AGNs. *ApJ*, 842:21, June 2017. doi: 10.3847/1538-4357/aa7206.

J. C. Mauduit et al. The Spitzer Extragalactic Representative Volume Survey (SERVS): Survey Definition and Goals. *Publications of the Astronomical Society of the Pacific*, 124:714, Jul 2012. doi: 10.1086/666945.

R. McMahon. The VISTA Hemisphere Survey(VHS) Science Goals and Status. In *Science from the Next Generation Imaging and Spectroscopic Surveys*, page 37, Oct. 2012.

D. Mehlert, D. Thomas, R. P. Saglia, R. Bender, and G. Wegner. Spatially resolved spectroscopy of Coma cluster early-type galaxies. III. The stellar population gradients. *A&A*, 407:423–435, Aug. 2003. doi: 10.1051/0004-6361:20030886.

P. Melchior et al. Mass and galaxy distributions of four massive galaxy clusters from Dark Energy Survey Science Verification data. *MNRAS*, 449:2219–2238, May 2015. doi: 10.1093/mnras/stv398.

E. Merlin et al. Chasing passive galaxies in the early Universe: a critical analysis in CANDELS GOODS-South. *MNRAS*, 473:2098–2123, Jan. 2018. doi: 10.1093/mnras/stx2385.

A. Mortlock et al. Deconstructing the galaxy stellar mass function with UKIDSS and CANDELS: the impact of colour, structure and environment. *MNRAS*, 447:2–24, Feb. 2015. doi: 10.1093/mnras/stu2403.

J. Moustakas et al. PRIMUS: Constraints on Star Formation Quenching and Galaxy Merging, and the Evolution of the Stellar Mass Function from z = 0-1. *ApJ*, 767:50, Apr 2013. doi: 10.1088/0004-637X/767/1/50.

A. Muzzin et al. The Evolution of the Stellar Mass Functions of Star-forming and Quiescent Galaxies to z = 4 from the COSMOS/UltraVISTA Survey. *ApJ*, 777:18, Nov 2013a. doi: 10.1088/0004-637X/777/1/18.

A. Muzzin et al. The Evolution of the Stellar Mass Functions of Star-forming and Quiescent Galaxies to z = 4 from the COSMOS/UltraVISTA Survey. *ApJ*, 777:18, Nov. 2013b. doi: 10.1088/0004-637X/777/1/18.

H. Nayyeri et al. A Study of Massive and Evolved Galaxies at High Redshift. *ApJ*, 794:68, Oct. 2014. doi: 10.1088/0004-637X/794/1/68.

K. Nyland et al. An Application of Multi-band Forced Photometry to One Square Degree of SERVS: Accurate Photometric Redshifts and Implications for Future Science. *The Astrophysical Journal Supplement Series*, 230:9, May 2017. doi: 10.3847/1538-4365/aa6fed.

M. Onodera et al. Deep Near-infrared Spectroscopy of Passively Evolving Galaxies at $z > 1.4$. *ApJ*, 755:26, Aug. 2012. doi: 10.1088/0004-637X/755/1/26.

S. Perlmutter et al. Measurements of Ω and Λ from 42 High-Redshift Supernovae. *ApJ*, 517:565–586, Jun 1999. doi: 10.1086/307221.

J. Pforr et al. Recovering galaxy stellar population properties from broad-band spectral energy distribution fitting. *MNRAS*, 422:3285–3326, June 2012. doi: 10.1111/j.1365-2966.2012.20848.x.

J. Pforr et al. Recovering galaxy stellar population properties from broad-band spectral energy distribution fitting - II. The case with unknown redshift. *MNRAS*, 435:1389–1425, Oct. 2013. doi: 10.1093/mnras/stt1382.

J. Pforr et al. Photometric redshifts for galaxies in the Spitzer Extragalactic Representative Volume Survey (SERVS). *MNRAS*, 483(3):3168–3195, 11 2018. ISSN 0035-8711. doi: 10.1093/mnras/sty3075. URL `https://doi.org/10.1093/mnras/sty3075`.

A. Pipino et al. The Formation of Globular Cluster Systems in Massive Elliptical Galaxies: Globular Cluster Multimodality from Radial Variation of Stellar Populations. *ApJ*, 665:295–305, Aug. 2007. doi: 10.1086/519546.

Planck Collaboration et al. Planck 2018 results. VI. Cosmological parameters. *arXiv e-prints*, art. arXiv:1807.06209, Jul 2018.

L. Pozzetti et al. zCOSMOS - 10k-bright spectroscopic sample. The bimodality in the galaxy stellar mass function: exploring its evolution with redshift. *A&A*, 523:A13, Nov 2010a. doi: 10.1051/0004-6361/200913020.

L. Pozzetti et al. zCOSMOS - 10k-bright spectroscopic sample. The bimodality in the galaxy stellar mass function: exploring its evolution with redshift. *A&A*, 523:A13, Nov. 2010b. doi: 10.1051/0004-6361/200913020.

W. H. Press and P. Schechter. Formation of Galaxies and Clusters of Galaxies by Self-Similar Gravitational Condensation. *ApJ*, 187:425–438, Feb. 1974. doi: 10.1086/152650.

M. L. Prevot et al. The typical interstellar extinction in the Small Magellanic Cloud. *A&A*, 132:389–392, Mar. 1984.

S. L. Reed et al. Eight new luminous $z > 6$ quasars discovered via SED model fitting of VISTA, WISE and Dark Energy Survey Year 1 observations. *MNRAS*, 468:4702–4718, July 2017. doi: 10.1093/mnras/stx728.

E. Ricciardelli and A. Franceschini. GECO: Galaxy Evolution COde - A new semi-analytical model of galaxy formation. *A&A*, 518:A14, July 2010. doi: 10.1051/0004-6361/200913374.

A. G. Riess et al. Observational Evidence from Supernovae for an Accelerating Universe and a Cosmological Constant. *AJ*, 116:1009–1038, Sep 1998. doi: 10.1086/300499.

B. M. Rossetto et al. The Dark Energy Survey: Prospects for Resolved Stellar Populations. *AJ*, 141:185, June 2011. doi: 10.1088/0004-6256/141/6/185.

M. Rowan-Robinson et al. The star formation rate density from z = 1 to 6. *MNRAS*, 461:1100–1111, Sept. 2016. doi: 10.1093/mnras/stw1169.

V. C. Rubin et al. Rotation velocities of 16 SA galaxies and a comparison of Sa, Sb, and SC rotation properties. *ApJ*, 289:81–98, Feb. 1985. doi: 10.1086/162866.

C. Sánchez et al. Photometric redshift analysis in the Dark Energy Survey Science Verification data. *MNRAS*, 445:1482–1506, Dec. 2014. doi: 10.1093/mnras/stu1836.

S. F. Sánchez et al. CALIFA, the Calar Alto Legacy Integral Field Area survey. I. Survey presentation. *A&A*, 538:A8, Feb. 2012. doi: 10.1051/0004-6361/201117353.

P. Santini et al. Star formation and mass assembly in high redshift galaxies. *A&A*, 504:751–767, Sept. 2009. doi: 10.1051/0004-6361/200811434.

M. Schmidt. Space Distribution and Luminosity Functions of Quasi-Stellar Radio Sources. *ApJ*, 151:393, Feb. 1968. doi: 10.1086/149446.

C. Schreiber et al. Jekyll & Hyde: quiescence and extreme obscuration in a pair of massive galaxies 1.5 Gyr after the Big Bang. *A&A*, 611:A22, Mar. 2018. doi: 10.1051/0004-6361/201731917.

J. M. Simpson et al. An Imperfectly Passive Nature: Bright Submillimeter Emission from Dust-obscured Star Formation in the $z = 3.717$ Passive System, ZF 20115. *ApJ*, 844:L10, July 2017. doi: 10.3847/2041-8213/aa7cf2.

L. R. Spitler et al. Exploring the z = 3-4 Massive Galaxy Population with ZFOURGE: The Prevalence of Dusty and Quiescent Galaxies. *ApJ*, 787: L36, June 2014. doi: 10.1088/2041-8205/787/2/L36.

D. P. Stark et al. The Evolutionary History of Lyman Break Galaxies Between Redshift 4 and 6: Observing Successive Generations of Massive Galaxies in Formation. *ApJ*, 697:1493–1511, Jun 2009. doi: 10.1088/0004-637X/697/2/1493.

M. Stefanon et al. What are the Progenitors of Compact, Massive, Quiescent Galaxies at z = 2.3? The Population of Massive Galaxies at $z > 3$ from NMBS and CANDELS. *ApJ*, 768:92, May 2013. doi: 10.1088/0004-637X/768/1/92.

C. M. S. Straatman et al. A Substantial Population of Massive Quiescent Galaxies at $z \sim 4$ from ZFOURGE. *ApJ*, 783:L14, Mar. 2014. doi: 10.1088/2041-8205/783/1/L14.

The Dark Energy Survey Collaboration. The Dark Energy Survey. *ArXiv Astrophysics e-prints*, Oct. 2005.

D. Thomas et al. The Epochs of Early-Type Galaxy Formation as a Function of Environment. *ApJ*, 621:673–694, Mar. 2005. doi: 10.1086/426932.

D. Thomas et al. Environment and self-regulation in galaxy formation. *MNRAS*, 404:1775–1789, June 2010. doi: 10.1111/j.1365-2966.2010.16427.x.

M. Trenti and M. Stiavelli. Cosmic Variance and Its Effect on the Luminosity Function Determination in Deep High-z Surveys. *ApJ*, 676:767–780, Apr. 2008. doi: 10.1086/528674.

D. A. Wake et al. The 2df SDSS LRG and QSO survey: evolution of the luminosity function of luminous red galaxies to z = 0.6. *MNRAS*, 372: 537–550, Oct. 2006. doi: 10.1111/j.1365-2966.2006.10831.x.

L. Wang et al. The galaxy population in cold and warm dark matter cosmologies. *ArXiv e-prints*, Dec. 2016.

K. E. Whitaker et al. Quiescent Galaxies in the 3D-HST Survey: Spectroscopic Confirmation of a Large Number of Galaxies with Relatively Old Stellar Populations at $z \sim 2$. *ApJ*, 770:L39, June 2013. doi: 10.1088/2041-8205/770/2/L39.

S. D. M. White and C. S. Frenk. Galaxy formation through hierarchical clustering. *ApJ*, 379:52–79, Sept. 1991. doi: 10.1086/170483.

S. D. M. White and M. J. Rees. Core condensation in heavy halos - A two-stage theory for galaxy formation and clustering. *MNRAS*, 183:341–358, May 1978. doi: 10.1093/mnras/183.3.341.

H. Yan et al. High-Redshift Extremely Red Objects in the Hubble Space Telescope Ultra Deep Field Revealed by the GOODS Infrared Array Camera Observations. *ApJ*, 616:63–70, Nov. 2004. doi: 10.1086/424898.

D. Zhao et al. Evolution of the brightest cluster galaxies: the influence of morphology, stellar mass and environment. *MNRAS*, 453:4444–4455, Nov 2015. doi: 10.1093/mnras/stv1940.

W. Zheng et al. Young Galaxy Candidates in the Hubble Frontier Fields. I. A2744. *ApJ*, 795:93, Nov. 2014. doi: 10.1088/0004-637X/795/1/93.